Technical University of Denmark

DTU

Analysis of flow maldistribution in fin-and-tube evaporators for residential air-conditioning systems

Kærn, Martin Ryhl; Elmegaard, Brian

Publication date:
2011

Document Version
Publisher's PDF, also known as Version of record

[Link back to DTU Orbit](#)

DTU Library
Technical Information Center of Denmark

Analysis of flow maldistribution
in fin-and-tube evaporators
for residential air-conditioning systems

PhD Thesis
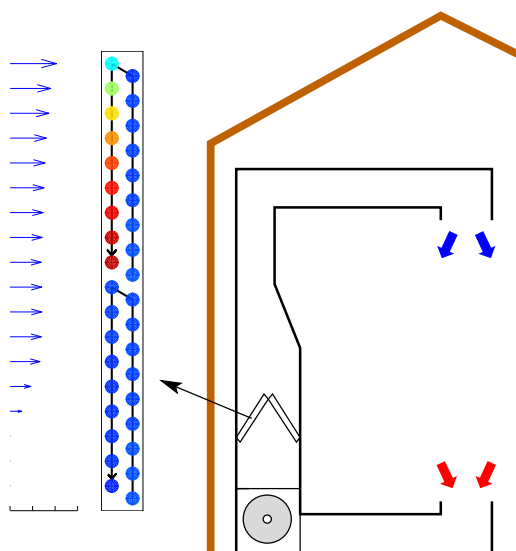
Martin Ryhl Kærn
DCAMM Special Report No. S132
August 2011

Analysis of flow maldistribution in fin-and-tube evaporators

for residential air-conditioning systems

Martin Ryhl Kærn

Ph.D. Thesis

Kongens Lyngby 2011

Technical University of Denmark

Analysis of flow maldistribution in fin-and-tube evaporators for residential air-conditioning systems

Preface

This thesis was prepared at the Section of Thermal Energy Systems, Department of Mechanical Engineering, Technical University of Denmark (DTU) and at Danfoss A/S Nordborg. It was submitted in partial fulfillment of the requirements for acquiring the Ph.D. degree. The work was carried out from July 2008 to August 2011 under supervision of Assoc. Prof. Brian Elmegaard (DTU), Ph.D. Lars Finn Sloth Larsen (Danfoss) and co-supervision of Ph.D. Morten Juel Skovrup (Institute for Product Development, IPU). The project was financed by the Danish Agency for Science, Technology and Innovation, under the industrial Ph.D. program, and by Danfoss.

The thesis is written as a monograph. It contains different studies of the effects of flow maldistribution in fin-and-tube evaporators for residential air-conditioning and the possible compensation potentials in terms of cooling capacity and coefficient of performance (COP). Furthermore, the thesis describes the development and implementation of the numerical model used in this work, which is written in the object-oriented modeling language Modelica®.

Lyngby, August 2011

Martin Ryhl Kærn

Acknowledgements

An industrial Ph.D. project is not an easy task always balancing on the border-line between interests of industry and academia. The task of writing a thesis with the right level of detail for various readers with different backgrounds and interests is challenging. I like to thank many people in helping me produce this thesis and in getting me through the industrial Ph.D. program.

I owe my principal supervisors Brian Elmegaard and Lars Finn Sloth Larsen a debt of gratitude for their support, advice, guidance and encouragement that have shaped this project and thesis. Thanks for allowing me to be supervised by you. I have enjoyed all our discussions and meetings. I would also like to thank my co-supervisor Morten Juel Skovrup for always being available for questions and discussions, and also for being very quick with updates on his thermophysical property package RefEqns.

I am grateful to Torben Funder Kristensen and Jørgen Holst for providing me with the opportunity to work at Danfoss A/S Nordborg and apply for the industrial Ph.D. program. During my stay at Danfoss A/S in Nordborg I have met many interesting people. I would like to give a special thanks to all of my colleagues at Danfoss A/S for providing an inspiring working environment. Many of you have always been very helpful and interested in my work. It has been a memorable one and a half year living in the southern part of Denmark.

I thank all my colleagues at the Section of Thermal Energy Systems at DTU. You are all part of an impressive research environment with unique mutual learning possibilities. I love this environment and I hope to stay in academia for many years. Thanks to all of you for providing a stimulating atmosphere filled with enthusiasm. A special thanks is given to Wiebke Brix for our collaboration and for helping me getting started quickly on the Ph.D. project. I will also like to thank Assoc. Prof. Emeritus Hans-Jørgen Høgaard Knudsen for his assistance with the two-phase flow modeling and understanding. I am also thankful to Assoc. Prof. Jens Honore Walther for helping me out with the

Abstract

This thesis is concerned with the effects of flow maldistribution in fin-and-tube A-coil evaporators for residential air-conditioning and compensation potentials with regards to system performance. The goal is to create a better understanding of flow maldistribution and the involved physical phenomenons. Moreover, the study investigates the individual and combined effects of non-uniform inlet liquid/vapor distribution, different feeder tube bending and non-uniform air-flow. In addition, the possible compensation of these maldistribution sources is investigated by control of individual channel superheat by distributing individual channel mass flow rate continuously (perfect control). The compensation method is compared to the use of a larger evaporator in order to study their trade-off in augmenting system performance (cooling capacity and COP).

The studies are performed by numerical modeling in the object-oriented programming language Modelica® and by using the commercial modeling environment Dymola 7.4 (2010). The evaporator model needs to be capable of predicting the flow distribution and circuitry effects, and for these reasons the dynamic distributed one-dimensional mixture two-phase flow model is implemented. The model is verified in steady state with commercial software Coil-Designer (Jiang et al., 2006) and compared to steady state experiments with acceptable results considering the unknown degrees of flow maldistribution for these experiments. Furthermore, the system dynamics in the model were validated and showed that a slip flow model need be used.

A test case 8.8 kW residential air-conditioning system with R410A as refrigerant is chosen as baseline for the numerical investigations, and the simulations are performed at standard rating conditions from ANSI/AHRI Standard 210/240 (2008). The investigations are performed on a simplified evaporator tube circuitry (two straight channels), a face split evaporator circuitry and an interlaced evaporator circuitry. The first case is a generic study and serves to provide general results independent of specific type of tube circuitry. The second and third cases are standard tube circuitry designs and these results

are thus tube circuitry specific. In addition, a novel method of compensating flow maldistribution is analyzed, i.e. the discontinuous liquid injection principle. The method is based upon the recently developed EcoFlow$^{\text{TM}}$ valve by Danfoss A/S, and controls the individual channel superheat by distributing individual mass flow rate discontinuously (on/off injection).

The results in this thesis show that flow maldistribution decreases system performance in terms of cooling capacity and COP, but may be compensated significantly by control of individual channel superheat. The generic study (two straight channels) shows that the airflow maldistribution has the largest effect, whereas the liquid/vapor maldistribution has smaller effect and the different feeder tube bending has a minor effect on system performance. The comparison between the face split and interlaced circuitry shows that the face split evaporator performs better at uniform flow conditions, whereas the interlaced evaporator performs better at flow maldistribution conditions. When compensating, the face split evaporator always performs best. A similar result is also obtained as the airflow profile across the A-coil evaporator was predicted by means of CFD simulation software STAR-CD 3.26 (2005) and applied in the numerical model. The main reason for the better face split evaporator performance at uniform conditions or when compensating, is that the superheated "weak" zones with low UA-value is located in the first tube row, where the heat transfer driving potential (temperature difference) is highest.

The discontinuous liquid injection principle showed that the cycle time is an important parameter for the performance of this compensation method. The cycle time is essentially the time it takes for distributing mass flow to each evaporator channels. It should be kept as low as possible. Furthermore, it is better to use a partial secondary flow into the remaining channels while distributing the main flow to each individual channel. The discontinuous liquid injection simulations showed spurious fluctuations in pressure, which have not been observed as high in any experiments carried out at Danfoss with high enough sampling frequency. It is believed that the absence of the interfacial dynamics in the mixture model and the use of correlations developed from steady state experiments may be the reasons for these fluctuations.

Resumé

Denne afhandling omhandler konsekvenser ved skæve strømningsfordelinger i fin-and-tube A-coil fordampere til luftkonditionering i husholdninger og dertil mulige kompenseringspotentiale i systemets ydeevne. Målet er at skabe en bedre forståelse af skævfordelingen og de involverede fysiske fænomener. Hertil analyseres individuelle og kombinerede konsekvenser af skævfordeling: Skæve fordelinger af væske og damp i fordamper indløb, forskellige bøjninger på disse indløb og skæve luftstrømsfordelinger. Desuden undersøges den mulige kompensering af disse skævfordelinger ved regulering af overhedningen på hvert fordamperløb ved distribution af individuel massestrøm kontinuert (perfekt styring). Denne kompenseringsmetode sammenlignes med brugen af en større fordamper for at finde deres udligning (trade-off) i forøgelse af systemets ydeevne (kølekapacitet og COP).

Analyserne er foretaget ved brug af matematisk modellering i det objektorienterede programmeringssprog Modelica® og det kommercielle modellerings og simuleringsprogram Dymola 7.4 (2010). Fordampermodellen skal være i stand til at forudsige skæve massestrømsfordelinger og modellere rørkredsløbet i A-coil fordampere, og af disse grunde er det valgt at implementere en distribueret en-dimensionel to-fase blandingsmodel. Modellen er verificeret i stationær tilstand med det kommercielle software Coil-Designer (Jiang et al., 2006) og sammenlignet i forhold til stationære forsøg med acceptable resultater i betragtning af den ukendte grad af skævfordeling i disse eksperimenter. Desuden blev systemdynamikken i modellen valideret og viste at en slip flow model skal anvendes.

Et 8,8 kW luftkonditioneringssystem med R410A som kølemiddel er valgt som udgangspunkt for de numeriske undersøgelser, og simuleringerne er udført ved standardbetingelser fra ANSI/AHRI Standard 210/240 (2008). Undersøgelserne er foretaget på et forenklet rørkredsløb (to lige rør), et face split rørkredsløb og et interlaced rørkredsløb i fordamperen. Den første undersøgelse er et generisk studie, der giver generelle resultater uafhængigt af bestemt rørkred-

sløb. Den anden og tredje undersøgelse er for standard rørkredsløb, og giver derfor specifikke resultater for disse. Derudover undersøges en ny metode til at kompensere skæv strømningsfordeling i fordampere, dvs. et diskontinuert væskeindsprøjtningsprincip. Metoden er baseret på den for nylig lancerede EcoFlow^{TM} ventil fra Danfoss A/S, og regulerer den individuelle overhedning på hvert fordamperløb ved distribution af individuel massestrøm diskontinuert (on/off indsprøjtning).

Resultaterne i denne afhandling viser, at skæv strømningsfordeling nedsætter systemets ydeevne med hensyn til kølekapacitet og COP, men kan kompenseres væsentligt ved regulering af de enkelte fordamperløbs overhedninger. Den generiske undersøgelse (to lige rør) viser, at skæv luftstrømsfordeling har den største betydning, hvorimod skævfordeling af væske og damp i fordamper indløb har mindre betydning og forskellige bøjninger på disse indløb har minimal betydning på systemets ydeevne. Sammenligningen mellem et face split og et interlaced rørkredsløb til fordamperen viser, at face split fordamperen præsterer bedre til jævne strømningsforhold, mens interlaced fordamperen præsterer bedre ved skæv strømningsfordeling. Ved kompensering af skævfordelingen præsterer face split fordamperen altid bedst. Det samme resultat blev også opnået idet luftstrømsprofilet igennem en A-coil fordamper, blev simuleret ved hjælp af CFD simuleringsprogrammet STAR-CD 3.26 (2005) og anvendt i den numeriske model. Den væsentligste årsag til at face split fordamperen viser bedre ydeevne ved jævne strømningsforhold eller ved kompensering af skæv strømningsfordeling, er at den overhedede "dårlige" zone med lav UA-værdi er lokaliseret i den første rørrække af fordamperen, hvor det varmedrivende potentiale (temperaturforskel) er højest.

Det diskontinuerte væskeindsprøjtningsprincip viste, at cyklustiden er en vigtig parameter for ydeevnen af denne kompenseringsmetode. Cyklustiden er den tid det tager for distribution af massestrøm til hvert enkelt fordamperløb. Denne skal holdes så lav som muligt. Desuden er det bedre at gøre brug af en sekundær massestrøm til de resterende løb, mens hovedmassestrømmen distribueres til hvert enkelt løb. Simuleringerne af det diskontinuerte væskeindsprøjtningsprincip viste større udsving i fordampningstryk, som ikke er observeret i så høj grad i eksperimenter udført hos Danfoss med tilstrækkelig høj samplingsfrekvens. Det vurderes, at væske/damp grænsefladedynamikken, som ikke er modelleret i den distribuerede blandingsmodel, og brugen af korrelationer, der er udviklet på baggrund af stationære eksperimenter, kan være årsager til disse udsving i fordampningstryk.

List of publications

Journal papers:

Kærn, M. R., Brix, W., Elmegaard, B., Larsen, L. F. S., 2011a. Compensation of flow maldistribution in fin-and-tube evaporators for residential air-conditioning. International Journal of Refrigeration 34 (5), 1230 – 1237.

Kærn, M. R., Brix, W., Elmegaard, B., Larsen, L. F. S., 2011b. Performance of residential air-conditioning systems with flow maldistribution in fin-and-tube evaporators. International Journal of Refrigeration 34 (3), 696 – 706.

Peer reviewed conference papers:

Kærn, M. R., Elmegaard, B., Larsen, L. F. S., 2011c. Comparison of fin-and-tube interlaced and face split evaporators with flow mal-distribution and compensation. In: 23th International Congress of Refrigeration. IIR/IIF, Prague, Czech Republic.

Kærn, M. R., Elmegaard, B., Larsen, L. F. S., 2011d. Experimental comparison of the dynamic evaporator response using homogeneous and slip flow modelling. In: 8th International Modelica Conference. Dresden, Germany.

Kærn, M. R., Elmegaard, B., Larsen, L. F. S., 2009. Effect of refrigerant mal-distribution in fin-and-tube evaporators on system performance. In: 50th International Conference of Scandinavian Simulation Society. Fredericia, Denmark, pp. 315 – 322.

Invited conference papers:

Kærn, M. R., Elmegaard, B., 2009. Analysis of refrigerant mal-distribution in fin-and-tube evaporators. In: Danske Køledage 2009. Odense, Denmark, pp. 25 – 35.

Contents

Nomenclature

Roman letters

A	area (m^2)
A_T	total surface area (m^2)
Bo	boiling number (-)
C	heat capacity flow (W K^{-1})
C_o	dimensionless parameter eq. C.1 (-)
c_p	specific heat capacity (J kg^{-1}K^{-1})
D	outer diameter (m)
D_c	collar diameter (m)
D_h	hydraulic diameter (m)
d	inner diameter (m)
E	convective enhancement factor (-)
E	total energy (J)
e	specific convected energy (J kg^{-1})
e_t	total specific energy (J kg^{-1})
F	force per unit volume (N m^{-3})
F_{air}	airflow distribution parameter (-)
F_{ft}	feeder tube bending parameter (-)
$F_{\dot{m}}$	mass flow difference parameter (-)
F_o	orifice flow ratio parameter (-)
F_p	fin pitch (m)
Fr	Froude number (-)
F_x	phase distribution parameter (-)
f_D	Darcy-Weisbach friction factor (-)
f_F	Fanning friction factor (-)
G	mass flux (kg m^{-2}s^{-1})
g	acceleration of gravity (m s^{-2})
$\dot{H}$	enthalpy flow (W)

h	specific enthalpy or mixed cup enthalpy (J kg^{-1})
$\bar{h}$	in situ mixture or bulk enthalpy (J kg^{-1})
h_c	convective boiling heat transfer coefficient (W m^{-2}K^{-1})
h_{NcB}	nucleate boiling heat transfer coefficient (W m^{-2}K^{-1})
h_{tc}	heat transfer coefficient (W m^{-2}K^{-1})
$\dot{I}$	momentum flow (kg m s^{-2})
j	Colburn factor (-)
j	superficial velocity (m s^{-1})
K	orifice flow coefficient
k	integrator gain (-)
k	thermal conductivity (W m^{-1}K^{-1})
L	length (m)
L_h	louver height (m)
L_p	louver pitch (m)
M	molecular weight (kg kmol^{-1})
m	mass (kg)
$\dot{m}$	mass flow rate (kg s^{-1})
N	dimensionless parameter eq. C.1 (-)
N_{col}	number of tube rows
N_{pass}	number of refrigerant passes (channels)
N_{row}	number of tubes per tube row
N_{slab}	number of slabs (coils)
N_{tot}	total number of tubes
NTU	Number of Transfer Units (-)
Nu	Nusselts number (-)
n	number cells per tube
OD	opening degree (%)
P	perimeter (m)
P	tube pitch (m)
Pr	Prandtl number (-)
p	pressure (Pa)
p_c	critical pressure (Pa)
p_r	reduced pressure (Pa)
$\dot{Q}$	heat flow rate (W)
q''	heat flux (W m^{-2})
R	bend radius (m)
R	thermal resistance (K W^{-1})
R_C	heat capacity flow ratio (-)
Re	Reynolds number (-)
R_{eq}	equivalent circular fin radius (m)
r	radius (m)
S	boiling suppression factor (-)
S	slip ratio (-)
St	Stanton number (-)

T	temperature (K)
TC	tube connectivity matrix
TC_num	number of tubes per pass (channel)
t	time (s)
t_f	fin thickness (m)
U	velocity (m s^{-1})
UA	overall heat transfer coefficient (W K^{-1})
u	specific internal energy (J kg^{-1})
V	volume (m^3)
$\dot{V}$	volume flow rate (m^{3}s^{-1})
$\dot{W}$	power (W)
We	Weber number (-)
X_L	geometric parameter (m)
X_M	geometric parameter (m)
X_tt	Martinelli parameter (-)
x	vapor quality (-)
x_st	static quality (-)
x_t	transition point
y	transverse coordinate (m)
z	axial coordinate (m)

Greek letters

α	void fraction (-)
Γ	interfacial mass transfer rate per unit volume (kg s^{-1}m^{-3})
δ	indicator function
ϵ	effectiveness (-)
η	efficiency (-)
Θ	distribution vector (-)
θ	horizontal inclination angle (°)
θ	bend angle (°)
μ	viscosity (kg m^{-1}s^{-1})
ρ	density (kg m^{-3})
$\bar{\rho}$	in situ mixture or bulk density (kg m^{-3})
ρ'	momentum density (kg m^{-3})
σ	surface tension (N m^{-1})
τ	shear stress (N m^{-2})
ϕ	two-phase multiplier (-)
φ	phase (rad)
ψ	thermodynamic quantity

Superscripts

| ‾ | average | ˆ | approximation |

Subscripts

a	air	damp	dampening
acc	acceleration	inj	injection
act	actual	is	isentropic
ax	axial	L	liquid
b	brine	l	longitudinal
c	condensation	m	mean
cyc	cycle	max	maximum
d	discharge	min	minimum
e	evaporation	o	overall
eq	equilibrium	out	outlet
exp	experiment	r	refrigerant
f	fin	rad	radial
f	saturated liquid	s	suction
fo	liquid only	sat	saturated
fr	frontal	sc	subcooling
fric	friction	sh	superheat
ft	feeder tubes	ss	steady state
G	gas or vapor	t	transverse
g	saturated gas or vapor	tot	total
geo	geometric	tp	two-phase
go	gas only	vol	volumetric
H	homogeneous	w	wall
I	interface	w	compression work
in	inlet		

CHAPTER 1

Introduction

1.1 Background

The focus of this thesis is to investigate the effects of flow maldistribution in fin-and-tube evaporators for residential air-conditioning systems and the possible compensation potentials in terms of overall UA-value, cooling capacity and coefficient of performance (COP).

The investigations are based on a typical residential air-conditioning system as shown on figure 1.1 for the United States market. The system consists of an outdoor unit and an indoor unit. The outdoor unit contains the condenser coil including fan and compressor, and the indoor unit contains the evaporator, expansion valve (not shown), air filter (not shown) and a blower/fan. The conditioned space receives cooled air from the evaporator through the ceiling, which is mixed with the space and returns to the blower through the floor to be cooled again. The refrigerant flowing to the indoor unit is expanded by the expansion valve close to the evaporator, where it is evaporated and sent back to the outdoor unit. The refrigerant entering the outdoor unit is compressed and condensed, and sent back to the indoor unit. The evaporator is a multi-channel A-coil evaporator, i.e. two coils forming an A-shape with a number of parallel refrigerant circuits (or channels).

Figure 1.2 shows pictures of a typical A-coil evaporator and a typical zoomed-in cut-through distributor. The A-coil picture also shows the location of the expansion valve, distributor and feeder tubes.

The tube circuitry defines the refrigerant channels through each coil and may be constructed arbitrarily by the manufacturers. However, two standard tube cir-
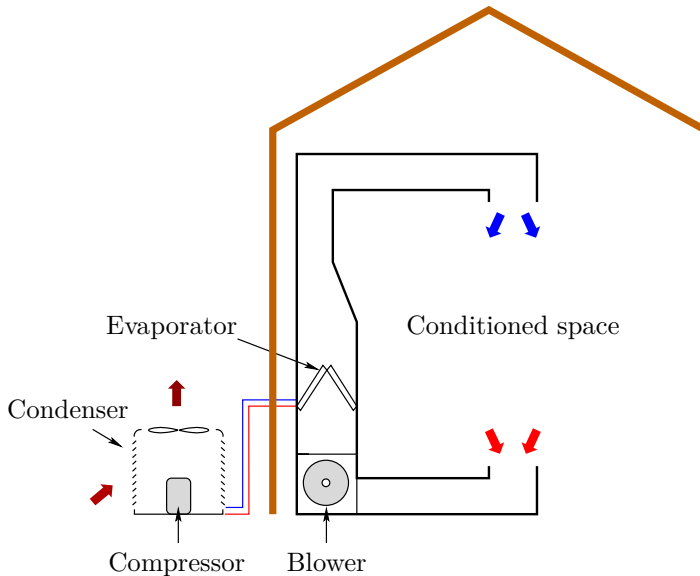
Figure 1.1: Sketch of a typical residential air-conditioning system.

cuitry designs exist, i.e the interlaced and the face split tube circuitries. Figure 1.2a shows the interlaced type of circuitry, where the two refrigerant channels through each coil shift tube row. For the face split evaporator the refrigerant channels are independent of each other, which means that the air travels across each channel independently, see figure 5.1 on page 87 for definitions of the face split and interlaced tube circuitries.

1.1.1 United States residential air-conditioning market

Residential air-conditioning for the United States market has a large sales volume of units. In 2005 the shipments of residential air-conditioners was 6.5 million in the United States (United States Department of Energy, 2011), however, in 2009 the number decreased to 3.5 million because of the global financial crises. Furthermore, the installation of air-conditioning in new single-family homes have increased steadily from 62% in 1980 to 90% in 2004, and stays around the same percentage still today.

In addition, the United States have the largest share of global primary energy consumption by any country. In 2008 the share was 20% according to United States Department of Energy (2011). In turn 22% of the United States primary energy consumption was used by residential buildings. Space cooling (or air-conditioning) consumed 14% of the end-use primary energy consumption, thus 3% of the total primary energy consumption in the United States was used

a **b**
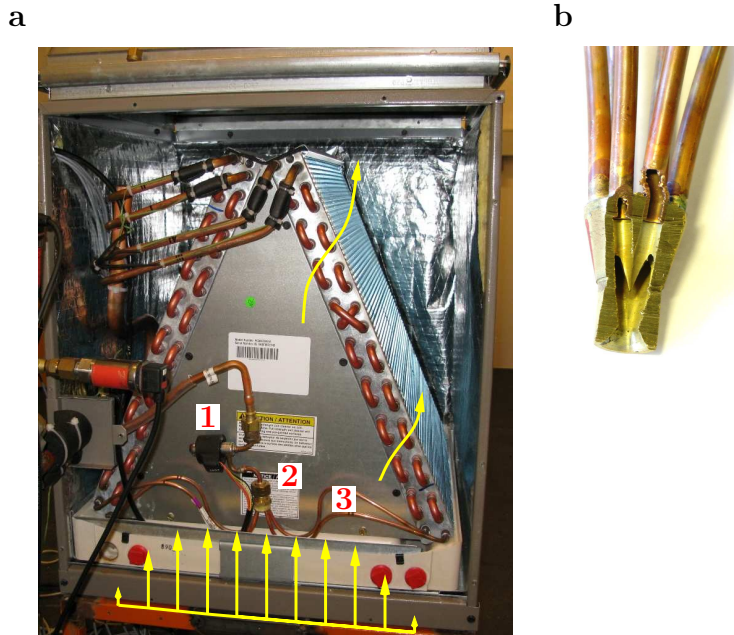
Figure 1.2: Picture of a fin-and-tube A-coil (a) and zoomed-in cut-through distributor (b), 1 = electronic expansion valve, 2 = distributor, 3 = feeder tubes.

for residential air-conditioning in 2008. The corresponding end-use electricity consumption was 1.02 exajoules (EJ = 10^{18} joules). It equals an emission of 179.8 10^9 kg of carbon dioxide.

The United States residential air-conditioning is thus an important application, which has a significant primary energy consumption, carbon dioxide emission and large sales volume.

1.2 Motivation

Reduction of energy consumption and refrigerant charge in residential air-conditioning systems is becoming increasingly important for environmental, legislative and economical reasons. Therefore, high performance and compact dry-expansion multi-channel evaporators are of interest for future residential air-conditioning technology such as fin-and-tube evaporators.

The use of multi-channel evaporators gives rise to refrigerant maldistribution. Before the refrigerant is distributed, the refrigerant is expanded from subcooled liquid into a two-phase mixture. The design of the expansion valve and the

distributor is essential for providing a good mixing of the phases before distribution. The picture of the distributor on figure 1.2b shows an orifice before the cone, which speeds up and separates the two-phase flow into each feeder tube. The liquid and vapor phases may be distributed unevenly, but also the mass flow distribution may be uneven, for example, caused by different feeder tube bends.

Furthermore, the residential air-conditioning industry aims to reduce the air duct dimensions in residential housing. As a consequence the fin-and-tube evaporators are typically aligned as A-coils (as shown on figure 1.2a) in order to increase the frontal area of the evaporator and at the same time keep the duct dimensions minimized. A drawback is that the airflow becomes non-perpendicular to the coil, resulting in airflow maldistribution. Figure 1.2a also shows how we believe the air to flow through the evaporator, i.e. more air will travel through the top of the two coils rather than the bottom of the two coils. This is a result of the velocity profile in the duct and the fact that the air will travel where the resistance is lowest, and thus collect near the top of the coil. The velocity profile is not uniform and essentially has the maximum velocity close to the centerline and zero velocity at the duct walls. Both effects result in airflow maldistribution.

The above issues are outside conditions to the evaporator that may cause flow maldistribution inside the evaporator. However, the inside of the fin-and-tube evaporator may also cause flow maldistribution. Moreover, the tube circuiting of a fin-and-tube evaporator may cause flow maldistribution in itself. The tube circuiting may also be used to optimize the evaporator according to a given maldistribution condition, hereby compensating flow maldistribution. However, it does not ensure optimal compensation at off-design conditions.

Flow maldistribution reduces energy efficiency of residential air-conditioning systems. The underlying mechanism is that flow maldistribution causes non-uniform superheated regions in the evaporator. At severe flow maldistribution, the liquid might not be fully evaporated through some of the channels. This surplus liquid will eventually be evaporated by mixing with increased super-heated regions in the other channels. The increased superheated region is ineffective, since the superheated regions have low heat transfer compared to the two-phase regions. Therefore, it is believed that an even superheated region in each channel (and the possible maximum two-phase area) are optimal conditions in fin-and-tube evaporators.

It is commonly known in the refrigeration and air-conditioning industry that flow maldistribution in multi-channel evaporators reduces the cooling capacity of the evaporator as well as the coefficient of performance (COP) of the system. As a result flow maldistribution in fin-and-tube evaporators for residential air-conditioning has gained an increased attention by researchers and developers within the last decade.

1.2.1 Literature review

Flow maldistribution in evaporators has been shown by many researchers to decrease heat transfer and energy efficiency for residential air-conditioning.

Flow maldistribution may be caused by different effects such as a non-uniform airflow velocity, temperature, moist condensation or frost, non-uniform fouling, an improper heat-exchanger, tube circuiting or distributor design and installation, or combinations all these factors.

Payne and Domanski (2003) and Choi et al. (2003) studied the potentials of using smart refrigerant distributors experimentally. The study showed that the capacity dropped as much as 41% and 32% for two different fin-and-tube evaporators using R22, when the superheat was allowed to vary between the circuits. The refrigerant maldistribution was essentially adjusted by individual needle valves, while the overall superheat was held at 5.6°C. They also studied the recovery of airflow maldistribution by controlling the individual circuit superheats by using the same needle valves. As some of the coil was blocked and the airflow rate was held constant, the recovery in cooling capacity was within 2% of the original cooling capacity under uniform airflow conditions. Furthermore, the authors upgraded the evaporator model EVAP5 (Domanski, 1999) from National Institute of Standards and Technology (NIST), to control refrigerant distribution. The model was used to evaluate the possible savings in evaporator core volume if refrigerant distribution was controlled. In extreme cases they found that the savings was up to 40% in core volume.

Lee et al. (2003) studied numerically the effect of different two-dimensional airflow profiles in fin-and-tube evaporators containing the zeotropic mixture R407C. They showed that the non-uniform airflow profiles reduce the capacity of the evaporator by up to 6%. The airflow may also create a recirculation zone in the lower part of the coil as pointed out by AbdelAziz et al. (2008), who carried out simulations of the airflow through an A-coil using computational fluid dynamics (CFD). Such recirculation zones in the coil lead to a reduction in cooling capacity, since the recirculated airflow is not exchanged. A similar recirculation zone was found in a numerical study by Yashar et al. (2008), however, a later study by Yashar and Domanski (2010) showed no recirculation zone in such coils.

Nakayama et al. (2000) studied a new type of distributor that had a capillary mixing space instead of the orifice of the conventional distributor. They showed that a vertical inclination angle of 15 degrees reduced the capacity of the evaporator by 1.5% using the conventional distributor, however, the new type of distributor showed only a reduction of 0.4%. The better mixing of the new type showed a capacity increase of 1.2% at vertical orientation compared to the conventional distributor. Li et al. (2005) studied refrigerant flow distribution in distributors by computational fluid dynamics. In general, they reported that the spherical base distributor achieves the best distribution, and that the orifice should be located close to the distributor base.

Kim et al. (2009a,b) studied both refrigerant and airflow maldistribution on a fin-and-tube five channel R410A heat pump numerically. Two and three of the channels, respectively, were treated similarly, i.e. essentially two circuits with one having 50% larger area. It was found that the cooling capacity and COP decreased by 12% and 8%, respectively, as the feeder tube diameter decreased by 25% or the inlet void fraction increased by 5.5% of one of the circuits. They also found that the cooling capacity and COP decreased 16% and 11% as the air-flow ratio between the circuits was 0.4, keeping the total volume flow constant. Furthermore, the authors studied the benefits of upstream vs. downstream control of individual channel superheat. Their method involved a fine-tuning of miniature valves located upstream or downstream of the evaporator along with an overall thermostatic expansion valve. Essentially, the method controlled the individual superheats by adjusting the pressure drop through the channels. The study showed that the upstream control outperformed the downstream control. They also found that the capacity reduction due to maldistribution could be recovered up to 99.9% by using upstream control. Using downstream control resulted in minor benefits due to the increased pressure drop at the exit of the evaporator.

Domanski and Yashar (2007) applied a novel optimization system called ISHED (intelligent system for heat exchanger design) to optimize refrigerant circuitry in order to compensate airflow maldistribution. They measured the air velocity profile using particle image velocimetry (PIV), used that as input to the model and reported that the cooling capacity was increased by 4.2% compared to an interlaced type of circuitry. Liang et al. (2001) investigated four different tube circuitries in fin-and-tube evaporators numerically. The results showed that the complex optimized refrigerant circuitry arrangement reduced the needed heat transfer area by 5% compared to a common circuiting for the same cooling capacity.

1.2.2   Contributions

Many aspects of flow maldistribution have been studied so far as given in the above literature review for fin-and-tube evaporators. Many have been in the context of understanding how much the flow maldistribution may reduce the performance in cooling capacity and COP. Others have studied the possible compensation of flow maldistribution. Despite, the previous studies not all the involved physical phenomenons and their significance have been fully understood. The main contributions from this thesis are aimed on achieving an increased understanding of:

- The involved physical phenomenons and sources that dictate flow maldistribution.
- The interactions of different sources that cause flow maldistribution, including tube circuiting effects.

- The possible performance recovery or compensation of flow maldistribution by control of individual channel superheat.

Furthermore, a number of papers have been published based upon the work presented in this thesis, see the list of publications on page ix.

1.3 Thesis statement

Flow maldistribution can be compensated by using an expansion valve for each channel. Another option is to increase the size of the evaporator. The first option is unfeasible due to the costs associated with installing additional expansion valves. The second option may have restrictions on the size of the air ducts and does not support evaporator compactness. For economical reasons (and in disregard of the second option restrictions), any type of refrigerant distribution control must be less expensive than the costs of increasing the size of the evaporator for the same cooling capacity and COP.

Devices and methods for controlling the superheat of each channel individually are of interest to compensate flow maldistribution. As an example Danfoss recently launched a new expansion product marketed as EcoFlow^{TM} (Funder-Kristensen et al., 2009; Mader and Thybo, 2010). The product is able to distribute the refrigerant flow individually into each channel, hereby ensuring uniform channel superheats and compensation of flow maldistribution. The working principle is discontinuous liquid injection into each channel.

It is believed that the key for even more effective products or system combinations are hidden in the understanding of the flow maldistribution. It is an essential task to document and analyze the implications on performance and possible measures for compensating flow maldistribution in fin-and-tube evaporators.

1.3.1 Thesis objectives and hypothesis

The main objective is to develop an increased understanding and knowledge of flow maldistribution and compensation in fin-and-tube evaporators for residential air-conditioning.

More specifically, the Ph.D. thesis aims to:

- Obtain a detailed understanding of the phenomenons leading to flow maldistribution and benefits of compensation by control of individual channel superheats.
- Provide a profitable, objective basis for selecting the right components and/or system designs for fin-and-tube evaporators with flow maldistribution and possible compensation.

- Provide guidelines that may be used as supplement to past experience. The guidelines may be rules of thumb or graphs that show the potential energy reduction by flow maldistribution and savings by compensation.
- Provide a simulation tool that may be used in future development, which enables a quick assessment of initial product ideas for compensation of flow maldistribution.

The central hypothesis in the thesis is that a significant increase in system performance may be obtained by compensating flow maldistribution. By investigating this hypothesis, the following questions arise that are sought to be answered:

- What are the reductions in cooling capacity and COP by flow maldistribution, both individual effects and combined?
- What are the energy savings potentials by compensation of flow maldistribution?
- When compensating, what is the equivalent additional material usage (heat exchanger area) for the same cooling capacity and COP?
- What is the influence of the standard tube circuitries (face split and interlaced) on flow maldistribution and possible compensation?
- What are the effects of the discontinuous liquid injection principle, which is employed by the EcoFlow valve?

1.3.2 Methodology

We will employ numerical modeling of a test case residential air-conditioning system in order to answer the above questions and meet the objectives. The test case is an R410A 8.8 kW system aimed for the United States market and operated at standard rating conditions according to ANSI/AHRI Standard 210/240 (2008).

We will develop different component models of the system with different detail levels that are required for each component. For example, the evaporator model needs to be capable of simulating different tube circuitries and predict the refrigerant flow distribution according to individual channel pressure drop. Furthermore, it needs to be dynamic for investigating the discontinuous liquid injection principle. Therefore, we chose to use a distributed one-dimensional mixture two-phase flow model for the evaporator. In contrast, a simpler moving boundary approach is used for the condenser, since it has no requirements with regards to modeling distribution or tube circuiting.

The component models are implemented in the object-oriented modeling language Modelica® (Modelica Association, 2010), which is a strong modeling language for physical modeling, model reuse and extension. Dymola 7.4 (2010) is a commercial software based on the Modelica language and facilitates a

strong modeling and simulation environment. Models may be written by their governing differential, algebraic and discrete equations (hybrid DAE's).

1.3.3 Approach

The approach for investigating the objectives of this thesis, is divided into three chronological steps. These three steps are reflected in chapter 4, 5 and 6, respectively:

Step 1: Systematically analyze the most important sources of flow maldistribution in the evaporator in a generic and general study, in order to decouple each effect of flow maldistribution and analyze them individually. This involves a quantification of the possible performance degradation and recovery by compensation in terms of cooling capacity and COP. This approach provides a basic understanding and knowledge of flow maldistribution effects and is used to generate guidelines for basic trends, consequences and compensation potentials of flow maldistribution. The method of compensation involves the concept of perfect control of individual channel superheats by distributing individual channel mass flow rate continuously.

Step 2: Systematically compare the performance of the standard evaporator tube circuitries (face split and interlaced) at flow maldistribution and compensation. This involves a quantification of the performance degradation and recovery by compensation on real type evaporators. In connection with the generic study, this approach gives information on the influence of different tube circuitries on flow maldistribution and possible compensation potentials. Moreover, the coupling between tube circuitry and compensation is investigated to generate guidelines for energy saving potentials considering the tube circuitry. The method of compensation is similar to the perfect control concept used in the generic study (step 1).

Step 3: Analyze the discontinuous liquid injection principle based on the working principle of the EcoFlow valve. Moreover, the effect of the liquid injection principle is investigated with regards to the cycle time and the size of an optional secondary flow into the other channels. This approach provides an increased understanding of the discontinuous liquid injection principle by focussing on the specifications and requirements for subcomponents (cycle time and orifice dimensions), in order to generate guidelines for these. In connection with the previous steps, we evaluate whether the liquid injection principle may result in increased cooling capacity and COP, compared to the perfect control concept. The injection principle is essentially two-phase flow pulsations that may increase heat transfer.

1.3.4 Geometry, conditions and delimitations

The test case residential air-conditioning unit is an R410A 8.8 kW unit. The fins on the air side is louvered type of fins. When modeling a larger evaporator we used the 10.5 kW unit size. The geometry data are partly measured or from manufacturer data.

The indoor and outdoor conditions (26.7°C and 35°C) are taken from standard rating conditions according to ANSI/AHRI Standard 210/240 (2008). Furthermore, the frontal velocity are computed from manufacturer rating data.

An important delimitation is that we did not consider humid conditions throughout the thesis, i.e. moist condensation or frost on the coil surface. This latent heat may be as high as 50% of the total capacity. It does not mean that the cooling capacity computed by the current model only becomes half of the actual cooling capacity, because it is only the air side heat transfer characteristics that are affected. For example, in humid conditions the air temperature difference is not as high as in dry air conditions for the same system and flow.

1.4 Thesis outline

The thesis contains 7 chapters and 4 appendixes. The contents are as follows:

Chapter 1 is the introduction which contains motivation, thesis statement, objectives, approach, literature review, and a description of the application.

Chapter 2 contains a description of the numerical model formulations of all the component models in the residential air-conditioning system, especially focusing on the distributed evaporator model. The chapter also explains why a given model approach has been chosen with regards to detail level and model assumptions.

Chapter 3 is a brief description of the model implementation in Modelica for the evaporator model. The chapter gives a condensed introduction to the Modelica language and shows the object-oriented methods that have been used in order to quickly exchange correlations and heat transfer models etc.

Chapter 4 presents the 1$^{\text{st}}$ step of the thesis approach. A generic study is performed of the effects of flow maldistribution and possible compensation potential in terms of cooling capacity and COP. Moreover, the various tube circuiting effects are decoupled by assuming the coil to be two straight and independent channels. In this way the individual sources of flow maldistribution are analyzed independently. The sources of interest are: Inlet liquid/vapor phase distribution, feeder tube bending and

airflow distribution. Furthermore, the recovery potential by compensation is addressed at different evaporator size, outdoor temperatures and combinations of flow maldistribution sources.

Chapter 5 presents the 2nd step of the thesis approach. It is a continuation of the generic study in chapter 4, however, performed on specific evaporator tube circuitries (face split and interlaced), meaning that the generic or generality in the results vanish. Moreover, the results are confined to these standard tube circuitries. The chapter compares the performance of the two circuitries in flow maldistribution conditions. Furthermore, the recovery potential by compensation is addressed at different evaporator sizes and combinations of flow maldistribution sources.

Chapter 6 presents the 3rd step of the thesis approach. A dynamic study of the discontinuous liquid injection principle is performed on the face split and interlaced tube circuitries from chapter 5. The chapter investigates the influence of different specifications and requirements. Moreover, the effect of the cycle time and the optional secondary flow is addressed with regards to cooling capacity and COP. Furthermore, the injection principle is evaluated at airflow maldistribution and compared to the results of the perfect control concept in chapter 5.

Chapter 7 is the discussion and conclusion of the thesis and recommendations for further research and product development.

Appendix A is a detailed derivation of the governing one-dimensional two-phase flow equations. The derivation is performed on each phase and clearly shows the phasic interactions that is not addressed in this thesis by using the mixture model formulation. The mixture model formulation is essentially obtained by adding the phasic equations, hereby the interfacial terms cancel out. The derivation is an even more detailed representation of the governing equations than given in the textbook by Ghiaasiaan (2008). It creates a better understanding of the two-phase one-dimensional flow modeling.

Appendix B is a detailed derivation of the moving boundary condenser model. It is the same model approach as shown by Zhang and Zhang (2006) on an evaporator, however, derived here for the condenser. The derivation is given with more details and serves to provide better understanding of the formulation.

Appendix C is a statement of all the correlations that are used from the literature. Moreover, correlations for refrigerant friction, heat transfer and void are given, plus correlations for air side heat transfer and fin efficiency.

Appendix D is a sensitivity study of the pressure fluctuations from the discontinuous liquid injection principle modeling. These fluctuations in pressure and other variables have not been observed as high in any experiments carried out at Danfoss. For this reason, the sensitivity of the fluctuations is addressed and compared with the sensitivity of the first order time constant based upon a step in opening degree. The two are believed to be related and the study serves to provide more information on the causes of the fluctuations in the model.

Component model formulations

This chapter goes through the mathematical formulations of the main component models that are implemented in Dymola 7.4. It should provide fundamental understanding of the model formulations in order to use or extend the models for investigating flow maldistribution. Furthermore, it should be used as reference for understanding the modeling details and results of later chapters in this thesis. The chapter works as documentation of the modeling formulation with references to details in the appendix.

2.1 Introduction

The object of the modeling work is to predict the distribution of the refrigerant in the evaporator, thus the evaporator model must be capable of handling the mass flow/pressure drop dependence of the refrigerant. The simplest form of the one-dimensional distributed two-phase flow models is chosen for this purpose, i.e. the mixture model. It is derived by performing a differential analysis on each phase and adding the phasic equations, see appendix A. Similarly, the wall and airflow are discritized in the refrigerant flow direction. Furthermore, the distributed model is able to model tube circuitry of fin-and-tube evaporators.

The moving boundary model approach is chosen for the condenser model, which averages or lumps the liquid, two-phase and vapor regions. We chose this

simpler approach because in this thesis, we do not address flow maldistribution and tube circuitry in the condenser. Both the models of the condenser and evaporator are dynamic so that they model the refrigerant migration between the two. Quasi-static model formulations are used for the expansion device and the compressor.

The chapter describes all these models. The focus is laid on the details of the one-dimensional distributed evaporator model. Moreover, the chapter provides a basic understanding of two-phase flow considered as a mixture and the inherent use of empirical correlations for heat transfer, friction and void.

Furthermore, the chapter describes the control of the evaporator superheat by the expansion valve model and the refrigerant charging of the system model during simulation startup by a filling station model.

Finally, the chapter describes the possibilities in the model to simulate flow maldistribution and compensation of flow maldistribution. The options in the refrigerant distributor model are to use either the *EXV flow*, *Even flow* or *Compensating flow* distribution. The first option is the traditional system using an electronic expansion valve (EXV) and a distributor, where the actual mass flow distribution is computed according to the individual channel pressure drop, which must be the same. The liquid and vapor phases may therefore be maldistributed for this option. In contrast, the latter two options have no liquid and vapor maldistribution and rather distribute the actual mass flow to each channel.

2.2   Evaporator

This section describes the distributed evaporator model. The focus is laid on the understanding of one-dimensional refrigerant flow considered as a mixture. The section gives an introduction to the governing equations, closure correlations for friction, heat transfer and void fraction, choice of dynamic and thermodynamic state variables, and discretization used in this work. Then the section covers the simpler wall and air-side modeling.

Components of the refrigerant, the wall and the air have been implemented in Dymola 7.4, and essentially arrays of these components are made and connected according to the geometry and flow arrangement of the evaporator, see figure 2.1 and 2.2. In fin-and-tube evaporators, the tubes are aligned in a cross flow of air (figure 2.2). Each cell is then considered as a small cross flow heat exchanger, where effectiveness-NTU relations are applied for cross flow heat exchangers.
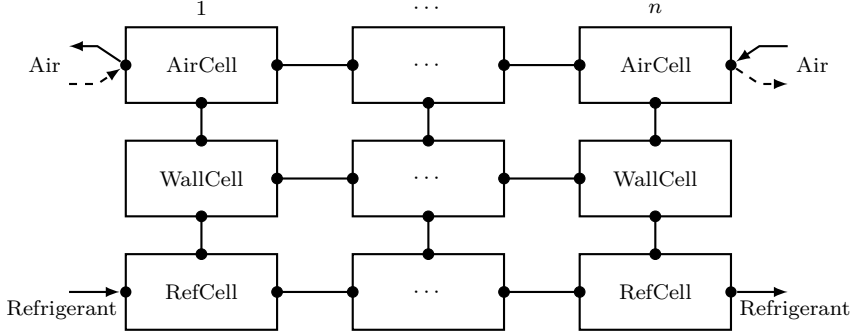
Figure 2.1: Heat exchanger architecture; full (air) arrows = counter flow, dashed (air) arrows = parallel flow.
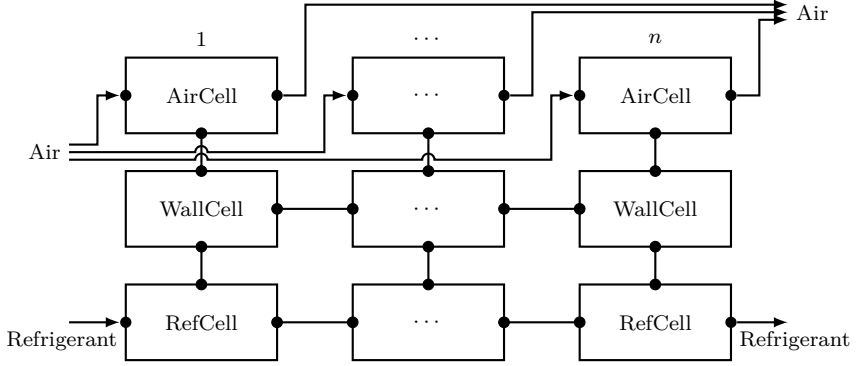
Figure 2.2: Heat exchanger architecture; cross flow.

2.2.1 Refrigerant flow

The governing one-dimensional mixture two-phase flow equations, i.e. mass conservation, momentum equation and energy conservation, are given as

$$A\frac{\partial \bar{\rho}}{\partial t} + \frac{\partial \dot{m}}{\partial z} = 0 \tag{A.36}$$

$$\frac{\partial \dot{m}}{\partial t} + \frac{\partial}{\partial z}\left(\frac{\dot{m}^2}{\rho' A}\right) = -A\frac{\partial p}{\partial z} - F_w A - \bar{\rho} g A \sin\theta \tag{A.37}$$

$$A\frac{\partial}{\partial t}\left(\bar{\rho}\bar{h} - p\right) + \frac{\partial}{\partial z}\left(\dot{m}h\right) = P q_w'' \tag{A.38}$$

where $\bar{\rho}$ is mixture density, $\dot{m}$ is mass flow rate, t is time, z is axial coordinate, ρ' is momentum density, A is cross-sectional area, p is pressure, F_w is wall-

friction, g is gravitational acceleration, θ is orientation, $\bar{h}$ is in situ enthalpy, h is mixed cup enthalpy, P is wall perimeter and q_w'' is wall heat flux.

Appendix A clearly shows the phase interactions on the interphase that we avoid by adding each phasic equations. Generally, it is assumed that changes in kinetic and potential energy are negligible as well as the heat diffusion (or conduction) in the refrigerant. Furthermore, thermodynamic equilibrium is assumed to exist, which means that only one energy equation should be used and that the heat transfer on the interphase is infinitively fast. By solving only one momentum equation individual phasic friction on the wall or interphase and individual acceleration are not resolved, in turn considered as a whole. Usually correlations of friction and heat transfer are given in forms of mixture quantities, which however ease the use of mixture equations. These correlations from the literature are closure relations in addition to the void fraction ($\alpha = A_g/A$), which determines the mixture density and in situ enthalpy given by equation A.6 and A.35.

$$\bar{\rho} = \rho_g \alpha + \rho_f (1 - \alpha) \tag{A.6}$$

$$\bar{h} = [\rho_f h_f (1 - \alpha) + \rho_g h_g \alpha]/\bar{\rho} \tag{A.35}$$

The in situ enthalpy is a bulk mixture property (based on a frozen field) and should not be confused with the mixed cup enthalpy, which is purely hydrodynamic (carried with the flow) and given by equation A.8.

$$
\begin{aligned}
\dot{m}h &= \dot{m}_g h_g + \dot{m}_f h_f \\
\Rightarrow \quad h &= x h_g + (1 - x) h_f \\
\Rightarrow \quad x &= (h - h_f)/(h_g - h_f)
\end{aligned}
\tag{A.8}
$$

The equation shows that there is a strict relationship between the mixed cup enthalpy and the vapor quality, which is defined by equation A.2.

$$
\begin{aligned}
x &= \dot{m}_g/(\dot{m}_g + \dot{m}_f) = \dot{m}_g/\dot{m} \\
&= \rho_g U_g \alpha/[\rho_g U_g \alpha + \rho_f U_f (1 - \alpha)]
\end{aligned}
\tag{A.2}
$$

Last but not least, the momentum density is given by equation A.24.

$$\rho' = \left(\frac{(1-x)^2}{\rho_f (1-\alpha)} + \frac{x^2}{\rho_g \alpha} \right)^{-1} \tag{A.24}$$

The liquid and vapor flow equations results when the void fraction equals zero and one, respectively. By using the thermodynamic equilibrium assumption,

the subscripts L and G, which denote the liquid and vapor phases from appendix A, turn into subscripts f and g, which denote the saturated liquid and saturated vapor phases, respectively.

Slip between the phases may be realized through the void fraction correlation. If we assume a homogeneous two-phase flow, i.e. no velocity slip between the phases($S = 1$), the void fraction can be calculated from equation A.4. It may be shown that for a homogeneous flow $\bar{h} = h$ and $\rho' = \bar{\rho} = \rho_H$, and that the homogeneous mixture density ρ_H is defined by equation A.7.

$$\alpha = \left(1 + \frac{\rho_g}{\rho_f} \frac{1-x}{x} S \right)^{-1} \tag{A.4}$$

$$\rho_H = \left(\frac{x}{\rho_g} + \frac{1-x}{\rho_f} \right)^{-1} \tag{A.7}$$

The void fraction is significant when predicting the refrigerant charge in the evaporator or condenser, and thus the dynamics of the system.

For steady state simulation, the predicted capacities become the same for both the homogeneous or slip flow modeling approach. This may be seen from the governing equations when the dynamic terms vanish. It is only the convective term and the gravitational term in the momentum equation that are influenced by the void fraction, and these terms normally have small impacts compared to friction. However, the charge is not the same for these modeling approaches. The void fraction becomes significant for the steady state capacity and COP only on a system level (closed cycle with a fixed charge), where the refrigerant is allowed to migrate between the condenser and evaporator between different steady states. Too low a charge will result in draining of the condenser into the evaporator at some conditions, which in worst case will result in a two-phase mixture fed to the expansion valve, thus unbalanced control of the evaporator superheat. Too high a charge will result in condenser flooding, i.e. the liquid takes up too much area of the condenser, which in turn results in increased condenser pressure, because of lower heat transfer.

Void fraction correlations

Many void fraction models are actually specifying the slip ratio. Using equation A.4 and a slip ratio correlation, the void fraction may be represented as function of vapor quality. Figure 2.3 shows a number of different void fraction models available to the developed `RefCell` component (figure 2.1 and 2.2) at typical evaporator conditions.

The void fraction predicted by Zivi (1964) and Smith (1969) are simple void fraction models and only functions of pressure and vapor quality. In contrast, the void fraction models by Premoli et al. (1971) and Steiners version of Rouhani and Axelsson (Steiner, 1993) are more sophisticated models and functions of pressure, vapor quality, surface tension, mass flux and gravity. The
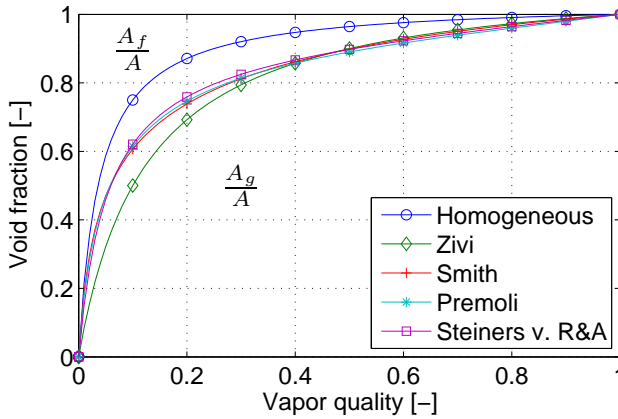
Figure 2.3: Void fraction vs. vapor quality; R410A at $T_{\text{sat}} = 10°$C, $G = 300\text{kgm}^{-2}\text{s}^{-1}$, $d = 7.6$mm.

homogeneous void fraction model underpredicts the refrigerant charge in the whole vapor quality range, whereas the Zivi model seems to overpredict in the low vapor quality region compared to the other void fraction models. The slip models are roughly comparable at vapor qualities above 0.4, however, recent studies by Maa et al. (2009) recommends the Premoli model for R410A room air-conditioners. The void fraction correlations are stated in appendix C.

Two-phase frictional pressure drop correlations

The frictional pressure drop may be predicted according to correlations from the literature. Figure 2.4 shows a number of correlations available to the `RefCell` component.
The correlations of Müller-Steinhagen and Heck (1986) and Grönnerud (1979) are independent of heat flux in contrast to Quibén and Thome (2007). The first two correlations are traditional simpler correlations, whereas the last correlation is an extensive calculation involving flow regime prediction (phenomenological model). The correlations are strong functions of refrigerant mass flux and diameter. It is interesting to note the differences in liquid and vapor frictional pressure drop at $x = 0$ and $x = 1$. The maximum frictional pressure drop is around $x = 0.8$, which is somewhat before the onset of dry-out according to Quibén and Thome (2007). The traditional correlations may differ by as much as 50% as indicated on the figure at $x = 0.8$. A statistical comparison by Quibén and Thome (2007) showed that the correlations by Grönnerud and Müller-Steinhagen and Heck were able to predict 41% and 50% of the data within an error of 20%, and 46% and 76% of the data within an error of 30%.
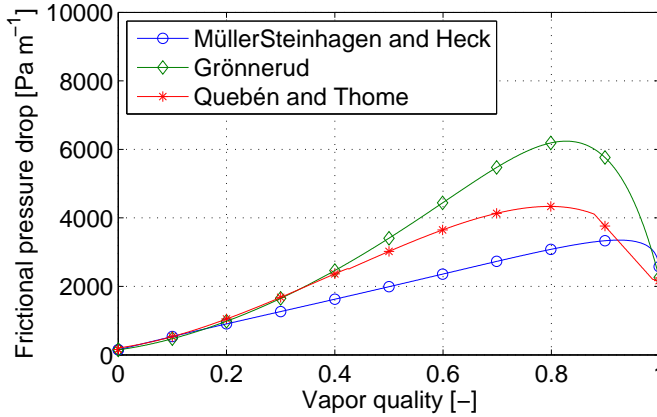
Figure 2.4: Frictional pressure drop vs. vapor quality; R410A at $T_{\text{sat}} = 10°$C, $G = 300\text{kgm}^{-2}\text{s}^{-1}$, $d = 7.6$mm, $q_w'' = 15\text{kWm}^{-2}$.

The flow regime dependent correlation by Quibén and Thome predicted 65% and 83% of the data within 20% and 30% error, respectively.

Smooth continuous functions have been used to ensure smooth transitions from two-phase to single-phase frictional pressure drop correlations. The smooth continuous function and friction correlations for two-phase and single-phase flow are stated in appendix C.

Two-phase heat transfer correlations

Figure 2.5 shows a number of heat transfer correlations from the literature available to the `RefCell` component.

All the correlations shown are functions of the mass flux, diameter and heat flux. Again two traditional correlations are chosen (Shah, 1982; Gunger and Winterton, 1987) together with the flow regime dependent correlation by Wojtan et al. (2005b). The traditional models are fairly in agreement, however, the phenomenological model is showing quite a different trend. The heat transfer coefficient is rising more steeply towards the dry-out point, and decreases hereafter linearly towards the vapor heat transfer coefficient. The authors claim that their correlation predicts especially the dry-out point well. The phenomenological model was able to predict 93% of the authors experimental data within 15% error. The correlation of Gunger and Winterton (1987) is a simpler correlation in contrast to their former (Gunger and Winterton, 1986). In the former, they found a mean error of 21% compared to their experiments and their newer showed similar accuracy. They also found that the correlation of Shah predicted their results with a mean error of 22%, which gives the Shah
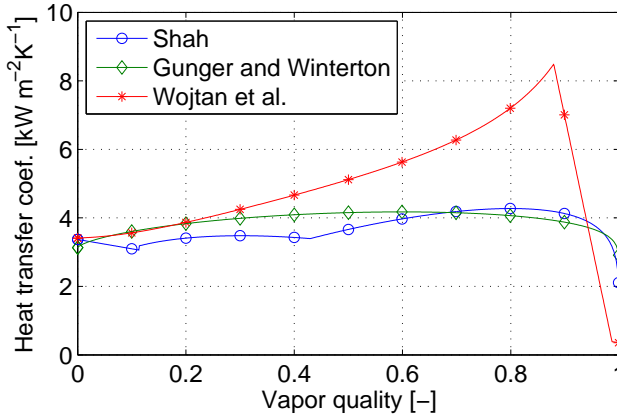
Figure 2.5: Heat transfer coefficient vs. vapor quality; R410A at $T_{\text{sat}} = 10°C$, $G = 300\text{kgm}^{-2}\text{s}^{-1}$, $d = 7.6\text{mm}$, $q_w'' = 15\text{kWm}^{-2}$.

correlation independent credibility.

Again, smooth continuous functions are used to ensure smooth transitions to the liquid and vapor heat transfer correlations. The heat transfer correlations and the smooth transition function are stated in appendix C.

State variables

It is favorable to explicitly compute the thermodynamic state from the dynamic state variables, in order to reduce iterations in refrigerant properties when stepping forward in time.

The thermodynamic state of a single-phase fluid is determined when two independent thermodynamic variables are known, e.g. pressure, temperature, enthalpy, density etc. For a two-phase one component mixture, pressure and temperature do not specify the thermodynamic state alone, however, pressure and enthalpy or internal energy etc. do.

On the other hand two of the dynamic state variables from the governing two-phase equations do not determine the thermodynamic state alone, i.e. $(p, \bar{h})$, $(p, \bar{\rho})$ or $(\bar{h}, \bar{\rho})$. Here the void fraction or slip ratio is needed.

It is apparent to get rid of the density as state variable in the liquid region, since it may result in a stiff system of equations because of the low compressibility (Bauer, 1999). For example, a small change in density causes a large change in pressure and/or enthalpy. Therefore, the pressure and the in situ enthalpy are chosen as the dynamic state variables. The derivative of the density with respect to time is then calculated by application of the chain rule keeping in

mind that $\bar{\rho} \equiv (p, \bar{h})$

$$\frac{\partial \bar{\rho}}{\partial t} = \frac{\partial \bar{\rho}}{\partial p}\bigg|_{\bar{h}} \frac{\partial p}{\partial t} + \frac{\partial \bar{\rho}}{\partial \bar{h}}\bigg|_p \frac{\partial \bar{h}}{\partial t} \tag{2.1}$$

where the partial derivatives of mixture density with respect to pressure and in situ enthalpy are calculated by numerical finite difference as

$$\frac{\partial \bar{\rho}}{\partial p}\bigg|_{\bar{h}} = \frac{\bar{\rho}(p + \Delta p, \bar{h}) - \bar{\rho}(p, \bar{h})}{\Delta p} \tag{2.2}$$

$$\frac{\partial \bar{\rho}}{\partial \bar{h}}\bigg|_p = \frac{\bar{\rho}(p, \bar{h} + \Delta \bar{h}) - \bar{\rho}(p, \bar{h})}{\Delta \bar{h}} \tag{2.3}$$

The thermodynamic state is known from the dynamic state variables when the void fraction or slip ratio is known and vice versa. In the special case of homogeneous flow ($S = 1$), the void fraction need not be determined since $\bar{h} = h$ and $\bar{\rho} = \rho_H$, thus the dynamic state becomes the thermodynamic state. The thermodynamic state properties are calculated from pressure, p, and mixed cup enthalpy, h, by the RefEqn package (Skovrup, 2009).

Discretization

The finite volume method is applied to discretize the governing one-dimensional equations. The finite volume method (in contrast to the finite difference method and finite element method) solves the equations in integral form by decomposing the pipe flow into a number of control volumes. The number of control volumes must be high enough to resolve the spatial distribution of properties. The staggered grid structure will be adopted as described by Patankar (1980). It means that the mass and energy conservation equations will be solved on the control volume cells, and the momentum equation will be solved on the staggered cells. The advantages are twofold. The mass conservation will not contain differences of adjacent mass flow rates (can prevent continuity in wavy flows) and the pressure difference between two adjacent control volume cells becomes the natural driving force for the mass flow rate in the staggered cells (control volume faces). The staggered grid structure is depicted in figure 2.6, where ψ denotes a thermodynamic quantity and $\hat{\psi}$ its approximation at the boundary of the control volume cells.

Integrating mass and energy conservation equations across the control volume length, Δz, results in

$$A\Delta z \frac{d\bar{\rho}_i}{dt} = \dot{m}_i - \dot{m}_{i+1} \tag{2.4}$$

$$A\Delta z \frac{d}{dt}\left(\bar{\rho}_i \bar{h}_i - p_i\right) = \dot{H}_i - \dot{H}_{i+1} + \dot{Q}_i \tag{2.5}$$
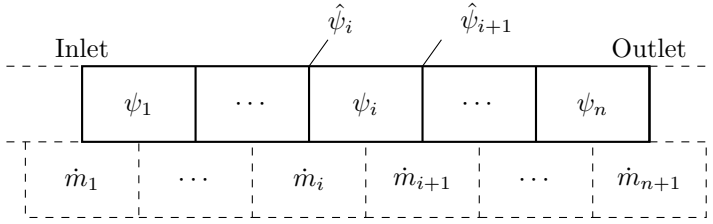
Figure 2.6: Staggered grid structure; full lines = control volume cells, dashed lines = staggered cells.

where the enthalpy flow and heat flow have been used as

$$\dot{H}_i = \dot{m}_i \hat{h}_i \tag{2.6}$$

$$\begin{aligned} \dot{Q}_i &= P\Delta z q''_{w,i} \\ &= P\Delta z h_{\text{tc,i}}(T_{w,i} - T_{r,i}) \end{aligned} \tag{2.7}$$

where the heat transfer coefficient h_{tc} is applied. The subscripts w and r denotes the wall and the refrigerant, respectively.

For convection dominated flows the upwind difference scheme is recommended to approximate thermodynamic quantities onto the staggered cells, because the central difference scheme may lead to non-physical solutions (Patankar, 1980). The 1st order upwinded scheme is obtained by taking the control volume face value (staggered cell center) to be equal to the nearest upstream control volume center, thus

$$\hat{\psi}_i \approx \delta_i \psi_i + (1 - \delta_i)\psi_{i-1} \qquad i = 1..n + 1 \tag{2.8}$$

where δ_i is the indicator function denoting the direction of the mass flow

$$\delta_i = \begin{cases} 0 & \dot{m} \geq 0 \\ 1 & \dot{m} < 0 \end{cases} \tag{2.9}$$

The momentum equation is integrated across the control volume length, Δz, and applied to the staggered cells.

$$\Delta z \frac{d\dot{m}_i}{dt} = \Delta \dot{I}_i - A(p_i - p_{i-1}) - F_{w,i}A\Delta z - \hat{\bar{\rho}}_i gA\Delta z \sin\theta \tag{2.10}$$

where the momentum flow has been used as

$$\dot{I}_i = \frac{\dot{m}_i^2}{\hat{\rho}'_i A} \tag{2.11}$$

The difference in pressure comes naturally from the adjacent control volume center, however, the difference in momentum flow $(\Delta \dot{I}_i)$ will be approximated

according to the 2$^{\text{nd}}$ order central difference scheme. This serves to avoid discontinuities in the momentum equation. The 2$^{\text{nd}}$ order central difference scheme simply averages the difference in momentum flow to each neighboring cell on the staggered grid, thus

$$\Delta \dot{I}_i \approx \frac{\left(\dot{I}_{i-1} - \dot{I}_i\right) + \left(\dot{I}_i - \dot{I}_{i+1}\right)}{2} = \frac{1}{2}\left(d\dot{I}_{i-1} + d\dot{I}_i\right) \tag{2.12}$$

where $d\dot{I}$ is the momentum flow difference between staggered grid cells, and will be computed in the control volume cell model.

Through the remainder of this thesis the control volume cell and the staggered cell will be referred to as the `VolCell` and the `FlowCell`. Each of these cells are components of the `RefCell` component from figure 2.1 and 2.2 as shown on figure 2.7.
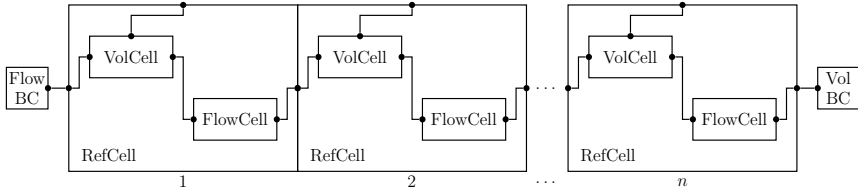
Figure 2.7: `RefCell` component connections; BC = Boundary condition.

Boundary and initial conditions

When simulating an evaporator, it is entirely free to choose the boundary conditions as long as the equations and variables are balanced. Three boundary conditions are essentially needed for the refrigerant flow. Normally, a steady state solution is achieved by specifying the thermodynamic state at the inlet of the evaporating tube and the mass flow rate at the outlet, which means that the evaporating temperature is fixed at the inlet. A bad example is to specify enthalpy at the inlet and mass flow rates at the inlet and outlet. Then the mass flows must be the same to achieve a steady state solution, however, this steady state is not fully specified, since it will depend on the initial conditions, i.e. the initial refrigerant charge in the evaporator.

Generally, the boundary conditions should be chosen such that the steady state is independent of initialization. We use the specific enthalpy and mass flow rate at the inlet and volume flow rate at the outlet as boundary conditions for the evaporator simulations.

For system simulation (including expansion valve, condenser and compressor) the steady state cannot be independent of the initialization (refrigerant charge). The simulation is just like reality where the system is charged with refrigerant according to a given subcooling at a predefined condition of the ambient. The

model should indeed facilitate a liquid filling of the system during simulation startup, see section 2.6.

It needs to be stressed out that the enthalpy boundary condition is the mixed cup enthalpy, thus the mixture enthalpy flowing through a cross sectional area, and not the in situ enthalpy, which is the bulk mixture enthalpy inside a control volume (based on a frozen field).

When specifying boundary conditions that are thermodynamic state variables, it is best to connect to a `FlowCell`. In contrast, it is best to connect to a `VolCell` when specifying the mass flow rate. There is nothing wrong not to obey these guidelines, however, fixing a mass flow rate to a `FlowCell` for example, results in a mass flow rate derivative of zero.

Other boundary conditions that must be computed in boundary models at inlet and outlet (see figure 2.7) are for the `FlowBC` $\left(d\dot{I}, \hat{\psi}\right)$ and for the `VolBC` $\left(\dot{H}, \dot{I}\right)$. The change of momentum flow $d\dot{I}$ at the inlet or outlet is set to zero, whereas the other variables are easily computed from the thermodynamic state.

2.2.2 Wall element

The Resistance-Capacitance method (Mills, 1999) is applied to each wall element (`WallCell`) in order to discretize the tube wall. The method essentially uses thermal resistances to describe the heat flows in and out of the lumped wall cell. The energy equation for the lumped tube element reads

$$\left(m_w c_{p,w} + m_f c_{p,f}\right)\frac{dT_w}{dt} = \dot{Q}_W + \dot{Q}_E + \dot{Q}_S + \dot{Q}_N \tag{2.13}$$

where $\dot{Q}_S = -\dot{Q}_i$ from equation 2.5, m_w and m_f are the mass of the wall and fins, $c_{p,w}$ and $c_{p,f}$ are the specific heat capacity of the wall and fins, T_w is the mean wall temperature and subscripts W, E, S, N denote west, east, south and north element boundary, respectively. Note that the thermal capacitance of the fins is included in the dynamics of the wall temperature. Figure 2.8 shows a sketch of the heat flows through the element boundaries. The tube element is assumed to have rotational symmetry, i.e. no azimuthal heat conduction in the θ-direction. The heat flows are computed as

$$\dot{Q}_W = \frac{T_W - T_w}{R_{\text{ax}}/2} \tag{2.14}$$

$$\dot{Q}_E = \frac{T_E - T_w}{R_{\text{ax}}/2} \tag{2.15}$$

$$\dot{Q}_N = \frac{T_N - T_w}{R_{\text{rad}}/2} \tag{2.16}$$

$$\dot{Q}_S = \frac{T_S - T_w}{R_{\text{rad}}/2} \tag{2.17}$$
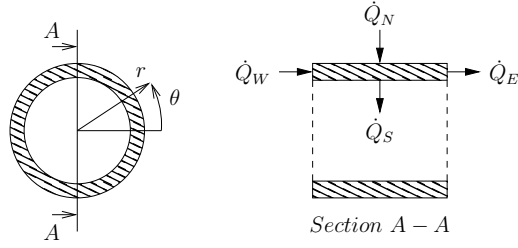
Figure 2.8: Energy balance principle on a wall cell.

where R_{rad} and R_{ax} are the thermal resistances across the tube element in the radial and axial direction computed as

$$R_{\text{ax}} = \frac{\Delta z}{k_w A_w} \qquad (2.18)$$

$$R_{\text{rad}} = \frac{\ln\left(\frac{D/2}{d/2}\right)}{2\pi k_w \Delta z} \qquad (2.19)$$

where k_w is the thermal conductivity of the wall, D is the outer diameter of the tube, d is the inner diameter of the tube and A_w is the cross-sectional area of the tube wall element.

The boundary conditions at the inlet and outlet of the tube are no heat flow in the axial direction.

2.2.3 Airflow

The airflow is assumed to be incompressible and static, i.e. no accumulation of mass or energy. The changes in kinetic and potential energy are neglected and pressure drop is not addressed. With these assumptions the mass and energy conservation equation reads

$$\dot{m}_{\text{in}} - \dot{m}_{\text{out}} = 0 \qquad (2.20)$$

$$(\dot{m}c_p T)_{\text{in}} - (\dot{m}c_p T)_{\text{out}} + \dot{Q} = 0 \qquad (2.21)$$

where $\dot{Q} = -\dot{Q}_N$ from equation 2.13. The equations are applied to each air cell. Since the air temperature changes through the cell (in contrast to a one-component two-phase mixture), we have to be careful which temperature difference we use as driving potential for the heat transfer ($\dot{Q}$). The air temperature change can be minimized if we have a parallel or counter flow heat exchanger by using more cells, however, this cannot be done for a cross flow heat exchanger.

Two different approaches are used to model the heat transfer in the `AirCell` component, which may be chosen by the user. The former is the simpler heat transfer approach and calculated by using the temperature difference from the wall to the mean air temperature, that is

$$\dot{Q} = h_{\text{tc}}\eta_o A_T (T_w - T_{a,m}) \qquad T_{a,m} = (T_{\text{in}} + T_{\text{out}})/2 \qquad (2.22)$$

where h_{tc} is the heat transfer coefficient on the air side, η_o is the overall surface fin efficiency and A_T is the total surface area. The overall surface fin efficiency is given by

$$\eta_o = 1 - \frac{A_f}{A_T}(1 - \eta_f) \qquad (\text{C.83})$$

where A_f is the surface area of the fins and η_f is the fin efficiency.

The latter is the effectiveness-NTU method, which is more sophisticated and depends on both the air and refrigerant heat capacity flow. It describes the actual heat flow by an effectiveness ϵ of the highest possible heat transfer, that is

$$\dot{Q} = \epsilon C_{\min}(-\Delta T_{\max}) \qquad (2.23)$$

where $C_{\min}$ is the minimum heat capacity flow and $\Delta T_{\max}$ is the maximum temperature difference computed by

$$C_{\min} = \min(\dot{m}_a c_{p,a}, \dot{m}_r c_{p,r}) \qquad (2.24)$$

$$\Delta T_{\max} = T_{\text{in}} - T_w \qquad (2.25)$$

where a and r denotes the air and refrigerant. Similarly we can compute the maximum heat capacity flow. In general, the effectiveness is a function of the ratio of the heat capacity flows $R_C = C_{\min}/C_{\max}$, number of transfer units $\text{NTU} = h_{\text{tc}}\eta_o A_T/C_{\min}$ and the flow arrangement of the heat exchanger (parallel, counter, cross flow etc.).

In the two-phase region, it can be shown that the effectiveness regardless of flow arrangement can be calculated by

$$\epsilon = 1 - \exp(-\text{NTU}) \qquad (2.26)$$

In the single-phase region of the heat exchanger, we must apply the appropriate effectiveness-NTU relation. For parallel and counter flow heat exchangers the air temperature change can be minimized by using more cells and equation 2.22, which makes the use of the effectiveness-NTU method superfluous. For this reason only one effectiveness-NTU relation for a cross flow heat exchanger

having one stream unmixed (air) and the other stream mixed (refrigerant) has been implemented.

$$\epsilon = \begin{cases} 1 - \exp\left(-\frac{1}{R_C}\left[1 - \exp(-\mathrm{NTU}R_C)\right]\right) & C_{\min} = \text{mixed} \\ \frac{1}{R_C}\left(1 - \exp\{-[1 - \exp(-\mathrm{NTU})]R_C\}\right) & C_{\min} = \text{unmixed} \end{cases} \quad (2.27)$$

The relations are found in heat transfer books, such as Mills (1999) or Incropera et al. (2007). The effectiveness-NTU method is another but similar formulation of the Logarithmic Mean Temperature Difference method (LMTD). In this method, flow arrangements other than parallel or counter flow are facilitated by the F-factor, which is computed by similar relations such as equation 2.27. The smooth continuous function (see appendix C) is applied at the transitions from the two-phase to the single-phase effectiveness-NTU relations, in order to ensure a smooth transition of ϵ and $C_{\min}$. Correlations for the heat transfer coefficient and fin efficiency must be applied to close the system of equations, see appendix C.

The boundary conditions for the air stream are simply inlet temperature and mass flow rate or velocity.

2.3   Condenser

Refrigerant migration between the evaporator and condenser is important to fully determine the performance of the system. This may be particularly of interest when investigating maldistribution. If a severe maldistribution occurs in the evaporator, the refrigerant will migrate to the condenser, and may cause condenser flooding. The requirements to the condenser model is to model the refrigerant charge and heat transfer. There is no reason to model pressure drop or detailed spacial heat transfer, since the refrigerant distribution in the condenser is not of interest in this project. Therefore, the moving boundary model are chosen for this purpose. There exist many forms of the moving boundary model. The chosen model formulation is described for an evaporator by Zhang and Zhang (2006), which is a further development of the Willatzen et al. (1998) model.

In this section, we present the moving boundary model used as the condenser. We present the model equations and show how we compute the heat transfer from the refrigerant to the air. We did not include the dynamics of the wall, since it has no impact on the refrigerant migration. The derivation of the used moving boundary model is given in appendix B.

2.3.1   Moving boundary model equations

As mentioned the dynamics of the wall is neglected. It can be included when the dynamics of the condenser wall are of interest. Both Zhang and Zhang

(2006) and Willatzen et al. (1998) describes a model of the wall, however, Jensen (2003) gives an overview of different approaches and their trade-offs. The model of the refrigerant flow is the same in Willatzen et al. (1998) and Jensen (2003).

The traditional moving boundary models solve only mass and energy conservation equations, thus pressure drop is neglected. These models cannot model refrigerant distribution, since they do not model the mass flow/pressure drop dependence between parallel channels. For modeling the refrigerant distribution using a moving boundary model, newer models must be used such as Zhang et al. (2009).

The moving boundary models do not have the ability to model tube circuitry, since the liquid, two-phase and vapor regions are lumped individually. Essentially, the evaporator tubes are assumed to be straight.

Figure 2.9 shows a sketch of the moving boundary model approach. The bar-operator (⁻) means here that the quantity is averaged in both cross-sectional area and length of the region.
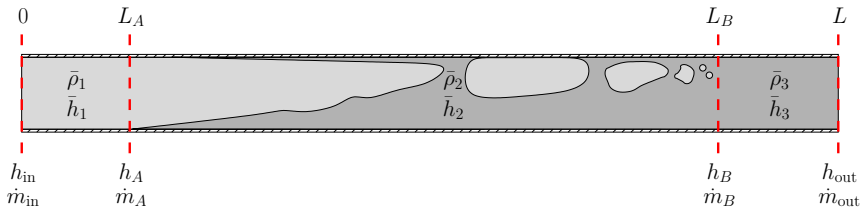
Figure 2.9: Moving boundary model structure (condenser).

Sometimes under larger disturbances, the liquid may be drained into the evaporator such that the liquid region in the condenser vanish. In this case the model equations switch such that two-phase flows out of the condenser. When 3 regions exist ($h_{out} < h_f$) the V-TP-L model is used and when 2 regions exist ($h_{out} \geq h_f$) the V-TP model is used. The model equations are shown below, i.e. mass and energy conservation equations. The derivatives of the mean densities and enthalpies are transformed using the mean void fraction in the two-phase region into derivatives of pressure, inlet enthalpy and outlet enthalpy. These are essentially different in the two-phase region for the V-TP model, since the void fraction will depend on outlet enthalpy also. The mean void fraction is computed by numerical integration of the local void fraction across the two-phase region by equation B.11 or B.38 depending on the model (V-TP-L or V-TP).

A detailed derivation of the moving boundary model are given in appendix B including these transformations.

V-TP-L model:

Two-phase region

$$A(L_B - L_A)\frac{d\bar{\rho}_2}{dt} + A(\rho_g - \bar{\rho}_2)\frac{dL_A}{dt} + A(\bar{\rho}_2 - \rho_f)\frac{dL_B}{dt} = \dot{m}_A - \dot{m}_B \quad \text{(B.4)}$$

$$A(L_B - L_A)\left(\frac{d\bar{\rho}_2\bar{h}_2}{dt} - \frac{dp}{dt}\right) + A(\rho_g h_g - \bar{\rho}_2\bar{h}_2)\frac{dL_A}{dt} +$$
$$A(\bar{\rho}_2\bar{h}_2 - \rho_f h_f)\frac{dL_B}{dt} = (\dot{m}h)_A - (\dot{m}h)_B + \dot{Q}_{\text{tp}} \quad \text{(B.8)}$$

Vapor region

$$AL_A\frac{d\bar{\rho}_1}{dt} + A(\bar{\rho}_1 - \rho_g)\frac{dL_A}{dt} = \dot{m}_{\text{in}} - \dot{m}_A \quad \text{(B.19)}$$

$$AL_A\left(\bar{\rho}_1\frac{d\bar{h}_1}{dt} + \bar{h}_1\frac{d\bar{\rho}_1}{dt} - \frac{dp}{dt}\right) + A(\bar{\rho}_1\bar{h}_1 - \rho_g h_g)\frac{dL_A}{dt} =$$
$$(\dot{m}h)_{\text{in}} - (\dot{m}h)_A + \dot{Q}_g \quad \text{(B.23)}$$

Liquid region

$$A(L - L_B)\frac{d\bar{\rho}_3}{dt} + A(\rho_f - \bar{\rho}_3)\frac{dL_B}{dt} = \dot{m}_B - \dot{m}_{\text{out}} \quad \text{(B.28)}$$

$$A(L - L_B)\left(\bar{\rho}_3\frac{d\bar{h}_3}{dt} + \bar{h}_3\frac{d\bar{\rho}_3}{dt} - \frac{dp}{dt}\right) + A(\rho_f h_f - \bar{\rho}_3\bar{h}_3)\frac{dL_B}{dt} =$$
$$(\dot{m}h)_B - (\dot{m}h)_{\text{out}} + \dot{Q}_f \quad \text{(B.29)}$$

V-TP model:

Two-phase region

$$A(L - L_A)\frac{d\bar{\rho}_2}{dt} + A(\rho_g - \bar{\rho}_2)\frac{dL_A}{dt} = \dot{m}_A - \dot{m}_{\text{out}} \quad \text{(B.33)}$$

$$A(L - L_A)\left(\frac{d\bar{\rho}_2\bar{h}_2}{dt} - \frac{dp}{dt}\right) + A(\rho_g h_g - \bar{\rho}_2\bar{h}_2)\frac{dL_A}{dt} = (\dot{m}h)_A - (\dot{m}h)_{\text{out}} + \dot{Q}_{\text{tp}}$$
$$\text{(B.37)}$$

Vapor region

Same equations as used in V-TP-L model.

Liquid region

The liquid region does not exist, thus
$$L_B = L$$
$$\dot{m}_B = \dot{m}_{\text{out}}$$

Correlations from the literature are needed for computing the void fraction in the two-phase region and the heat transfer in all the regions ($\dot{Q}_{\text{tp}}$, $\dot{Q}_g$ and $\dot{Q}_f$).

2.3.2   Heat transfer

The heat transfer is modeled similarly to the heat transfer in the distributed model for the evaporator. Therefore, it may be chosen to use a simple heat transfer approach or the effectiveness-NTU method. The main difference from the distributed model is that the dynamics of the wall is neglected, thus the heat transfer is modeled all the way from the refrigerant to the air. Furthermore, the heat transfer is described for each region of the evaporator that is occupied by liquid, vapor or two-phase as a whole.
Using the simpler approach the heat transfer is computed for each regions by

$$\dot{Q} = \text{UA}(T_{a,m} - T_{r,m}) \tag{2.28}$$

where subscript m denotes the mean, r the refrigerant and a the air. The overall UA-values are computed by

$$\text{UA} = \left[\frac{1}{h_{\text{tc,r}}A_r} + \frac{1}{h_{\text{tc,a}}\eta_o A_a} \right]^{-1} \tag{2.29}$$

where A_r is the internal surface area of the wall and A_a is the outer surface area including fins for each regions. The mean two-phase heat transfer coefficient is computed by numerical integration as shown by equation B.15 or B.42 depending on the model (V-TP-L or V-TP). For all other heat transfer coefficients (liquid, vapor or air) and the fin efficiency, mean properties are used to compute the mean heat transfer coefficient and mean fin efficiency.
For condensation, the two-phase heat transfer correlations are a bit different compared to evaporation. For evaporation, the heat transfer mechanisms are partly nucleate boiling and convective boiling. Nucleate boiling is essentially bubble formation created at nucleation sites on the wall, whereas convective boiling is heat transfer on the liquid and vapor interphase. For condensation, we have only the convective heat transfer contribution. Shah (1979) has also made a condensation heat transfer correlation as shown in figure 2.10.
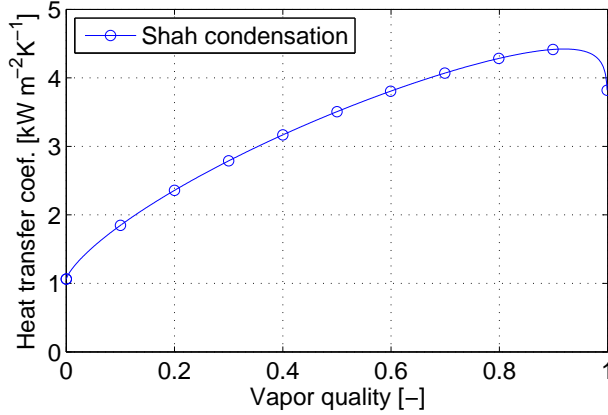
Figure 2.10: Heat transfer coefficient vs. vapor quality; R410A at $T_{\text{sat}} = 45°\text{C}$, $G = 300\text{kgm}^{-2}\text{s}^{-1}$, $d = 7.6\text{mm}$.

Using the effectiveness-NTU method, the heat transfer for each region is described by

$$\dot{Q} = \epsilon C_{\min}(-\Delta T_{\max}) \tag{2.30}$$

where $C_{\min}$ is the minimum heat capacity flow and $\Delta T_{\max}$ is the maximum temperature difference computed by

$$C_{\min} = \min(\dot{m}_a c_{p,a}, \dot{m}_r c_{p,r}) \tag{2.31}$$

$$\Delta T_{\max} = T_{r,in} - T_{a,in} \tag{2.32}$$

Similarly, we can compute the maximum heat capacity flow and thus the heat capacity ratio $R_C = C_{\min}/C_{\max}$. The Number of Transfer Units (NTU) may be calculated by the UA-values above for each region, $\text{NTU} = \text{UA}/C_{\min}$, and finally, we can compute the effectiveness for each region by equations 2.26 or 2.27.

2.4 Compressor

Compressors for residential air conditioning are typically scroll compressors and part of the outdoor unit. Application of the energy conservation principle to a control volume surrounding the compressor, as depicted in figure 2.11, reads

$$\frac{dE}{dt} = (\dot{m}e)_1 - (\dot{m}e)_2 + \dot{Q} + \dot{W} \tag{2.33}$$
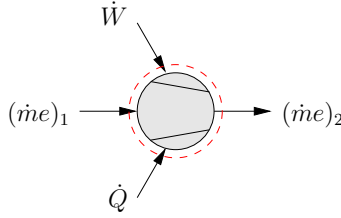
Figure 2.11: Energy conservation principle around the compressor.

where $\dot{Q}$ is the heat flow across the control volume boundary (heat loss), $\dot{W}$ is the power applied to the control volume, e is the specific convected energy defined by equation A.26 and E is the total energy in the control volume ($E = \rho V e_t$). ρ is the density in the control volume, V is the volume and e_t is the total specific energy defined by equation A.25.

The compressor is assumed to be quasi-static, since the compressor dynamics are much quicker than the time-scales of interest in this project. The mass flow rate in and out becomes the same and the mass flow subscripts are omitted for now for simplicity. Furthermore, the changes in kinetic and potential energies are neglected. With these assumptions the energy conservation equation becomes

$$\dot{W} = \dot{m}(h_2 - h_1) - \dot{Q} \tag{2.34}$$

The compression is modeled using the isentropic efficiency, which is defined by

$$\eta_{\text{is}} = \frac{\dot{W}_{\text{is}}}{\dot{W}} = \frac{h_{2,\text{is}} - h_1}{h_{2,w} - h_1} \tag{2.35}$$

where subscripts is and w denote the isentropic compression and actual compression work, respectively. Figure 2.12 shows a sketch of the different points in the $\log(p)h$ diagram.

Using these symbols the heat loss is defined by $\dot{Q} = \dot{m}(h_2 - h_{2,w})$ and is usually around 3% of the power $\dot{W}$ for scroll compressors. For simplicity the heat loss will be neglected ($h_{2,w} = h_2$), and the energy equation becomes.

$$\dot{W} = \dot{m}(h_2 - h_1) \tag{2.36}$$

where the isentropic efficiency from equation 2.35 is used to calculate the outlet enthalpy. The mass flow rate is determined by the inlet density, the geometric volume flow of the compressor and the volumetric efficiency as

$$\dot{m} = \rho_1 \dot{V}_{\text{geo}} \eta_{\text{vol}} \tag{2.37}$$

where $\eta_{\text{vol}} = \dot{V}_{\text{act}}/\dot{V}_{\text{geo}}$, i.e. the actual volume flow divided by the geometric volume flow.
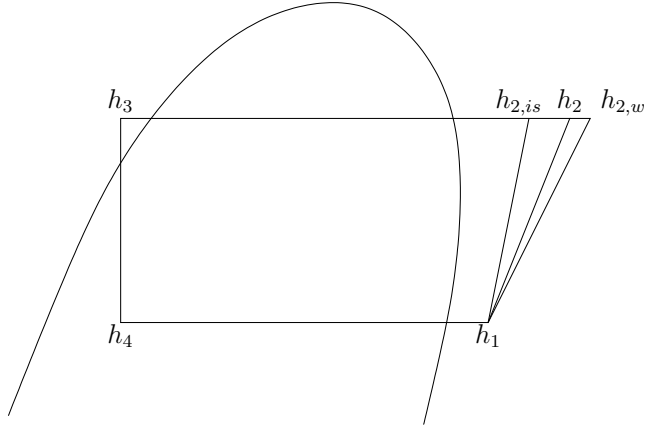
Figure 2.12: $\log(p)h$ diagram.

To close the system of equations, we need polynomials for the isentropic and volumetric efficiency. These depend on the specific compressor type, size and fluid.

2.4.1 Isentropic and volumetric efficiency

Compressors for the residential air-conditioning market are rated according to e.g. EN 12900 (2005) or ANSI/AHRI Standard 540 (2004). A standard ten coefficient polynomial is specified in both references that may be used to compute the mass flow rate, cooling capacity and power consumption for different suction and discharge temperatures at fixed superheat and subcooling (rated conditions). The refrigerant is fixed for the compressor of interest. The polynomial has the following form:

$$
\begin{aligned}
X = C_1 + C_2 T_s + C_3 T_d + C_4 T_s^2 + C_5 T_s T_d + C_6 T_d^2 \\
+ C_7 T_s^3 + C_8 T_d T_s^2 + C_9 T_s T_d^2 + C_{10} T_d^3
\end{aligned}
\tag{2.38}
$$

where T_s and T_d are the suction and discharge dew point temperatures, C are the coefficients and X may be mass flow rate, cooling capacity or power consumption according to the coefficients used.

Knowing the geometric volume flow $\dot{V}_{\text{geo}}$, equation 2.38 may be used to compute the volumetric and isentropic efficiencies at rated conditions. These efficiencies are assumed to be independent of superheat and directly used in equation 2.35 and 2.37 to compute the actual mass flow rate and outlet enthalpy at actual superheat.

2.5   Expansion valve

The expansion is modeled as an isenthalpic process. The mass flow rate is controlled by the superheat control as illustrated on figure 2.13.
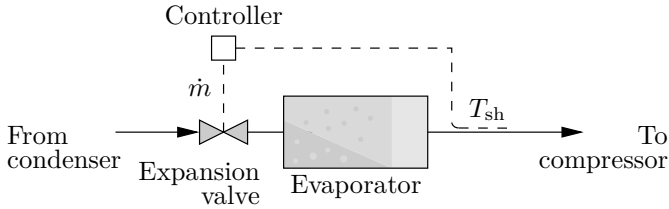
Figure 2.13: Superheat control.

In this project, we used only continuous controllers, i.e. an integral controller (I-controller) and a proportional-integral controller (PI-controller), similar to the models available in the Standard Modelica Library, but with minor modifications. A reference temperature must be specified in the superheat controller, the gain for the I-controller, and the gain and time constant for the PI-controller.
The PI-controller showed better performance in our simulations when considering the control stability and simulation time to reach a steady state.

2.6   Filling station

For dynamic system simulation we need to charge the system during startup, just like in real systems at first installation. This is carried out by controlling the subcooling to 2 K by the refrigerant charge at standard conditions ($T_{\text{indoor}} = 26.7^{\circ}\text{C}$, $T_{\text{outdoor}} = 35^{\circ}\text{C}$), as shown on figure 2.14.
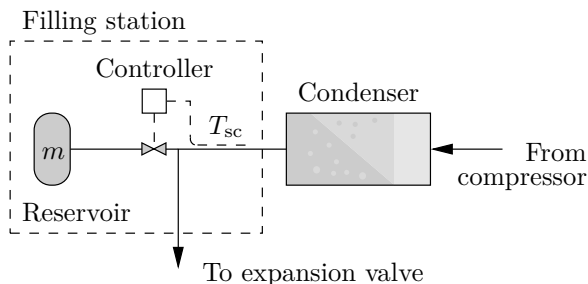
Figure 2.14: Filling station control.

The mass conservation equation is applied to the filling station as

$$\frac{dm}{dt} = \dot{m}_{\text{in}} - \dot{m}_{\text{out}} \tag{2.39}$$

where m is the mass in the infinite reservoir. The derivative of the mass may be seen as the change of refrigerant charge in the refrigeration cycle. Using an I-controller, the derivative of the change in refrigerant charge during start-up becomes

$$\frac{dm}{dt} = k(T_{\text{sc}} - T_{\text{sc,setpoint}}) \tag{2.40}$$

where k is the integrator gain. Otherwise $\frac{dm}{dt} = 0$.

2.7   Refrigerant distributor

The refrigerant is distributed into the individual channels of the multi-channel evaporator or condenser. In this section, we will address the refrigerant distributor for the evaporator only. The distribution to the condenser model is uniform due to the lumped model assumption.

The number of outlets in the distributor model can be either one, two or four, but may be updated to more if necessary. The purpose of the distributor is to distribute the entering two-phase refrigerant evenly to the individual channels. It is located as close as possible to the expansion device, so that phase separation is minimized, and the mass flux is kept high to ensure a homogeneous mixture before distribution.

The model of the distributor may be chosen to run in different modes:

1. *EXV flow*
2. *Even flow*
3. *Compensating flow*

The first mode is the traditional system using an electronic expansion valve (EXV) and a distributor, where the actual mass flow distribution is computed according to the individual channel pressure drop, which must be the same. The liquid and vapor phases may therefore be maldistributed for this mode. In contrast, the latter two modes have no liquid and vapor maldistribution and rather distribute the actual mass flow to each channel. The *Even flow* mode distributes the mass flow evenly. The *Compensating flow* mode distributes the mass flow according to the control of individual channel superheats.

In the following the modes are described in more detail.

2.7.1 EXV flow mode

The sources of refrigerant flow maldistribution caused by the distributor can be either different mass flow distribution, different phase distribution or different feeder tube bending. In this project, we want to predict the refrigerant mass flow distribution, that may be computed according to individual pressure drop through the evaporator. Therefore, we have defined two distribution parameters, one considering the phase distribution F_x, the other considering the feeder tube bending F_{ft}. Both the different phase distribution and feeder tube bending may alter the individual channel pressure drop, which must be the same and thereby alter the mass flow distribution.

The distribution parameters are described in the following. They are only defined for two channels, but may be updated if necessary. Figure 2.15 shows the symbols to be used in the definitions of the distribution parameters.
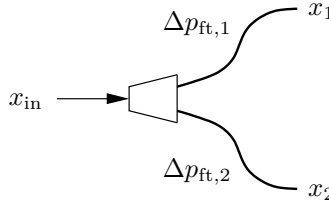
Figure 2.15: Sketch of the distributor.

The phase distribution parameter is defined by

$$F_x = \frac{x_2}{x_{\mathrm{in}}} \qquad 0 \leq F_x \leq 1 \tag{2.41}$$

$$F_x = 2 - \frac{x_1}{x_{\mathrm{in}}} \qquad 1 < F_x \leq 2 \tag{2.42}$$

When F_x is unity, the vapor quality into the feeder tubes is equal. When F_x is zero, only liquid is fed into channel 2. When F_x is two, only liquid is fed into channel 1. Mass and energy conservation equations are applied to compute the vapor quality into the remaining channel.

$$\dot{m}_{\mathrm{in}} = \sum_{i=1}^{N} \dot{m}_i \tag{2.43}$$

$$(\dot{m}h)_{\mathrm{in}} = \sum_{i=1}^{N} (\dot{m}h)_i \tag{2.44}$$

where N is the number of channels, h is the mixed cup enthalpy defined by equation A.8, from which the vapor quality may be computed. Furthermore, the distributor and the feeder tubes are assumed to be adiabatic.

The feeder tube bending parameter is defined by

$$\Delta p_{\text{ft},1} = F_{\text{ft}}\Delta p_{\text{fric},1} + \Delta p_{\text{acc},1} \qquad 1 \leq F_{\text{ft}} \leq 5.5$$
$$\Delta p_{\text{ft},2} = \Delta p_{\text{fric},2} + \Delta p_{\text{acc},2}$$

(2.45)

where F_{ft} is multiplied to the frictional pressure drop of channel 1 only, which imposes a degree of bending (the maximum factor of 5.5 was assumed). The accelerational pressure drop is not a function of the length. Therefore, the feeder tube bending parameter can be viewed as an equivalent length multiplier. When F_{ft} is unity, the feeder tubes are straight tubes, in contrast to when $F_{\text{ft}} > 1$.

The frictional pressure drop is calculated similarly to equation A.40 and A.45 according to two-phase flow correlations from the literature. Note that we apply these correlations at small diameter tubes (3mm) and thus high mass fluxes, which in turn is outside the limits of the correlations. No correlation has been found in the literature for feeder tube pressure drop, and therefore the traditional two-phase flow correlations are used.

$$\Delta p_{\text{fric},i} = -f_{D,i}\frac{L_{\text{ft}}}{d_{\text{ft}}}\frac{\dot{m}_i^2}{2\bar{\rho}_{\text{in},i}A^2} \qquad i = 1..N$$

(2.46)

where the *Darcy-Weisbach friction factor* has been used. The accelerational pressure drop, which is the difference in momentum flows, is computed by

$$\Delta p_{\text{acc},i} = \frac{\dot{m}_i^2}{(\bar{\rho}_{\text{in},i} - \bar{\rho}_{\text{out},i})A^2} \qquad i = 1..N$$

(2.47)

All densities are computed by assuming homogeneous flow according to equation A.7.

2.7.2   Even flow and compensating flow modes

When using the *Even flow* and *Compensating flow* modes the phase distribution parameter F_x is unity, since the modes simulate a method that distributes the refrigerant before the expansion. Moreover, the individual enthalpy out of the feeder tubes is equal to the inlet enthalpy, and the use of F_x becomes superfluous. The mass flow distribution is then specified into each feeder tube. In order to allow a specified mass flow distribution into the evaporator channels, the individual pressure drop through the channels need not be the same. In other words, the individual pressure drop dictates the mass flow distribution when they are set to be equal. To specify a mass flow distribution, we need to introduce a pressure drop difference between the channels in the distributor. This is carried out by introducing a pressure drop difference variable Δp, that

is used when connecting inlet pressure of the distributor and outlet pressures of the feeder tubes as

$$\left.\begin{array}{l} p_{\text{in}} = p_{\text{out},1} - \Delta p_{\text{ft},1} + \Delta p \\ p_{\text{in}} = p_{\text{out},2} - \Delta p_{\text{ft},2} \end{array}\right\} \quad p_{\text{out},1} \leq p_{\text{out},2} \quad (2.48)$$

$$\left.\begin{array}{l} p_{\text{in}} = p_{\text{out},1} - \Delta p_{\text{ft},1} \\ p_{\text{in}} = p_{\text{out},2} - \Delta p_{\text{ft},2} + \Delta p \end{array}\right\} \quad p_{\text{out},1} > p_{\text{out},2} \quad (2.49)$$

The pressure drop difference variable Δp is allowing the pressure drops through each channel all the way to the manifold to be different. The conditional constraint is ensuring that the pressure cannot rise across the feeder tubes.
The *Even flow* and *Compensating flow* modes may also be run with four feeder tube outlets, where three pressure drop difference variables have been defined similarly to equation 2.48 and 2.49.
When the *Even flow* is used the mass flows are evenly distributed as

$$\dot{m}_i = \frac{\dot{m}_{\text{in}}}{N} \qquad i = 1..N \quad (2.50)$$

where N is the number of outlets.
When the *Compensating flow* mode is used, the distribution needs to be specified as an input to the distributor model. This input mass flow distribution is achieved by control of individual channel superheat of the evaporator, as shown on figure 2.16 for two evaporator channels.
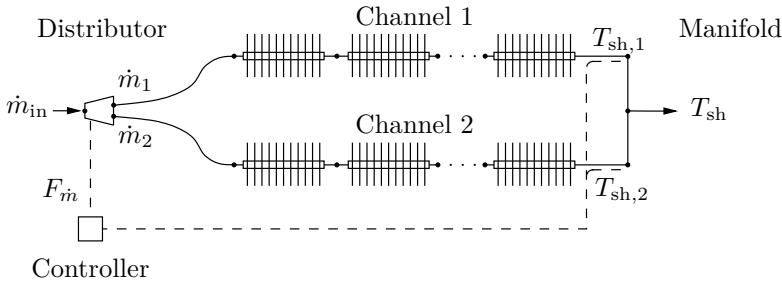
Figure 2.16: Control of mass flow distribution.

When simulating two evaporator channels with the *Compensating flow* mode, we use the mass conservation equation in the distributor, and control the difference in the individual superheats to be zero by the mass flow difference parameter $F_{\dot{m}}$, defined by

$$F_{\dot{m}} = \dot{m}_1 - \dot{m}_2 \quad (2.51)$$

This way we can keep the overall superheat control as described in section 2.5, i.e. control of overall superheat by the mass flow through the expansion valve. Figure 2.16 is essentially the evaporator on figure 2.13. If the difference in mass flow distribution $F_{\dot{m}}$ equals zero then the mass flow rate is distributed evenly. When simulating four evaporator channels, we control the first three channel superheats by each channel mass flow rate, and use mass conservation to find the fourth channel mass flow, and control the overall mass flow by the mass flow through the expansion valve.

For the control of the mass flow distribution, we only use I-controllers similar to the continuous integrator (I-controller) in the Standard Modelica Library.

2.8 Airflow distribution

The sources of maldistribution from the airflow may be uneven temperature, humidity and velocity distribution to the evaporator. In this thesis we do not consider humid or frost conditions and the airflow is always considered as dry. Furthermore, the uneven temperature distribution seems less apparent than the velocity distribution, and thus we address only the velocity distribution in this work.

Similar to the distributor model, we define an airflow distribution parameter. This parameter is defined differently when modeling two straight evaporating tubes and when modeling actual circuiting. The differences are shown in this section.

2.8.1 Two straight evaporator tubes

In the following, the symbols on figure 2.17 are used.
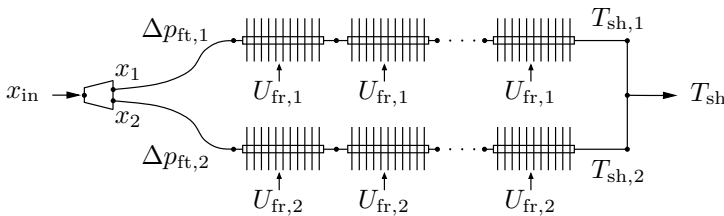
Figure 2.17: Sketch of the two channel evaporator.

In order to study the airflow distribution, we have defined the airflow distribution parameter as

$$F_{\text{air}} = \frac{U_{\text{fr},2}}{U_m} \qquad 0 \le F_{\text{air}} \le 2 \tag{2.52}$$

where U_{fr} is the frontal velocity and U_m is the mean frontal velocity across the two tubes. When F_{air} is unity, the airflow is distributed equally across the two tubes. When F_{air} is zero, the air flows across channel 1 only. When F_{air} is two, the air flows across channel 2 only. The mass flow rate across the evaporator is kept constant and the mass conservation equation is used to compute the frontal velocity of channel 1.

2.8.2 Evaporator circuitry

The above definition of the airflow distribution parameter works only for 2 straight evaporator tubes. When one wants to simulate the circuitry of an evaporator (e.g. facesplit or interlaced), then the definition becomes different as shown on figure 2.18.
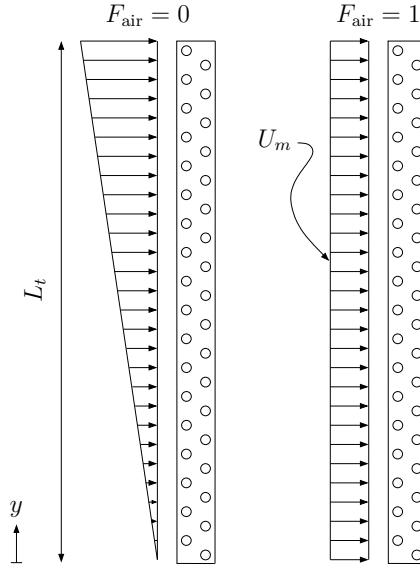
Figure 2.18: Sketch of the evaporator for circuitry modeling.

The airflow distribution parameter F_{air} is then defined by

$$U(y) = U_m F_{\mathrm{air}} + y\frac{2U_m(1 - F_{\mathrm{air}})}{L_t} \qquad 0 \leq F_{\mathrm{air}} \leq 2 \qquad (2.53)$$

where y is the transverse coordinate and L_t is the transverse length of the coil. When F_{air} is unity, the airflow profile is uniform across the coil. When F_{air} is zero or two, the airflow profile becomes the worst possible linear one-dimensional profile in the transverse direction.

2.9 Refrigerant manifold

The manifold is modeled simply by mixing of a given number of streams at equal pressures, i.e. no pressure drop due to friction or mixing, see figure 2.19. Mass and energy conservation are applied and reads
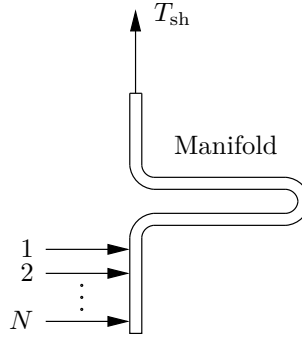
Figure 2.19: Sketch of the manifold.

$$AL\frac{d\bar{\rho}}{dt} = \sum_{i=1}^{N} \dot{m}_{\text{in}} - \dot{m}_{\text{out}} \tag{2.54}$$

$$AL\frac{d}{dt}\left(\bar{\rho}\bar{h} - p\right) = \sum_{i=1}^{N}(\dot{m}h)_{\text{in}} - (\dot{m}h)_{\text{out}} + \dot{Q} \tag{2.55}$$

where N is the number of entering streams to the manifold, A is the cross sectional area, L is the length and $\dot{Q}$ is the heat flow from the manifold wall to the refrigerant described by Newton's law of cooling (constant heat transfer coefficient and positive for $T_w > T_r$). The manifold is assumed to be adiabatic with the surroundings, however, the heat capacity of the wall has been included by

$$A_w L \rho_w c_{p,w}\frac{dT_w}{dt} = -\dot{Q} \tag{2.56}$$

where A_w, ρ_w, $c_{p,w}$ and T_w are the cross-sectional area, density, specific heat capacity and temperature of the manifold wall, respectively.

The inclusion of the heat capacity of the manifold wall and the refrigerant volume have no effects on the steady state results and may both be neglected in the model, if dynamics of the manifold wall and volume are not of interest.

2.10   Summary

This chapter presented the model formulations of the components of the air-conditioning system.

The chapter goes through the model details of the distributed evaporator model, the moving boundary model, the quasi-static compressor and expansion models. Furthermore, it gives an introduction to one-dimensional two-phase flow with use of empirical correlations for heat transfer, friction and void.

Then the control of evaporator superheat and the refrigerant charging during startup is presented.

Finally, the capabilities of simulating flow maldistribution and compensation by using the defined distribution parameters (F_x, F_{ft} and F_{air}) and distributor options (*EXV flow*, *Even flow* and *Compensating flow*) are described.

The equations shown in this chapter may be implemented in any programming languages supporting events. Chapter 3 continues with the implementation.

CHAPTER 3

Modelica implementation

The Modelica language offers object-oriented modeling tools for simulation of large and complex physical systems involving events. The language is open-source and maintained by the Modelica Association (2010). The models can be described by differential, algebraic and discrete equations (hybrid DAE's). Dymola is a commercial software based on the Modelica language and facilitates a strong modeling and simulation environment. New system models can quickly be constructed by connecting component models in a visual interface.

This chapter goes through the implementation of the numerical model in Modelica. It should provide a fundamental understanding to the reader about the hierarchical structure in the model such that continuing development or use of the model may be accomplished by experienced Modelica users.

3.1 Introduction

The implementation of the equations in chapter 2 may be done based on previously developed Modelica libraries such as the free Modelica Fluid library, which is part of the Standard Modelica library. Alternative classes for balance equations, fluid properties and correlations may be built on top of such libraries. Similarly, other (however commercially available) libraries such as

the AirConditioning library by Modelon AB (Eborn et al., 2005) or the TIL library by TLK-Thermo GmbH (Richter, 2008) may be used.

The best way to get familiar with Modelica is, in essence, to code the models from scratch. Furthermore, the object-oriented capabilities in Modelica are used quite intensively in the libraries mentioned above, and it may seem difficult to understand the class hierarchy in such models at first sight. In particular, object-oriented relations between classes are used such as inheritance, aggregation, composition and class parameters (also known as polymorphism). It is therefore a difficult task for newcomers to Modelica to use other libraries as building blocks to develop new models. An advanced understanding of the Modelica language must be acquired first.

For these reasons, all the equations from chapter 2 were implemented while keeping in mind how other libraries have been developed in past, see for example Tummescheit (2002) and Richter (2008). The modeling work in this project was not intended to be a new library for general industrial or educational use. Moreover, the modeling work was intended to be used for flow maldistribution analysis with regards to continuing product development at Danfoss, as carried out in later chapters. Therefore, the main effort was not made on making a better code readability, hierarchy or user-interface, but rather on making the model work and be capable of studying maldistribution issues using exchangeable heat transfer, void and friction correlations and choice of tube circuiting in fin-and-tube evaporators.

Reusability and extendability of the modeling work in this project should be accomplished by experienced Modelica users with the help of this chapter.

The chapter starts with a brief introduction to the Modelica Language. For more intensive introductions to the Modelica language, please consult PhD theses Tummescheit (2002) and Richter (2008) or textbooks such as Fritzson (2004) and Tiller (2001). Furthermore, the chapter goes through examples of object-oriented relations used in this work and the hierarchical structure of the distributed evaporator model. When understanding the hierarchical structure of the distributed evaporator model, it should be easy to browse through all the other simpler models. Finally, it is shown how to define different tube circuitries for simulation and how the circuitry is constructed in the model.

3.2 The Modelica language

The Modelica language is an equation-based object-oriented modeling language that enables graphical editing such that component models may used graphically to create system models. The first Modelica language description was published in September 1997 and is continuously being improved and maintained by the Modelica Association (2010).

The Modelica language defines the data types `Real`, `Integer`, `Boolean` and `String`, similar to other programming languages, and may be further specified

by keywords (prefixes) such as `constant`, `parameter`, `input` or `output`. The data types need to be declared at the top of a class to be used in equations or algorithms within the class. The data types have attributes such as the `value`, `quantity`, `unit`, `fixed` or `start`, which may be modified from outside the class using modifications. Algorithms may be encapsulated using functions, where the input and output prefix are given in the function declaration. Furthermore, external functions may be used to provide access to other programming language functions. The attributes fixed and start are used to specify initial values and initial guesses to variables. Initial equations or initial algorithms may also be used in a class to compute initial values.

Classes are the building blocks in object-oriented programming. A model is the Modelica equivalent of a class. Objects are instantiated from models and called instances or components (if they are part of a system). Relationships between the models are in this work described by *part-of*-relations representing composition and aggregation or *is-a* relations representing inheritance. Class parameters (or polymorphism) are a way to make objects or classes replaceable and the replacement may be restricted to be of the same class type.

In the following sections the graphical notation style defined in the Unified Modeling Language (UML) will be used to represent the Modelica class diagrams, which show the implementation graphically. Moreover, the object-oriented relations between classes will be represented as shown on figure 3.1.
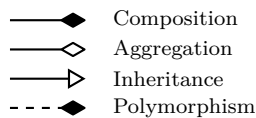
Figure 3.1: UML graphical notation style used in class diagrams.

Objects on the same hierarchical level may interact with each other using connectors, which are a restricted type of class, where no equations are allowed. Three types of variables may be declared, i.e. nonflow (no prefix), `flow` and `stream`. The nonflow variable represents a potential (e.g. pressure, energy or voltage), the flow variable represents a flow (e.g. mass flow or current) whereas the stream variable represents a potential, which is carried with the flow or current. When using the nonflow variable, the variable connected becomes equal in the connector. When using the flow connector, the variable must sum to zero in the connector (Kirchhoff's 1$^{\text{st}}$ law). The stream connector is rather new and introduced in Modelica specification 3.1. It is provided in order to avoid discontinuities in potential variables, which are carried with the flow at flow reversals (e.g. specific mixed-cup enthalpy flowing to and from the connector). In this work we did not simulate flow reversals and therefore the stream variable was not used. More information about the stream variable is given in Franke et al. (2009).

The Modelica language also supports hybrid modeling in a simple way carried out by if-expressions (conditional expressions), if-clauses (conditional equations) or when-clauses (conditional evaluation). These conditional constructs create events where the simulation integrator stops and crossing functions are generated. These may be eliminated by the `noEvent` operator, however, the conditional equation or equations should be smooth. The `noEvent` operator may speed up the simulation time.

In Modelica, for-loops and multi-dimensional arrays are also supported as in most programming languages. Arrays of both data types such as `Real` and `Integer`, but also arrays of objects or components may be made.

3.3 Object-oriented relations

An example of *composition* is shown in figure 3.2 of the `RefCell` model from figure 2.7 with the two component models `VolCell` and `FlowCell`, which are *part-of*-relations. The figure shows the UML class diagram and the corresponding Modelica code is shown in Modelica code 3.1. The variable declarations and equations etc. are omitted throughout this section for simplicity. The `VolCell` and `FlowCell` models are simply instantiated in the `RefCell` model, where
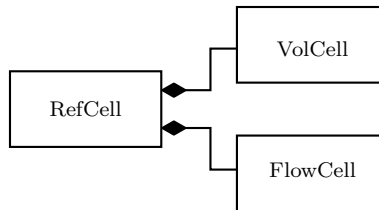
Figure 3.2: An example for composition in UML graphical notation.

```
model FlowCell
end FlowCell;

model VolCell
end VolCell;

model RefCell
  FlowCell flowCell;
  VolCell volCell;
end RefCell;
```

Modelica code 3.1: An example for composition in Modelica.

`VolCell` is the class (model) and `volCell` is the instance of the class (object or component). Dot-notation may be used to access variables from `volCell`, for example `volCell.p`, where p must be declared in the `VolCell` model. The hierarchical level of `VolCell` and `FlowCell` is below `RefCell`.

Aggregation differs from composition by using pointers to other objects that may be located at higher hierarchical level. The `inner`/`outer`-concept in Modelica may be seen as aggregation, however, the term aggregation has not been used for this concept in many Modelica-related publications, as pointed out by Richter (2008). An example of aggregation is seen graphically on figure 3.3 and Modelica code 3.2 shows the code.

The `RefCell` model now contains an object or component (`refrigerant`) that is marked with the prefix `inner`. It means that this component may be referenced (or pointed to) from lower hierarchical level than the owner `RefCell` by using the prefix `outer`, as done in the `VolCell` and `FlowCell` models. This
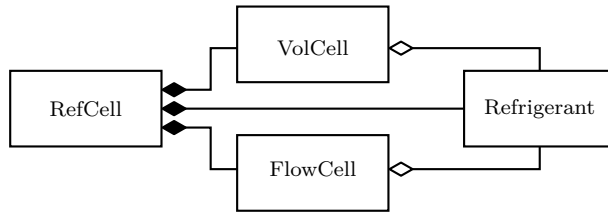
Figure 3.3: An example for aggregation in UML graphical notation.

```
model FlowCell
  outer Refrigerant refrigerant;
end FlowCell;

model VolCell
  outer Refrigerant refrigerant;
end VolCell;

model Refrigerant
end Refrigerant;

model RefCell
  inner Refrigerant refrigerant;
  FlowCell flowCell;
  VolCell volCell;
end RefCell;
```

Modelica code 3.2: An example for aggregation in Modelica.

becomes a nice way to make the refrigerant properties available at lower level models.

The `inner`/`outer`-concept is not only restricted to classes but may be carried out on variables (data types). For example, the variable mass flow may be declared in `RefCell` by using the prefix `inner` and then pointed to from lower level hierarchy using the prefix `outer`.

Inheritance may be seen as an *is-a*-relation and means that *all* the declarations and equations etc. in a parent class is passed to a child class. Figure 3.4 shows an example of the graphical representation of inheritance. The `Homogen`, `Zivi` and `Premoli` model are all used to compute `RefrigerantAndVoid` properties, for example the `Zivi` model *is-a* void model and used to compute all refrigerant properties and bulk mixture properties using the void fraction.

The corresponding Modelica code is seen in Modelica code 3.3. The child models all extends (inherits) their parent model using the prefix `extends`. The parent model is here used with the prefix `partial`, which means that the `RefrigerantAndVoid` model cannot be instantiated by itself, but needs to be inherited before instantiation.

A powerful object-oriented feature supported by the Modelica language is *poly-*
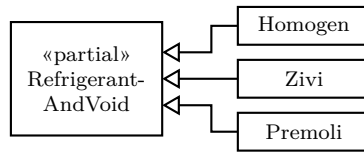
Figure 3.4: An example for inheritance in UML graphical notation.

```
partial model RefrigerantAndVoid
end RefrigerantAndVoid;

model Homogen
  extends RefrigerantAndVoid;
end Homogen;

model Zivi
  extends RefrigerantAndVoid;
end Zivi;

model Premoli
  extends RefrigerantAndVoid;
end Premoli;
```

Modelica code 3.3: An example for inheritance in Modelica.

morphism and shown graphically on figure 3.5. Polymorphism is a way to make objects or local classes exchangeable. Here we only consider exchangeable local class. It means that a local model may be exchanged by other models. The `Homogen`, `Zivi` or `Premoli` model become exchangeable local models inside the `RefCell` model, and restricted to be of type `RefrigerantAndVoid`.
Modelica code 3.4 shows the corresponding code. Inside the `RefCell` model the local model `LocalRefrigerantAndVoid` is declared with prefix `replaceable` and specified to be `Homogen` by default. Furthermore, it is restricted to be of
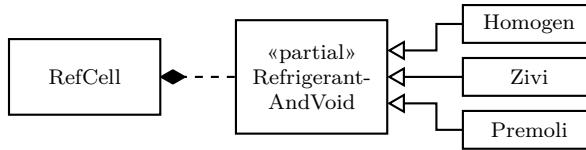
Figure 3.5: An example for polymorphism in UML graphical notation.

```
partial model RefrigerantAndVoid
end RefrigerantAndVoid;

model Homogen
  extends RefrigerantAndVoid;
end Homogen;

model Zivi
  extends RefrigerantAndVoid;
end Zivi;

model Premoli
  extends RefrigerantAndVoid;
end Premoli;

model RefCell
  replaceable model LocalRefrigerantAndVoid = Homogen
  constrainedby RefrigerantAndVoid;
  LocalRefrigerantAndVoid refrigerantAndVoid;
end RefCell;

model Cells
  RefCell refCell[10](redeclare model LocalRefrigerantAndVoid = Zivi);
end Cells;
```

Modelica code 3.4: An example for polymorphism in Modelica.

type `RefrigerantAndVoid` by using the keyword `constrainedby`. It means that the local model may be replaced by children of their parent. The local model must also be instantiated inside the `RefCell` model. The model `Cells` instantiates an array of the `RefCell` model and modifies the local model by the prefix `redeclare` to become the `Zivi` model.

The replaceable models may also be exchanged in Dymola's graphical environment simply by using the annotation `choicesAllMatching=true` on the replaceable local model. A change here simply changes the modification of the component `refCell`.

3.4   Structure of the evaporator model

The aforementioned examples of relationships and polymorphism are only examples. This section goes through the actual implementation in Modelica of the distributed evaporator model, which is the most complicated class hierarchy used in this work. When the user has learned the object-oriented methodology used here, it should be easier to browse through simpler models such as the moving boundary condenser model or other models, which will not be covered here.

3.4.1   Refrigerant cells

The implemented structure of the `RefCell` model is seen graphically on figure 3.6.

Aggregation has been used for the `RefrigerantAndVoid` model such that it may be pointed to from heat transfer and pressure drop correlation models. Furthermore, polymorphism is used to make all correlations exchangeable. The heat transfer correlations may be specified individually for each region, i.e. liquid, vapor or two-phase, whereas the pressure drop models are combinations of single and two-phase correlations that may be chosen. Smooth transition functions are applied in the `HeatTransfer` and `PressureDrop` model, in order to smoothen the transitions in the correlations.

The most important variables, that is, mass flow, heat flux, mixed-cup enthalpy and pressure have been declared in the `RefCell` model. Mixed-cup enthalpy and pressure are sent to the `RefrigerantAndVoid` model by modification to be used for computation of refrigerant properties. Furthermore, the `inner/outer`-concept has been used for the mass flow rate and heat flux such that they also are available to all correlations.

3.4.2   Air cells

The `AirCell` model is constructed as seen on figure 3.7. The air properties are made available by aggregation to both the correlations for heat transfer and
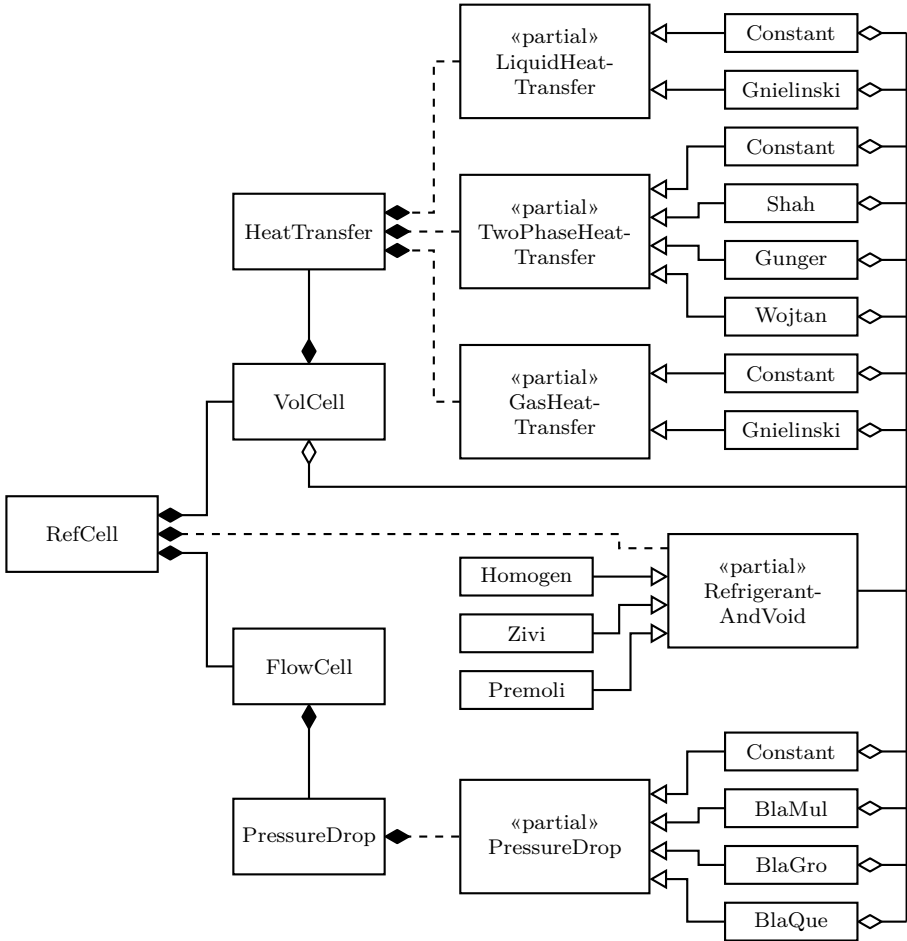
Figure 3.6: UML class diagram of the `RefCell` model.

fin efficiency, but also the heat transfer mode. Polymorphism is used to make the correlations and the mode exchangeable. The heat transfer mode may be chosen to be the simpler approach (equation 2.22) or the effectiveness-NTU method (equation 2.23, for cross flow only).

3.4.3 Geometry, material and refrigerant properties

All the models of figure 3.6 and 3.7 point to a higher level geometry record, which must be instantiated at higher hierarchical level using prefix `inner`. The class `record` is a restricted class in Modelica, where only parameters and con-
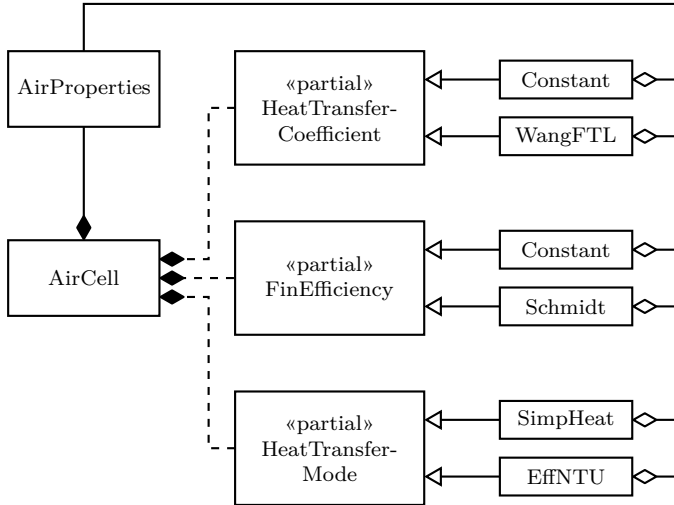
Figure 3.7: UML class diagram of the `AirCell` model.

stants may be declared. The geometry record also specifies material properties for the copper tube and aluminium fins.

The computation of the refrigerant properties also needs an `Integer` (index), which specifies the used refrigerant such that more refrigerants may be used when using the RefEqn package (Skovrup, 2009). The specification of the refrigerant used is done in the top-level model by instantiating the `RefrigerantName` model as shown in Modelica code 3.5 for one refrigerant only. The `inner`/`outer`-concept has been used again to make the `RefrigerantName` model available to all sub-models.

The model uses the keyword `import` to the class `RefEqn`. The class is of type

```
model RefrigerantName
  import RefEqn;
  parameter Integer Ref1(fixed=false);
  parameter String Ref1name="R410a";
initial algorithm
  Ref1:=RefEqn.GetRefrigerant();
  RefEqn.SetRNumber(Ref1,Ref1name);
  RefEqn.SetTemperatureUnit(Ref1,0); // Kelvin
  RefEqn.SetPressureUnit(Ref1,0); // Pascal
end RefrigerantName;
```

Modelica code 3.5: Refrigerant specification in the RefEqn package.

`package` in Modelica and contains functions with external function calls to the RefEqn package. By using the prefix `import`, these functions are available in the `RefrigerantName` model.

The refrigerant is set by calling the package for an index, which is allocated to the name of the chosen refrigerant. The index must then be used to call for this refrigerant properties. The index is computed in an initial algorithm that is only evaluated once. The index parameter is not fixed in the declaration by using the modification `fixed=false`. The units of the RefEqn package may be specified as shown for temperature and pressure. Zero is chosen by default (Kelvin and Pascal) and means that the two last lines in the `RefrigerantName` model are superfluous. For information on the specific function calls and settings of the RefEqn package, see Skovrup (2009).

3.4.4   A straight evaporator tube

The previous sections showed how the architecture and the correlation exchangeability etc. are made in the `RefCell` and `AirCell` model. In the WallCell model nothing has been made exchangeable and only the geometry and material properties are supplied by aggregation, thus it has not been chosen to show graphically.

The architecture of a straight tube heat exchanger should now be easily understood as shown on figure 2.1, 2.2 and 2.7 from chapter 2. The model is made by performing an array of the instance of the model `Cell`, which is shown on figure 3.8. The model of the straight evaporating tube is shown on figure 3.9.
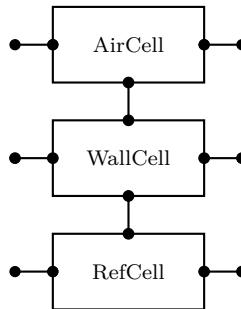
Figure 3.8: Sketch of model `Cell`.

The refrigerant boundary models for the discretization are shown together with some chosen boundary conditions for this evaporator model as shown in parentheses, i.e. temperature and velocity of inlet air, refrigerant mixed-cup enthalpy and mass flow rate at inlet and volume flow rate at outlet. The refrigerant source and sink models may be interpreted as a `Reservoir` and `Pump` and is thus denoted by such. The refrigerant boundaries could for example also be chosen as mixed-cup enthalpy and pressure at inlet and mass flow rate at outlet.
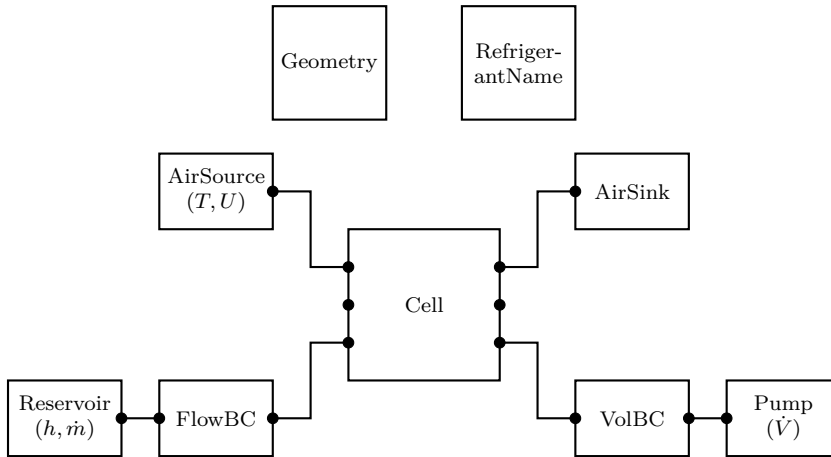
Figure 3.9: Sketch of a straight evaporator tube model.

The `AirSource` and `AirSink` models are also made arrays of and connected to the `AirCell` connectors. The `FlowBC` and `VolBC` models are only connected to first and last `RefCell`, respectively. The internals of the cell array, i.e. wall and refrigerant connections, must also be connected. The wall inlet and outlet heat flow are simply set to zero when they are not connected, since the `flow` variable are used for the heat flow and must sum to zero in connectors.

3.4.5 Tube circuiting

A fin-and-tube heat exchanger usually have a complicated circuiting inside each coil, which is far from a straight tube. By circuiting we mean the refrigerant paths (or channels) through the tubes of the coil, see figure 5.1 on page 87 for standard tube circuitries. By composition of the model `Cell` from figure 3.9 the model `Tube` with a given number of cells (n) may be instantiated as an array with size equal to the number of tubes (N_{tot}) in the coil.

The geometry record also includes the specification of the tube circuiting of a coil. The specific variables needed to define the tube circuiting in a coil are:

- N_{row}: Number of tubes per tube row
- N_{col}: Number of tube rows
- N_{pass}: Number of refrigerant passes through the coil
- $TC[N_{pass}, TC_{num}[1, 1]]$: Tube connectivity matrix
- $TC_{num}[N_{pass}, 1]$: Number of tubes per pass

The total number of tubes, N_{tot}, is equal to $N_{row} \cdot N_{col}$. Before we may define the tube circuiting in a coil we need to give the tubes numbers. The tube

numbering methodology is illustrated in table 3.1, where each table cell is a tube and the air flows from left to right.

Table 3.1: Tube numbering.

1	$N_{\text{row}} + 1$	$2 \cdot N_{\text{row}} + 1$	$\cdots$	$(N_{\text{col}} - 1)N_{\text{row}} + 1$
2	$N_{\text{row}} + 2$	$2 \cdot N_{\text{row}} + 2$	$\cdots$	$(N_{\text{col}} - 1)N_{\text{row}} + 2$
$\vdots$	$\vdots$	$\vdots$		$\vdots$
N_{row}	$N_{\text{row}} + N_{\text{row}}$	$2 \cdot N_{\text{row}} + N_{\text{row}}$	$\cdots$	$(N_{\text{col}} - 1)N_{\text{row}} + N_{\text{row}}$

Note that $(N_{\text{col}} - 1)N_{\text{row}} + N_{\text{row}} = N_{\text{row}} \cdot N_{\text{col}}$. Applying the methodology on a two tube row evaporator ($N_{\text{col}} = 2$) with 3 tubes per row ($N_{\text{row}} = 3$) gives the numbering as illustrated on figure 3.10. The figure also shows a chosen refrigerant circuiting through the coil, i.e. the refrigerant pass.

$$N_{\text{row}} = 3$$
$$N_{\text{col}} = 2$$
$$N_{\text{pass}} = 1$$
$$TC = [1, 2, 3, 6, 5, 4]$$
$$TC_{\text{num}} = [6]$$
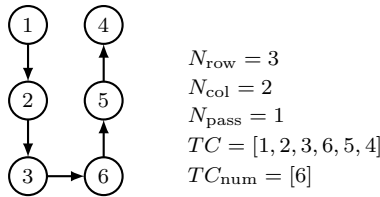
Figure 3.10: An example of a simple coil circuiting. Arrows show one refrigerant pass.

Figure 3.11 shows a more complicated example with two passes, 7 tubes in the first pass and 5 tubes in the other. Note that the pass with the highest number of tubes must be located in the first row of the tube connectivity matrix (TC), otherwise TC will be declared too small because TC is declared by $TC[N_{\text{pass}}, TC_{\text{num}}[1, 1]]$. Furthermore, the zeroes on the second row of TC will not be used but are needed for instantiation.

$$N_{\text{row}} = 4$$
$$N_{\text{col}} = 3$$
$$N_{\text{pass}} = 2$$
$$TC = [11, 10, 6, 2, 1, 5, 9; 12, 8, 4, 3, 7, 0, 0]$$
$$TC_{\text{num}} = [7; 5]$$
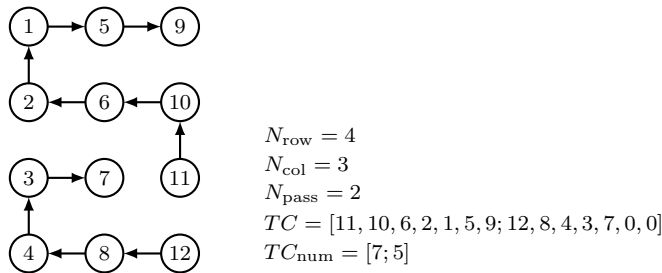
Figure 3.11: An example of a simple coil circuiting. Arrows show two refrigerant passes.

The air flows by definition from left to right on the figures. The examples shows only an in-line arrangement, however, the tubes may also be arranged in a staggered arrangement, which is normally the case for a cross flow heat exchanger.

If we neglect the presence of bends in the coil (will be included later), the refrigerant and wall connections are quite simple following the refrigerant path. First, each cell needs to be connected internally in all tubes. Then we use the tube connectivity matrix to connect the tubes outflow and inflow by marching through the matrix. Then we apply boundary models (`VolBC` and `FlowBC`) similar to figure 3.9 for each pass inflow and outflow.

There is a limitation to the implementation, i.e. it does not support refrigerant pass splitting and joining inside the coil. However, this limitation also makes the refrigerant flow direction known, if we assume that the refrigerant in the first tube in each pass flows into the paper always on the illustrations.

The connectivity of the air cells is more difficult, since we need to track the refrigerant flow direction of the tubes and connect the cells accordingly. If we consider tube 1 and 4 of figure 3.10, flow in tube 1 goes into the paper and flow in tube 4 goes out of the paper. When choosing three cells ($n = 3$) in each tube the air cell connection of tube 1 and 4 becomes as shown in Modelica code 3.6.

```
connect(tube[1].cell[1].portOut,tube[4].cell[3].portIn);
connect(tube[1].cell[2].portOut,tube[4].cell[2].portIn);
connect(tube[1].cell[3].portOut,tube[4].cell[1].portIn);
```

Modelica code 3.6: Air cell connections of tube 1 and 4 of figure 3.10.

If we consider tube 7 and tube 11 on figure 3.11 both refrigerant flows goes into the paper. The corresponding air cell connections become as shown in Modelica code 3.7.

```
connect(tube[7].cell[1].portOut,tube[11].cell[1].portIn);
connect(tube[7].cell[2].portOut,tube[11].cell[2].portIn);
connect(tube[7].cell[3].portOut,tube[11].cell[3].portIn);
```

Modelica code 3.7: Air cell connections of tube 7 and 11 of figure 3.11.

Uneven index numbers of the rows in the tube connectivity matrix means that the refrigerant flow goes into the paper, and even index numbers means that the refrigerant flow goes out. The possibilities of connection methods become four, i.e. even-even, uneven-even, even-uneven and uneven-uneven, and the connections may thus be created accordingly.

Figure 3.12 shows the air cell connections of each tube and the auxiliary models for air split, join, source and sink models for a staggered tube arrangement.

Figure 3.12: Sketch of a staggered coil showing air connections only.

Half and half splitting of the airflow is assumed in the `AirSplit` model. Again arrays of size n (number of cells in each tube) are made of the models `AirSplit`, `AirJoin`, `AirSource` and `AirSink`, before they are composed in the `TubeRow` and `TubeInternals` models. Arrays of the `TubeRow` and `TubeInternals` models are then made of size N_{row}. Then each model are connected as indicated on figure 3.12 taking the refrigerant flow directions of the tubes into account. The dashed lines are artifacts from the staggered tube arrangement and are assumed adiabatic despite that they flow across fin material. They vanish if the in-line tube arrangement is chosen. Similarly, the flow split and join are not needed for the in-line tube arrangement.

The addition of refrigerant U-bends is simply additions of `RefCell` models (called `UBendRefCell`) with a volume and flow cell. The bends are assumed to be adiabatic and it may be chosen to use empirical correlations for the frictional pressure drop, i.e. combination of a two-phase and a single-phase correlation,

or use of a constant friction coefficient. It is constructed similar to figure 3.6 without the heat transfer part.

It is easy to use the connectivity matrix to find out where to connect the bends, which always will be $N_{\text{tot}} - N_{\text{pass}}$ bends to connect. The complicated part becomes the computation of the bend radius, which is needed to compute refrigerant volume and friction. It is carried out by tracking the row number (x) and column number (y) of each tubes, as indicated on figure 3.13.

$$x = 1 \quad \cdots \quad x = N_{\text{col}}$$
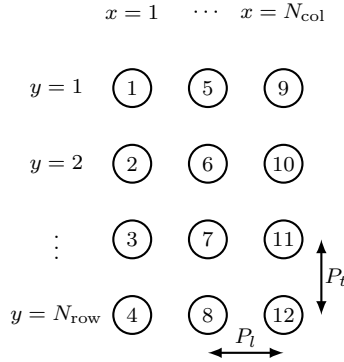
Figure 3.13: Tracking of tube locations.

P_l is the longitudinal tube pitch and P_t is the transverse tube pitch. We may then compute the radius of the U-bends by equation 3.1 for in-line tube arrangements as

$$R = \frac{1}{2}\sqrt{[P_l(x_{\text{out}} - x_{\text{in}})]^2 + [P_t(y_{\text{out}} - y_{\text{in}})]^2} \tag{3.1}$$

If the tube arrangement are staggered, we may use the above equation only when x_{in} and x_{out} are both even or uneven numbers. If this is not the case we may compute the radius according to

$$
\begin{aligned}
R = \frac{1}{2}\sqrt{[P_l(x_{\text{out}} - x_{\text{in}})]^2 + [P_t(y_{\text{out}} - y_{\text{in}}) + P_t/2]^2} \qquad & x_{\text{in}} < x_{\text{out}} \\
R = \frac{1}{2}\sqrt{[P_l(x_{\text{out}} - x_{\text{in}})]^2 + [P_t(y_{\text{in}} - y_{\text{out}}) + P_t/2]^2} \qquad & x_{\text{out}} > x_{\text{in}}
\end{aligned}
\tag{3.2}
$$

This finalizes the connections of the tube circuitries. All the above connections are created by many if-expressions and for-loops in model `HXbaseline`, which is composed by `Tube`, `TubeRows`, `TubeInternals`, `UBendRefCell`, `Geometry`, `VolBC`, `FlowBC`, `Nslab`, `Vsplit`, `Distributor` and `Manifold`.

The last four models have not been mentioned in this section so far. The `Nslab` model is a simple model and divides the inlet refrigerant mass flow rate and multiplies the outlet refrigerant mass flow rate by the number of identical slabs (coils). In this way we may assume identical coil performance and conditions,

thus only simulate one of the coils. Remember that the mass flow of air should also be divided by the number of slabs if not the air velocity is used as air boundary condition.

The `Vsplit` model simply holds the equations from section 2.8 (Airflow distribution), where F_{air} must be specified as an input.

The `Distributor` model holds the equations from section 2.7 (Refrigerant distributor), where F_x must be specified as an input together with the choice of mode, i.e. *EXV flow*, *Even flow* or *Compensating flow*.

Similarly, the `Manifold` model holds the equations from section 2.9 (Refrigerant manifold).

There is essentially no limitations in the number of tubes per row N_{row} or total tube number N_{tot}. The number of tube rows N_{col} is limited to 4, because of the way the connections have been constructed, however, most coils for residential air-conditioning do not exceed this limitation. The number of refrigerant passes N_{pass} is limited by the total number of tubes N_{tot}.

3.4.6 Initialization

Initialization is probably the most important difficulty when simulating refrigerant flow. This is not just the case for distributed models but also the case for moving boundary models. It is recommended to initialize as close to a steady state as possible in order to eliminate large transients at initial simulation. Especially, the initialization may create a lot of pressure waves traveling back and forth in the channels in the distributed evaporator model, which reduces the initial simulation time.

We chose to initialize by a linear mixed-cup enthalpy distribution and pressure distribution in all channels. These are computed by initial equations in the `HXbaseline` model. It must be emphasized that the steady state at which initialization is carried out should be without too large initial transients. For example, the guesses on mass flow through the evaporator should be the same as through the compressor, condenser and expansion valve. Otherwise, it may slow the initial simulation time. Furthermore, the wall temperature start value should be in between the refrigerant saturation temperature and air temperature.

3.5   Summary

In this chapter the implementation in Modelica of the distributed evaporator model is shown.

The chapter starts with a brief introduction to the Modelica Language. Then the chapter continues with a representation of the object-oriented relations between classes that are used in most developed models.

Then the chapter presents how the evaporator model is created using object-oriented methods such that different correlations may easily be exchanged and different tube circuitries may easily be constructed. These features are important for model reuse and extension in order to simulate flow maldistribution in typical fin-and-tube evaporators.

There is a limitation to the implementation though, i.e. it does not support refrigerant pass splitting and joining inside the coil. Otherwise, the capabilities of simulating flow maldistribution in typical fin-and-tube evaporators are strong.

Two straight channels - a generic study

This chapter presents a generic study of flow maldistribution in fin-and-tube evaporators for residential air-conditioning on both evaporator and system level. It is a generic study because it is not confined to a specific tube circuitry of fin-and-tube evaporators, e.g. face split or interlaced circuiting. Moreover, the evaporator coils are assumed to be two straight channels with air flowing across each channel independently. The study may therefore be considered as a general study showing general trends and results.

Most of the presented results are also discussed in Kærn et al. (2011b) and Kærn et al. (2011a).

4.1 Introduction

The focus of the chapter is to study the effect of flow maldistribution in the evaporator and compensation potential of flow maldistribution on component and system performance in terms of cooling capacity and COP.
The reason why the study is performed is to generate an increased basic understanding and knowledge of flow maldistribution effects and the involved physical phenomena. The study is expected to provide guidelines on basic trends, consequences and compensation potentials of flow maldistribution that illustrates the general feasibility of compensation. The method of compensation involves

the control of individual channel superheats by distributing individual mass flow rates continuously.

The first objective is to investigate the influence of the main maldistribution sources in terms of cooling capacity and COP, i.e. (1) the non-uniform inlet liquid/vapor phase distribution, (2) the different feeder tube bends and (3) the non-uniform airflow. The second objective is to study the benefits of compensation and compare the recovery potential with the use of a larger evaporator. The chapter starts with a brief description of the modeling framework with reference to the formulation in chapter 2. Then the model is verified by comparison to results from the commercial software Coil-Designer (Jiang et al., 2006).

Then each source of flow maldistribution is investigated by imposing it to the model individually. Furthermore, the significance of two-phase frictional pressure drop and heat transfer correlations is investigated. Many two-phase friction and heat transfer correlations exist, and they may yield different results. It is investigated how the choice of these influences the flow maldistribution results, thus three different two-phase friction correlations and three different heat transfer correlations are used in the evaporator model.

Finally, the feasibility of the compensation method is addressed. As baseline for comparison, an analysis of flow maldistribution is carried out, where the combination of maldistribution sources is considered at different evaporator sizes and outdoor temperatures. The performance of the compensation method is then compared to the baseline results of the combined flow maldistribution. The test case is an R410A 8.8 kW residential air-conditioning unit. The evaporator is based on an A-coil, i.e. two coils forming an A. Each coil is assumed to be in similar flow distribution conditions, thus only one coil is essentially modeled. The coil is assumed to be two straight channels, where each channel is aligned in the first row and thus sees the same inlet air temperature. The inputs to the model HXBaseline from section 3.4.5 is simply: $N_{\mathrm{row}} = 2$, $N_{\mathrm{col}} = 1$, $N_{\mathrm{pass}} = 2$, $TC = [1; 2]$ and $TC_{\mathrm{num}} = [1; 1]$.

4.2 Modeling framework

This chapter presents only steady state results even though the system model is dynamic. A detailed formulation of the numerical model is given in chapter 2.

The focus of the model is the evaporator in order to predict the maldistribution in the evaporator and its effect on component and system performance. Simple quasi-static model formulations are used for the expansion device and the compressor. The evaporator model is a distributed one-dimensional mixture model and the condenser model is a simpler moving boundary model, which averages the liquid, two-phase and vapor regions. Pressure drop is only considered in the evaporator and its feeder tubes in order to predict the mass flow distribution.

Both the evaporator and condenser models are dynamic, and thus they model the refrigerant migration between the evaporator and the condenser.

4.2.1 Geometry and correlations

Table 4.1 shows the main geometry of the test case evaporator and condenser. The length of each evaporator channel in the model thus becomes 18·444.5 mm. The condenser is a bit different since four of the channels with gas entering and two-phase exiting are combined into a fifth channel, in order to speed up the liquid. For simplicity it is assumed to be 4 straight tubes of length 5/4·6·2100 mm without flow maldistribution.
The feeder tubes to the evaporator have an internal diameter of 3 mm and a length of 300 mm.

Table 4.1: Main geometry of the evaporator and condenser.

	Evaporator	Condenser
Number of coils	2	1
Number of channels in each coil	2	5
Number of tubes in each channel	18	6
Tube length [mm]	444.5	2100
Inner tube diameter [mm]	7.6	7.6
Outer tube diameter [mm]	9.6	9.6
Transverse tube pitch [mm]	25.4	25
Longitudinal tube pitch [mm]	21.25	
Fins	Louvred	Louvred
Fin pitch [mm]	1.81	1.15
Total outside area [m^2]	17.3	52.2
Number of cells	30	

Figure 4.1 shows a sketch of the model setup, including a zoomed-in sketch of the evaporator, which only shows one of the two evaporator coils. Each discrete cell of the evaporator is modeled as a small heat exchanger with uniform transport properties. Mass, momentum and energy conservation equations are applied to the refrigerant in each cell, where homogeneous flow and thermodynamic equilibrium is assumed. Furthermore, changes in kinetic and potential energy are neglected. It is assumed that the tube walls have rotational symmetry, i.e. no heat conduction in the azimuthal direction. Mass and energy conservation equations are applied to the air, which is assumed to be dry.
Similar assumptions are used in the condenser model of the refrigerant and airflow, however, the heat resistance and the dynamics of the condenser wall are neglected. The used correlations for both the evaporator and the condenser are given in table 4.2. The first listed two-phase correlations for the evaporator will be used primarily in this chapter, unless specified otherwise. Furthermore, appropriate effectiveness-NTU relations for cross flow heat exchangers are used.
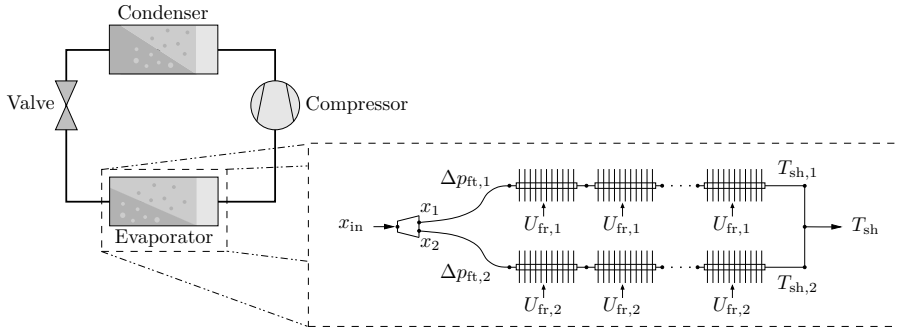
Figure 4.1: Sketch of the model setup.

Table 4.2: Overview of used correlations.

Air-side	
Heat transfer	Wang et al. (1999)
Fin efficiency	Schmidt (1949), (Schmidt approximation)
Single-phase	
Heat transfer	Gnielinski (1976)
Friction	Blasius (2002)
Two-phase (evaporator)	
Heat transfer	Shah (1982)
	Gunger and Winterton (1986)
	Wojtan et al. (2005b)
Friction	Müller-Steinhagen and Heck (1986)
	Grönnerud (1979)
	Quibén and Thome (2007)
Two-phase (condenser)	
Heat transfer	Shah (1979)

The expansion valve is quasi-static, adiabatic and modeled as an isenthalpic process. It essentially controls the superheat out of the evaporator manifold by the mass flow rate through the valve. The manifold is also quasi-static, adiabatic and modeled by mixing of the inlet refrigerant streams.

The geometric volume flow of the compressor is $6.239 \text{ m}^3\text{h}^{-1}$ and the compressor model is also quasi-static and adiabatic. Polynomials from the rating of the compressor are used to compute the isentropic and volumetric efficiencies.

4.2.2   Distribution parameters

The symbols used in the following are shown in figure 4.1. In order to study different inlet liquid/vapor phase distributions, different feeder tube bends and non-uniform airflow distributions to the evaporator, three distribution parameters are defined.

The phase distribution parameter is defined by

$$F_x = \frac{x_2}{x_{\text{in}}} \qquad 0 \leq F_x \leq 1 \tag{2.41}$$

When F_x is unity, the vapor quality into the feeder tubes is equal. When F_x is zero, only liquid is fed into channel 2. Mass and energy conservation equations are applied to compute the vapor quality into channel 1.

The feeder tube bending parameter is defined by

$$\begin{aligned} \Delta p_{\text{ft},1} &= F_{\text{ft}} \Delta p_{\text{fric},1} + \Delta p_{\text{acc},1} \qquad 1 \leq F_{\text{ft}} \leq 5.5 \\ \Delta p_{\text{ft},2} &= \Delta p_{\text{fric},2} + \Delta p_{\text{acc},2} \end{aligned} \tag{2.45}$$

where F_{ft} is multiplied to the frictional pressure drop of channel 1 only, imposing a degree of bending (here a maximum factor of 5.5 is assumed). The accelerational pressure drop is not a function of length, thus the feeder tube bending parameter can be viewed as an equivalent length multiplier. When F_{ft} is unity, the feeder tubes are straight tubes, in contrast to when $F_{\text{ft}} > 1$.

The airflow distribution parameter is defined by

$$F_{\text{air}} = \frac{U_{\text{fr},2}}{U_m} \qquad 0 \leq F_{\text{air}} \leq 2 \tag{2.52}$$

where U_m is the mean frontal velocity across the two tubes. When F_{air} is unity, the airflow is distributed equally across the two tubes. When F_{air} is zero, the air flows across channel 1 only. When F_{air} is two, the air flows across channel 2 only. The mass flow rate of air across the evaporator is held constant and the mass conservation equation is used to compute the frontal velocity of channel 1.

4.2.3   Boundary conditions and solution methodology

The system uses an electronic expansion valve (EXV) that controls the overall superheat to 5 K. When compensating, the individual channel superheats are controlled to 5 K by distributing individual mass flow rate. The two cases correspond to the *EXV flow* model mode and the *compensating flow* model mode of the distributor model from section 2.7. During start-up of the simulation at no maldistribution the charge of the system is determined so that the subcooling becomes 2 K (see filling station model from section 2.6). Then the different distribution parameters are varied individually and each steady state result is obtained. Unless specified otherwise, the boundary conditions are as specified in table 4.3.

Table 4.3: Boundary conditions.

Superheat	5 K
Subcooling (startup)	2 K
Outdoor air temperature	35°C
Outdoor frontal air velocity	0.68 m s^{-1}
Indoor air temperature	26.7°C
Indoor frontal air velocity	1.16 m s^{-1}

4.3   Steady state verification

No experimental data are available that may validate the model in details. As the best possible alternative, we perform a verification with a commercial code (Coil-Designer, Jiang et al. (2006)). This gives a good and reasonable assessment of the reliability of the model.

The evaporator and the condenser models are verified in steady state and under uniform flow conditions, i.e. no maldistribution. The verification is carried out on a simplified tube layout corresponding to the current model geometry. We used 30 cells in both the distributed evaporator model and Coil-Designer simulations.

The steady state after start-up of the current system model, will be used in the verification. The boundary conditions are shown in table 4.3. Essentially the inlet thermodynamic states to the evaporator and condenser are needed as further input to Coil-Designer and it will compute the mass flow and capacity to be compared. The inlet pressure and vapor quality to the evaporator model are 11.18 bar (11.1°C) and 0.28, respectively. The inlet pressure and temperature to the condenser are 28.6 bar and 74.8°C, respectively.

Table 4.4 shows the comparison of the computed mass flow rate and capacity for both the evaporator and the condenser. Note that three different two-phase heat transfer correlations are compared for the evaporator.

The first two comparisons of the evaporator show larger differences than the third comparison. This is mainly because of the smooth functions that are applied at the two-phase to vapor phase transition as described in appendix C.3. The result is a smaller heat transfer in the current model, since the two-phase heat transfer coefficient and the heat exchanger effectiveness decrease faster towards the vapor region values. This is depicted on figure 4.2 in terms of temperature profiles through the evaporator of the first comparison. It is seen that the air temperature difference of the current model decreases before the point of full evaporation, i.e. where the refrigerant temperature starts to rise.

The third comparison of the evaporator involves a newer correlation for the two-phase heat transfer coefficient that already predicts a decrease in the heat transfer coefficient in the two-phase region (i.e onset of dry-out, see figure 2.5).

Table 4.4: Comparison of mass flow rate and capacity, (CM=current model, CD=Coil-Designer).

		Capacity [kW]	Mass flow [kg s^{-1}]
Evaporator			
Shah (1982)	CM	10297	0.0668
	CD	11116	0.0726
	Error	7.4%	8.0%
Gunger and Winterton (1986)	CM	10704	0.0693
	CD	11492	0.075
	Error	6.9%	7.6%
Wojtan et al. (2005b)	CM	10544	0.0682
	CD	10703	0.0699
	Error	1.5%	2.4%
Condenser			
Shah (1979)	CM	12859	0.0668
	CD	12372	0.0645
	Error	3.9%	3.6%

This results in a better comparison, since the smoothing process of the current model has less impact here.

Note that the total cooling capacity of the evaporator is higher than the rated 8.8 kW. This is because of the simplified tube layout, where each channel is aligned in the first row. The channels see a higher air temperature, in contrast to when they are aligned in the second row.

The current condenser model averages the two-phase and single-phase regions, however, the comparison of the mass flow rate and the capacity is in good agreement. Figure 4.3 shows the temperature profile comparison with Coil-Designer. Note that the refrigerant temperature of the current model is drawn linearly throughout the vapor, two-phase and liquid regions and that the outlet air temperature is a mean in each region.

The temperature comparison is also in good agreement and it can be concluded that both the evaporator and condenser model are verified in steady state with Coil-Designer, which is validated experimentally. The models are thus suitable for further analysis with regards to maldistribution.

4.4 Effects of flow maldistribution

In this section the results of the simulations of flow maldistribution are presented without compensation. The simulation continues from the verified
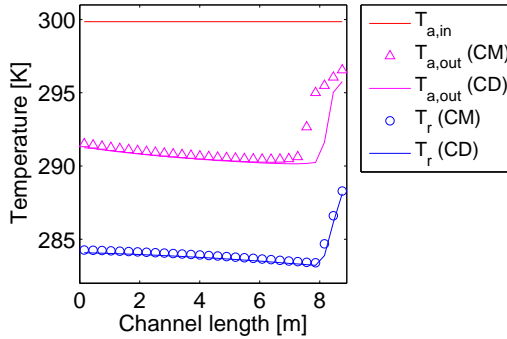
Figure 4.2: Temperature profile comparison of the evaporator using the Shah (1982) correlation (CM=current model, CD=Coil-Designer).
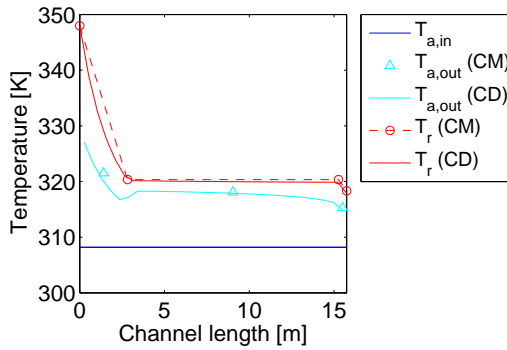
Figure 4.3: Temperature profile comparison of the condenser (CM=current model, CD=Coil-Designer).

steady state in section 4.3 with similar conditions from table 4.3 and parameters from section 4.2.1. Then each maldistribution source will be imposed to the model individually, i.e. by varying the phase distribution parameter, F_x, the feeder tube bending parameter, F_{ft}, and the airflow distribution parameter, F_{air}.

4.4.1 Maldistribution from the distributor

The distribution of refrigerant mass flow as a function of the phase distribution parameter, F_x, is shown in figure 4.4a.

It shows that the mass flow distribution is dependent on F_x so that more mass comes through the channel with lower inlet vapor quality (channel 2) and
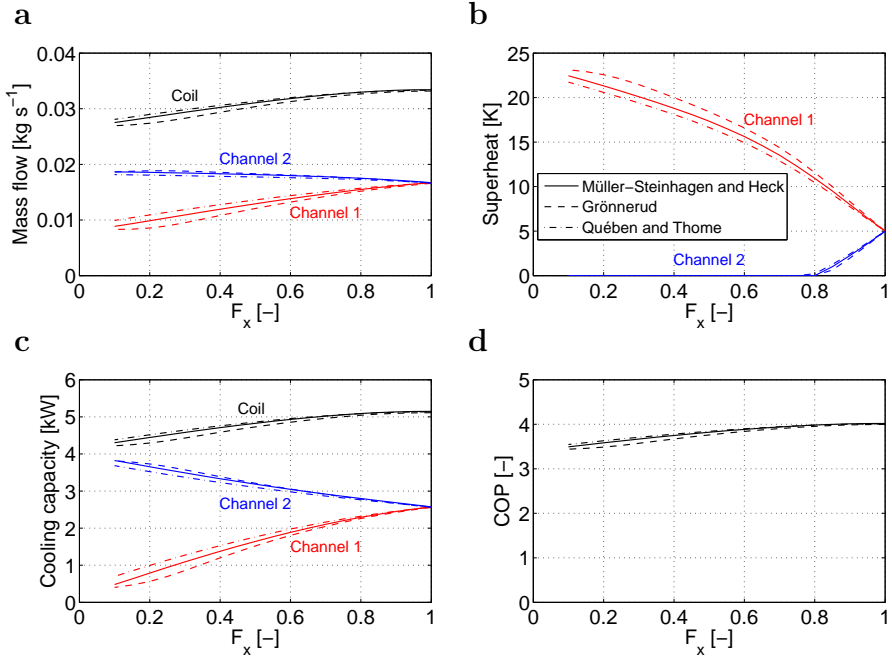
Figure 4.4: Selected parameters vs. the phase distribution parameter.
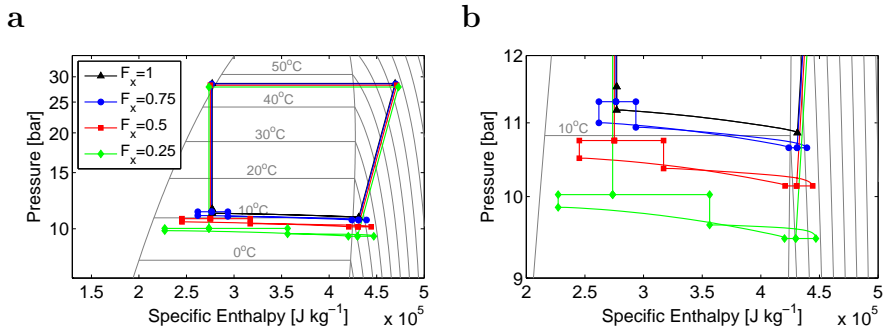
Figure 4.5: $\log(p)h$ cycles at different phase distribution parameter.

less mass comes through the channel with higher inlet vapor quality (channel 1). This is determined by the pressure drop across the channels that must be equal. Indeed more mass will travel through the channel with lower vapor quality, since the pressure drop of the liquid phase is lower than the pressure drop of the vapor phase.

The consequence of the refrigerant maldistribution is seen in figure 4.4b, which shows the individual superheats. At $F_x = 0.8$, liquid is flowing out of channel 2. These points are important because the two-phase area of the evaporator decreases, when full evaporation is not reached. A larger superheated area in channel 1 is required in order to evaporate this surplus liquid, thus the overall UA-value decreases.

Since the UA-value decreases, the cooling capacity, COP and evaporation temperature decrease as shown in figure 4.4c, 4.4d and 4.5a. The capacity of the channel that receives more mass flow increases, however, the capacity of the channel that receives less mass flow decreases even more so that the total cooling capacity of the coil decreases.

Figure 4.5b also shows a zoomed-in $\log(p)h$ diagram of the thermodynamic states through the distributor, feeder tubes, evaporator channels and the manifold. It shows that the pressure drop ratios between the feeder tubes and evaporator channels are altered as the phase distribution parameter decreases. For channel 1 the pressure drop through the feeder tube increases, however, for channel 2 the pressure drop through the feeder tube decreases.

The total cooling capacity and COP decreases by 16.4% and 13%, respectively, as F_x goes from 1 to 0.1.

4.4.2 Maldistribution from the feeder tube bends

The distribution of refrigerant mass flow, superheat, cooling capacity and COP as functions of the feeder tube bending parameter are shown in figure 4.6.

A similar mass flow distribution trend is seen for different feeder tube bends as F_{ft} goes towards 5.5. The pressure drop through feeder tube 1 becomes higher than feeder tube 2, thus more refrigerant will travel through channel 2 in order to ensure equal pressure drop through the channels. The fact that more mass travels through channel 2 also results in a higher pressure drop of channel 2, and thus has some compensating effect. The trend of the superheat curves might indicate this effect, where liquid starts to flow out of channel 2 at $F_{\text{ft}} = 2.75$.

The total mass flow in each coil does not decrease as much as when we considered the inlet liquid/vapor maldistribution. This also results in a smaller reduction in cooling capacity and COP. It shows that maldistribution from different feeder tube bends is insignificant compared to inlet liquid/vapor maldistribution. The two are not considered to interact significantly, i.e. the distribution of liquid and vapor phases is a separation phenomena in the distributor, and thus not affected by the pressure drop through the feeder tubes.

Note that a compact fin-and-tube heat-exchanger consists of a number of tubes connected by U-bends. The presence of U-bends would reduce the influence of the feeder tube pressure drop to the total pressure drop, and hence its effect on maldistribution.
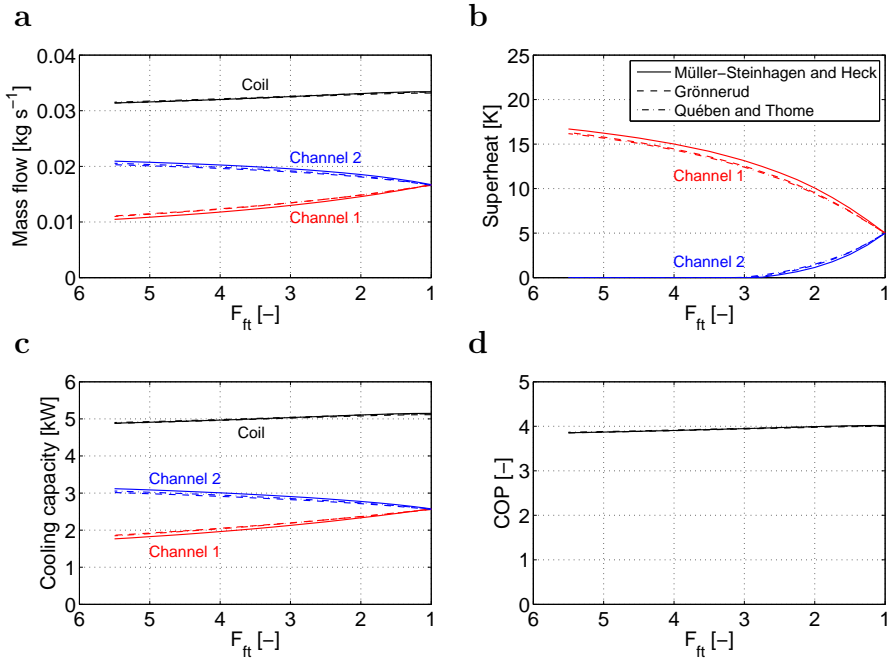
Figure 4.6: Selected parameters vs. the feeder tube bending parameter.
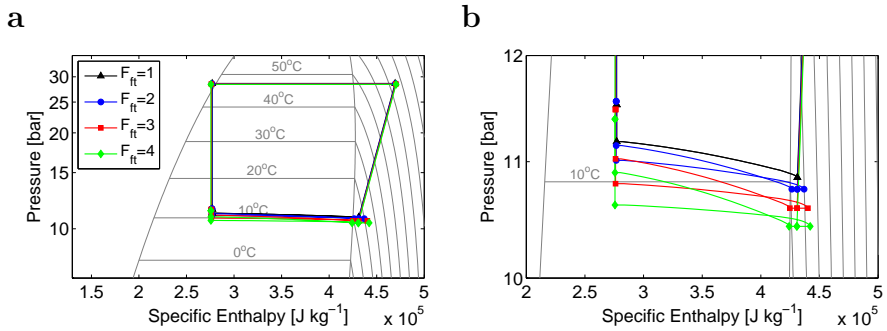
Figure 4.7: $\log(p)h$ cycles at different feeder tube bending parameter.

Figure 4.7a shows the corresponding $\log(p)h$ diagram. It shows that the evaporation temperature decreases, however, not significantly. Figure 4.7b indicates that the small decrease in the evaporation temperature, is caused by the increased pressure drop through the feeder tubes, which is higher for feeder tube 1.

The cooling capacity and COP decreases by 5.2% and 4.1%, as F_{ft} goes from 1 to 5.5. It means that the feeder tube bends have small significance compared to the inlet liquid/vapor maldistribution.

4.4.3   Maldistribution from the airflow

The distribution of refrigerant mass flow, superheat, cooling capacity and COP as functions of the airflow distribution parameter are shown in figure 4.8.

Interestingly, the mass flow distribution is almost equal in each channel as F_{air} decrease. However, they are both reduced significantly in order to ensure the overall superheat temperature of 5 K. The reduction of the mass flows together with different superheated areas have a significant degrading effect on the cooling capacity and COP.

As F_{air} approaches 0.1 it is close to an air blockage of channel 2. Of course this is quite impractical, but it indicates that a channel that receives almost no airflow (could also be a recirculation zone in the coil, see CFD simulation in section 5.6) will have liquid refrigerant flowing through that must be evaporated. Unfortunately, it will be evaporated by mixing the refrigerant with increased superheat from the other channel. This is also indicated in figure 4.8b, where the superheat of channel 1 increases quite drastically. The result is a decrease in overall UA-value, cooling capacity and COP.

The evaporating temperature also decreases quite drastically as seen on figure 4.9a. Figure 4.9b shows that the feeder tube pressure drop are almost the same for each channel. Furthermore, the ratio of the feeder tube pressure drop to the evaporator channel pressure drop is unchanged as the airflow distribution parameter decrease.

The cooling capacity and the COP decrease by 49.9% and 43.2% as F_{air} goes to 0.1.

Other types of evaporators were studied in Kim et al. (2009b,a) and Brix et al. (2009, 2010), however, the results of the sections 4.4.1, 4.4.2 and 4.4.3 give similar results and trends of flow maldistribution in general.

4.4.4   Significance of the choice of correlations

Figures 4.4a-4.4c, 4.6a-4.6c and 4.8a-4.8c show the results of 3 different two-phase frictional pressure drop correlations from the literature, i.e.

1. Müller-Steinhagen and Heck (1986)
2. Grönnerud (1979)
3. Quibén and Thome (2007)

We have chosen to use two of the most well known traditional correlations (1-2) together with a more sophisticated newer correlation (3). The traditional correlations are somewhat simple correlations in contrast to the latter, which
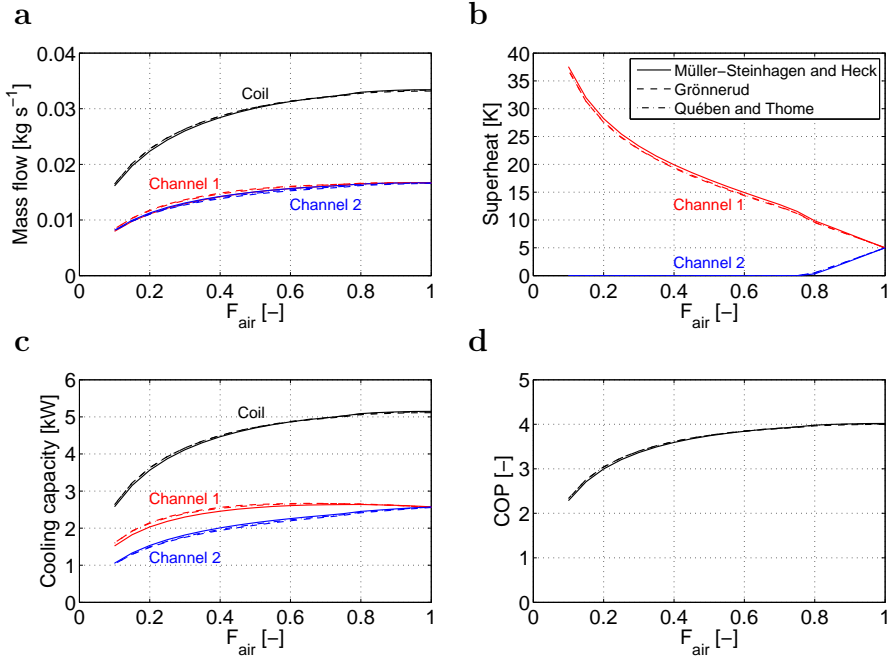
Figure 4.8: Selected parameters vs. the airflow distribution parameter.
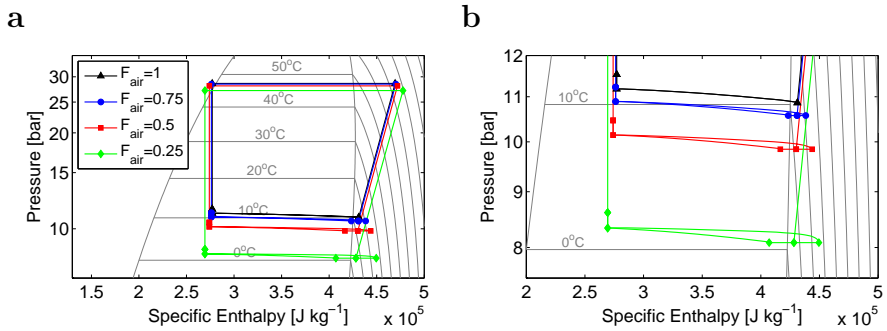
Figure 4.9: $\log(p)h$ cycles at different airflow distribution parameter.

is a phenomenological correlation, i.e. it involves prediction of the flow regimes during the evaporation. When applying correlation 3 the first correlation was, however, used to model the frictional pressure drop of the feeder tubes, since correlation 3 showed unreasonable frictional pressure gradients at the high mass fluxes through the feeder tubes.

The total pressure drop across the channels is different for all the correlations, however, the difference in terms of cooling capacity and COP are insignificant as depicted on figure 4.4c, 4.6c and 4.8c. The distribution of mass flow and cooling capacity for each channel might indicate small differences, but the total is quite similar. The choice of two-phase frictional pressure drop correlation is thus insignificant, when studying maldistribution effects from the distributor, feeder tubes and airflow, for the current RAC unit of interest.

Figure 4.10 shows the results of the cooling capacity and COP for three different two-phase heat transfer correlations from the literature at different F_x, F_{ft} and F_{air}. All the curves coincides and the correlations are as follows:

1. Shah (1982)
2. Gunger and Winterton (1987)
3. Wojtan et al. (2005b)

Again two well known traditional two-phase heat transfer correlations (1-2) have been chosen together with a more sophisticated phenomenological and newer correlation (3). Correlation 3 uses the same flow map (Wojtan et al., 2005a) for flow regime prediction as for the frictional pressure drop correlation of Quibén and Thome (2007) used previously.

Again the cooling capacities and COP's are not affected much by the choice of correlation, and thus insignificant when studying maldistribution effects. The verification shown in table 4.4 suggests that the cooling capacity should be different by up to 7%, when applying different two-phase heat transfer correlations. However, the inlet thermodynamic state and superheat were fixed in that comparison. In the present simulation the inlet thermodynamic state is not fixed and the evaporating temperature may vary between the simulations. The cooling capacity is thus compensated by a lower evaporation temperature in the system. The change in evaporation temperature is, however, small and not significant on system performance in terms of COP as indicated on figure 4.10.

Note that the correlation of Gunger and Winterton (1987) is not available in Coil-Designer, thus the earlier Gunger and Winterton (1986) was used in the comparison in section 4.3. The newer was recommended as the better of the two in a study by Thome (1996), and thus used here.

A similar study of the significance of different two-phase flow correlations, was carried out by Brix et al. (2010) on mini-channels. They also found that the choice of different two-phase flow correlations was not significant for the predicted maldistribution and the degradation of the cooling capacity.

4.5   Compensation of flow maldistribution

The compensation method involves a coupled expansion and distributor device, which is able to distribute the mass flow according to the individual
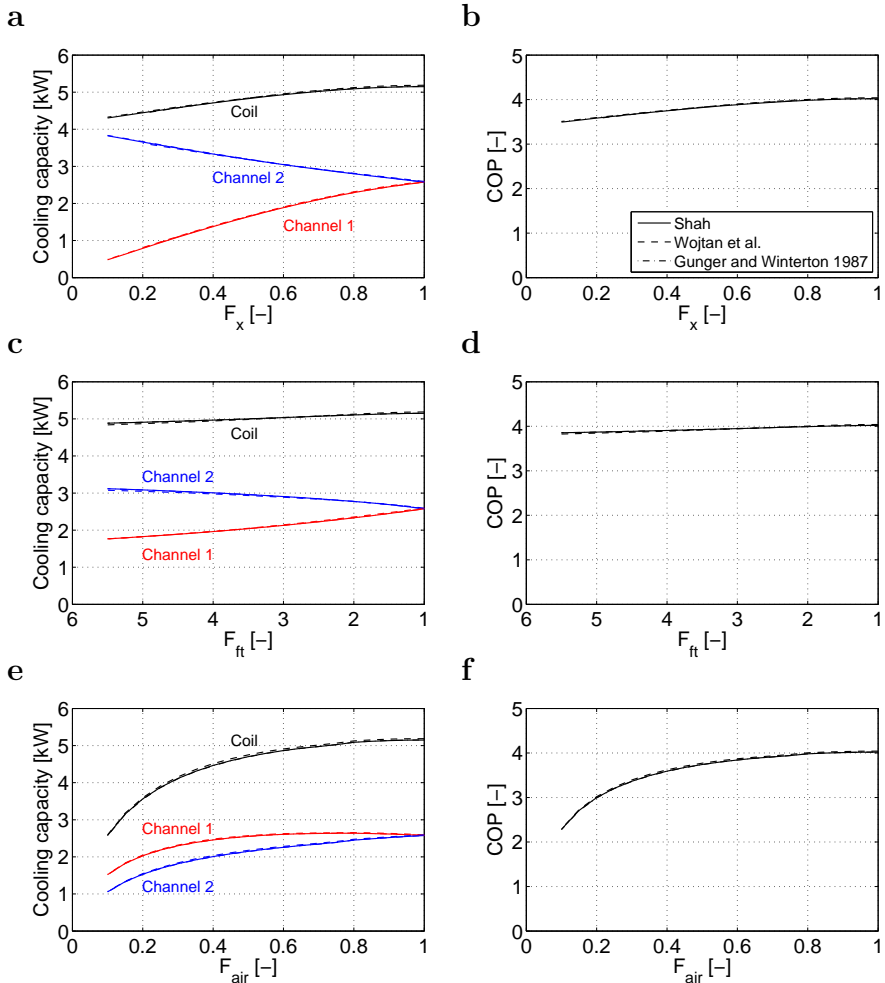
Figure 4.10: Individual channel and coil cooling capacity and COP vs. the different distribution parameters. The results are given for different heat transfer correlations.

superheat of each channel. The distribution occurs before the expansion, and the actual expansion is occurring into the individual feeder tubes. Thus the liquid/vapor phase cannot be maldistributed. Moreover, the compensation method distributes the liquid and vapor phases uniformly, i.e. the inlet mixed-cup enthalpy to each channel is the same. Thus, in this section we only vary the airflow distribution parameter and compare the performance of the system with compensation and the system without compensation from section 4.4.3.

By allowing the individual mass flows to be controlled, the pressure drop through each channel is not necessarily equal. Therefore, an additional inlet pressure difference is allowed in the model, see equation 2.48 and 2.49. Figure 4.11a shows the comparison of the refrigerant mass flow rates as function of the airflow distribution parameter, at compensation and no compensation.
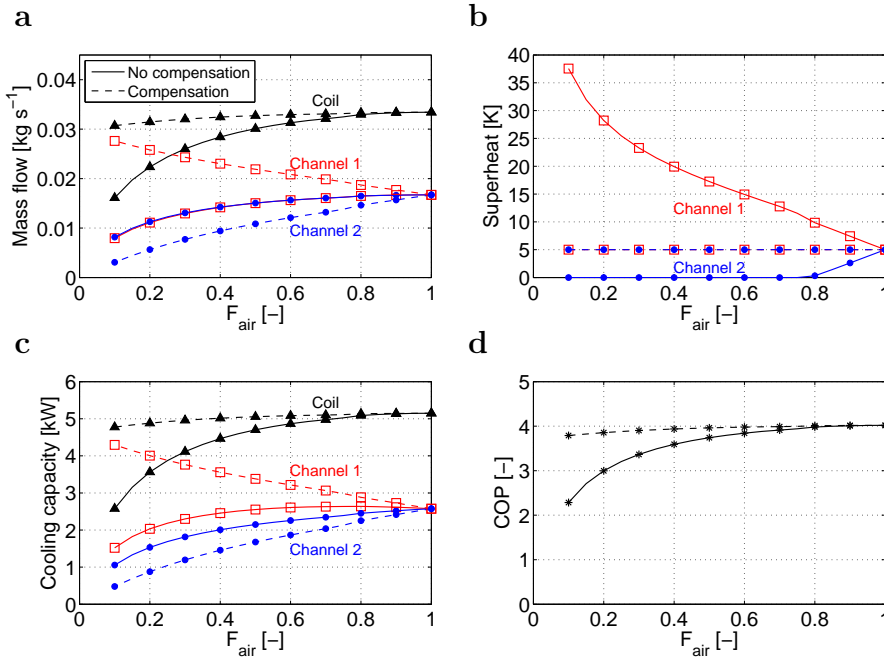
Figure 4.11: Selected parameters vs. the airflow distribution parameter; Solid lines = no compensation of maldistribution, dashed lines = compensation by control of individual superheat.

It shows how the mass flows should be distributed as function of the airflow distribution parameter, in order to ensure equal superheat out of the channels. The total mass flow through the coil can thus be held high, indicating a higher cooling capacity at compensation. The channel that receives less airflow also receives less refrigerant flow and vice versa. At no compensation the individual mass flow curves coincide as discussed in section 4.4.3.

The control of the individual channel superheat eliminates the different super-heated regions as shown in figure 4.11b. It eliminates the decrease in the overall UA-value as liquid starts to come out of channel 2 ($F_{air} = 0.8$) at no compensation. A higher superheated region with lower UA-value will be required in channel 1 to evaporate this surplus liquid. In turn, the lower UA-value results in a lower mass flow rate in order to ensure the overall superheat of 5 K.

The result of the recovered overall UA-value and mass flow rate is a recovery of the cooling capacity and COP as indicated on figure 4.11c and 4.11d. When compensating airflow maldistribution the degradation in total cooling capacity is only 7.2% compared to 49.9% at $F_{air} = 0.1$. The degradation in COP is only 5.7% compared to 43.2% at $F_{air} = 0.1$.

Kim et al. (2009b) also performed a system level analysis of compensation of flow maldistribution in evaporators. They found that the cooling capacity and COP could be recovered to 99.9% at $F_{air} = 0.71$ by controlling individual superheat. The results of this study showed a cooling capacity recovery of 99.1% and a COP recovery of 99.3% at $F_{air} = 0.71$. There is thus a good correspondence between the results of the two findings.

4.6 Combination of flow maldistribution and compensation

To fully evaluate the benefits of compensation, we also need to address the combined effects of flow maldistribution in the comparison and the fact that the sources of flow maldistribution may act together or compensate each other. In section 4.4.2, it was found that the different feeder tube bends had minor effect on flow maldistribution in terms of cooling capacity and COP. Therefore, we only include the combined effects of inlet liquid/vapor phase distribution and airflow distribution in the comparison in this section.

The comparison of the systems with compensation or without compensation of flow maldistribution are also made at different evaporator size and outdoor condition. Furthermore, we show the total cooling capacity of the evaporator in this section and not only the cooling capacity of one of the two coils.

The individual effect on the cooling capacity as F_{air} goes from 0.5 to 1.5 and F_x goes from 1 to 0.2 is seen in figure 4.12 with and without compensation.
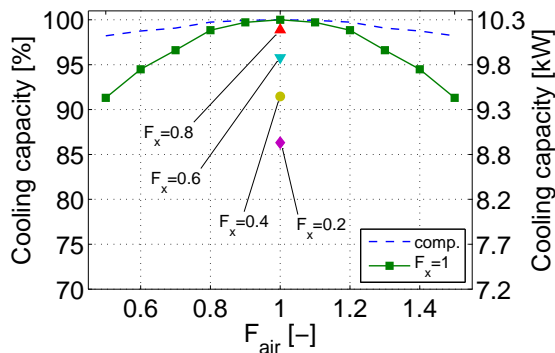
Figure 4.12: Evaporator capacity vs. individual maldistribution source.

The figure works as an introduction to the next figures in this section. The results on the figure in simply the same results as was shown in prior sections. When F_{air} and F_x is unity, i.e. at uniform flow conditions, the cooling capacities coincide at the maximum.

The combined maldistribution is studied by varying both F_{air} and F_x simultaneously. Figure 4.13a and 4.13b show the cooling capacity and the COP of the system with and without compensation. The graphs show both the actual values and the relative performance compared to the maximum.

Figure 4.13: Combined maldistribution of inlet liquid/vapor and airflow (8.8 kW evaporator, outdoor temperature = 35°C). Evaporator capacity (a), COP (b), Individual superheat (c) and two-phase part (d).

The figures show that the individual maldistribution sources may act together or cancel out each other. They act together when $F_x < 1$ and $F_{air} < 1$. When $F_x < 1$, a higher superheated area is present in channel 1, since channel 2 receives more liquid. Simultaneously, the airflow across channel 1 increases for $F_{air} < 1$ so that an even higher superheated area in channel 1 occurs (see figure 4.13c). When $F_x < 1$ and $F_{air} > 1$ they compensate each other. The airflow maldistribution is compensated by the inlet liquid/vapor distribution to give a higher cooling capacity and COP, as the values for $F_x < 1$ become higher than the values for $F_x = 1$ (i.e. in the right corner of the graphs).

The maximum of each curve without compensation (full lines) is close to the compensated case (dashed line) where the individual channel superheats are controlled, indicating a maximum performance. Figure 4.13c shows the individual channel superheats in each coil for the case without compensation. We find it interesting that the maximum performance at combined flow maldistribution is not obtained when the individual superheats are equal, however it is quite close. The curve $F_x = 0.8$ shows a maximum performance at $F_{air} = 1.2$, however, the individual superheats are equal at $F_{air} = 1.24$. Furthermore, the curve $F_x = 0.6$ shows a maximum performance at $F_{air} = 1.4$, whereas the individual superheats are equal at $F_{air} = 1.48$.

The maximum performance at combined flow maldistribution might be when the two-phase area in the evaporator is highest, since the two-phase area has a higher heat transfer than the single-phase area. Figure 4.13d shows the percentage of the two-phase area in the evaporator. The values are discrete values, since the evaporator model is discritized in the flow direction. We observe that the two-phase area cannot be used as a true measure of the maximum performance at combined flow maldistribution. For instance, the curve $F_x = 0.6$ shows that the highest two-phase area is more or equal to $F_{air} = 1.5$, however, the curve's maximum performance was at $F_{air} = 1.4$.

4.6.1   Different evaporator size

The penalties of airflow and inlet liquid/vapor maldistribution may be compensated by control of individual superheats. A common alternative to increase the COP is to increase the area of the evaporator. It may therefore be viewed as a method of compensation of flow maldistribution also, despite that the larger evaporator also are subject to flow maldistribution. There will be a trade-off between the use of the compensation method and the use of a larger evaporator in terms of cooling capacity and COP.

Figure 4.14a and 4.14b show the combinational effects of flow maldistribution for the same 8.8 kW system, but having a larger evaporator, i.e. the evaporator that is used for the 10.5 kW system. The evaporator basically has the same coil geometry, but two extra tubes in each channel. Note that the results in Kærn et al. (2011a) are based on using a larger indoor unit (including fan) such that the mean frontal air velocity became higher. In the following, we want to show only the effect of the evaporator area, thus we keep the mean frontal air velocity the same so that the heat transfer characteristics are the same for the comparison.

Note that increasing the evaporator size from 8.8 to 10.5 kW will not give 1.7 kW extra cooling capacity, if the compressor, condenser and fans are not upgraded similarly.

Furthermore, the relative degradations seem to be the same when using a larger evaporator and the main difference is only the scale on the right hand side of the graphs.
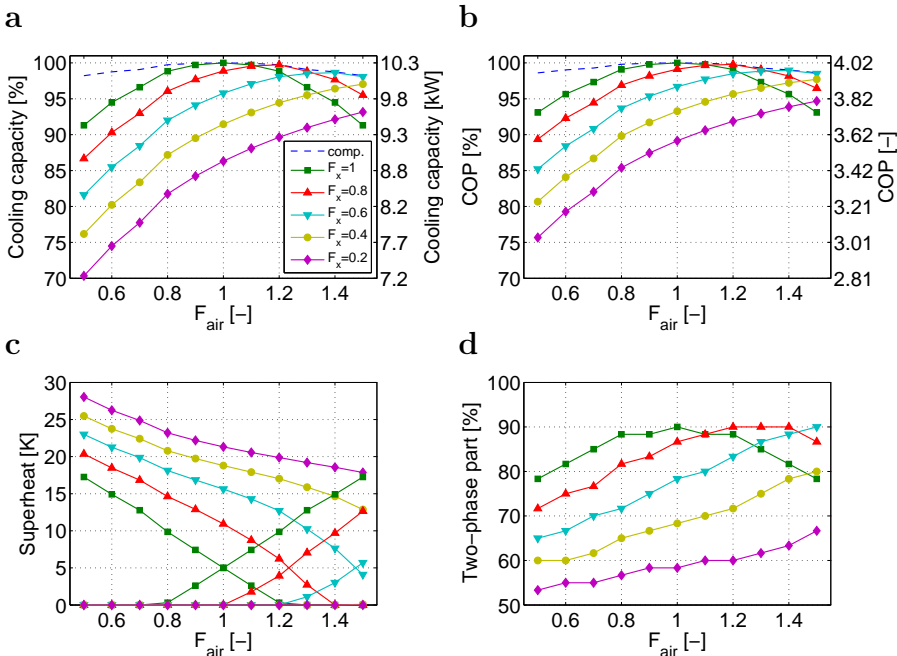
Figure 4.14: Combined maldistribution of inlet liquid/vapor and airflow (10.5 kW evaporator, outdoor temperature = 35°C). Evaporator capacity (a) and COP (b).

Figure 4.14 also shows the results of the 8.8 kW evaporator system with compensation. This curve defines the actual trade-off between using the compensation by control of individual channel superheat or the use of a larger evaporator. It is essentially better to use the larger evaporator if there is no flow maldistribution, which is quite intuitive. However, if the evaporator is subject to flow maldistribution it might be better to use the compensation method. The span at which it is better to use the larger evaporator seems to be small for the current comparison.

The intersections between the 8.8 kW evaporator system with compensation and the 10.5 kW evaporator system without compensation (full lines), defines the trade-offs in terms of the actual flow maldistribution conditions, e.g. the flow maldistribution cases $F_{air} = 0.68$ and $F_x = 1$, $F_{air} = 0.85$ and $F_x = 0.8$, $F_{air} = 1.1$ and $F_x = 0.6$, and so on. For these trade-offs the cost of the compensation method must then be less than the difference in cost between the two evaporators plus the EXV valve.

4.6.2   Different outdoor temperature

Figure 4.15a and 4.15b shows the effects of the combined maldistribution for the 8.8 kW evaporator at an outdoor temperature of 27.8°C.

The degradation in cooling capacity and COP shows similar trends as for the higher outdoor temperature considered previously. Since the temperature difference between the indoor and the outdoor is smaller, the COP of the system is higher. As the outdoor temperature decreases, the inlet quality to the evaporator also decreases, and thus the potential of inlet liquid/vapor maldistribution is lower. This can be seen on the curves when $F_x < 1$, which show less percent degradation compared to figure 4.13.
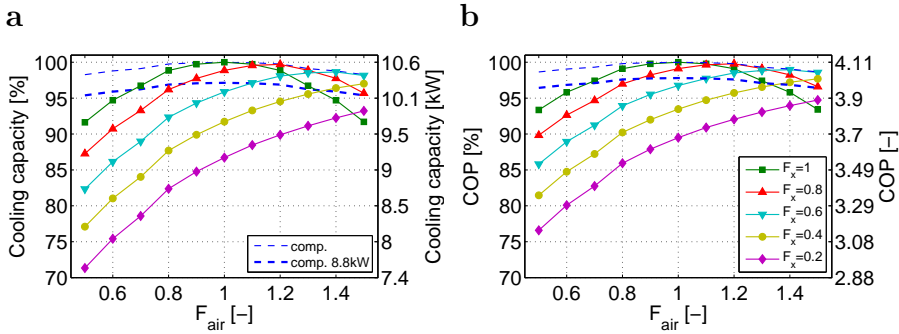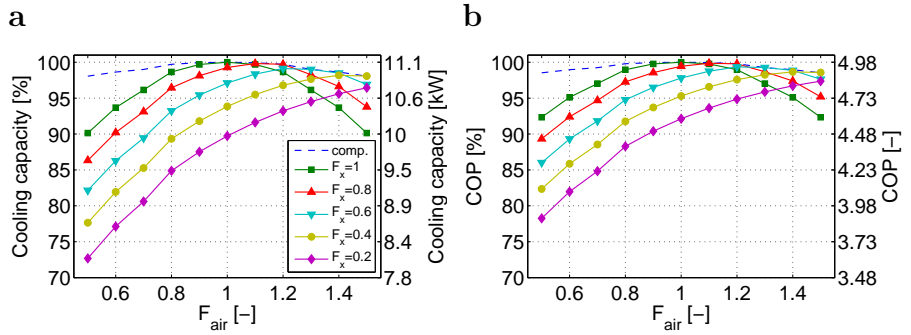
Figure 4.15: Combined maldistribution of inlet liquid/vapor and airflow (8.8 kW evaporator, outdoor temperature = 27.8°C). Evaporator capacity (a) and COP (b).

4.7 Discussion and summary

In this chapter we presented a generic study of flow maldistribution in evaporators for residential air-conditioning with refrigerant R410A. For this purpose we simplified the evaporator circuiting to be two straight channels such that the results from this chapter are not confined to a specific type of tube circuiting, but may be viewed as general results and trends.

The results may be used as graphical guidelines for predicting the possible degradation or recovery in cooling capacity and COP at flow maldistribution in the evaporator. The readers need to be cautioned that it is not practical to have evaporator coils consisting of two straight tubes. However, the presented graphical guidelines may be used by the readers by making a qualitative guess on the degree of flow maldistribution (i.e. the distribution parameters F_x, F_{ft} and F_{air}) considering the actual tube circuiting, refrigerant flow and airflow arrangement.

Note that we assumed the two coils in the A-coil evaporator to work under similar maldistribution conditions. However, there could be maldistribution between the coils themselves. Maldistribution may also be worse when the system is in part-load operation or operated under off-design non-standard conditions. Furthermore, dehumidifying conditions, which were not considered here, may cause larger airflow maldistribution as was shown experimentally by Yashar and Domanski (2010).

The conclusions of the chapter are summarized in the following summary and may be viewed by the readers as rules of thumb.

Summary

Firstly, the numerical models of the evaporator and condenser were verified with commercial software code Coil-Designer (Jiang et al., 2006). Secondly, the individual sources of flow maldistribution were studied, i.e. a non-uniform inlet liquid/vapor distribution, different feeder tube bends and a non-uniform airflow. Using the current definitions of the distribution parameters (F_x, F_{ft} and F_{air}) the main conclusions were:

- Non-uniform airflow significantly reduces the cooling capacity and COP.

- Non-uniform inlet liquid/vapor distribution has smaller reductions compared to the airflow.

- Different feeder tube bends (feeder tube pressure drop) have minor effect on the cooling capacity and COP.

- The reductions in COP were as much as 13%, 4.1% and 43.2% for non-uniform inlet liquid/vapor distribution, different feeder tube bends and non-uniform airflow, respectively.

- The results and trends were similar at different two-phase frictional and heat transfer correlations, thus the significance of these were minor in predicting flow maldistribution.

Thirdly, the compensation of flow maldistribution was studied using the control of individual channel superheats by distributing individual channel mass flow rates. In addition, the compensation was compared to the combined flow maldistribution of the inlet liquid/vapor phases and the airflow. The main conclusions were:

- The compensation method recovers the airflow maldistribution significantly in terms of cooling capacity and COP. The reduction in COP is only 5.7% compared to 43.2% at $F_{\mathrm{air}} = 0.1$.

- Combinations of inlet liquid/vapor phase distribution and airflow distribution may either outbalance and compensate each other or worsen the degradations in cooling capacity and COP. When the sources outbalance the result may be a recovery similar to the system with compensation.

- The effects of the different evaporator size or outdoor temperature on the degradation of the cooling capacity and COP were shown to be minor in percent relative to the maximum.

- The trade-offs between the use of a larger evaporator and the use of the compensation by control of individual channel superheats, showed that the span in terms of flow maldistribution conditions at which the larger evaporator is preferable, was small.

- However, if there is no particular flow maldistribution, then the larger evaporator will always be the most favorable.

CHAPTER 5

Face split vs. Interlaced

This chapter is a continuation of the generic study presented in chapter 4. The only difference is the modeling of the actual tube circuitry of the evaporator. Moreover, the chapter compares the performance in terms of cooling capacity and COP of the standard interlaced and face split types of circuitries in flow maldistribution conditions with and without compensation. The results of this chapter is therefore confined to these circuitries and the generality from chapter 4 is eliminated.

The first parts of the presented results are also discussed in Kærn et al. (2011c).

5.1 Introduction

The focus in this chapter is to study the flow maldistribution conditions in A-shaped fin-and-tube evaporators for residential air-conditioning including tube circuitry.
The reason why the study is performed is to evaluate and quantify the implications of flow maldistribution on real type evaporator circuitries and possible compensation potentials. Especially, the coupling between the tube circuiting and the compensation potential is important to clarify and gain more insight about the involved physical phenomena. This coupling will be investigated in order to generate guidelines that illustrates the feasibility for the standard tube circuitries with and without compensation. The method of compensation is the same as used in chapter 4.

The chosen type of circuitry by the manufacturers have changed a couple of years ago. It changed from the face split to the interlaced circuitry, see figure 5.1. The interlaced circuitry has shown a significant increase in cooling capacity compared to the face split circuitry. The main reason is the better compensation of flow maldistribution by design, i.e. tube circuiting.

The first objective is to investigate the flow maldistribution in the face split and interlaced circuitry, i.e. (1) non-uniform inlet liquid/vapor phase distribution and (2) non-uniform airflow distribution. Different feeder tube bends were shown in chapter 4 to have minor effect on the performance in terms of cooling capacity and COP. The second objective is to consider further compensation of flow maldistribution by control of individual channel superheats.

The chapter starts with a verification of the circuitry modeling and partial validation of the numerical model with experiments carried out at Danfoss on the interlaced circuitry. The validation is partial since the flow maldistribution was not measured or eliminated, and thus needs to be guessed.

Then the flow maldistribution sources are investigated individually for each type of circuitry. In addition, the benefits of using the compensation by control of individual channel superheats is addressed for both circuitries. Furthermore, the combination of flow maldistribution sources are considered for the two circuitries with and without compensation. Finally, the airflow distribution is computed by computational fluid dynamics (CFD) (STAR-CD 3.26, 2005) and applied to the numerical model of each circuitries, in order to gain more insight about the airflow distribution and its implications.

5.2   Model setup

Compared to the model setup in chapter 4, the only difference is in fact the tube circuiting. Exactly the same model assumptions are used for all the components of the same R410A 8.8 kW air-conditioning unit, despite the tube circuiting in the evaporator. For these reasons the model assumptions will not be explained again. A detailed model formulation including model equations etc. is given in chapter 2 and the circuitry modeling is explained in chapter 3. In the following, the differences compared to chapter 4 will be explained together with the main model setup.

5.2.1   Correlations and geometry

The modeling of the tube circuitries involve additional U-bends that increases the pressure drop compared to the straight channel approach. The chosen correlations for frictional pressure drop through U-bends are shown in table 5.1 together with all other correlations that are used throughout this chapter. Again effectiveness-NTU relations for cross flow heat exchangers are employed.

a

b

Air flow

Air flow
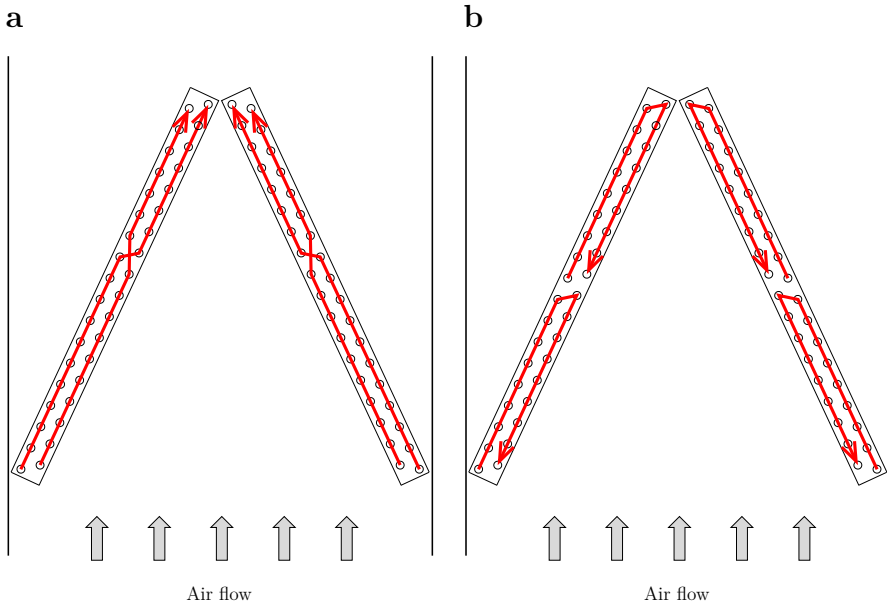
Figure 5.1: Tube circuitries of the interlaced evaporator (a) and the face split evaporator (b).

Table 5.1: Overview of used correlations.

Air-side	
Heat transfer	Wang et al. (1999)
Fin efficiency	Schmidt (1949), (Schmidt approximation)
Single-phase	
Heat transfer	Gnielinski (1976)
Friction	Blasius (2002)
Bend friction	Ito (1960)
Two-phase (evaporator)	
Heat transfer	Shah (1982)
Friction	Müller-Steinhagen and Heck (1986)
Bend friction	Geary (1975)
Two-phase (condenser)	
Heat transfer	Shah (1979)

Note that the coil geometry is the same for both the interlaced and face split evaporator (see table 4.1), however, the tube circuiting (or connections) are different as shown on figure 5.1. Again the two coils in the evaporator are

assumed to be in similar maldistribution conditions, and essentially only one coil is simulated.

5.2.2 Distribution parameters

Before we may define the distribution parameters, we need to gives the channels numbers, see figure 5.2a.
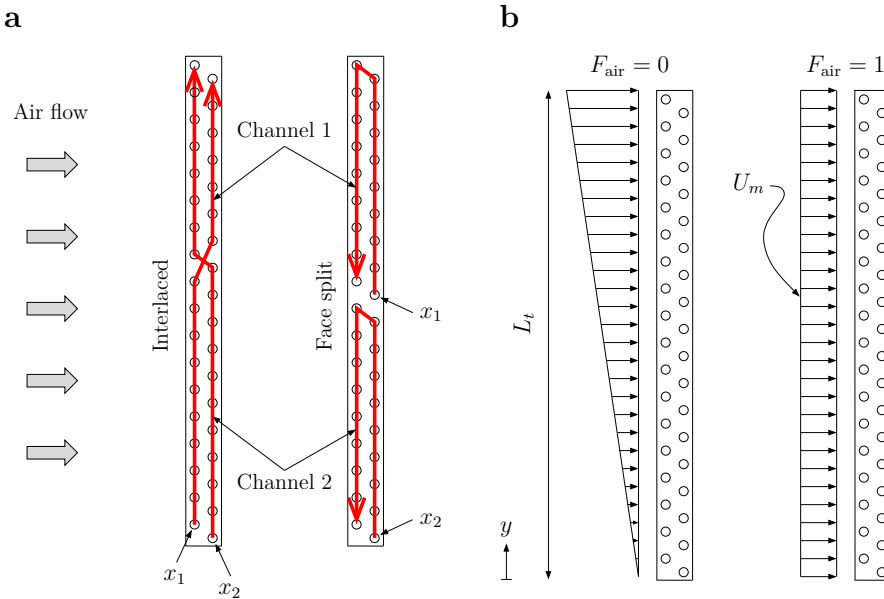
Figure 5.2: (a) channel numbering for each evaporator and (b) one-dimensional airflow profiles.

The phase distribution parameter F_x is defined as

$$F_x = \frac{x_2}{x_{\text{in}}} \qquad 0 \leq F_x \leq 1 \tag{2.41}$$

$$F_x = 2 - \frac{x_1}{x_{\text{in}}} \qquad 1 < F_x \leq 2 \tag{2.42}$$

When F_x is unity, the vapor quality into the feeder tubes is equal. When F_x is zero, only liquid is fed into channel 2. When F_x is two, only liquid is fed into channel 1. Mass and energy conservation equations are applied to compute the vapor quality into the remaining channel.

The airflow distribution parameter F_{air} is defined by

$$U(y) = U_m F_{air} + y \frac{2U_m(1 - F_{air})}{L_t} \qquad 0 \leq F_{air} \leq 1 \qquad (2.53)$$

where U_m is the mean frontal velocity, y is the transverse coordinate and L_t is the transverse length of the coil.

When F_{air} is unity, the airflow profile is uniform across the coil. When F_{air} is zero, the airflow profile becomes the worst possible linear one-dimensional profile in the transverse direction, see figure 5.2b. More air is believed to travel through the top of the coil in real applications with maldistribution that we simulate via the linear profile.

5.2.3 Boundary conditions and solution methodology

The boundary conditions are the same as in chapter 4. The overall superheat is controlled to 5 K. When compensating, both channel superheats are controlled to 5 K by distributing individual channel mass flow rate. During start-up of the simulation at no maldistribution, the charge of the system is determined so that the subcooling becomes 2 K. Then the different distribution parameters are varied individually and each steady state result is obtained. The indoor and outdoor air temperatures are 26.7°C and 35°C, respectively. The mean frontal air velocities are 1.16 and 0.68 m s^{-1} to the evaporator and condenser, respectively. The geometric volume flow of the compressor is 6.239 m^{3}h^{-1}.

5.3 Verification and validation

The verification is performed on a 10.5 kW interlaced coil, since this is the experimental test case for model validation. The verification will be performed with commercial software Coil-Designer (Jiang et al., 2006) under uniform flow conditions. The validation is performed by assuming a degree of airflow maldistribution in the model. The result is compared to the experiments together with the uniform flow case from the verification and the simplified two channel case from chapter 4. The experiments were carried out by Fösel (2009) at Danfoss in Nordborg 2008. No experiments were carried out with uniform flow conditions to the evaporator that could validate the model without guessing the degree of flow maldistribution. Furthermore, no experiments were carried out where the flow maldistribution were measured. Note, that we consider only dry air in the numerical model, however, these experiments were carried out with low relative humidity in the indoor room such that no condensate were formed on the evaporator surface.

5.3.1 Steady state verification

The experimental test boundary conditions used in Fösel (2009) will be used
in the verification as shown in table 5.2.

Table 5.2: Boundary conditions for verification.

Superheat	13 K
Refrigerant inlet pressure	9.869 bar
Refrigerant inlet quality	0.22
Indoor air temperature	24.4°C
Indoor frontal air velocity	2.45 m s^{-1}

The geometry is similar to table 4.1 although the table shows the 8.8 kW evap-
orator. Two extra tubes in each channel are used for the 10.5 kW evaporator
and it means that the outer surface area becomes 19.2 m^2 (for both coils). In
the verification we consider only one coil. Furthermore, we used 5 cells per
tube, i.e. 100 cells per channel plus 18 bend cells.

The interlaced circuitry and corresponding refrigerant temperature contour
through the center of the coil are shown on figure 5.3a. The channel numbering
are similar to figure 5.2a. It means that channel 1 has higher heat transfer in
the beginning of the refrigerant path, since the temperature difference between
refrigerant and air is higher in row 1 than row 2. This is also indicated in
the temperature contours as channel 1 becomes superheated before channel 2.
This is however easier to see on figure 5.3b, which shows the comparison of
the corresponding refrigerant temperature profiles with Coil-Designer. Figure
5.3c shows the comparison of the corresponding refrigerant pressure profiles
through the coil.

Both the refrigerant and pressure profile comparison are in good accordance
and we may state that the circuitry modeling is verified. There is some minor
differences in the pressure drop prediction, which may be due to differences
in mass flow distributions in the simulations. In the current model (CM) we
predict the actual mass flow distribution to each channel according to each
channel pressure drop, whereas Coil-Designer (CD) distributes the mass flows
to each channel evenly. Furthermore, the pressure profiles indicate that the
U-bend pressure drop is higher than a straight tube of the same length.

Table 5.3 shows the comparison of the cooling capacity and mass flow rate for
the coil.

Again, there is good accordance between the simulations. Coil-designer predicts
a slightly higher heat transfer and mass flow, which most likely are due to the
smooth functions applied at the two-phase to vapor phase transition. The same
observation was found in section 4.3, where 3 different two-phase heat transfer
correlations were investigated for the straight tube verification.
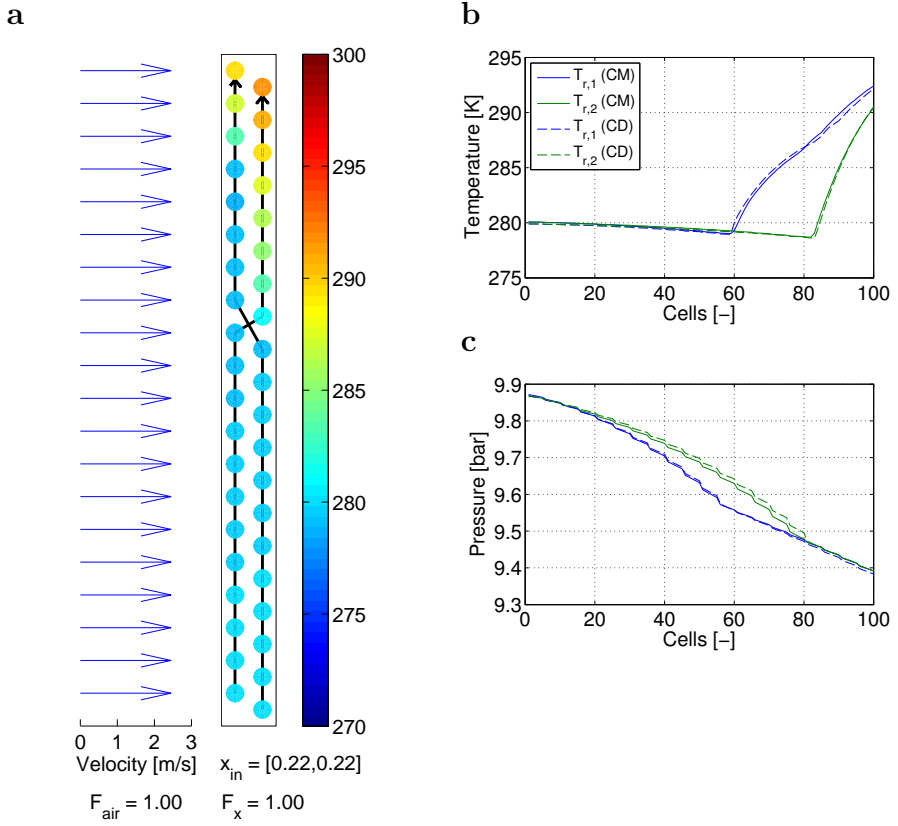
Figure 5.3: Refrigerant temperature contours through center of interlaced coil (a). Verification of refrigerant temperature and pressure profile following the refrigerant channel flow (b,c).

Table 5.3: Comparison of mass flow rate and cooling capacity at $n = 5$, (CM=current model, CD=Coil-Designer).

		Capacity [kW]	Mass flow [kg s^{-1}]
Interlaced coil			
	CM	5905	0.0329
	CD	6110	0.0339
	Error	3.3%	2.8%

5.3.2 Convergence

The convergence of the numerical solution is addressed in this section. The question of interest is: How many cells per tube is required to reach a reasonable convergence? Throughout all simulations in this thesis we used a tolerance of 10^{-4} in Dymola. This tolerance is essentially the same for both absolute and relative tolerances, if not a nominal value is given as an attribute in Dymola. Figure 5.4a and 5.4c shows the convergence of the refrigerant temperature profiles and the normalized cooling capacity as n goes from 1 to 5 per tube, i.e. 20 to 100 cells per channel + 18 U-bend cells.
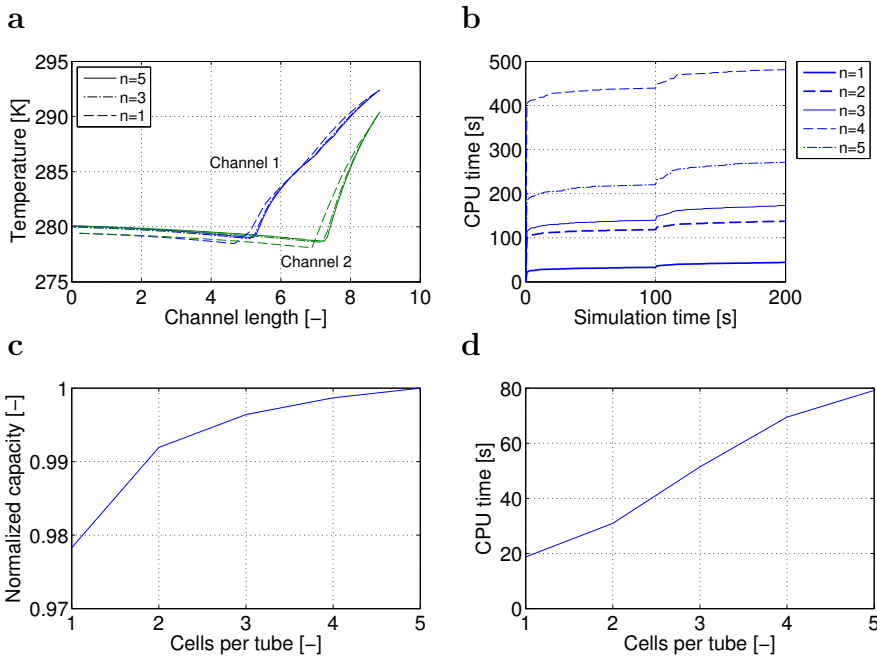
Figure 5.4: Convergence of interlaced circuitry model (a,c) and corresponding CPU time with and without initialization (b,d).

It shows that the convergence in the refrigerant temperature profile is reasonable for $n \geq 3$. The coil capacity already shows good convergence at $n = 1$. If we consider the uncertainty of the applied correlations for two-phase heat transfer and frictional pressure drop etc., which should be expected around 30%, then the convergence is by far acceptable.

By increasing the number of cells the CPU time also increases as indicated on figure 5.4b. The figure shows that the initialization takes most of the CPU time for the current simulations. At time equals 100 the controller starts to

control the refrigerant superheat according to table 5.2. At time equals 200 the steady state is achieved. The initialization at $n = 4$ took longer time than $n = 5$, which remains unexplainable and we may only guess that something have triggered the solver to become slower. However, if we subtract the CPU time for initialization, we get a more clear picture of the needed CPU time as function of n as shown in figure 5.4d. Interestingly, the CPU time seems to scale linearly for the current simulations.

Throughout this chapter we chose to use $n = 3$, i.e. 3 cells per tube.

5.3.3 Experimental validation

The experiments were carried out by Fösel (2009) at Danfoss in Nordborg 2008. There was no information about calibration or uncertainty measures for these experiments. The compressor speed was varied from 70 to 52.5 to 35 Hz, however, we will only compare the steady state results in this section (averages of the three compressor speeds). The experiments are shown on figure 5.5. The test case corresponds to the previous verified case with conditions from $0 \leq \text{time} \leq 2516$. The condenser was a micro-channel, the compressor was a hermetic scroll and the expansion valve was an electronic expansion valve. The figure shows the results for the total evaporator, thus both two interlaced fin-and-tube coils.

Figure 5.5a indicate that the cooling capacity decreases as the compressor speed decreases. Furthermore, the evaporating and condensing pressure increases and decreases, respectively, as shown on figure 5.5b. These trends are normal and as expected.

In the following, the experimental data is reduced in order to use them as input to the numerical model.

Model input

The refrigerant mass flow rate was only measured after the condenser in these experiments. Therefore, we used the mean mass flow rate from figure 5.5c to compute the volume flow rate at the evaporator outlet (figure 5.5d), and used that as input to the model. The mass flow rate at inlet to the evaporator is then controlled by the mean superheat in figure 5.5e, and the inlet vapor quality is computed by the liquid subcooling in figure 5.5f.

The indoor temperature (inlet air) is shown on figure 5.5g and kept constant by a secondary heating system. Unfortunately, the air mass flow rate through the evaporator was not measured. In contrast, we used the energy balance from the refrigerant to the air, in order to compute the air mass flow rate, see figure 5.5h. This is not considered as the most elegant method, however, the best possible for these experiments. The air mass flow is then converted by the coil geometry and air density into a frontal velocity of 2.45 m s^{-1}.
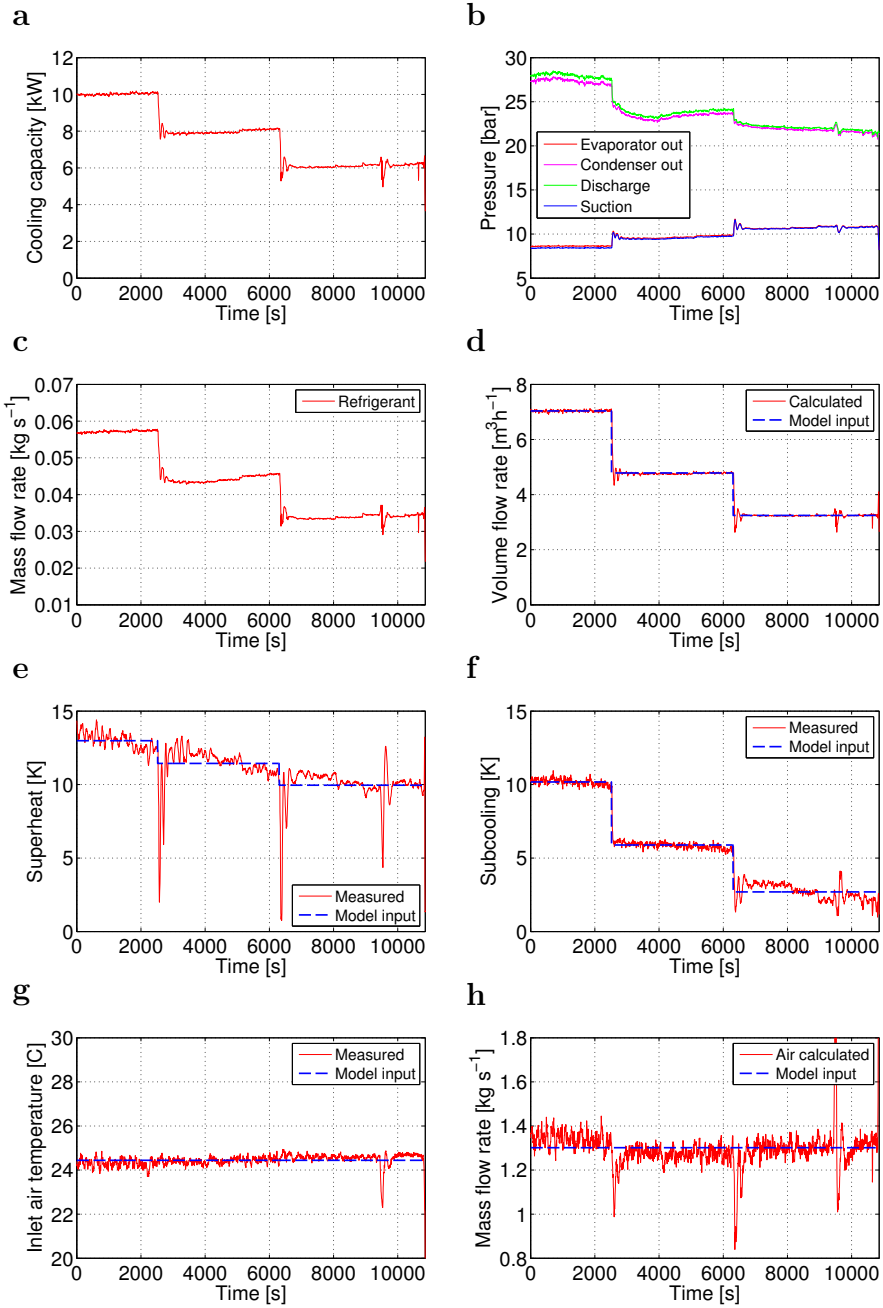
Figure 5.5: Experiments and calculated inputs.

Experimental comparison

In this section the experimental results are compared with three different model cases:

1. The two straight channels approach at uniform conditions (circuitry simplification), $F_{air} = 1$.
2. Actual circuitry modeling at uniform conditions, $F_{air} = 1$.
3. Actual circuitry modeling with maldistribution, $F_{air} = 0$.

Note that the definition of the airflow distribution parameter F_{air} is different in the first case compared to the second and third case.

The results of the experimental comparison are shown in figure 5.6. The dynamics shown in the model results can not be used for validation, since we apply steps in the refrigerant boundary conditions (model inputs from figure 5.5), thus only steady state results should be considered here.
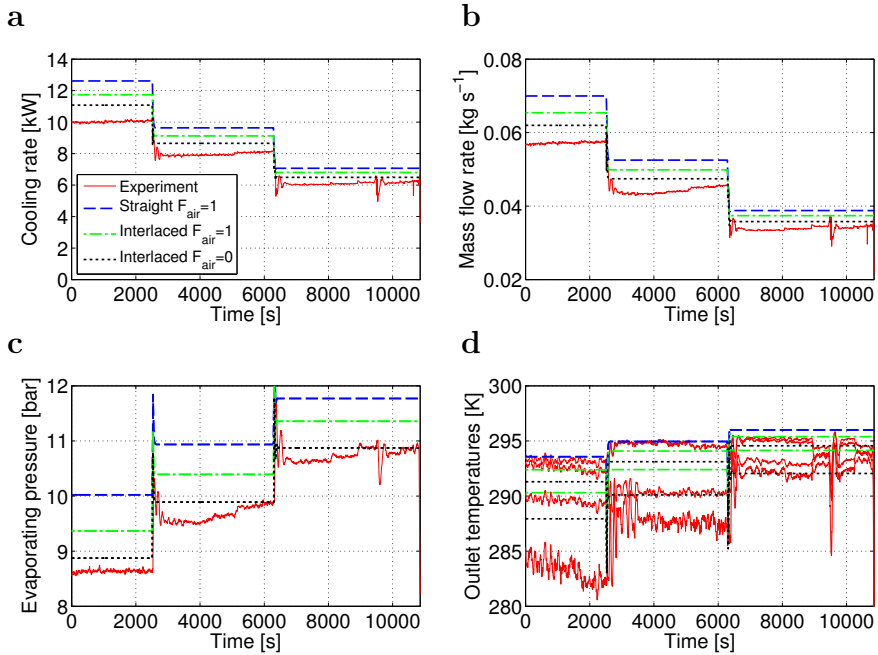
Figure 5.6: Experimental comparison.

The first case (two straight channels) shows the highest heat transfer, i.e. cooling capacity and mass flow rate. This is also expected since both channels sees the highest air temperature, i.e the inlet air temperature. For the second

case the circuitry is modeled and consequently the second row in the coil will meet a lower air temperature, thus a lower heat transfer. The temperature driving potential for heat transfer is thus higher for case one than case two. The evaporation pressure also becomes higher for case one, because of higher heat transfer.

The first two cases show higher cooling capacity and mass flow rate than the experimental results, which indicates that the experiments are carried out in flow maldistribution conditions. In the third case the circuitry is modeled and the worst possible linear velocity profile is applied. Again the numerical results shows higher heat transfer, i.e. cooling capacity, mass flow rate and evaporating pressure. It indicates that the experiments may have been conducted at worse maldistribution conditions.

There may be many reasons for the lower experimental capacity. The air profile may be even worse, the liquid/vapor phases may be distributed unevenly and there may be airflow maldistribution between the coils themselves. The degree of flow maldistribution may be indicated by figure 5.6d, which shows the outlet refrigerant temperatures. The experimental results show larger difference in outlet temperatures, whereas the numerical results show lower differences in outlet temperatures. It indicates that larger flow maldistribution conditions are present in the experimental results.

In conclusion, we cannot fully validate the numerical model with these experimental results. Firstly, we need to address the experimental uncertainty measures and propagation of error. Secondly, we need to either eliminate the flow maldistribution or measure the actual flow maldistribution. In these experiments we are faced with the difficult task of guessing degrees of flow maldistribution. The experimental comparison presented here does, however, give some credibility and reliability to the model.

In addition to the verification with Coil-Designer performed in section 5.3.1, the numerical model shows good results and we may conclude that the model is applicable for investigating flow maldistribution with actual circuitry modeling.

5.4 Effects of flow maldistribution

In this section the results of the simulations of flow maldistribution are presented for each standard circuitry type, i.e. the interlaced and the face split evaporator. The model setup follows from section 5.2. The distribution parameters are varied individually from 1 to 0, imposing an increasing degree of flow maldistribution. Firstly, we consider the cases without compensation, secondly, we consider the case with compensation. In contrast to chapter 4, it is chosen to show the overall UA-value instead of the cooling capacity, because the UA-value is decoupled from the temperature difference between refrigerant and air, in contrast to the cooling capacity. The UA-value gives a better identification of the coil performance independent of temperature difference.

5.4.1 Maldistribution from the distributor

The distribution of refrigerant mass flux as function of the phase distribution parameter is shown on figure 5.7a for each coil of the evaporators. It shows that the mass flux distribution is dependent on F_x, so that more mass comes through the channel with lower inlet vapor quality (channel 2) and less mass comes through the channel with higher inlet vapor quality (channel 1). This is determined by the pressure drop through the channels that must be equal. Indeed more mass will travel through the channel with lower vapor quality, since the pressure drop of the liquid phase is lower than the pressure drop of the vapor phase. At no maldistribution ($F_x = 1$) the face split evaporator shows higher mass fluxes for both channels indicating a higher cooling capacity, however, they decrease at higher maldistribution and become lower than the interlaced evaporator at $F_x = 0.55$.
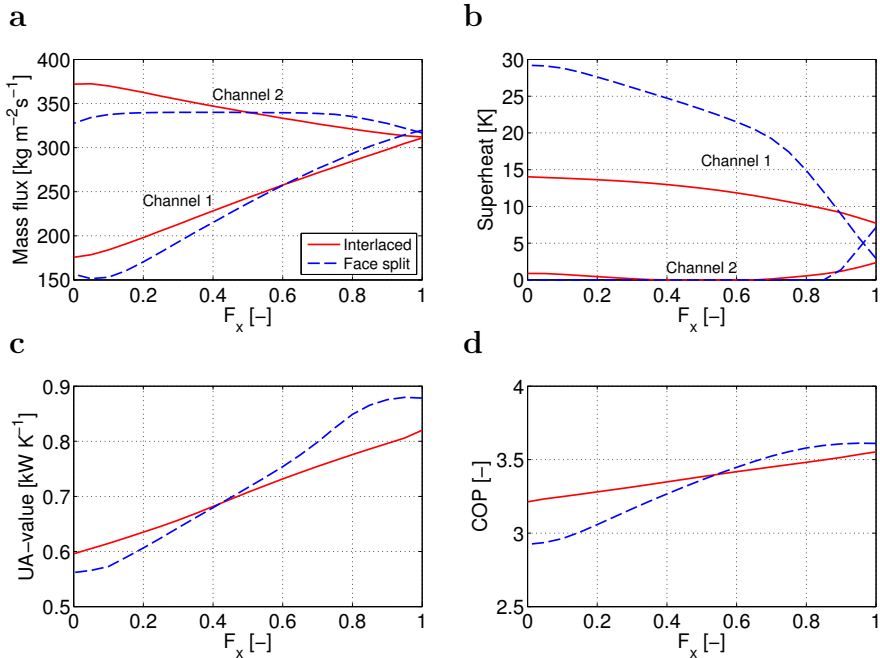
Figure 5.7: Selected parameters vs. the phase distribution parameter.

The consequence of the refrigerant maldistribution is seen in figure 5.7b, which shows the individual channel superheats for each coil of the evaporators. At $F_x = 0.85$, liquid is flowing out of channel 2 for the face split evaporator. This point is important because the two-phase area of the face split evaporator decreases, when full evaporation is not reached in channel 2. A larger superheated area in

channel 1 is required in order to evaporate this surplus liquid, thus the overall UA-value decreases as seen on figure 5.7c. The interlaced evaporator does not experience the same degree of superheat non-uniformity, and it therefore has a smaller reduction in the overall UA-value as F_x decreases. Figure 5.8 and 5.9 show that the superheat may actually increase and decrease in the second tube row of the interlaced evaporator, which somehow contradicts the better performance at higher inlet liquid/vapor maldistribution. The air is thus cooled in the first row and heated in the second, which should be avoided.

The face split evaporator performs better at low maldistribution. This is because of the tube circuitry. The two channels of the face split evaporator are counter-cross flow, however, the interlaced is both counter-cross flow (channel 2) and parallel-cross flow (channel 1). When constructing a heat exchanger it should always be attempted to use the temperature potential between the heat exchanging fluids in the best possible way. It is not the case when the superheated regions, which have lower UA-value, are aligned next to each other in the airflow direction. This is the case for the interlaced evaporator as illustrated in figure 5.8. There is a higher temperature potential for heat transfer in both the superheated regions of the face split evaporator, since they are aligned in the first tube row. In turn, the face split evaporator will minimize the superheated region, since the gradient of the refrigerant vapor temperature is higher than for the interlaced evaporator at low maldistribution, see figure 5.9.

The COP of the two systems (figure 5.7d) is affected in similar manner as the UA-value, however, not as dramatic. The tradeoff between the face split and the interlaced evaporator is at $F_x = 0.55$ for the current systems.

5.4.2   Maldistribution from the airflow

The distribution of refrigerant mass flux as function of the airflow distribution parameter is shown on figure 5.10a for each coil of the evaporators. For the face split evaporator, the refrigerant mass flux distribution is almost equal in each channel as F_{air} decreases. For the interlaced evaporator there is some divergence. The mass fluxes are again higher for the face split evaporator at low maldistribution indicating a higher cooling capacity and performance. However, the mass fluxes of the face split evaporator decrease even more than the interlaced evaporator at higher maldistribution.

Figure 5.10b shows the corresponding superheat of each channel in the coils of both evaporators. It is seen that the interlaced evaporator recovers the airflow maldistribution quite well, i.e. the superheated region of the evaporator is not increased. This is in contrast to the face split evaporator, which shows that liquid comes out of channel 2 at $F_{air} = 0.75$, thus the superheat of channel 1 increases in order to ensure an overall superheat of 5 K.

Figure 5.11 and 5.12 show the refrigerant temperature contours in the coils and profiles following the refrigerant channel flows. For the interlaced evaporator
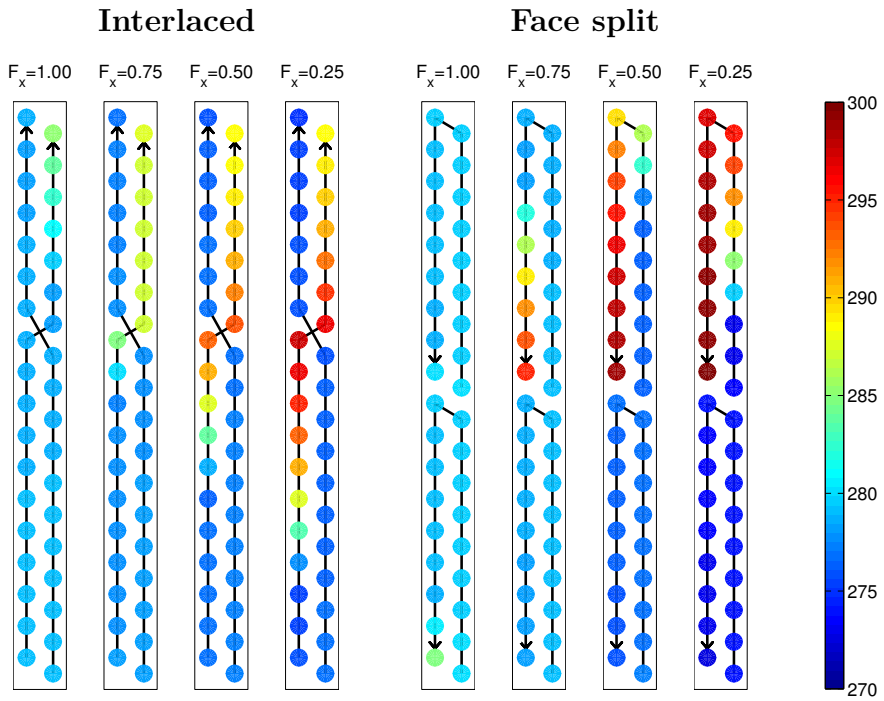
Figure 5.8: Refrigerant temperature contours through center of coils.
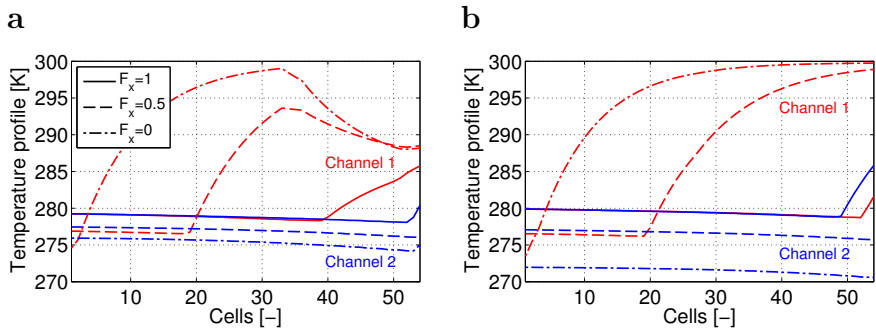
Figure 5.9: Refrigerant temperature profile for interlaced (a) and face split (b) coils.
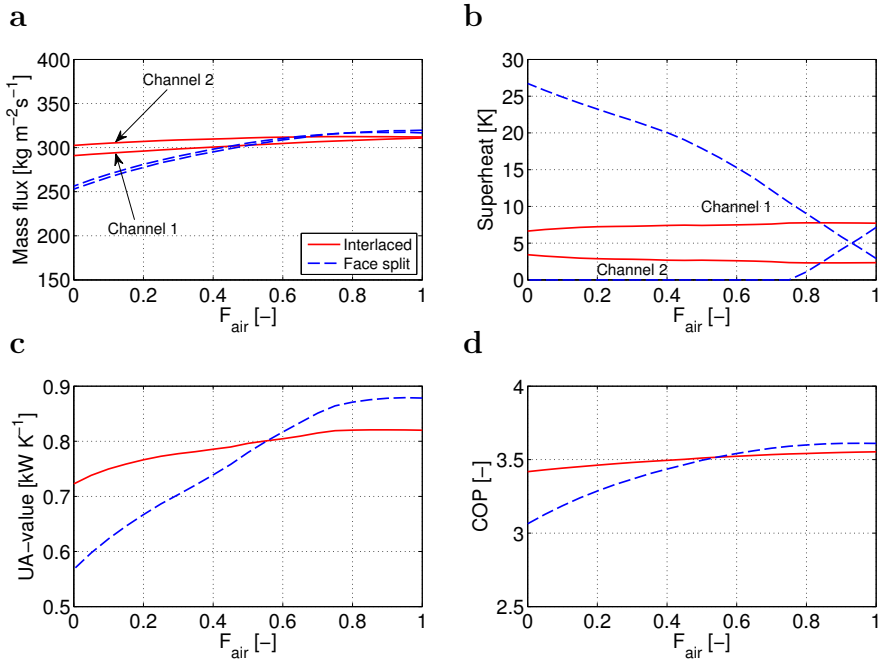
Figure 5.10: Selected parameters vs. the airflow distribution parameter.

the superheated zone is larger at the beginning, but actually becomes smaller as F_{air} decreases. This is because of the larger heat transfer due to higher air velocity across the top of the coil, thus resulting in larger vapor temperature gradient. However, the face split evaporator shows the minimum superheated area at no maldistribution and it increases at higher airflow maldistribution.

Despite the interlaced superior flow maldistribution recovery, the face split evaporator performs better at $F_{\mathrm{air}} > 0.55$ and $F_x > 0.55$ in terms of overall UA-value and COP, see figure 5.7c, 5.7d, 5.10c and 5.10d. As mentioned in the previous section, this is because the superheated regions with low UA-value are placed in the first row of the coils in the face split evaporator, where the temperature driving potential is highest. It seems a coincidence that the trade-off value is 0.55 for both F_{air} and F_x, however, the trade-off is subject to their definitions in section 5.2.2. The reason why the interlaced evaporator is used today seems because of the flow maldistribution, which is better recovered by the interlaced evaporator.
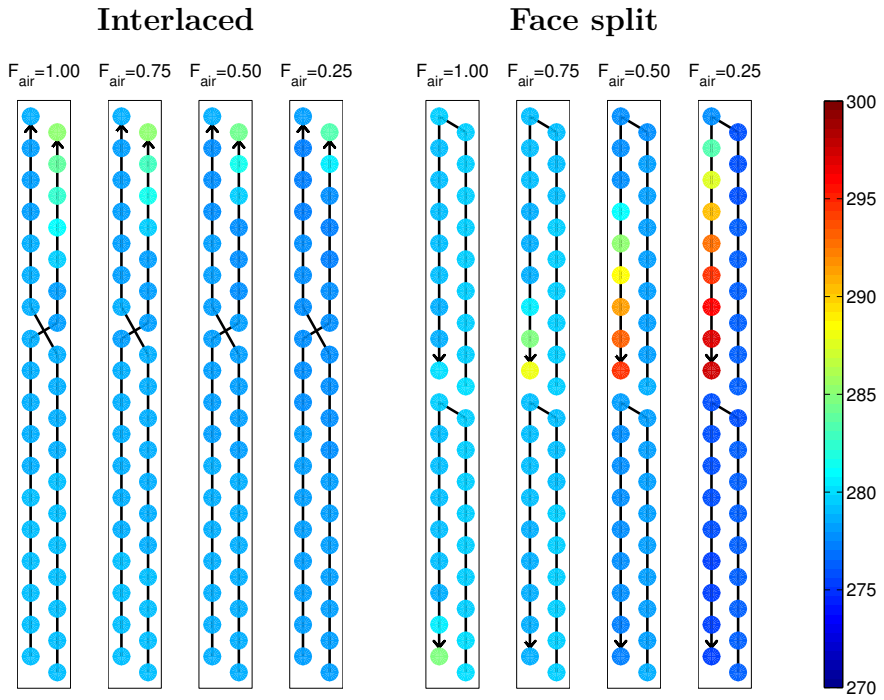
Figure 5.11: Refrigerant temperature contours through center of coils.
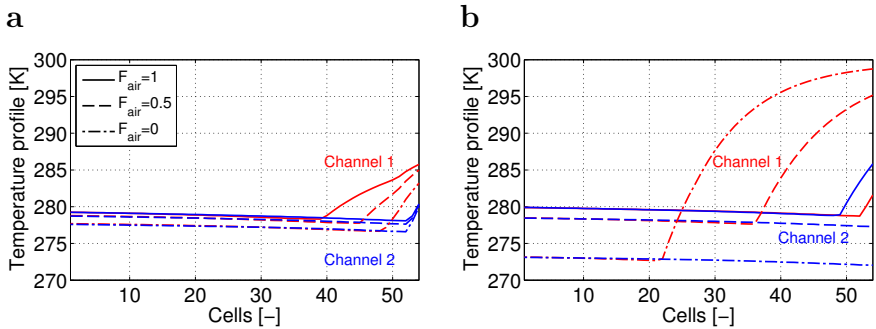
Figure 5.12: Refrigerant temperature profile for interlaced (a) and face split (b) coils

5.4.3 Compensation of flow maldistribution

Compensation of flow maldistribution will be investigated in this section. As mentioned in chapter 4, the compensation method already compensates the inlet liquid/vapor phase maldistribution by design, since the distribution of refrigerant happens before the refrigerant expansion. Thus, in this section we only vary the airflow distribution parameter. When distributing the mass flow, the pressure drop through each channel need not necessarily be equal. Therefore, an additional inlet pressure difference is allowed in the model (see section 2.7.2). Figure 5.13 shows the UA-value and COP as F_{air} goes from 1 to 0.
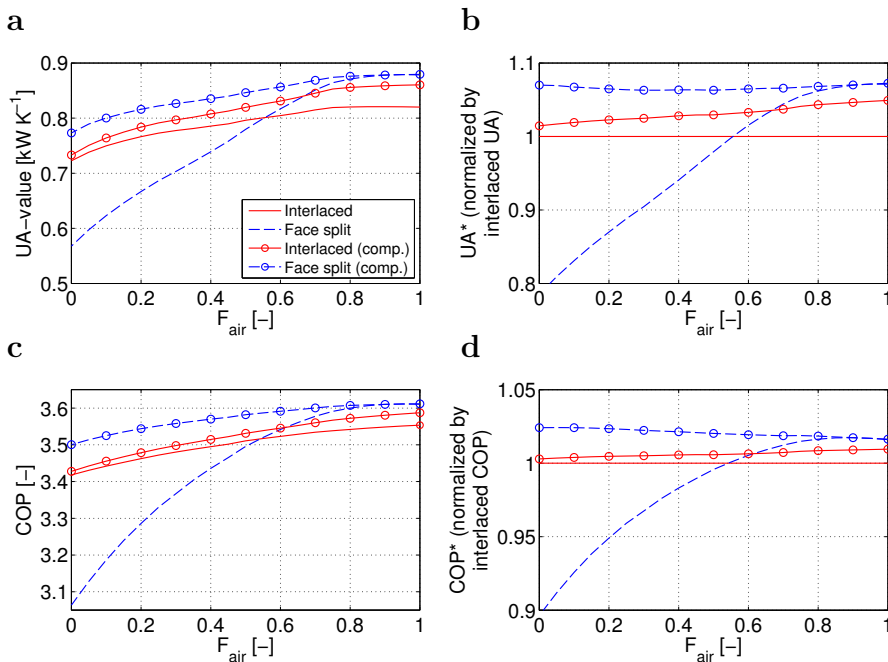
Figure 5.13: Comparison of UA-value and COP with and without compensation of airflow maldistribution (8.8 kW evaporator).

It shows that the control of the individual channel superheat eliminates the different superheated regions in both evaporators. The elimination of the superheated region is, however, higher for the face split evaporator, as indicated on figure 5.12, since the interlaced evaporator already by design compensates airflow maldistribution to some extend. The result is an increased overall UA-value and COP as depicted on figure 5.13a and 5.13c.
Both evaporators experience a better performance when controlling the indi-

vidual superheat. Despite the better performance of the interlaced evaporator with compensation, it does not perform better than the face split evaporator without compensation at $F_{air} > 0.65$. The face split evaporator with compensation performs the best at all values of F_{air}. Interestingly, the difference in COP between the two evaporators with compensation is increasing slightly as F_{air} decreases.

If we normalize the results from figure 5.13a and 5.13c with the current evaporator used today, i.e. the interlaced without individual superheat control, we see the actual increase in performance when applying the compensation method to each systems as function of F_{air}, see figure 5.13b and 5.13d. For the face split with compensation, this increase in UA-value stays around 7% as F_{air} decreases, however, the interlaced with compensation shows a decrease from 4.9% to 1.5% increase. The COP increases from 1.6% to 2.4% increase for the face split evaporator with compensation as F_{air} decreases, however, the interlaced evaporator with compensation shows a decrease from 1.0% to 0.3% increase.

5.5 Combination of flow maldistribution and compensation

Similarly to chapter 4, we also need to address the combined effects of flow maldistribution in order to fully evaluate the benefits of using the compensation method, and the fact that the flow maldistribution sources may act together or compensate each other. In the following, the results of the combined flow maldistribution will be compared to the compensation method. Furthermore, the comparison are also made at different evaporator size.

The combined maldistribution is studied by varying both F_{air} and F_x simultaneously. Figure 5.14a-d shows the overall UA-value and COP of the 8.8 kW system with and without compensation.

Similarly to the chapter 4 the individual maldistribution sources may act together or cancel out each other. For the face split evaporator (figure 5.14b and 5.14d) the sources act together when $F_x < 1$ and $F_{air} < 1$. In contrast, the sources compensate each other when $F_x > 1$ and $F_{air} < 1$. The maximum of the individual source compensation (dashed lines) becomes equal to the compensation results, where each individual channel superheats are controlled. The face split results are fairly similar to the results of the two straight channel simplification from section 4.6, since the airflow across each refrigerant channel is independent, in contrast to the interlaced channels.

The interlaced evaporator shows quite different characteristics (figure 5.14a and 5.14c). Most of the curves do not cross each other. From 5.14c it seems that the COP curves coincide with the compensated results when F_x equals 1.1 to 1.3, and interestingly independent of F_{air}. It shows that the interlaced are more stable to airflow maldistribution. It is also to some extent stable towards

Figure 5.14: Combined maldistribution of inlet liquid/vapor and airflow using the 8.8 kW evaporator; interlaced (a,c,e) and face split (b,d,f).

inlet liquid/vapor maldistribution, i.e. the curves do not decrease as much as for the face split evaporator. This may better be observed in figure 5.14e and 5.14f, which shows the corresponding surface plots of the COP. The interlaced UA-curves for F_x equals 1.2 to 1.3 are actually higher than the compensated case, but however not really observable in the COP.

Interesting conclusions may be drawn from these figures. For example if we assume an airflow distribution of $F_{\text{air}} = 0.5$ and phase distribution of $F_x = 0.8$, the COP of the interlaced and face split evaporator becomes 3.43 and 3.34, respectively. However, a similar case where $F_{\text{air}} = 0.5$ and $F_x = 1.2$ gives 3.54 and 3.58, respectively. It is essentially similar degrees of flow maldistribution, however, the difference is significant and the COP increases by 3.2% and 7.0%. The most important conclusion here is that the case $F_{\text{air}} = 0.5$ and $F_x = 1.2$ corresponds to the compensated case for both circuitries. It means that the compensation may show an increase of 3.2% and 7.0% for the interlaced and face split evaporator, respectively, but at similar degrees of flow maldistribution, it may show 0% improvement. It will depend on the actual flow maldistribution conditions.

5.5.1   Different evaporator size

As mentioned in chapter 4, a common way to increase the COP is to increase the area of the evaporator. It may therefore be viewed as a method of compensation of flow maldistribution also, despite that the larger evaporator will also be subject to flow maldistribution conditions. We are especially interested in the trade-offs between the use of the compensation method and the use of the larger evaporator.

In this section we show the compensation of airflow maldistribution for the same system, but having the larger evaporator (10.5 kW). It is the same evaporator size as the one used for verification and validation. Note that the mean frontal air velocity across the coil is kept constant at 1.16 m s^{-1} for both evaporators, which corresponds to the ratings of 8.8 kW evaporator, in order to decouple any velocity difference effects between the two evaporators.

Figure 5.15 shows the results of combined flow maldistribution with and without compensation for the 10.5 kW interlaced and face split evaporators. The figure (a-d) also shows the 8.8 kW evaporator results with compensation by control of individual channel superheat.

The increase in UA-value and COP are significant when upgrading the evaporator for both the interlaced and face split evaporators. Otherwise, the combined flow maldistribution case for the 10.5 kW evaporators shows similar trends and degradations as for the 8.8 kW evaporators. This is in accordance with the generic study in chapter 4, were the percent degradations for the 8.8 and 10.5 kW evaporators were almost the same.

If we compare the results to the 8.8 kW evaporators with compensation of flow maldistribution from section 5.5 (the thick dashed curve), it shows that the compensation method cannot compete with the larger evaporator using the interlaced circuitry. In fact, it is only at $F_x < 0.75$ independently of F_{air}, where the compensation method used with the 8.8 kW evaporator, performs better than the 10.5 kW evaporator for the interlaced circuitry (figure 5.15a and 5.15c).
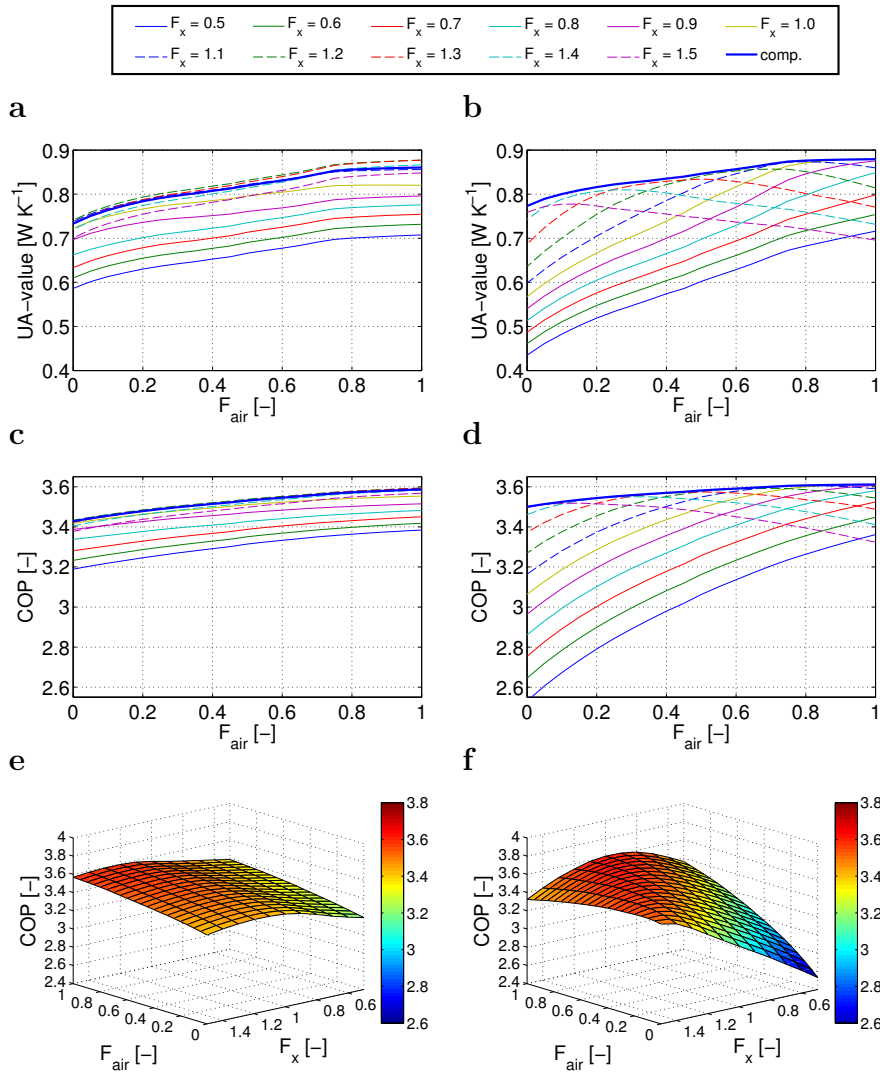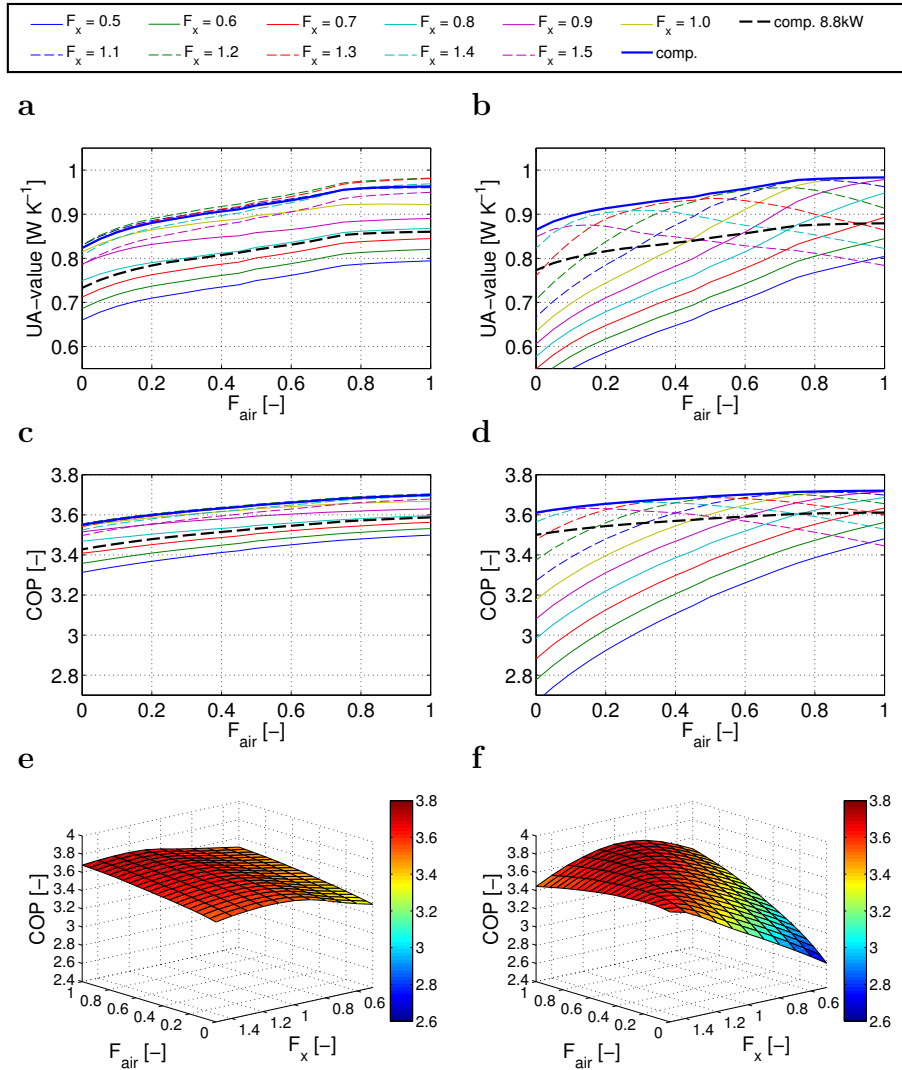
Figure 5.15: Combined maldistribution of inlet liquid/vapor and airflow using the 10.5 kW evaporator; interlaced (a,c,e) and face split (b,d,f).

For the face split evaporator circuitry the results are different and look more like the results of the generic study performed in chapter 4. Essentially, if there is no particular flow maldistribution, then it is always better to use the larger evaporator. However, if the face split evaporator are in flow maldistribution conditions, then the compensation by control of individual channel superheat

is superior. Many trade-off maldistribution conditions may be defined by the intersections of the 8.8 kW curve with compensation. For these trade-offs the cost of the compensation method must be less than the costs of the larger evaporator. The span at which the larger face split evaporator performs better than the smaller face split evaporator with compensation is however small in COP.

For these reasons, it seems that only the face split 8.8 kW evaporator with compensation may compete with the 10.5 kW evaporators without compensation.

5.6 CFD predicted airflow

This section serves to bring more insight about the airflow profile across the evaporator coils. The airflow profile across an evaporator A-coil is never uniform. There will always be some degree of airflow maldistribution. In this section, the airflow profile across an A-coil is predicted by computational fluid dynamics (CFD) simulations using the commercial CFD code STAR-CD 3.26 (2005). The airflow profile is then applied to the Modelica model of the 8.8 kW RAC unit used in previous sections. The CFD prediction will give valuable information about the degree of airflow maldistribution, however, it must be kept in mind that numerical tools need experimental validation or verification in order to be fully reliable.

The section goes through the setup in STAR-CD, extraction of perpendicular coil velocity, convergence and application of the velocity profile to the interlaced and face split circuitries with and without compensation.

5.6.1 CFD setup and results

We have simplified the air duct flow to be two-dimensional, however, in reality fluid flow is always three-dimensional. It is essentially a matter of how much the third dimension matters. For example, near the duct walls or in between the fins, there will be three-dimensional effects. It is believed that the main flow is governed by a two-dimensional flow, which simplifies the problem of interest significantly. This is the same simplification as other investigators have done (AbdelAziz et al., 2008; Yashar et al., 2008; Yashar and Domanski, 2010), who used CFD or PIV measurements to obtain the airflow profile. Furthermore, we do not address the presence of the fins, which will create larger pressure drop across the coil.

The computational domain is constructed as shown on figure 5.16, which also shows the boundary conditions and grids. For the outlet boundary we chose both the outlet and the pressure boundary condition in STAR-CD, but it did not have any influence on the velocity profile through the coil (results using outlet boundary is shown here).
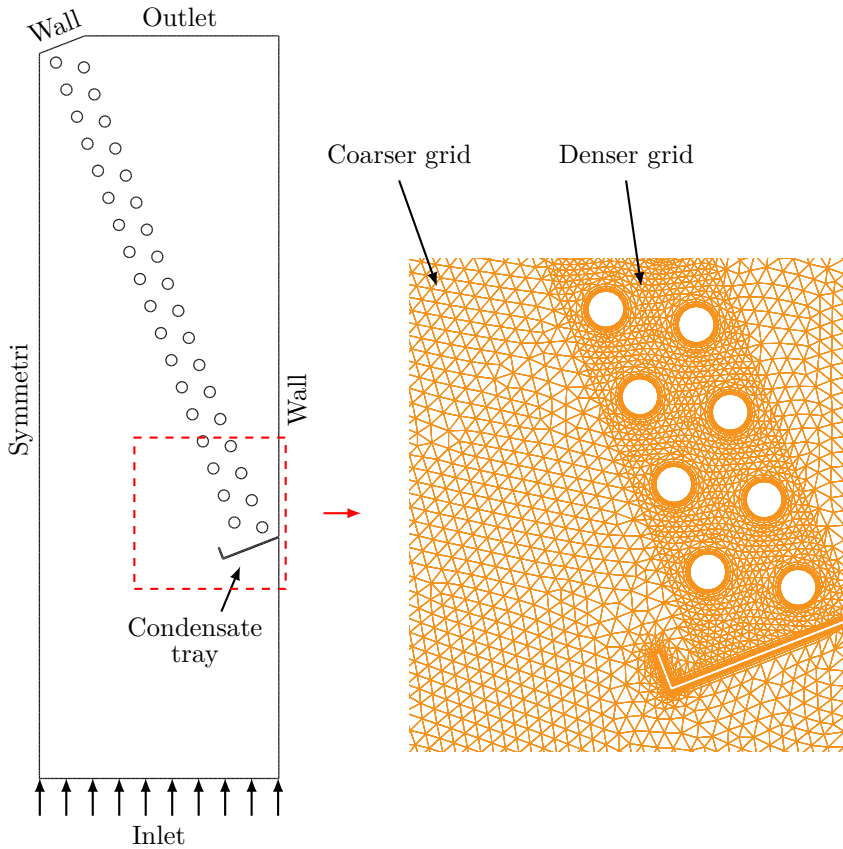
Figure 5.16: Computational domain, boundary conditions and grids (tetrahedra mesh type); coarse grid = 4mm, dense grid = 2mm.

The alignment of the coil is in upwards flow direction with a condensate tray for dehumidifying conditions. Symmetric flow is assumed for both coils, i.e. each half of the air duct is symmetric. Furthermore, the inlet air velocity is assumed to be uniform and computed to be 2.6 m s^{-1} by conservation of mass, where the mean frontal velocity is 1.16 m s^{-1} across the coil. The air properties are evaluated at 25°C. The Reynolds number based on tube diameter becomes 1600 and 700 based on inlet velocity and mean frontal velocity, respectively.

The low Reynolds number k-ϵ turbulence model ($y^+ \sim 1$) is used. The turbulence intensity and turbulent length scale at the inlet is specified to 10% and $D/2$, respectively. For discretization, the central difference scheme (CDS) is used for the momentum equations and the upwind difference scheme (UDS) is used for the k-ϵ equations.

The tetrahedra mesh type is chosen for the computational domain. A denser grid (2mm) is used near the coil and a coarser grid (4mm) is used in the surroundings of the coil. Furthermore, a subsurface is created very close to all the walls with 4 layers. It essentially means a splitting of the cells closest to the walls by 4 layers. The number of cells for the computational domain is 30000. Finally, the residual tolerance is chosen to be 10^{-3}.

The results of the CFD simulations are shown in figure 5.17. The y^+ value became no higher than 7 near the walls and a solution to the problem was found in steady state. Note that other turbulence models claims to be better near the wall, but may cause the solution to become unsteady.

Figure 5.17a-b show that there is a recirculation zone in the bottom of the coil. The observation is similar to the findings of AbdelAziz et al. (2008); Yashar et al. (2008), however, no recirculation zone was found in Yashar and Domanski (2010). The recirculation zone results in very low air velocities in this region and consequently low heat transfer. The reason for the recirculation zone is essentially the condensate tray, which also causes the air to be increased upstream (to the left). Despite the recirculation zone in the bottom, the air seems to flow quite uniformly across the coil or slowly increasing towards the top linearly. Figure 5.17c shows the top of the coil and reveals that the air travels right by the tubes near the top. However, the air in the middle of the coil (bottom of figure 5.17c) seems to flow right into each tube through the coil, which should increase heat transfer.

Figure 5.17d shows the relative pressure distribution. It shows that there is a small pressure drop through the coil. If fins were present this pressure drop would be increased and may alter the airflow distribution across the coil. Figure 5.17e shows the turbulent kinetic energy distribution. It shows that the turbulence kinetic energy is highest in the coil and in front of the condensate tray.

5.6.2   Perpendicular velocity profile

From the previous CFD results, the perpendicular velocities in the front and back of the coil are extracted, as shown on figure 5.18a.

The velocity profile shows the presence of the tubes by variations in the profile along the coil. The variations are larger in the back of the coil. Figure 5.18a also shows the tube average velocities that are needed as boundary condition to the Modelica model. The Modelica model handles only one velocity profile through the coil, thus the mean of the front and back profile is computed as shown in figure 5.18b. Furthermore, the negative part of the velocity profile cannot be handled by the implemented Modelica model. The negative part is caused by the recirculation zone and it is corrected by ensuring mass conservation, as illustrated on figure 5.18b. The corrected mean velocity profile is then used as boundary condition to the implemented Modelica model.

We also performed a test of the convergence of the mean air profile though the
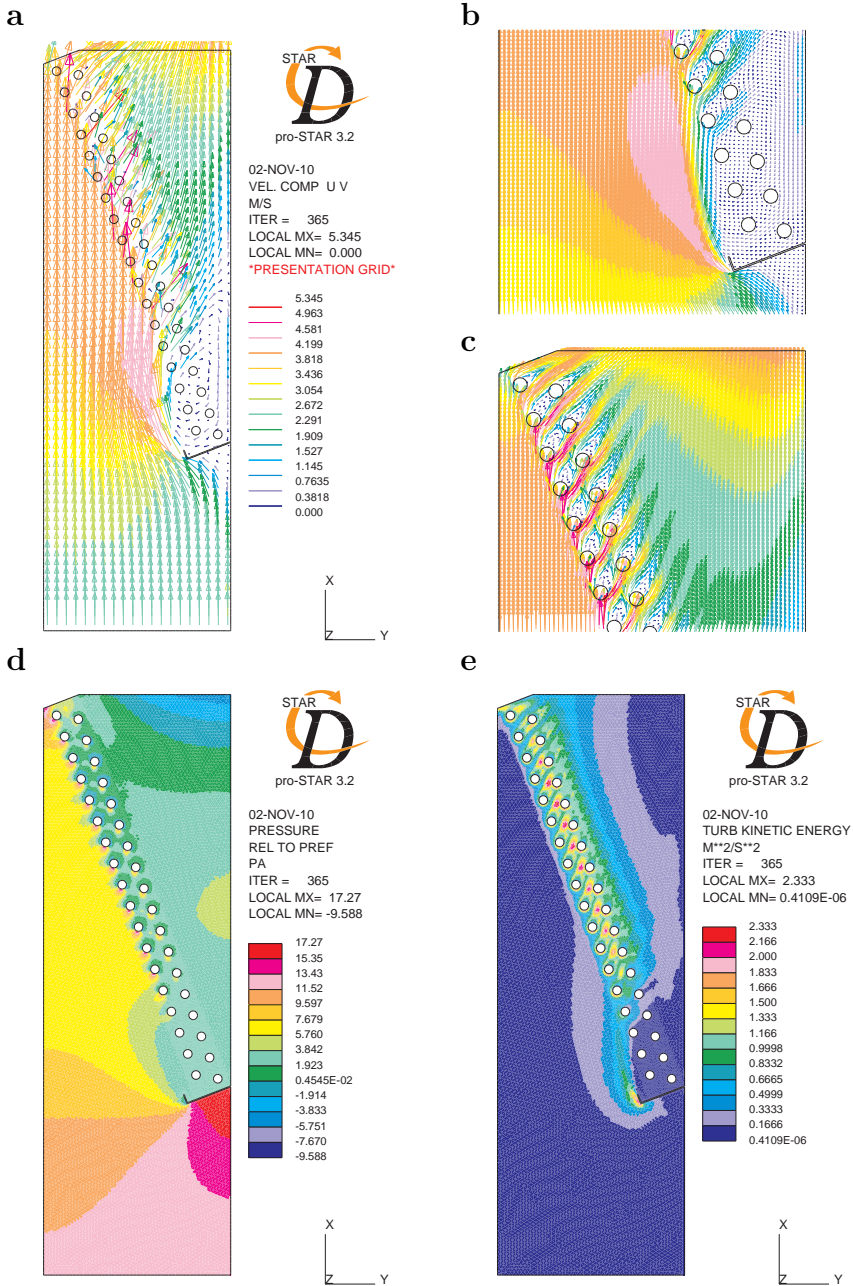
Figure 5.17: Selected CFD results; velocity distribution (a,b,c), relative pressure distribution (d) and turbulent kinetic energy distribution (e).

a

b

c
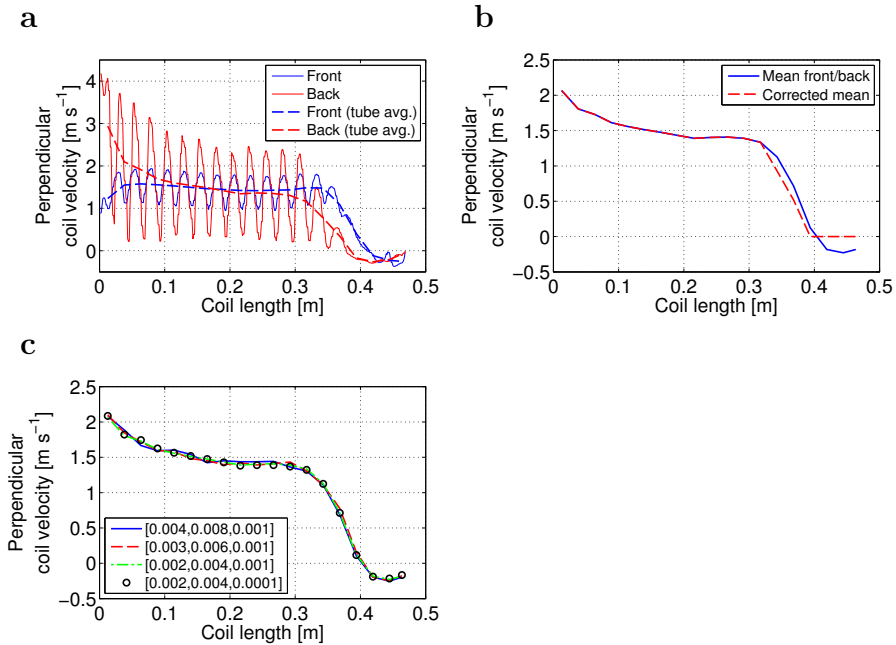
Figure 5.18: Perpendicular velocity profile in front and back of coil (a), correction of mean profile (b) and convergence of mean profile (c) [dense grid size, coarse grid size, max. res. tol.].

coil by changing the grid and residual tolerance as shown in 5.18c. It shows that the velocity profile is converged.

5.6.3 Results using CFD predicted air profile

The refrigerant temperature contours through the center of the coils are shown in figure 5.19 for the interlaced and face split evaporator with and without compensation (EXV and comp).

It shows that the interlaced circuitry compensates the airflow non-uniformity by design better than the face split circuitry. It is observed by the increased superheated area in the upper coil of the face split evaporator (EXV), which is not present in the interlaced coil (EXV). If we use the compensation by control of individual channel superheats, then there is not much change in the results of the interlaced evaporator. However, the non-uniform superheated areas in the face split evaporator are eliminated. Table 5.4 shows the results of the overall UA-value and COP. The table also shows the percentage increase or decrease compared to the interlaced evaporator without compensation (EXV).
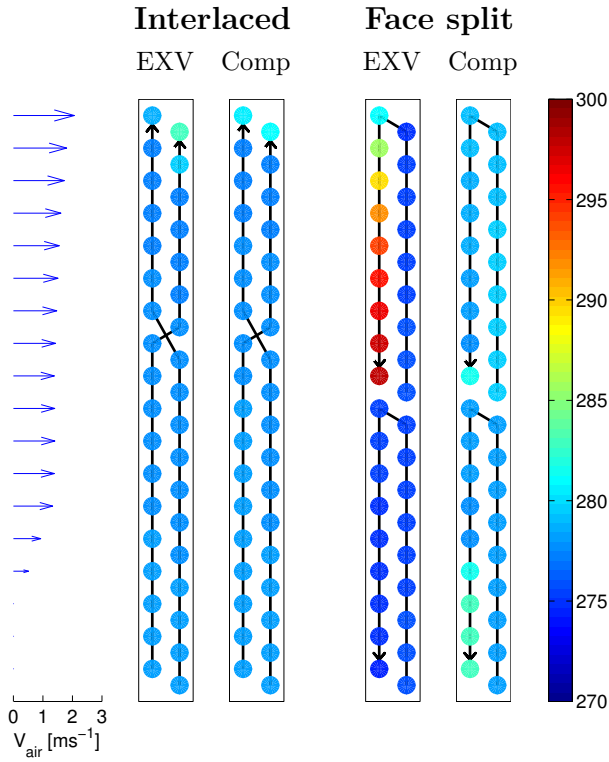
Figure 5.19: Refrigerant temperature contours through center of coils.

Table 5.4: Comparison of overall UA and COP using CFD air profile with or without compensation.

	UA	COP	UA %-change	COP %-change
Face split (compensated)	756.1	3.512	5.7%	1.3%
Interlaced (compensated)	728.1	3.477	1.8%	0.3%
Interlaced (EXV)	715.1	3.466	0%	0%
Face split (EXV)	607.2	3.257	-15%	-6%

The conclusions are similar to previous sections, where a linear velocity profile is applied. The face split evaporator performs better than the interlaced circuitry with compensation, since the superheated area with lower heat transfer is aligned in the first row of the face split and thus has a higher temperature difference (heat transfer potential). The use of compensation on the interlaced circuitry will give increased UA-value and COP, but not as much as for

the face split circuitry. The face split circuitry without compensation suffers significantly from the airflow maldistribution.

When comparing the UA-values to figure 5.13b, i.e. with -15% without compensation and +6% with compensation for the face split evaporator, the corresponding linear velocity profile is roughly around $0.15 \leq F_{\mathrm{air}} \leq 0.20$.

5.7 Discussion and summary

In this chapter we presented a numerical study of flow maldistribution in the standard interlaced and face split evaporators with and without compensation by control of individual channel superheats. The main difference compared to chapter 4 is that the actual evaporator circuitry is addressed and not only simplified to be two straight tubes.

Moreover, the chapter provides graphical guidelines of the effect of flow maldistribution and compensation considering the tube circuiting that may be used by the readers by making a qualitative guess on the degree of flow maldistribution (i.e. the distribution parameters F_x and F_{air}) considering the flow arrangement.

It may however be difficult to estimate the velocity profile for a given type of A-coil, since it depends on many factors such as apex angle, mounting brackets, condensate pans, upstream and downstream flow obstructions, bends or blower locations in the duct system. All these effects must be weighted when qualitatively guessing the airflow parameter by the reader. The velocity profile is never fully linear as shown by the CFD simulations in section 5.6. Furthermore, the CFD simulations assumed uniform upstream airflow, which may not be the case at installation of these systems.

Similarly to chapter 4, the compensation benefits that are shown in this chapter are at similar flow maldistribution in each coil. However, there could also be coil to coil flow maldistribution. Furthermore, there could be other causes of maldistribution for example fouling. These issues may contribute to the total degradation and compensation potential of flow maldistribution.

Furthermore, an increase in the number of tube rows in larger coils is expected to contribute to the performance difference between the face split evaporator with compensation and the interlaced evaporator without compensation (mostly used today). This is because of the superheated zones in the third and/or fourth tube rows, which are inefficient for the interlaced evaporator. By definition all the superheated zones are located in the first tube row for the face split evaporator.

The conclusions of the chapter are summarized in the following summary and may be viewed by the readers as rules of thumb.

Summary

Firstly, we verified the circuitry modeling and the accompanied U-bend pressure drop computation with commercial software code Coil-Designer (Jiang et al., 2006). Secondly, we validated the model in steady-state to some extend with experiments carried out at Danfoss. To some extend means that the degree of flow maldistribution needed to be guessed in the model, thus the flow maldistribution was not measured or eliminated in the experiments.

Thirdly, the individual maldistribution sources that has shown significance were investigated, i.e. non-uniform inlet liquid/vapor distribution and non-uniform airflow. Using the current definitions of the distribution parameters (F_x and F_{air}) the main conclusions were:

- At uniform flow conditions, it is always better to place the superheated regions with low UA-value in the first row of the coils, where the temperature driving potential is highest. This is done in the face split evaporator.

- At non-uniform flow conditions, the interlaced evaporator becomes better than the face split evaporator, since the interlaced to some extend compensates the flow maldistribution by design (circuitry).

- However, already at small degrees of inlet liquid/vapor maldistribution in the interlaced evaporator, the superheated region in the second row shows no heat transfer. The superheat may even be cooled by the colder air coming from row one at worse degrees of inlet liquid/vapor maldistribution.

- The trade-off between the interlaced and face split evaporator was found to be at $F_x = F_{air} = 0.5$. Since the interlaced evaporator are used mostly today, it seems that there are significant degrees of flow maldistribution in these evaporators.

Fourthly, the benefits of compensation of flow maldistribution by control of individual channel superheats were considered. In addition, the combined effects of maldistribution sources were investigated at different evaporator size. The main conclusions were:

- At compensation the face split evaporator shows the best performance.

- The interlaced evaporator also shows a performance increase at compensation, however, not as high.

- Compared to the interlaced evaporator without compensation, the increase by using the face split evaporator with compensation is 7% in overall UA-value and 1.6% to 2.4% in COP.

- At combined flow maldistribution, the interlaced evaporator shows much better stability towards flow maldistribution than the face split evaporator.

- Two similar combined maldistribution cases may show significant or no compensation potential at all, i.e. ($F_{air} = 0.5$ and $F_x = 0.8$) and ($F_{air} = 0.5$ and $F_x = 1.2$).

- The span in terms of combined flow maldistribution conditions at which the larger evaporator (10.5 kW) are better than the smaller evaporator (8.8 kW) with compensation is small for the face split evaporator circuitry.

- For the interlaced evaporator circuitry the compensation method seems to be unable to compete with the larger evaporator. This is because the interlaced evaporator already by design compensates the flow maldistribution to some extend.

Fifthly, we predicted the air velocity profile using computational fluid dynamics (CFD) and applied it as boundary condition to our model. The main conclusions were:

- The airflow through the coil shows a recirculation zone with low heat transfer in the bottom of the coil, which is caused by the condensate tray for dehumidifying conditions.

- Otherwise, the perpendicular velocity profile through the coil seems to be slightly increasing linearly towards the top.

- Again the face split evaporator with compensation shows the best performance when applying the CFD predicted air velocity profile. Again, the interlaced evaporator shows minor performance increase with compensation.

- The results in overall UA-value by using the CFD predicted velocity profile show that the corresponding airflow distribution parameter is around $0.15 \leq F_{\mathrm{air}} \leq 0.20$.

CHAPTER 6

Liquid injection principle

The previous chapters employed perfect control of individual channel superheats as the method of compensation by distributing individual channel mass flows continuously. In this chapter a working principle for individual distribution is analyzed, which is based upon the recent product development (EcoFlow$^{\text{TM}}$) at Danfoss (Funder-Kristensen et al., 2009; Mader and Thybo, 2010). The method is discontinuous liquid injection into each individual channels during a specified cycle time. Moreover, the influence of the cycle time will be investigated together with an optional secondary flow into the other channels with regards to cooling capacity, overall UA-value and COP.

6.1 Introduction

Perfect control of individual channel superheats means that a thermostatic or electronic expansion valve is located on each channels and thus controls each superheat to be the same. It is not beneficial for economic reasons to install an expansion valve for each channel. Therefore, the discontinuous liquid injection is considered in this chapter as a promising method for controlling individual channel superheat.

The reason why the numerical study is performed is to gain more understanding and insight in the liquid injection principle and its implications for evaporator and system performance in terms of overall UA-value, cooling capacity and COP. Especially, we strive to optimize the discontinuous liquid injection prin-

ciple by studying the effects of different specifications and provide guidelines for optimal energy efficiency. The injection principle is essentially two-phase flow pulsations and the study may show the potential of increasing capacity and COP by employing pulsations to the flow.

The modeling of the liquid injection dynamics showed spurious fluctuations in pressure, which have not been observed as high in any similar experiments carried out at Danfoss. The current analysis should therefore be seen as a first study of the injection dynamics with the current model approach and limitations.

When simulating the injection dynamics, we must keep in mind that the correlations for heat transfer, friction and void may become invalid at large transients in mass flow, since they are developed from steady state experiments. Furthermore, the discontinuous refrigerant injection is essentially pulsating two-phase flow, and the significance of the liquid/vapor interfacial dynamics may become important such as interfacial friction and drag and/or thermodynamic non-equilibrium effects, which is not included in the current mixture model.

6.1.1 Liquid injection principle

As mentioned above the method of compensation used in this chapter is based on the working principle of the recently developed Danfoss product (EcoFlow$^{\text{TM}}$). Before we may define the objectives of analyzing the working principle, basic knowledge is needed about how the EcoFlow valve works.

Actually, the EcoFlow valve does not measure the individual channel superheats but only the overall superheat. Furthermore, it does not provide continuous refrigerant flow in each channel, but rather discontinuous individual channel injection (modulation of each channel flow) with optional secondary flow to the other channels. The optimal distribution of mass flow rate (or individual refrigerant injection) is then found from a distribution analysis performed at specific time intervals during operation, see Mader and Thybo (2010). The distribution analysis is essentially carried out by control algorithms, where the importance of each individual channel on the overall superheat is measured in order to find the optimal distribution. The individual channel superheats become the same at the optimal mass flow distribution.

Figure 6.1 and 6.2 shows the EcoFlow valve, the superheat sensor and the main components of the EcoFlow valve.

The individual injection is performed by the stepper motor, which rotates the distributor disc, see figure 6.3a. The EcoFlow valve comes in two different designs, i.e. a multi-orifice (MO) design (main orifice + secondary orifices) and a single-orifice (SO) design (main orifice only), see figure 6.3b and 6.3c. The orifice size of the SO design is larger, since more refrigerant needs to pass through the main orifice. The SO design enables the possibility of individual channel defrost during cooling operation (no defrost periods) for the face split evaporator only. As we shall see in later sections, the results show that the
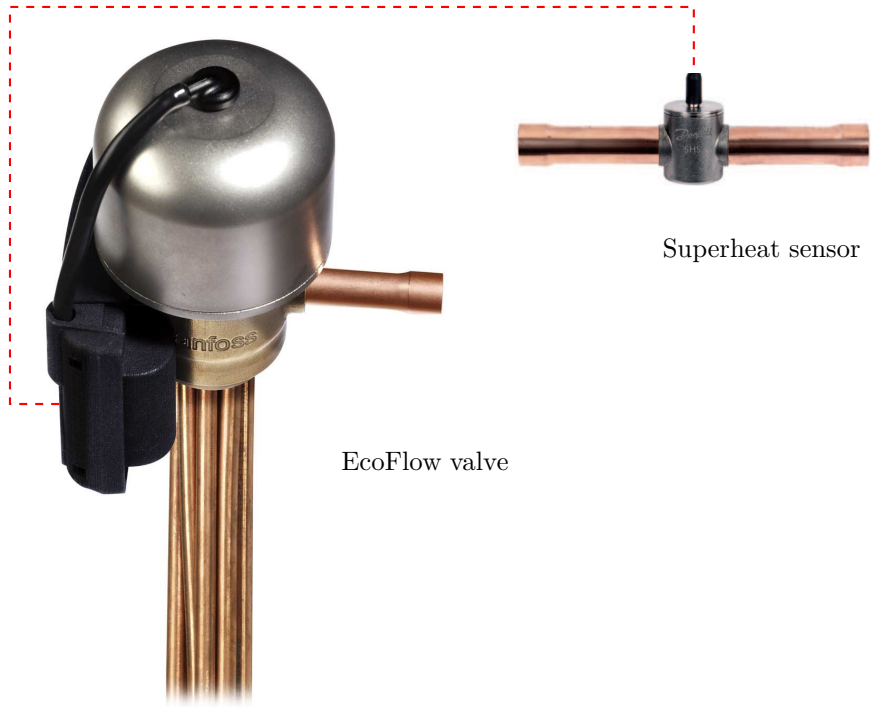
Figure 6.1: EcoFlow valve and superheat sensor

performance in steady state without considering frost build-up becomes a bit smaller when using the SO concept. Furthermore, all orifices of both designs are closed in between each channel injection.

The distribution details are explained in greater detail in section 6.3.

6.1.2   Objectives and contents in this chapter

The first objective is to evaluate the effect of the cycle time for the MO and SO design concepts, i.e. the time it takes for one revolution. The second objective is to evaluate the size of the secondary orifices in the MO design compared to the main orifice. These objectives will be addressed at uniform flow conditions for simplicity, i.e. no maldistribution. The third objective is then to compare at flow maldistribution the refrigerant injection modeling results with the perfect control of each channel superheat from chapter 5.

The questions that are sought to be answered are:
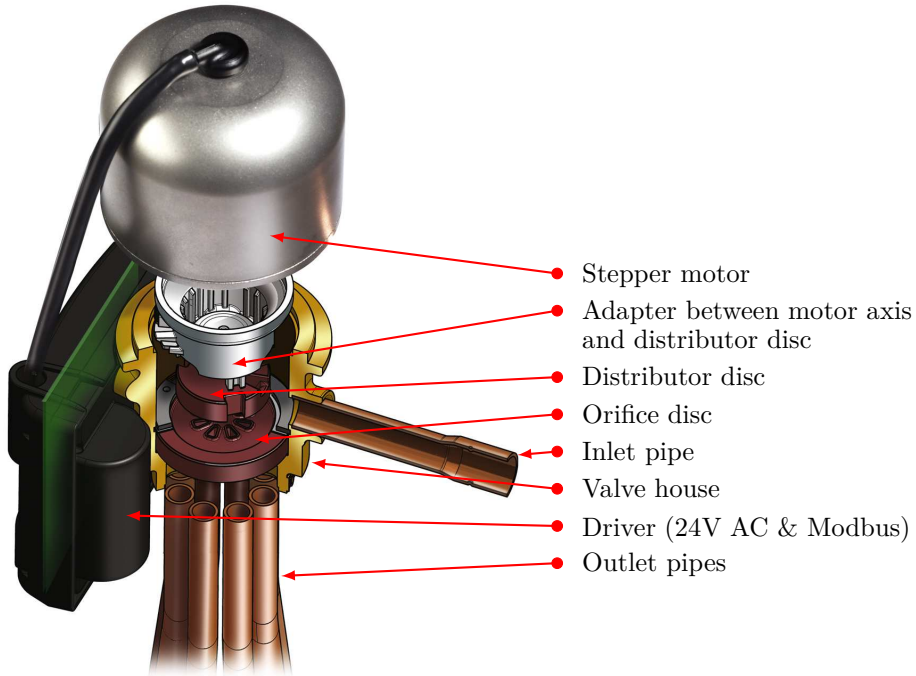
Figure 6.2: Main components of the EcoFlow valve

- What is the minimum cycle time for discontinuous liquid injection? Too large cycle times will cause too much dry-out of the channels.

- Does capacity decrease or increase by the discontinuous liquid injection (pulsating flow)?

- How much refrigerant should pass through the main and secondary orifices in the MO design?

Note that the results in this chapter is focussed on the steady state performance in terms of overall UA-value, cooling capacity and COP, where the dynamics of the refrigerant injection is modeled.

The chapter starts by a validation of the main evaporator dynamics with experiments carried out by Antonius (1998) on a simple coaxial evaporator with ethanol as the cooled fluid and R22 as the refrigerant. The results of this validation is also discussed in Kærn et al. (2011d). Then the chapter covers the additional modeling work and use of experimental results for evaluating orifice flow coefficients for the actual MO and SO designs. Then the pressure
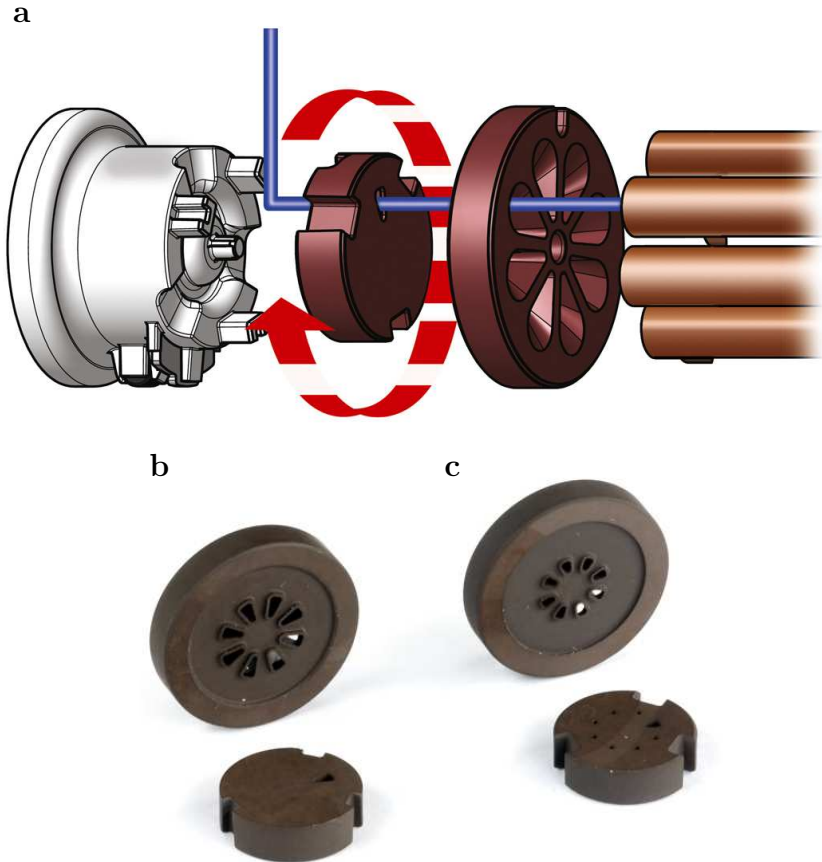
Figure 6.3: EcoFlow distribution method and refrigerant flow through discs (a), single-orifice (SO) discs (b) and multi-orifice (MO) discs (c).

fluctuations caused by the refrigerant injection modeling is considered and an accompanied sensitivity analysis of these fluctuations is performed. The sensitivity analysis should give more detail to the causes of the fluctuations, however, they could not be eliminated satisfactorily compared to experiments by varying sensitive variables such as two-phase heat transfer, friction and void or increased manifold volume.

Finally, the effect of the cycle time and flow ratio between main and secondary orifices of the MO concept are investigated. Furthermore, the performance of the liquid injection principle is evaluated at airflow maldistribution and compared to the perfect control method in chapter 5.

6.2   Validation of the evaporator dynamics

In this section the main dynamics of the evaporator model is validated. It is
not the actual injection principle that is being validated. This would require
an extensive experimental effort. Moreover, the dynamic evaporator response
upon a step change in volume outflow is validated and not the on/off operation
of an electronic expansion valve or the individual liquid injection. The valida-
tion serves to give credibility and insight to the numerical model with regards
to the dynamic modeling and especially the choice of void fraction correlation.
A chosen set of void fraction correlations (slip flow) and the assumption of
homogeneous flow will be compared to experiments carried out on a simple
coaxial type evaporator by Antonius (1998), see figure 6.4. A brief description
of the experiments, the boundary conditions and the test rig is given, before
the results of the dynamic evaporator response validation are shown.

6.2.1   Homogeneous or slip flow modeling?

The key variable for the dynamic evaporator response is the void fraction,
which essentially determines the refrigerant charge in the evaporator. The void
fraction may be computed by assuming no slip (homogeneous flow model), i.e.
use of equation A.4 with slip ratio $S = 1$. The void fraction may also be
computed by use of correlations from the literature (slip flow model). The
question in mind is: When is it sufficient to use the homogeneous flow model,
in contrast to the slip flow models?
Many void fraction correlations exist in the literature. Some are rather sim-
ple analytical relations, others are quite sophisticated and of empirical nature.
Woldesemayat and Ghajar (2007) compared 68 void fraction correlations in
order to find an acceptable void fraction correlation that could predict most of
the collected experimental data for all inclination angles, fluids and flow pat-
terns. They developed a modified version of the Dix (1971) model, however,
the model does not ensure a smooth transition at the two-phase to vapor phase
transition. For dynamic simulation the transition and its derivatives should
be continuous or at least be made smooth. Furthermore, the correlation com-
plexity should be sought to a minimum while capturing the main dynamics of
interest.
Woldesemayat and Ghajar (2007) also gave void fraction correlation recom-
mendations, considering each specific type of flow. For horizontal flow, as is
the case of consideration in the validation and throughout this thesis, the void
fraction of Premoli et al. (1971) was worth the general recommendation among
others, regardless of flow regime and fluids. Recently, the same void fraction
model was recommended by Maa et al. (2009) and Mader et al. (2010) as the
best choice for R410A air-conditioners. The model also ensures a smooth tran-
sition at the two-phase to vapor-phase transition, and for these reasons the
Premoli et al. (1971) model is used for the current validation.

Wojtan et al. (2005c) recommends Steiners version of the Rouhani and Axelsson void fraction model (Steiner, 1993), and uses this model in their general flow map (Wojtan et al., 2005a) for predicting both two-phase heat transfer and pressure drop in a flow regime dependant way. The earlier versions of the Rouhani and Axelsson model did not ensure a smooth transition from two-phase to vapor phase, however, Steiner modified the model for horizontal flow in a way that ensures a smooth transition. The Steiner version of the Rouhani and Axelsson model is also included in this study.

The two aforementioned void fraction correlations are both sophisticated models and functions of pressure, p, vapor quality, x, mixture mass flux, G, surface tension, σ, and acceleration of gravity, g. Simpler models exist that are only dependent on pressure and vapor quality, e.g. the Zivi (1964) model, which is one of the simplest void fraction models. The inclusion of the Zivi (1964) model fulfills our set of slip flow models to be investigated for validation.

6.2.2 Experimental data

The experimental data are obtained from the master thesis of Antonius (1998), who compared the experimental results with commercial software Sinda/Fluint (2008). The thesis is written in Danish, however, the main results are given in English in Jakobsen et al. (1999). Sinda/Fluint is a general thermo-fluid network analyzer capable of simulating static and dynamic behavior of multiphase fluid networks as they interact with thermal structures, using a lumped parameter finite-difference approach. It is quite similar to the numerical model introduced in chapter 2. However, the empirical correlations for heat transfer, friction and void fraction are restricted to predefined possibilities, and tube circuitry may not be modeled.

The test case geometry and boundary conditions were kept as simple as possible in order to focus on the two-phase flow. Figure 6.4 shows a sketch of the test case coaxial evaporator and corresponding boundary conditions for the numerical simulations. The outer tube wall is insulated to minimize heat flow from the surroundings. R22 is the refrigerant flowing in the inner tube, whereas ethanol with 10% water by mass is flowing in countercurrent direction in the outer tube shell.

Both a step in refrigerant mass inflow and volume outflow was considered in the work by Antonius (1998). Unfortunately, the original data no longer exist,

Figure 6.4: Sketch of test case evaporator

however, the boundary conditions as function of time, as indicated on figure 6.4, was curve fitted in the work to be used as input to Sinda/Fluint. Only one set of these curve fits is available in the thesis, whereas the rest are missing. For these reasons it is only possible to reproduce the evaporator response on a step change in volume outflow. The dynamics of the mass outflow and outlet pressure is then compared to the homogeneous model and slip flow models. The mass inflow, mass outflow and outlet pressure are obtained from figures in Antonius (1998) by graphical means for the comparison.

6.2.3 The test rig

A schematic of the test rig is shown in figure 6.5. The test case coaxial evaporator is 7 m long and made of cobber. The inner tube has an internal and outer diameter of 11.1 and 12.7 mm, respectively, and the outer tube outer diameter is 20.18 mm.

The following data are used to obtain the appropriate boundary conditions as
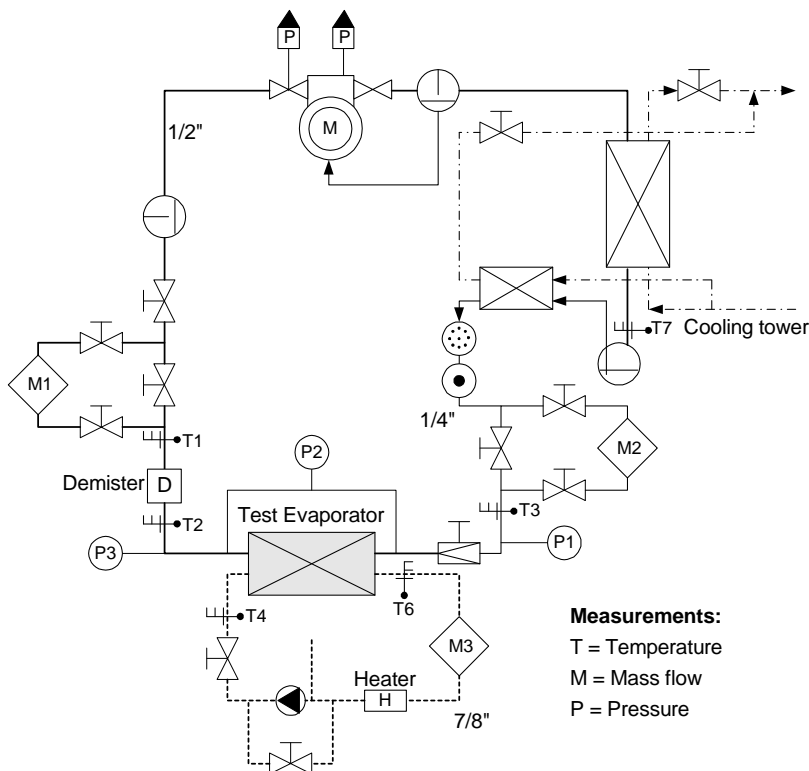
Figure 6.5: Evaporator test rig

shown in figure 6.4. At the inlet of the evaporator, the mass flow is measured directly by M2, the mixed-cup enthalpy h is found using the subcooled liquid temperature T3 and pressure P1. The volume flow at the outlet of the evaporator is found using the mass flow M1 and the density of the superheated vapor at temperature T1 and pressure P3. The mass flow M3 and temperature T4 are directly applicable as boundary conditions for the brine system.

A thorough documentation of the test rig (e.g. apparatus, calibration and data acquisition method) can be found in Antonius (1998).

6.2.4 Model setup

The numerical model is constructed similarly to figure 3.9 with liquid (ethanol) as the cooled fluid instead of air. Furthermore, the cells are connected to form a counter flow evaporator as shown in figure 2.1. We chose to use 30 cells in our simulations for validation. The heat transfer of both the refrigerant and the liquid is computed by using the heat transfer coefficient and the mean temperature difference in each cells. The used correlations for heat transfer, friction and void are summarized in table 6.1 and given in appendix C.

Table 6.1: Overview of used correlations

Liquid brine	
Heat transfer	Dittus and Boelter (1930)
Single phase refrigerant	
Heat transfer	Gnielinski (1976)
Friction	Blasius (2002)
Two-phase refrigerant	
Heat transfer	Shah (1982)
Friction	Müller-Steinhagen and Heck (1986)
Void fraction	Zivi (1964)
	Premoli et al. (1971)
	Steiners version of Rouhani and Axelsson (1993)

Thermophysical properties for R22 are obtained from the Refeqns package (Skovrup, 2009). Thermophysical properties for ethanol with 10% water by mass are obtained from VDI Wärmeatlas (2002).

6.2.5 Validation and results

In this section, the numerical results are compared to the experimental data at a step decrease or increase in volume outflow. The cases correspond to a change in outflow by capacity control of the compressor. Firstly, we address the different void fraction correlations to be used for the current refrigerant.

Comparison of the void fraction models

Using equation A.4 with $S = 1$ is the homogeneous model, where each phase travels with the same velocity. If we use the slip ratio correlation by Zivi (1964) in equation A.4, i.e. $S = (\rho_g/\rho_f)^{-1/3}$, we get the Zivi void fraction model. The Premoli et al. (1971) model and the Steiners version of the Rouhani and Axelsson model Steiner (1993) depend on both flow and fluid properties in more complicated ways. The void fraction models are compared in figure 6.6 as functions of vapor quality.
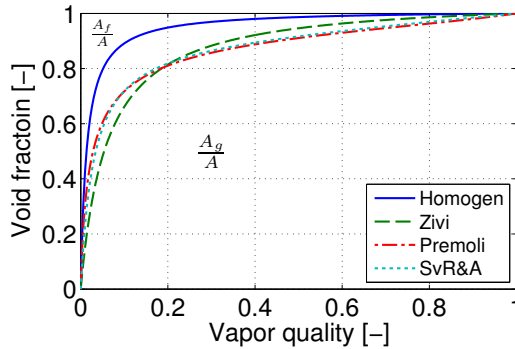
Figure 6.6: Comparison of the chosen void fraction models. (R22, $T_{\text{sat}} = -5.7°\text{C}$, $p = 4.12$ bar, $G = 124$ kg m^{-2}s^{-1})

It is clearly seen that the area of the liquid is smaller in the homogeneous model, which indicates a faster dynamic response compared to all the other models. The Premoli model and the Steiners version of the Rouhani and Axelsson model seems almost the same for the specific refrigerant and conditions. At low vapor qualities the Zivi model shows the largest amount of liquid, however, at vapor qualities above 0.2, which is often the case for dry-expansion systems, it shows less liquid than the Premoli model and the Steiners version of the Rouhani and Axelsson model, indicating a faster dynamic response, however, not as fast as the homogeneous model.

A step decrease in volume outflow

In figure 6.7, the response of the mass outflow and the outlet pressure are compared at a step decrease in volume outflow.
At time equals 5 seconds the step occurs. The step shows an undershoot in mass outflow in the experiment and the models. The models have a sharp edge at the peak of the undershoot, which originates from the curve fitted boundary condition for volume outflow. After the undershoot the mass outflow

a

b
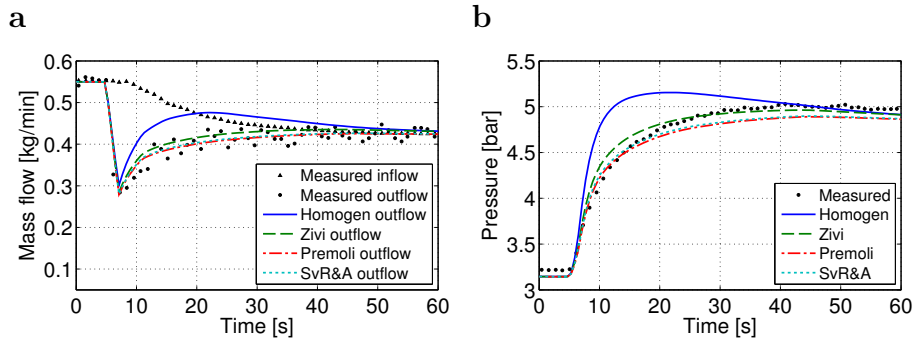
Figure 6.7: Mass outflow (a) and pressure outlet (b) response on decrease in volume outflow

increases and adjusts to a new steady state after approximately 40 seconds. Only the homogeneous model shows an overshoot during the transient response. Similarly, the pressure increases as the volume outflow decreases, however, only the homogeneous model shows an overshoot here.

A step increase in volume outflow

In figure 6.8, the response of the mass outflow and the outlet pressure are compared at a step increase in volume outflow.

a

b
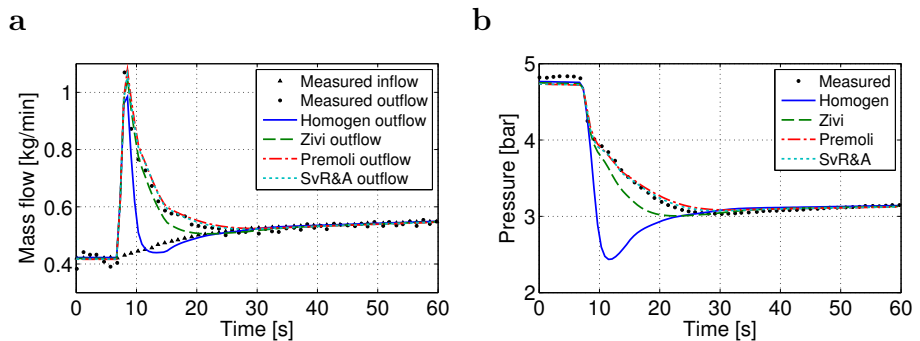
Figure 6.8: Mass outflow (a) and pressure outlet (b) response on increase in volume outflow

At time equals 7 seconds the increase in volume outflow occurs. The step shows a quite large overshoot in the mass outflow, however, it adjusts quicker to the new quasi-steady state after approximately 25 seconds. Again the homogeneous

model shows another undershoot after the overshoot. The pressure decreases on the step increase of volume outflow. Again the homogeneous model shows an undershoot in contrast to the other void fraction models.

Discussion

Apparently, the homogeneous model reacts too quickly. The response of the Premoli model and the Steiners version of the Rouhani and Axelsson model seem to predict almost the same and the most accurate responses from the evaporator. The Zivi model seem to be quite close to the experimental data, and can be considered as an easy way to capture the main dynamics of the evaporator, however, if the dynamics are more important, one should turn to the more sophisticated void fraction models.

Another observation is that the steady state values are not affected by the individual void fraction models. This is because the two-phase heat transfer and frictional pressure drop correlations are functions of vapor quality and not the choice of the void fraction correlation. Some more sophisticated two-phase heat transfer and frictional pressure drop correlations incorporate their own void fraction correlation in for example the heat transfer correlation of Wojtan et al. (2005b). One may inspect the equations A.36, A.37 and A.38 and find that almost only the dynamic terms are affected by the void fraction model. Other terms that are affected by the choice of void fraction model are the accelerational and gravitational pressure drop terms. For horizontal flow the gravitational pressure drop vanish, however, usually both these terms are approximately an order of magnitude less than the frictional pressure drop (Richter, 2008; Jiang, 2003). Furthermore, they do not influence the heat transfer and corresponding evaporation pressure.

The refrigerant charge in the evaporator (both two-phase and superheated area) are shown in table 6.2 at time equals 0 from figure 6.7 and 6.8, i.e. the two different steady states.

Table 6.2: Refrigerant charges in the evaporator

	Homogen [g]	Zivi [g]	Premoli [g]	SvR&A [g]
Steady state from figure 6.7 at time=0	10.7	16.8	24.0	22.6
Steady state from figure 6.8 at time=0	26.3	57.9	79.8	76.2

The two-phase area was approximately 35% of the evaporator at time=0 from figure 6.7, however, on figure 6.8 at time=0 the two-phase area was approximately 85% in the evaporator. This leads to the differences in the refrigerant charge predictions in table 6.2. When the volume flow goes down the pressure increases, both the overall UA-value and temperature difference between the refrigerant and the brine decreases, and it results in a smaller heat transfer and

larger two-phase area. In other words, the refrigerant will be sucked out of the evaporator as the volume outflow increases at no control of the superheat.

Using the Premoli model and the Steiners version of the Rouhani and Axelsson model, as the most accurate void fraction models, shows that the homogeneous model underpredicts the refrigerant charge by approximately 2-3 times. The Zivi model lies in between.

In conclusion, we may state that the main evaporator dynamics is captured by the slip flow models considered here, thus the main dynamics in the numerical model is validated. The actual slip flow model to be chosen must be considered for both numerical and accuracy reasons, which unfortunately are contradicting. We may continue to use the numerical model for dynamic investigations.

6.3   Injection modeling

This section describes the experimental data reduction that was performed of actual EcoFlow capacity tests, in order to obtain the orifice flow coefficients for both MO and SO designs (see figure 6.3). There was no information about calibration or uncertainty measures for these capacity tests. The goal of the data reduction is to compute the mass flow through the main orifice and secondary orifices at different pressure levels and opening degrees (when the expansion valve is open only). The capacity tests provide continuous capacity or mass flow rate through the valve, but we are only interested in the mass flow through the valve when it is open. When knowing the orifice flow coefficient K, the mass flow through the valve may be computed by the single phase orifice equation as

$$\dot{m}_{\text{open}} = KA\sqrt{2\rho_f(p_{\text{in}} - p_{\text{out}})} \tag{6.1}$$

where A is the flow area of the orifice, ρ_f is the saturated liquid density, p_{in} and p_{out} are the pressure at inlet and outlet of the valve.

Two-phase flow effects such as partial vaporization (flashing) are included in the flow coefficient. Furthermore, the capacity tests of the orifice discs were only carried out at standard conditions. It means that K will not be dependent on the pressure levels, and thus assumed to be constant at different pressure levels. The standard conditions for these capacity tests are: Evaporation at 5°C, condensation at 32°C, 4 K subcooling and no superheat. The relation between the experimental mass flow rate and cooling capacity is thus

$$\dot{Q}_{\text{exp}} = \dot{m}_{\text{exp}}[h_g(p_{\text{out}}) - h(p_{\text{in}}, T_{\text{in}})] \tag{6.2}$$

Before we may obtain the flow coefficients, we need to understand the working principle of the EcoFlow valve in detail.

6.3.1 Working principle details

The stepper motor has 48 steps per revolution equaling 7.5 degree rotation per step. The step time is 10 ms per step, i.e. a minimum of 480 ms per revolution (minimum cycle time). Due to the opening and closing of the valve, the liquid refrigerant before the valve will create a *fluid hammer* (also called a *hydraulic shock*). The moving liquid is suddenly forced to stop, and the pressure builds up before the valve and a pressure wave will propagate upstream. In order to eliminate the peak forces acting on the valve, the speed of the stepper motor is dampened as the valve opens and closes. Figure 6.9 shows the opening areas of the MO design as function of the rotation angle. When the rotation angle is $0°$ and $22.5°$, the valve is closed and open, respectively. The damping happens from $15°$ to $22.5°$, where the step time may be increased. The closing of the valve is performed in similar manner with damping from $22.5°$ to $30°$ and is fully closed at $45°$.

a

b
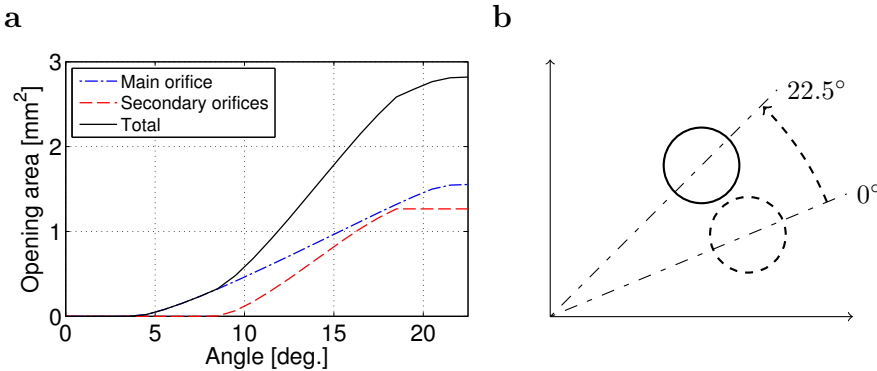
Figure 6.9: Multi-orifice opening areas (a) and angle identification (b); dashed circle = closed, full circle = open

The total injection time as function of the opening degree OD, may be computed by

$$t_{\text{inj}} = t_{\text{open}}\frac{OD}{100} + N_{\text{damp}}t_{\text{damp}} \tag{6.3}$$

where t_{open} is the maximum time the valve may be open, N_{damp} is the number of dampened steps and t_{damp} is the damping time. The additional contribution of the damping time needs to be accounted for in equation 6.3, since the valve is almost fully open as indicated by figure 6.9, from $15°$ to $22.5°$.

When the cycle time t_{cyc} and damping time t_{damp} are chosen, the total injection

time may be computed by

$$t_{\text{inj}} = \left(t_{\text{cyc}} - N_{\text{step}}t_{\text{step}} - N_{\text{damp}}t_{\text{damp}}\right)\frac{OD}{100} + N_{\text{damp}}t_{\text{damp}} \qquad (6.4)$$

where N_{step} and t_{step} are the number of steps without damping and the step time, respectively. A four channel design will give $N_{\text{step}} = 40$ and $N_{\text{damp}} = 8$, which sums to 48 steps. An eight channel design gives $N_{\text{step}} = 32$ and $N_{\text{damp}} = 16$.

The total mass flow rate through the valve when open may then be computed by

$$\dot{m}_{\text{open}} = \dot{m}_{\text{exp}}\frac{t_{\text{cyc}}}{t_{\text{inj}}} \qquad (6.5)$$

and used in equation 6.1 to compute the flow coefficient K for the total flow through main and secondary orifices. The flow coefficient is thus function of the number of discharge channels, opening degree, cycle time, step time and damping time.

6.3.2 Capacity tests and flow coefficient results

Throughout this thesis we have only considered a four channel evaporator, i.e. two coils with two channels each. Therefore, the flow coefficients were only computed on the four channel orifice discs with MO and SO designs.

Some of the capacity tests of the four channel MO design is shown on figure 6.10.

Figure 6.10a shows that the capacity $\dot{Q}_{\text{exp}}$ (or the continuous mass flow rate $\dot{m}_{\text{exp}}$) is increased as the cycle time is increased at high OD. This is because

a

b
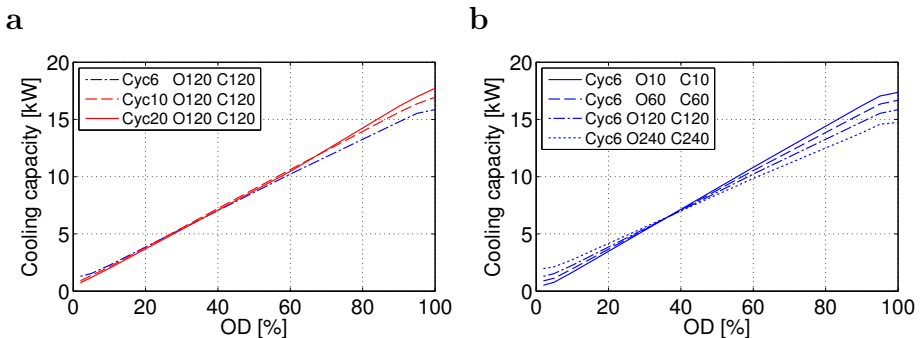
Figure 6.10: Capacity tests of the MO design vs. cycle time (a) and damping time (b); cyc=cycle time [s], O=opening damping time [ms], C=closing damping time [ms].

the period with closed valve become less at higher cycle times. At low *OD* the highest capacity is at the lowest cycle time. This is because the damping time in total is higher for low cycle times and that mass flows through the valve when damping, see figure 6.10b at low *OD*. The higher damping time the higher mass flow through the valve at small *OD*. However, at high *OD* the result is the opposite. This is because the capacity is higher when open in contrast to when damping (almost open or beginning of closing).

The standard EcoFlow time settings are a step time of 10 ms and a damping time of 120 ms for both opening and closing. Using the capacity tests, we computed the flow coefficients for the total flow as function of opening degree for cycle times 6, 10 and 20 seconds for both MO and SO designs. For the SO design the total flow comes through the main orifice, however, for the MO design we need additional information on how much flow that goes into the main and secondary orifices, respectively.

Fortunately, a capacity test was also performed at steady state conditions, i.e. no rotation of the distributor disc and fully open continuous flow. The test was done at all orifices open, but also at main orifice closed, which gives us the flow ratio parameter between the main orifice flow and total flow in steady state as

$$F_o = \frac{\dot{m}_{\mathrm{main,ss}}}{\dot{m}_{\mathrm{tot,ss}}} = \frac{9\mathrm{kW}}{18.3\mathrm{kW}} = 0.492 \tag{6.6}$$

The ratio is assumed to be independent of the cycle time and damping time, and thus directly used to distribute the total mass flow to the main and the secondary orifices when the valve is open. The total mass flow when the valve is open and the corresponding steady state mass flow are shown on figure 6.11a. Figure 6.11b shows the corresponding flow coefficients.
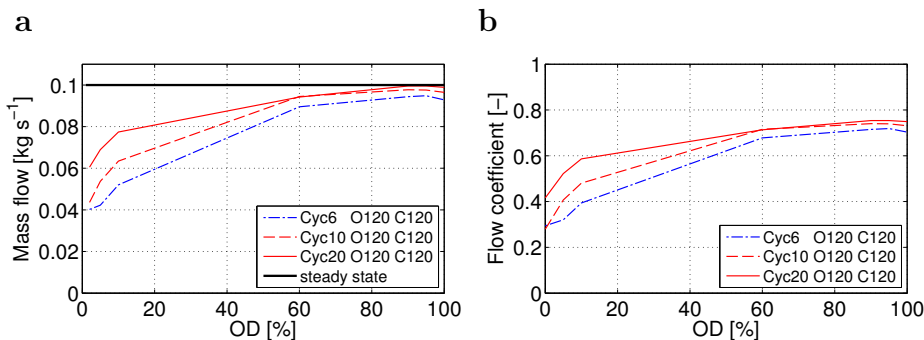
Figure 6.11: Total mass flow rate when valve is open (a) and flow coefficients (b) as function of opening degree (MO design); cyc=cycle time [s], O=opening damping time [ms], C=closing damping time [ms].

We believe that the accelerational effects of the fluid at opening and closing may cause the differences in the flow coefficients and mass flows, which tends to differ more at low opening degree, where the accelerational effect should play a larger role. It seems that the curves to some extend coincide above 60% opening degree. Unfortunately, there were no measurements between 10% and 60% opening degree.

As expected, the mass flow curves are below the steady state mass flow and becomes closer at high opening degree. A variation of inlet and outlet pressures are carried out individually in figure 6.12, in order to illustrate the use of the flow coefficients to find the mass flow as function of opening degree.
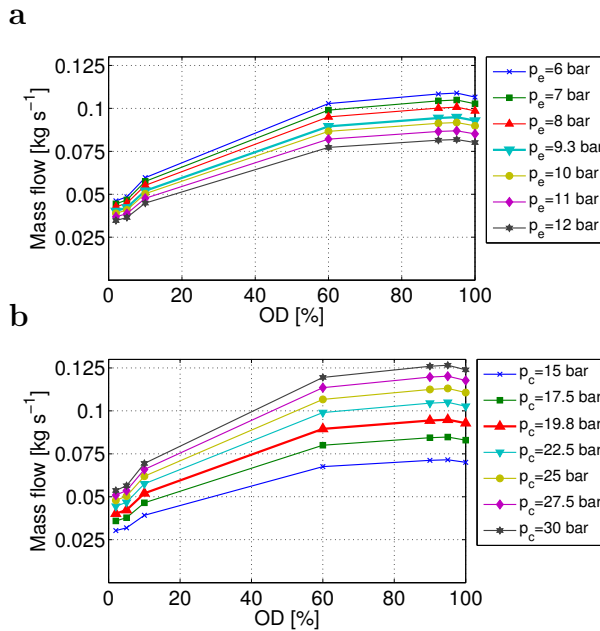
Figure 6.12: Total mass flow rate when valve is open at different evaporating pressures (a) and different condensing pressures (b) as function of opening degree; MO design, cycletime = 6 s; p_e = 9.3 bar and p_c = 19.8 bar is the standard condition (one held constant while varying the other).

The expansion process may experience choking of the flow, i.e. the mass flow may not increase by decreasing the downstream pressure and is only a function of upstream conditions. Using the above modeling approach does not include the choking phenomenon and the mass flow is essentially a function of pressure difference. It is thus assumed that choking of the flow is not existing. The variability of the evaporation pressure is, however, not high for air-conditioning

in contrast to the condensing pressure, which is in accordance with any presence of flow choking (only upstream conditions matters).

6.3.3   Implementation

The implementation of the liquid injection model in Modelica is done by using the `CombiTable1D` model from the Standard Modelica Library, i.e. one-dimensional linear table interpolation of the flow coefficients. The mass flow rates through the main orifice and secondary orifices (MO) are then computed using equation 6.1 and 6.6. Now it is just a matter of computing the individual channel opening and closing time during each cycle.

A distribution vector is defined as

$$\sum_{i=1}^{N} \Theta_i = 1 \tag{6.7}$$

which determines the time period associated with each channel $t_{\text{tube},i}$ as

$$t_{\text{tube},i} = t_{\text{cyc}}\Theta_i \tag{6.8}$$

where i denotes the channel numbers and N the total number of channels. The injection time for each channel thus becomes

$$t_{\text{inj},i} = \left(t_{\text{tube},i} - \frac{N_{\text{step}}t_{\text{step}}}{N_{\text{tube}}} - \frac{N_{\text{damp}}t_{\text{damp}}}{N_{\text{tube}}}\right)\frac{OD}{100} + \frac{N_{\text{damp}}t_{\text{damp}}}{N_{\text{tube}}} \tag{6.9}$$

The opening of each channel is assumed to be at $t_{\text{tube},i}/2 - t_{\text{inj},i}/2$. The closing is then at $t_{\text{tube},i}/2 + t_{\text{inj},i}/2$. The changes in mass flow rate are made smooth by use of the first order continuous function in appendix C for numerical reasons. The transition time was chosen to be 0.1 seconds.

If the liquid injection model runs in *even flow* mode, the distribution vector becomes $\Theta = [0.25, 0.25, 0.25, 0.25]$ for a four channel evaporator. In *compensating flow* mode the values in the distribution vector is controlled in the numerical model according to the individual channel superheat. Thus we do not simulate the actual distribution analysis as mentioned in the beginning of the chapter, in order to find Θ.

Figure 6.13 shows some examples of the MO liquid injection model at a cycle time of 10 seconds. It illustrates the working principle of the liquid injection model as the opening degree and the distribution vector are changed.

6.4   Initial simulation with the liquid injection principle

This section covers initial simulations of the R410A residential air-conditioning system including the liquid injection principle. The evaporator is the interlaced
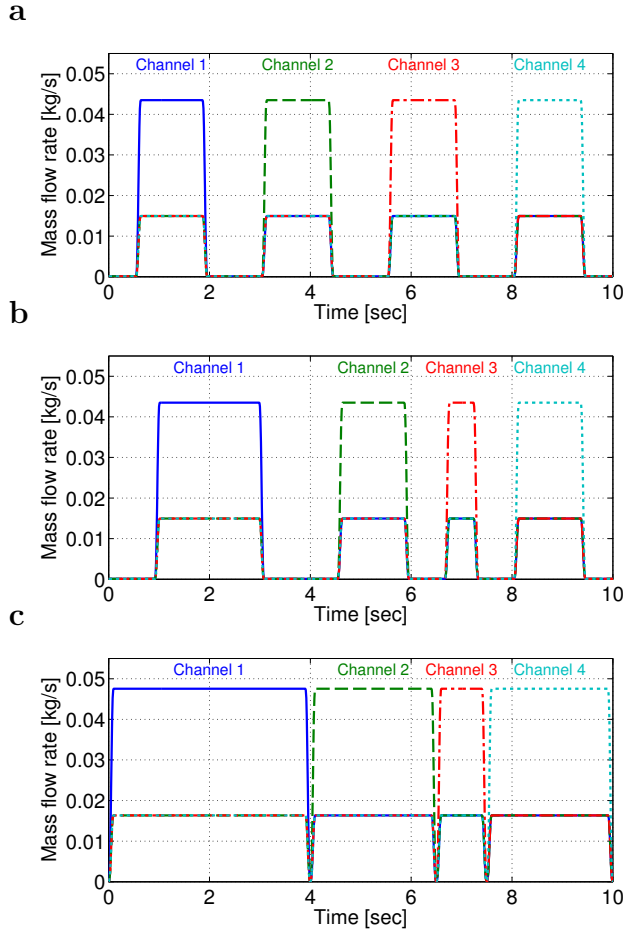
Figure 6.13: Mass flow distributions for liquid injection model with MO design at cycletime = 10 s; $\Theta = [0.25, 0.25, 0.25, 0.25], OD = 50\%$ (a); $\Theta = [0.4, 0.25, 0.1, 0.25], OD = 50\%$ (b); $\Theta = [0.4, 0.25, 0.1, 0.25], OD = 100\%$ (c); $p_e = 9.3$ bar and $p_c = 19.8$ bar (standard condition).

type and upgraded to model all four refrigerant channels, i.e. both coils, at no maldistribution ($F_{air} = F_x = 1$), and using *Even flow* mode, see figure 6.13a. The simulations have shown important observations in the use of void fraction correlations and effectiveness-NTU relations, which need to be addressed carefully when simulating the injection dynamics.

Furthermore, the dynamic behavior observed in the simulations showed fluctuations in important variables such as superheat and evaporating pressure. To

better understand the causes of these fluctuations a sensitivity analysis of the fluctuations is performed using the current numerical model, see appendix D. The fluctuations in the model and similar experimental results will be compared in this section, together with main conclusions from the sensitivity analysis.

6.4.1 Model setup

The model setup is almost the same as in previous chapter (see section 5.2), where the face split and interlaced tube circuitry were modeled. The main differences are summarized below. Unless indicated otherwise, the evaporator is the 8.8 kW size:

- The feeder tubes inner diameter is now 4.5 mm. This is similar to the EcoFlow design, since more mass needs to travel through each feeder tube when the valve is open.
- The effectiveness-NTU relation for the single phase region (equation 2.27) becomes inappropriate when the refrigerant mass flow rate tends to zero. It may happen when the valve is closed. It means that the minimum heat capacity flow for air-side heat transfer is the refrigerant heat capacity flow, thus the air-side heat transfer tends to zero also, even though the air flows continuously with a larger temperature than the wall. For this reason the two-phase effectiveness-NTU relation (equation 2.26) is used for the single-phase region also.
- Throughout this chapter all channels in the evaporator is modeled. It is chosen because we want to evaluate the full effects of individual liquid injection to the four channel evaporators (two coils with two channels each).
- The injection modeling was very time consuming, and for this reason we chose to use only one cell per tube throughout this chapter.
- The tube circuiting of the two coils of the standard interlaced and face split evaporator are a bit different from coil to coil, as indicated in figure 6.14 compared to previous chapter similar coil assumption in figure 5.1.
- The refrigerant and wall dynamics in the manifold are included in this chapter (see section 2.9), since the manifold pipe length showed a damp-ening effect on the fluctuations. The manifold pipe is insulated and con-sidered as the pipe connecting the evaporator and compressor, and not only the mixing region of the evaporator channel flows. The inner and outer diameter of the manifold pipe is 16 and 19 mm, respectively, and the length is assumed to be 5 m. Furthermore, a constant heat transfer coefficient of 700 $Wm^{-2}K^{-1}$ was assumed.
- The void fraction model is chosen to be the simple Zivi (1964) model. We chose the simpler model in contrast to the more sophisticated models considered in section 6.2, because the latter are functions of refrigerant mass flux. When the valve is closing the refrigerant mass flux tends

to zero abruptly in the first part of the channel, resulting in unrealistic void fraction profile as function of vapor quality using such void fraction models. Note that these correlations were not developed at such low mass fluxes.

a   **b**
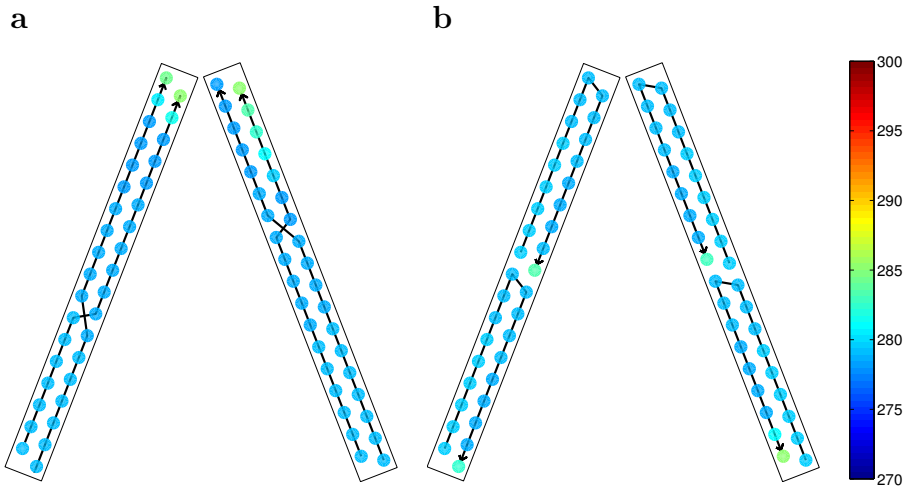
Figure 6.14: Tube circuitries and temperature contours of the interlaced evaporator (a) and the face split evaporator (b).

6.4.2   Pressure fluctuations, experiments and sensitivity

As mentioned the initial liquid injection simulations showed fluctuations in important variables such as superheat and evaporating pressure. It called for a sensitivity analysis of these fluctuations. In the following we present the fluctuations in the model and a comparison to similar experiments. Furthermore, the main conclusions of the sensitivity analysis are presented. For more information on the details of the sensitivity analysis, refer to appendix D.

The fluctuations in the model have a time period corresponding to the cycle time of the liquid injection model divided by the number of channels in the evaporator (for *even flow* mode). These fluctuations have not been observed as high in any experiments carried out at Danfoss, where the sampling frequency has been high enough to capture these fluctuations. The sampling frequency is often chosen to be $1\,\text{s}^{-1}$ for refrigerant temperature and pressure measurements at Danfoss, which is too low for capturing the injection dynamics seen in the numerical model.

Experimental comparison of the fluctuations

The following EcoFlow experiments were carried out on the same system as used in Fösel (2009), i.e. the system used for validation in section 5.3.3 except for the use of an early EcoFlow version. The experiments were performed by the same researcher and coworkers later in 2009. However, the experiments have not been published prior to this thesis. The system comprises a 10.5 kW interlaced evaporator, a hermetic scroll compressor, micro-channel condenser and an early MO disc version. The early design of the MO disc is estimated to have a flow ratio parameter F_o (equation 6.6) of 0.8, which reflects the earlier versions cross-sectional areas of the main and secondary orifices. For the final MO disc design this flow ratio parameter is 0.492. Furthermore, the flow coefficients, the step time and damping time are assumed to be the same as the final MO disc design. The cycle time was six seconds in the experiments and the flow distribution mode was *even flow*, see figure 6.13a.

These experiments are the most recent experiments carried out at Danfoss in Nordborg on a fin-and-tube four channel evaporator using the EcoFlow valve. Later experiments were performed with the final EcoFlow version, however, on larger capacity units with six or eight channels each, which complicates the simulations drastically. For these reasons, the earlier EcoFlow MO experiments were chosen for the comparison. Again, there was no information about calibration or uncertainty measures for these experiments.

The experimental data is shown in figure 6.15 and reduced to be used as input to the numerical model of the evaporator. The procedure is similar to section 5.3.3.

The experimental results also show fluctuations in cooling capacity, refrigerant mass flow, refrigerant volume flow and air mass flow. However, the fluctuations are on a much larger time-scale than the cycle time of EcoFlow. The pressure out of the condenser also shows quite large fluctuations. It is essentially the opening and closing of the EcoFlow valve (causes hydraulic shocks) in combination with the use of a micro-channel condenser that we believe is responsible for these fluctuations. These shocks have been largely removed by damping of the opening and closing in later versions of the EcoFlow valve. With these pressure fluctuations out of the condenser, the refrigerant mass flow rate is measured inaccurately. Note that the refrigerant mass flow was sampled at every 5 seconds, in contrast to temperature and pressure, which were sampled every second. The fluctuations of the refrigerant mass flow propagate in the computation of the cooling capacity, the volume flow out of the evaporator and the air mass flow rate as indicated on figure 6.15 (a,c,d,f). It propagates from the refrigerant mass flow to the air mass flow, because the measured refrigerant cooling capacity was used to compute the air-side mass flow rate.

Nevertheless, we use mean values of the refrigerant volume flow out of the evaporator and air mass flow rate as input to the numerical model. The air mass flow is converted by frontal area and air density into a mean frontal
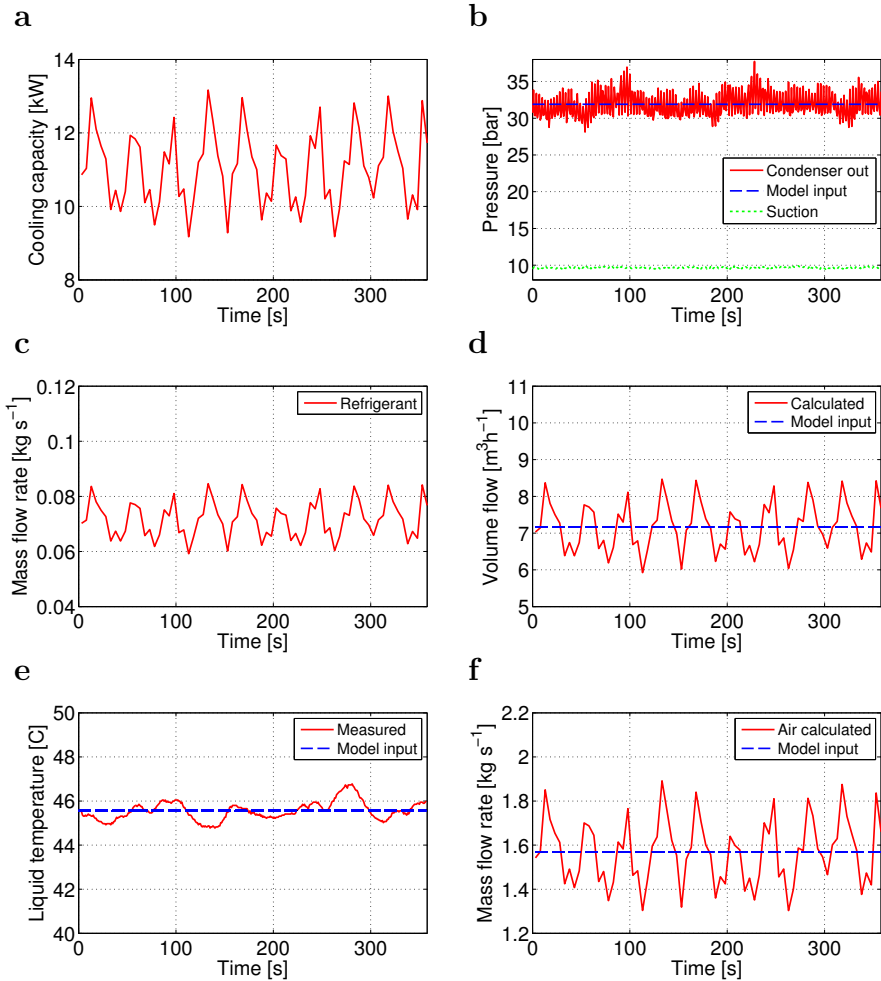
Figure 6.15: Experiments and calculated inputs

velocity. Despite, the erroneous mass flow measurement, the suction pressure and liquid temperature before expansion seems not to fluctuate severely as shown on figure 6.15e and 6.15b. Therefore, since we use mean values of the measurements as input to the model, the experimental comparison is legitimate. Table 6.3 lists the model inputs to the experimental comparison.

Figure 6.16a and 6.16b show the experimental superheat and pressure fluctuations during three cycles. The corresponding model results are shown in figure 6.16c and 6.16d for a uniform airflow. Figure 6.17a and 6.17b shows the cor-

Table 6.3: Model input/boundary conditions for experimental comparison

Superheat	5 K
Pressure out of condenser	31.9 bar
Liquid temperature out of condenser	45.6 °C
Volume flow out of evaporator	7.17 m^3h^{-1}
Indoor air temperature	24.3°C
Indoor frontal air velocity	2.98 m s^{-1}

responding model results for a non-uniform airflow, where the worst possible linear velocity profile is applied, see figure 5.2b. Note that the thick curve around 5 K is overall superheat. Furthermore, the experiments show a bit higher individual superheats. This is because that they were measured on the tube wall surface with insulation around the tube, and may had heat entering from the surroundings.

First of all it is hard to see the differences using the uniform or non-uniform airflow, despite the smaller pressure level in the non-uniform airflow case, which
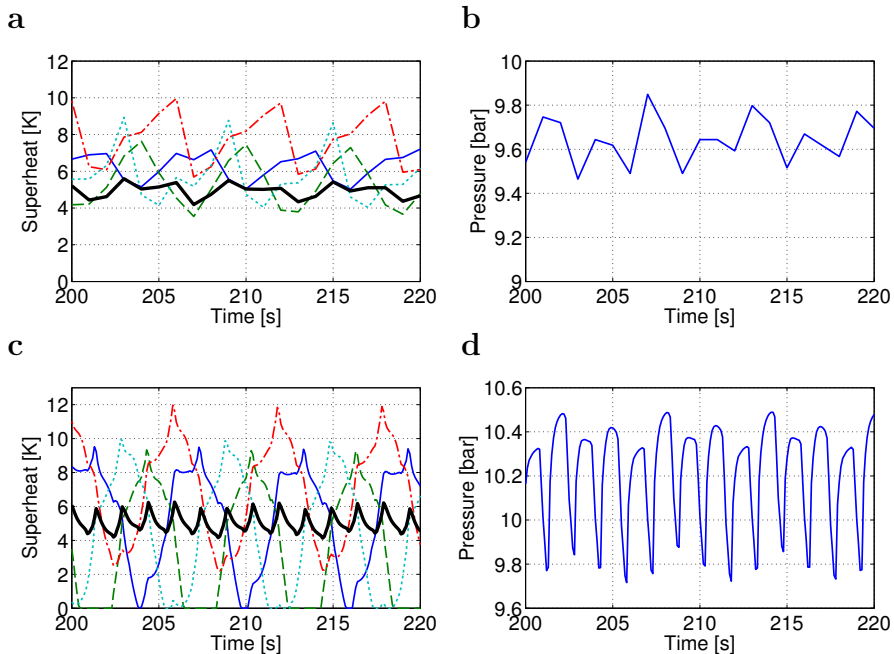
Figure 6.16: Zoomed-in superheats and suction pressure; Experimental results (a,b), Model results with uniform airflow (c,d).

a

b

c

d

e

f
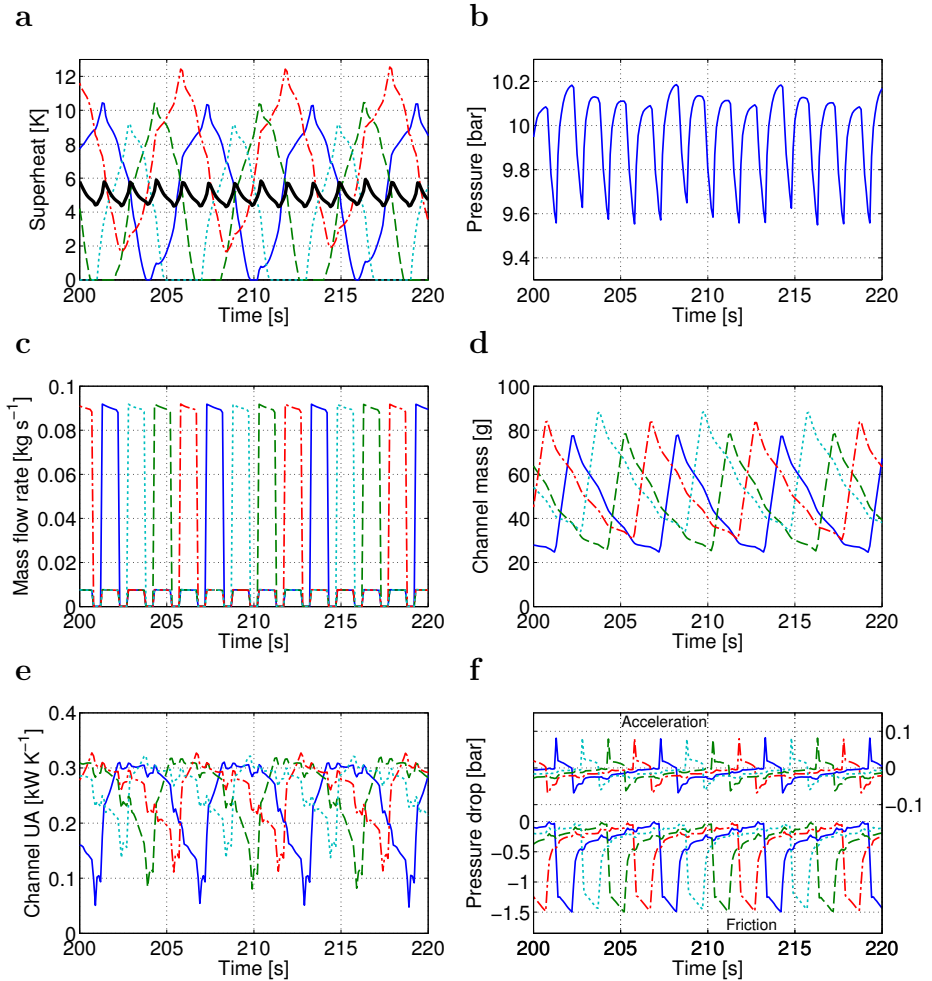
Figure 6.17: Model results with non-uniform airflow

indicates a smaller heat transfer. The pressure and superheat fluctuations are almost the same in the two simulations.

When comparing to the experimental data, it is seen that the pressure fluctuations are smaller (approximately one third in amplitude of the numerical results). It is difficult to make this conclusion based on these experimental results, since the sample time was only 1 s^{-1} for the pressure. However, the experiments carried out at Danfoss with higher frequency did not show as high fluctuations as the numerical model does here. Unfortunately, these experi-

ments were performed on six to eight channel evaporators and not the four channel evaporator. The reason for these high fluctuations in the numerical model have not been obtained so far. However, we believe that the interfacial dynamics of the two-phase flow and the presence of thermodynamic non-equilibrium are responsible for the dampening of the pressure fluctuations in the experiments. These are inherently exclusive in the mixture two-phase flow model.

If we compare the individual superheat measurements and the prediction by the numerical model, then the accordance is much more acceptable. Both the measurements and the model predictions show the effect of the liquid injection into each channel, since they fluctuate similarly at a time period corresponding to the cycle time. Furthermore, the superheat decreases as the refrigerant enters through the main orifice into each channel as indicated on figure 6.17c for the non-uniform airflow case. The corresponding mass inside each channel is shown on figure 6.17d, which increases when the refrigerant enters through the main orifice and otherwise decreases.

What is probably most important is the individual channel overall UA-value in figure 6.17e, which shows a decrease just before new refrigerant is fed to the corresponding channel. There may be an optimization potential here if the cycle time is chosen such that the UA-value decrease is avoided. Figure 6.17f shows the corresponding individual channel pressure drop by friction and acceleration due to density and mass flux differences. When considering the individual channel pressure drop due to friction and acceleration, one may expect that this is the cause of the pressure fluctuations, however, the sensitivity analysis proves otherwise. It is interesting to note that the accelerational pressure drop is positive as the refrigerant is fed to each channel. This is because the refrigerant mass flow is higher at the beginning compared to the end of the channel, i.e. the difference in momentum flow between inlet and outlet is positive.

Table 6.4 shows the comparison of the mean (steady state) cooling capacity and mass flow rate for the evaporator. It shows that the numerical model with the worst possible linear airflow profile is close to the experimental results, however, we may not know the exact degree of flow maldistribution in the experiments. Furthermore, the quality of these data is not acceptable for conclusions with regards to model validation. Higher sample time should have been used.

Main results of the sensitivity analysis

The objective of the sensitivity analysis is to investigate the amplitude of the liquid injection fluctuations and the time constant based on a step in valve opening degree. We chose to include the time constant since it is the most typical measure used for control. Furthermore, we believed that there was some correlation between the time constant and the fluctuations, however, the simulations showed otherwise. For these reasons, the results of the amplitude sensitivity are only presented here. Again, uniform flow conditions are assumed

Table 6.4: Comparison of mean mass flow rate and cooling capacity

		Capacity [kW]	Mass flow [kg s^{-1}]
Experimental results		11.04	0.0716
Uniform airflow		11.58	0.0758
	Error	4.9%	5.9%
Non-uniform airflow		11.27	0.0738
	Error	2.1%	3.1%

and the interlaced circuitry is chosen, since it is the most used today.

Besides the evaluation of the sensitivity in amplitude and time constant in appendix D, the appendix also presents the steady state sensitivity of the continuous *EXV flow* system and the discontinuous liquid injection system in terms of cooling capacity, overall UA-value and COP. The model setup is exactly the same as introduced in section 6.4. The injection model is set to have a cycle time of 6 seconds, even distribution mode and multi-orifice design.

The method used for testing the sensitivity involves a baseline simulation with baseline input parameters. These parameters are then varied one at a time and a new simulation is performed at each variation. The input parameters are divided in *uncertainty parameters* and *other parameters*. The uncertainty parameters are actually correction factors multiplied to the correlations applied in our model. The correlations are the same as shown in table 5.1 including the use of constant slip ratios (the baseline slip ratio of 3.4 is what the Zivi (1964) correlation predicts for these conditions). The factors are varied up and down according to the typical uncertainty in these correlations, see table 6.5. The other parameters are geometric constraints and input conditions to the model. These are varied within a specified realistic range as indicated in table 6.6.

The simulation methodology is shown in figure 6.18. In order to avoid the use of filtering of the fluctuations when evaluating the time constants, we chose to evaluate the time constants on the system with the conventional electronic expansion valve and distributor from 0 to 500 seconds with continuous refrigerant flow to each channel. The liquid injection principle is then modeled from 500 to 900 seconds.

We simulate from 0-200 seconds with control, from 200-500 seconds without control and from 500-900 seconds with control. We do this to avoid the effects of the control devices on the time constants. By control, we mean the control of the superheat according to table 6.6 and control of the subcooling to 2 K. The superheat is controlled by the opening degree of the expansion valve and the subcooling is controlled by the charge in the system.

The amplitude of the liquid injection fluctuations is recorded between 700 and 900 seconds and taken as half of the maximum change, i.e. maximum ampli-

Table 6.5: Uncertainty parameters

Input parameters		min		base		max
Refrigerant friction correction factor (fc)		0.6	0.8	1	1.2	1.4
Two-phase heat transfer correction factor (htc 2p)		0.6	0.8	1	1.2	1.4
Vapor heat transfer correction factor (htc vp)		0.8	0.9	1	1.1	1.2
Air heat transfer correction factor (htc air)		0.85	0.925	1	1.075	1.15
Phase velocity slip-ratio (Slip)	1*	2.04	2.72	3.4	4.08	4.76

* Homogeneous flow assumption (special case outside the uncertainty measure)

Table 6.6: Other parameters

Input parameters	min		base		max
Manifold/suction pipe length [m] (Lman)	2	3.5	5	6.5	8
Superheat [K] (Tsh)			5	10	15
Outdoor temperature [°C] (Tout)	27.8	31.4	35		
Air velocity [m s^{-1}] (Vair)	0.696	0.928	1.16	1.392	1.624
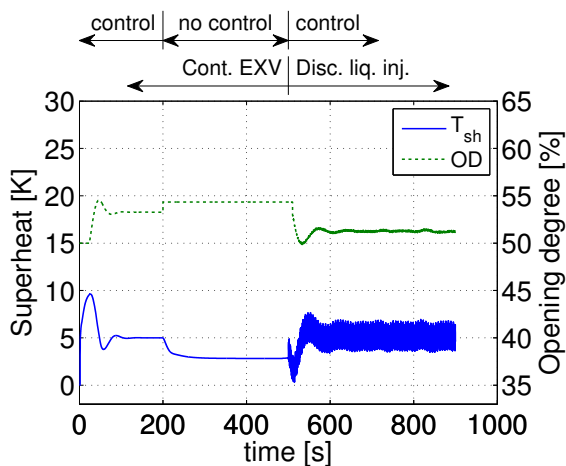
Figure 6.18: Simulation methodology

tude. The standard deviation is also computed to characterize the fluctuations, because the maximum amplitude may include slower fluctuations from the control of the system than what we are interested in. The standard deviation gives a better estimate of the fluctuations, however, it does not show how large the fluctuations are. Only the relevant parameters from table 6.5 and 6.6 are shown that actually have an effect compared to the baseline fluctuations. The results of the amplitude sensitivity are shown in figure 6.19.
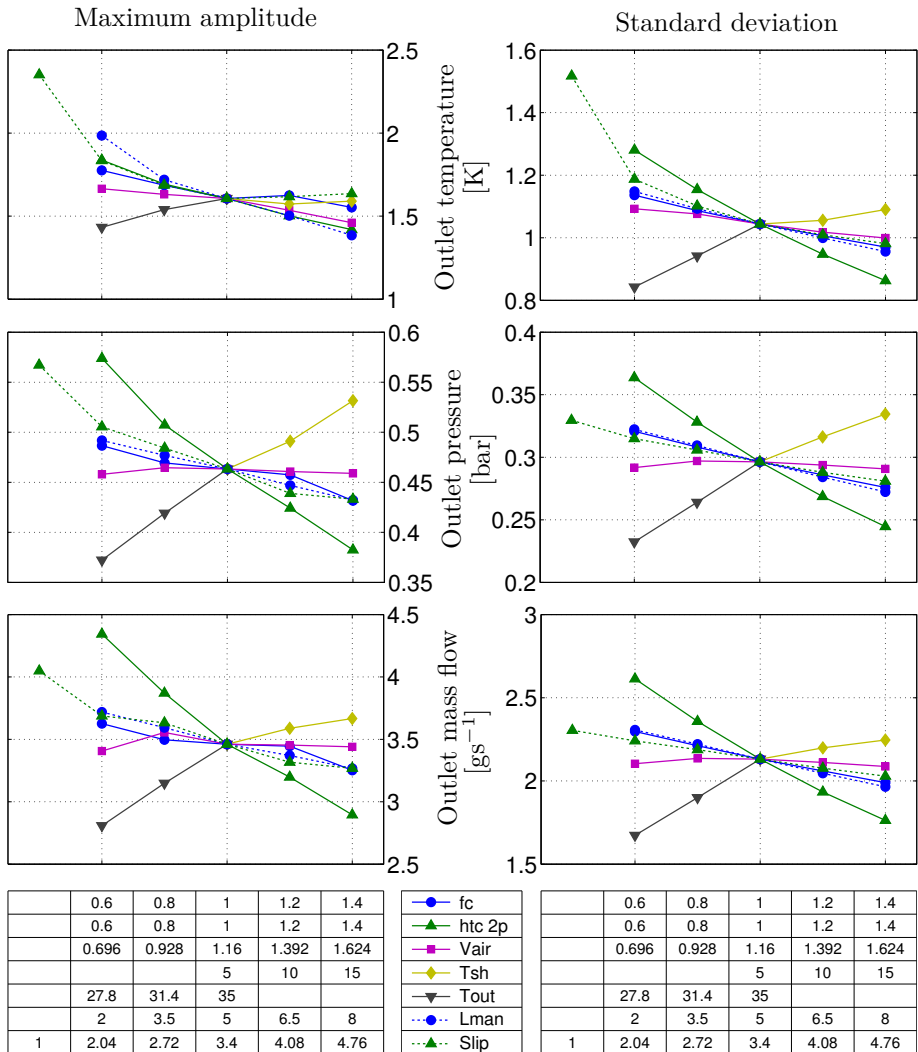
Figure 6.19: Sensitivity of maximum amplitude and standard deviation

The results indicate that the considered input parameters are not able to eliminate the fluctuations within their specified limits. Since the fluctuations have not been observed in experiments so far, the injection phenomenon is still to be fully understood. We believe that the fluctuations in our mixture model may be a result of or combination of different reasons:

- Use of steady state heat transfer, pressure drop and void fraction correlations at large transients in mass flow.
- The assumption of thermodynamic equilibrium.
- The absence of the liquid-vapor interfacial friction and drag dynamics.

What actually reduces the fluctuations in the model, is an increase in slip ratio, i.e. a higher refrigerant charge. However, it seems that there is a limit to the reduction by this factor considering the maximum amplitude, since it goes towards a constant value as the slip ratio increases. In contrast, the standard deviation seems to decrease linearly as the slip ratio increases. The reduction in the fluctuations is however minor.

The two-phase heat transfer coefficient has the most significant effect together with the outdoor temperature. The two-phase heat transfer coefficient may be the first thing to study in order to eliminate the fluctuations. Indeed, the heat transfer coefficient is believed to be altered drastically as the refrigerant are injected into the individual channels. It seems that the steady state correlations are insufficient to model the dynamic behavior at large transients in mass flow. The decrease in outdoor temperature will eventually reduce the pressure difference across the liquid injection model, and result in a higher opening degree to keep up the mass flow rate. Furthermore, the decrease in outdoor temperature results in decreased inlet vapor quality and consequently more mass in the evaporator. The manifold length also has an effect on the fluctuations as expected, but minor.

The conclusion of the sensitivity analysis is that the numerical model cannot in its present form eliminate the fluctuations caused by the liquid injection model. By choosing a void fraction (or slip flow) correlation that predicts larger refrigerant charge, the fluctuations may be minimized, but not significantly. Therefore, other phenomenons such as dynamic heat transfer, interfacial dynamics and thermodynamic non-equilibrium effects seems to prevail in this novel area of the injection dynamics. No heat transfer correlations exist for dynamic two-phase flow known to the author, and the steady state heat transfer correlations seem to be insufficient.

Furthermore, there was not found any particular similarity between the dynamic evaporator response (time constant) and the amplitude of the fluctuations. From the investigation of the time constants in appendix D, we found that the responses are different for the refrigerant entering the manifold and the refrigerant exiting the manifold. The thermal capacitance of the manifold pipe wall and the heat transfer from the wall to the refrigerant in the manifold was

the mechanism for this difference. It produced a slower temperature response at the outlet of the manifold rather than in the beginning, where the refrigerant streams are mixed, while having no effect on the pressure response. For these reasons we believe the pressure is the key variable for these fluctuations, i.e. the pressure fluctuations propagate to the other variables. The most important parameter for the dynamic response is the slip ratio, i.e. the refrigerant charge in the evaporator. The more mass the slower the response. Appendix D gives a more detailed description of the sensitivity analysis.

6.5   Effects of liquid injection specifications at uniform flow conditions

Despite the presence of the pressure fluctuations, the numerical model is used to perform simulations of the significance of the cycle time for both the multi-orifice (MO) and single-orifice (SO) designs. Furthermore, the flow ratio parameter F_o (equation 6.6) for the MO design will be investigated, i.e. the flow distribution between the main and secondary orifices of the MO design.

6.5.1   Cycle time

Figure 6.20 (a,c,e) shows the UA-value, cooling capacity and COP of the *continuous EXV flow* system and the *discontinuous liquid injection* systems with MO and SO designs as function of the cycle time. The EXV performance values are evaluated at time equals 200 and the liquid injection performance values are averaged between 700 and 900 seconds as indicated in figure 6.18. The orifice flow coefficients for the 3 second cycle time simulations were assumed to be the same as for the 6 second cycle time case.

The results show that both the face split and the interlaced evaporator perform better using the continuous EXV flow system at no flow maldistribution, i.e. continuous individual channel flow according to individual channel pressure drop. It reveals that the liquid injection principle (or flow pulsation) seems to decrease rather than increase the heat transfer mechanism at these cycle times and when using the current mixture model approach developed in this thesis. The question if flow pulsations decrease or increase heat transfer may not be concluded by this analysis alone. It should be investigated in more detail both experimentally and numerically with regards to the pressure fluctuations.

The liquid injection MO model performs better than the SO model in terms of UA-value, cooling capacity and COP as shown on figure 6.20 (a,c,e). Furthermore, the results show that the cycle time should be kept as low as possible. The simulation using the SO model at a cycle time of 20 seconds failed and was not obtainable. It also seems that this case decreases the performance drastically. The question regarding which cycle time is the maximum limit is
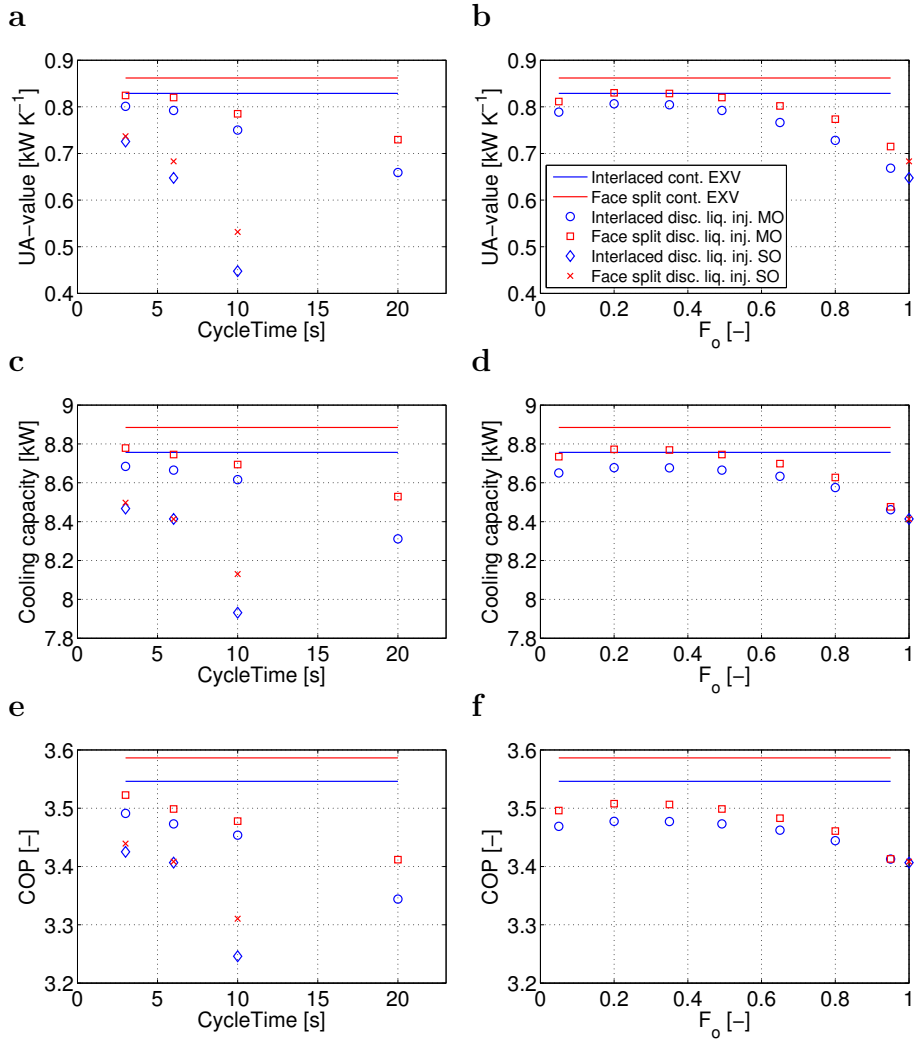
Figure 6.20: UA-value, cooling capacity and COP vs. the cycle time (a,c,e) at $F_o = 0.492$ for the MO design; UA-value, cooling capacity and COP vs. the flow ratio parameter (b,d,f) at cycle time $t_{cyc} = 6$ seconds.

difficult to answer. For these four channel evaporators it seems that the maximum cycle time is 10 and 6 seconds for the MO and SO design, respectively. Otherwise, the channels dry-out too much when the valve is closed.

Again, the face split circuitry shows better performance in contrast to the interlaced circuitry at uniform flow conditions for each distribution method.

6.5.2 MO flow ratio

Figure 6.20 (b,d,f) shows the UA-value, cooling capacity and COP as function of the flow ratio parameter F_o, and at a cycle time of 6 seconds. It shows that the maximum performance is when F_o equals 0.25, which means that the main and secondary orifices have the same dimension, thus no possibility to distribute mass individually. Essentially, all the curves on figure 6.13a coincides, i.e. the flow is distributed evenly to all orifices at each injection.

It shows that for uniform flow conditions, the optimal refrigerant mass flow distribution is uniform. However, the decrease in performance as F_o increases is small and the maximum limit seems to be around 0.6. Otherwise the secondary channels will dry-out too much. This is essentially the case for the SO design, but as mentioned earlier in this chapter the SO design has the possibility to eliminate defrosting periods by defrosting each channel at a time. This works for the face split evaporator only and not the interlaced, but may increase overall energy performance in defrosting conditions.

The $F_o = 95\%$ results of the MO design seems to be close to the SO design results presented here at $F_o = 100\%$. The difference in the two designs is essentially the flow coefficients and therefore the value of the opening degree in the simulations (61% for SO and 53% for MO). However, the overall mass flow through the evaporator becomes the same. In turn the performance becomes similar for the two designs as F_o approaches 100%.

6.6 Liquid injection dynamics with airflow maldistribution

The performance of the liquid injection principle with compensation is compared to the perfect control of individual channel superheat (from chapter 5) at airflow maldistribution. By perfect control, we mean that the individual superheats were controlled to 5 K by providing continuous individual channel mass flow rates. The liquid injection model with MO design is included in the comparison only. The cycle time is 6 seconds and the flow ratio parameter is 0.492.

Figure 6.21 shows the comparison, where the continuous *EXV flow* and continuous *compensating flow* results are the same as shown in figure 5.13 from chapter 5.

Again, the results show that the discontinuous liquid injection principle has a degrading effect on the performance compared to the case with continuous mass flow distribution. It may be that the pressure fluctuations shown in the injection dynamics modeling or the model limitations with regards to the interfacial dynamics are responsible for these differences. If not there is an optimization potential here, i.e. instead of using discontinuous liquid injection, it may be better to use a variable throttle area for controlling individual and
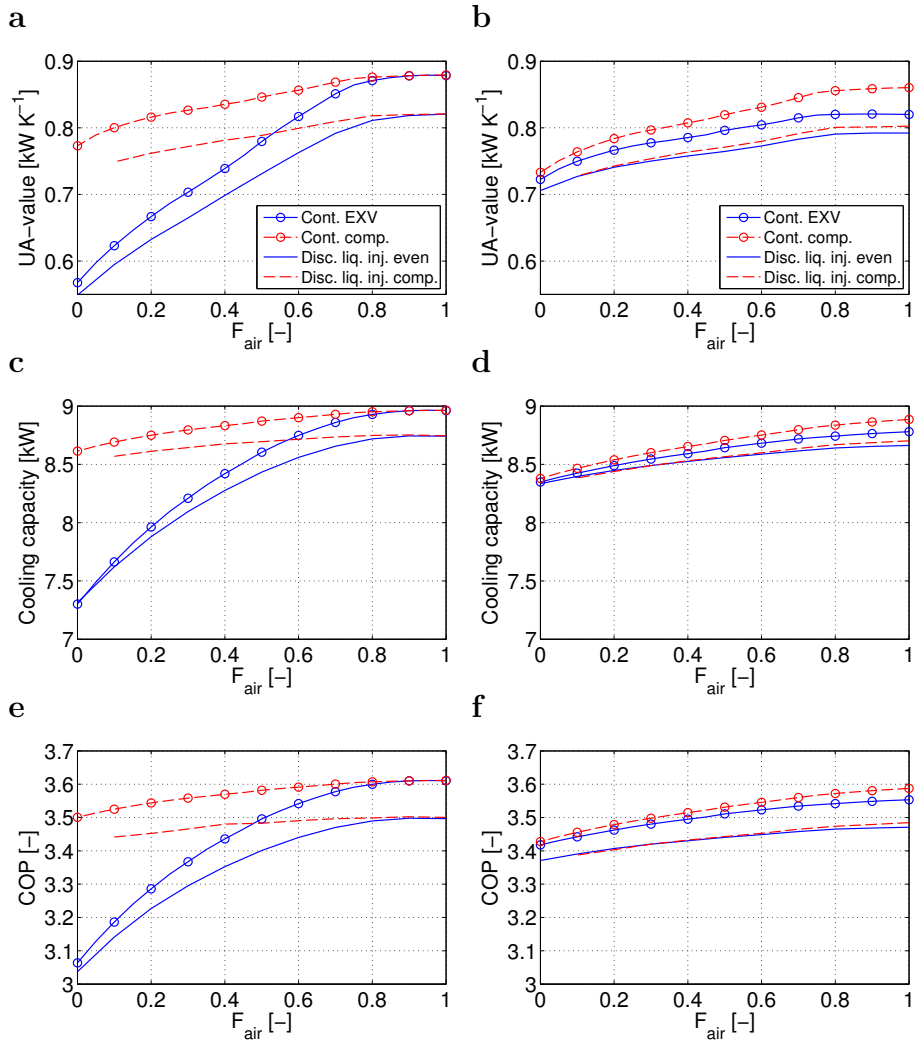
Figure 6.21: UA-value, cooling capacity and COP vs. the airflow distribution parameter for the face split (a,c,e) and interlaced (b,d,f) evaporator.

overall superheat.

An important point is that the results of the discontinuous liquid injection model with compensation showed a limitation for $F_{air} < 0.1$ for the face split evaporator, i.e. one of the distribution vector values became below zero, which may never happen. The limitation is caused by the MO flow ratio parameter, which should be higher to compensate such airflow maldistribution for the

face split evaporator. The problem is that more refrigerant goes through the secondary orifices than supposed to and thus the distribution control band becomes too low. The interlaced evaporator does not show a problem when approaching $F_{air} = 0$.

Despite the better performance of the continuous mass flow distribution or perfect control, the continuous *EXV flow* system shows lower performance than the discontinuous liquid injection system with compensation at $F_{air} < 0.5$ for the face split evaporator. As expected the discontinuous liquid injection system with *even flow* performs the worst at airflow maldistribution when using the face split evaporator. However, when using the interlaced evaporator there is no particular difference in the discontinuous liquid injection model with *even flow* or *compensating flow*. This is because the interlaced evaporator already by design compensates the airflow maldistribution to some extend. For the interlaced evaporator the continuous refrigerant flow cases show better performance at all values of F_{air}.

The trends of the discontinuous liquid injection modeling is the same as the trends of the continuous flow modeling (or prefect control) from chapter 5 for airflow maldistribution. The performance is, however, decreased by using the discontinuous liquid injection principle. We must remember that this decrease may be a cause of the pressure fluctuations in the numerical model and the absence of two-phase interfacial dynamics. A further study should be carried out with regards to these issues, in order to clarify the potential of altering the two-phase heat transfer mechanism by discontinuous liquid injection, (or flow pulsation).

6.7   Discussion and summary

In this chapter we performed dynamic simulations of the discontinuous liquid injection principle, both for the multi-orifice (MO) and the single-orifice (SO) design concepts. For this purpose the numerical model was upgraded from chapter 5 in order to model all four refrigerant channels. The simulations were carried out on the interlaced and face split circuitries with and without airflow maldistribution.

The chapter provides a basic understanding of the discontinuous liquid injection principle and its implications on system performance. The results are in the form of graphical guidelines, which show the effect of the cycle time for each injection concept (MO and SO), and the effect of the secondary flow for the MO design (flow ratio parameter between main and secondary orifices, F_o). Based upon the four channel evaporator that are analyzed in this thesis, it is recommended that the cycle time should be kept below 10 and 6 seconds for the MO and SO designs, respectively. Furthermore, the flow ratio parameter should be around 0.6, or adapted to specific tube circuitry (i.e. face split or interlaced).

The discontinuous liquid injection principle is essentially pulsations applied to the two-phase refrigerant flow. The results obtained using the current mixture model indicate that these flow pulsations do not increase heat transfer, but rather decrease the heat transfer mechanism. It is however difficult to make this conclusion by this study alone. Firstly, the two-phase flow regimes are broken up by the flow pulsations and giving rise to new discontinuous flow patterns, which are not properly reflected in the steady state correlations for refrigerant heat transfer, pressure drop and void fraction. Secondly, the numerical model showed spurious pressure fluctuations, which have not been observed as high in any experiments carried out at Danfoss. The amplitude of the fluctuations are approximately 3 times higher in the model compared to similar experiments.

A sensitivity analysis of the fluctuations in the model showed that the main sensitive variables did not eliminate the fluctuations. The readers need to be cautioned that the results and conclusions from the liquid injection modeling are obtained despite the presence of these fluctuations. It is believed that the absence of the two-phase interfacial dynamics in the current mixture model is the main cause of the high pressure fluctuations.

The conclusions of the chapter are summarized in the following summary and may be viewed by the readers as rules of thumb regarding the main evaporator dynamics and the liquid injection principle. The main evaporator dynamics were validated with old experiments carried out on a simple coaxial evaporator in order to give the model credibility, before the liquid injection principle were modeled. A discussion on the main evaporator dynamics is given in section 6.2.5.

Summary

Firstly, the main dynamics of the numerical model was validated on a simple coaxial type evaporator. This simple geometry was chosen in order to focus on the two-phase flow dynamics. This was essentially not a validation of the liquid injection principle, which is on/off flow modulation, but rather a validation of the main evaporator dynamics. Moreover, the dynamic evaporator response based upon a step change in volume outflow was used for validation. The main conclusions were:

- The homogeneous model is insufficient for modeling of the dynamic evaporator response of the current coaxial evaporator.

- If one wants to investigate the dynamic behavior due to refrigerant movement and amount of refrigerant in the evaporator, then a slip flow model is needed, i.e. use of a void fraction model.

- The Premoli et al. (1971) void fraction model and the Steiner (1993) version of the Rouhani and Axelsson void fraction model gave the most accurate evaporator response.

- The simpler void fraction model by Zivi (1964) gave less accurate results, but quite reasonable considering the simplicity of the model.

Secondly, the chapter describes the discontinuous liquid injection principle and modeling, i.e. working principle, experimental data reduction for evaluation of orifice flow coefficients and implementation.
Thirdly, initial simulations of the liquid injection principle are performed and compared to similar experiments. The simulations showed spurious fluctuations, which have not been observed as high in any experiments carried out at Danfoss in Nordborg, thus it called for a sensitivity analysis of these fluctuations using the numerical model. The main conclusions were:

- The pressure fluctuations are approximately one third in the experiments compared to the simulations.

- The individual channel superheats of the experiments and simulations are in good concord.

- The sensitivity analysis showed that the current mixture model formulation were unable to eliminate the pressure fluctuations.

- There was no correlation between the amplitude of the fluctuations and the first order time constant based upon a step in opening degree.

- We believe that the fluctuations in our mixture model may be a result of or combination of the different reasons:

    o Use of steady state heat transfer, pressure drop and void fraction correlations at large transients in mass flow.

    o The assumption of thermodynamic equilibrium.

    o The absence of the liquid-vapor interfacial friction and drag dynamics.

Fourthly, the numerical model is used despite the pressure fluctuations to analyze the cycle time of the liquid injection model with MO and SO designs, and the flow ratio between the main and secondary orifices in the MO design. Fifthly, the liquid injection principle is compared to the continuous flow assumption with perfect individual channel superheat control from chapter 5 at airflow maldistribution. The main conclusions were:

- The injection dynamics or flow pulsations decreased the performance slightly in terms of UA-value, cooling capacity and COP.

- The performance decreases as the cycle time increases.

- The MO design show better performance compared to the SO design (in dry air conditions).

- The main flow and the individual secondary flows in the MO design should be kept as even as possible, while having the required distribution control band.

- The control band depends on the evaporator circuitry type, for example, the face split needs larger control band compared to the interlaced at airflow maldistribution. The current MO design cannot handle airflow maldistribution in the face split evaporator at $F_{air} < 0.1$.

- At airflow maldistribution, the trends of the liquid injection dynamics are similar to the perfect control method from chapter 5, despite the small performance decrease.

- The liquid injection principle with *even flow* and *compensating flow* mode using the interlaced circuitry showed almost the same performance at airflow maldistribution.

CHAPTER 7

Concluding remarks

The aim of this thesis was to study the effects of flow maldistribution in fin-and-tube evaporators for residential air-conditioning systems and the possible compensation potential in terms of system performance. A test case 8.8 kW system with R410A as refrigerant was chosen as baseline for investigation. The compensation method was control of individual channel superheats by distributing individual channel mass flow rate.

The study gives an increased understanding of the main phenomenons that lead to flow maldistribution, such as non-uniform inlet liquid/vapor phase distribution, different feeder tube bends, non-uniform airflow distribution, typical tube circuitry effects and interactions of all these phenomenons.

The study is divided in three steps, i.e. a generic study, a tube circuitry study and a liquid injection study. The first study was a generic study that did not depend on tube circuiting effects, i.e. two straight and independent channel simplification, thus it may be considered as a general study showing general results and trends of flow maldistribution. The second study considered the actual tube circuiting effects in typical A-coil evaporators, i.e. the face split and the interlaced tube circuitries. The third study analyzed a new control concept for compensation of flow maldistribution, i.e. the discontinuous liquid injection principle.

7.1 Discussion

In order to study the flow maldistribution, we defined a number of distribution parameters, F_x, F_{ft} and F_{air}. These parameters may be estimated qualitatively by the readers in order to obtain graphically a specific performance degradation or compensation potential by control of individual channel superheats, using the general results in chapter 4 or using the actual tube circuitry results in chapter 5. The results provide an objective basis for decision with regard to the use of the compensation method, as well as in combination with tube circuitry design. This decision will depend on the degree of flow maldistribution, i.e. the distribution parameters. The feeder tube bending parameter F_{ft} showed minor effect on system performance and need not be taken into account.

It is however difficult to determine the phase distribution parameter F_x and the airflow distribution parameter F_{air}. These parameters may be different for different types of evaporator circuitries, evaporator sizes, expansion valve and distributor designs, operating conditions and installations of the evaporator. For example, the upstream airflow may be non-uniform caused by bends, flow obstructions or fan location in the duct system. All these effects must be taken into account when qualitatively estimating the distribution parameters. At uniform upstream airflow velocity the CFD simulations showed a corresponding airflow distribution parameter of around $0.15 \leq F_{air} \leq 0.20$, and may be used as a first guess for the results in chapter 5. Otherwise, the expected span of the distribution parameters have not been established and is considered for further work. Note that it was assumed in chapter 4 and 5 that both coils of the A-coil evaporator worked under similar maldistribution conditions. However, there may be flow maldistribution between the coils themselves. There may also be other causes of maldistribution such as fouling or moisture condensate. Furthermore, part-load operation or off-design non-standard conditions may result in increased flow maldistribution.

We may answer the hypothesis raised in the introduction (section 1.3.1), by stating that a significant increase in system performance by compensating flow maldistribution is possible, if the system is operated at flow maldistribution conditions. However, if the maldistribution do not occur or individual sources of maldistribution compensate each other, there may be no improvement. The questions raised in section 1.3.1, i.e. what is the performance reduction due to flow maldistribution, what is the recovery potential and the additional evaporator size, all become subject to specific maldistribution conditions and tube circuitry for the given A-coil evaporator under consideration.

In this thesis we only considered a typical four channel evaporator with either simplified straight channels, face split circuitry or interlaced circuitry. Therefore, when one wants to analyze another evaporator size or circuitry, it is recommended to use the developed simulation model as a tool in order to obtain more precise results for the actual evaporator of interest.

The developed simulation model may be used to evaluate the performance of various circuitry combinations with or without compensation by control of individual channel superheats. Furthermore, the model may be used to simulate system dynamics, for example, evaluation of time constants, control designs and testing.

The simulation model was used to simulate the discontinuous liquid injection principle in chapter 6, which essentially is a control design (or method for compensating flow maldistribution). The results showed too large fluctuations in pressure compared to experiments, which reveals that not all the relevant phenomenons are accounted for at on/off discontinuous two-phase flow modeling (large transients in mass flow at small time-scales). Furthermore, a sensitivity analysis of these fluctuations was undertaken in order to clarify if the fluctuations could be eliminated or minimized in the model, however, the analysis was unsuccessful. Therefore, the results of the liquid injection analysis should be viewed as a first study of the injection dynamics with the current model approach and limitations. The model is a mixture two-phase flow model and it is believed that the absence of the interfacial dynamics in the model or the use of steady state correlations for heat transfer, friction and void might be responsible for the fluctuations.

7.2   Conclusion

This conclusion summarizes the main conclusions from chapter 4, 5 and 6. These chapters represent the three steps of the investigation approach that are used in this thesis.

Step 1: Two straight channels - a generic study

With the current definitions of the distribution parameters (F_x, F_{ft} and F_{air}), it is found that the airflow maldistribution reduces the cooling capacity and COP significantly, whereas the inlet liquid/vapor maldistribution has smaller impact. Different feeder tube bends were shown to have minor effect on system performance. The reductions in COP were as much as 13%, 4.1% and 43.2% for non-uniform inlet liquid/vapor distribution, different feeder tube bending and non-uniform airflow, respectively. The compensation by control of individual channel superheat resulted in a COP reduction of only 5.7% compared to 43.2% at worst case of airflow maldistribution.

The considered combinations of inlet liquid/vapor and airflow maldistribution mostly resulted in reductions in cooling capacity and COP, however, the sources of flow maldistribution may also compensate each other with a maximum performance similar to the compensation method. Furthermore, the trade-off between using the compensation method or a larger evaporator (10.5 kW), showed that the span at which the larger evaporator system performed better was small.

Step 2: Face split vs. interlaced

The comparison of the face split and interlaced tube circuitries revealed that the face split evaporator performs better at uniform flow conditions, whereas the interlaced evaporator performs better at flow maldistribution conditions. The trade-off was found to be at $F_x = F_{air} = 0.5$. At compensation by control of individual channel superheat the face split evaporator always performs better. Compared to the interlaced evaporator without compensation (the case mostly used today), the face split evaporator with compensation gives 7% increase in overall UA-value and up to 2.4% increase in COP.

The main reason for these conclusions is that the superheated zones with low UA-value is located in the first tube row of the coils for the face split evaporator, thus the driving potential for heat transfer (temperature difference) is the highest possible in these "weak" zones. In contrast, the interlaced evaporator has more than half of the superheated zone in the second tube row of the coils. At combined flow maldistribution of the inlet liquid/vapor phase maldistribution and the airflow maldistribution, the interlaced evaporator shows much better stability towards flow maldistribution than the face split evaporator. We find it interesting, that two similar combined maldistribution cases may show significant or no compensation potential at all, i.e. ($F_{air} = 0.5$ and $F_x = 0.8$) gives +3.2% and +7.0% for the interlaced and face split evaporator, respectively, and ($F_{air} = 0.5$ and $F_x = 1.2$) gives ∼0%. Only the face split evaporator with compensation seems to be able to compete with the use of the larger evaporator (10.5 kW) in the baseline system.

Since the interlaced circuitry is used today, it may be concluded that $F_{air} < 0.5$ if there is no inlet liquid/vapor maldistribution. Furthermore, the CFD simulation of the airflow profile across an A-coil revealed that the corresponding airflow distribution factor was around $0.15 \leq F_{air} \leq 0.20$. The CFD simulations showed a recirculation zone in the lower part of the coil, which causes low air velocities, poor air mixing and low heat transfer. Again, the face split evaporator with compensation performed best at these conditions.

Step 3: Liquid injection principle

The validation of the system dynamics in the numerical model showed that a slip flow model should be used for dynamic investigations. The homogeneous flow assumption gives too quick evaporator response, whereas the simple slip flow model by Zivi (1964) shows quite good comparison with experiments.

The liquid injection principle is essentially discontinuous liquid injection into each evaporator channels, thereby controlling individual channel superheats by distributing individual channel mass flow rate discontinuously. Two orifice designs were investigated, i.e. the multi-orifice (MO) design and the single-orifice (SO) design. The multi-orifice design allows for a secondary flow into the remaining channels at each channel injection.

The simulations of the discontinuous liquid injection principle showed that the performance decreases as the cycle time increases, i.e. the time it takes for one revolution where each channels are fed with refrigerant. Furthermore, the MO design showed better performance compared to the SO design, without considering the possible individual channel defrost possibility of the SO design for the face split circuitry. In addition, the main flow and the individual secondary flows in the MO design should be kept as even as possible while having the required mass flow distribution control band.

Based upon the four channel evaporator that are analyzed in this thesis, it is recommended that the cycle time should be kept below 10 and 6 seconds for the MO and SO designs, respectively. Furthermore, the flow ratio parameter should be around 0.6, or adapted to specific tube circuitry.

The simulations of the discontinuous liquid injection principle showed that the two-phase flow pulsations reduce the system performance. At airflow maldistribution, the trends of the discontinuous liquid injection principle are similar to the perfect control method (continuous mass flow distribution) used in chapter 5 in terms of overall UA-value, cooling capacity and COP for both the interlaced and the face split evaporator.

It should be stressed out that the correlations in the numerical model does not reflect the dynamic behavior of the pulsating flow, since they are based upon steady state experiments. Furthermore, the model showed spurious fluctuations in evaporating pressure. To draw detailed conclusions, further studies on pulsating flow in evaporators should be conducted.

7.3   Recommendations for further work

The recommendations for further work are divided into the following three groups: Model improvement, experimental validation and other further work.

Model improvement

There are several recommendations to improve the numerical model that are implemented in Modelica. The suggestions are listed below:

1. The refrigerant circuitry modeling does not support refrigerant splitting and joining inside the coil, and should be updated to model such evaporator circuitry.

2. The model supports only the louvered fin design and should be updated by implementing correlations for other fin designs also in order to model such. Furthermore, the correlations for frictional pressure drop should be implemented such that the fan power may be modeled and included in the definition of COP. This is especially important for part-load operation studies with varying fan speed.

3. An important delimitation in the model is that dehumidifying conditions are not supported. When the airflow is cooled the water vapor may partly condense on the evaporator surface. Typically, up to 50% of the total cooling capacity goes to the latent heat (water vapor condensation). Normally, the condensate is created in the first part of the evaporator seen from the airflow (first tube rows), and it may cause further degradations in cooling capacity and COP due to flow maldistribution. Therefore, it is an important point for further investigation.

4. The numerical model showed spurious fluctuations in pressure as the discontinuous liquid injection principle was simulated. These fluctuations have not been observed as high in any experiments carried out at Danfoss with high enough sampling frequency. For this reason, an investigation should be carried out in order to understand the causes of these fluctuations in the model. When these causes are established, the applicability of pulsating the two-phase flow for heat transfer augmenting may be analyzed.

5. The user-interface in Dymola should be improved for better ease of usability by developers and researchers. Furthermore, the documentation of the modeling work is so far limited to chapter 2 and 3 in this thesis, and should be improved and written in Modelica itself.

Experimental validation

The numerical model has been validated partly in steady state with experiments, however, these experiments were always system experiments and not dedicated to model validation. Moreover, the experiments did not measure individual channel mass flow rate, individual channel inlet vapor quality or airflow distribution such that all these variables needed to be guessed. A dedicated experiment with uniform inlet vapor quality, mass flow and airflow would have been sufficient to fully validate the model. Therefore, it is recommended to establish such experiments in order to achieve full model validation.

The actual value of the distribution parameters may also vary and are dependent on expansion valve, distributor and evaporator design and flow conditions. Experiments may also be carried out in order to measure the actual degrees of flow maldistribution that are caused by each phenomenon. For example, the airflow may be predicted by particle image velocimetry (PIV) measurements and the individual mass flow distribution may be measured at the individual channel outlets.

Furthermore, the introduction of pulsations to the two-phase flow should be investigated experimentally in order to fully evaluate the causes in cooling capacity and COP.

Other further work

It is obvious to perform an economic analysis by using the results of this thesis, including the variation in distribution parameters. A given improvement in UA-value can be translated into material cost saving, and a given improvement in COP can be translated into a running cost saving. These savings can be used to obtain guidelines for the maximum price of a compensation device that controls the individual channel superheats. The material cost savings directly gives the price to compare, however, the running cost savings also need the estimation of different payback times.
In this thesis we considered the flow maldistribution in the evaporator, however, there is also maldistribution issues in the condenser. For example, the inlet mass flow distribution and the airflow may be non-uniform. An analysis of the possible degradations in capacity and COP due to flow maldistribution in the condenser is also recommended for further work.

Bibliography

AbdelAziz, O., Singh, V., Aute, V., Radermacher, R., 2008. A-type heat exchanger simulation using 2-d cfd for airside heat transfer and pressure drop. In: 12th International Refrigeration and Air-Conditioning Conference at Purdue. No. 2200. West Lafayette, IN, USA.

ANSI/AHRI Standard 210/240, 2008. Performance Rating of Unitary Air-Conditioning & Air-Source Heat Pump Equipment. Air-Conditioning, Heating, and Refrigeration Institute, Arlington, VA 22201, USA.

ANSI/AHRI Standard 540, 2004. Standard For Performance Rating Of Positive Displacement Refrigerant Compressors And Compressor Units. Air-Conditioning, Heating, and Refrigeration Institute, Arlington, VA 22201, USA.

Antonius, J., 1998. Distribuerede fordampermodeller på flere detaljeringsniveauer. Master's thesis, Technical University of Denmark, Department of Energy Engineering.

Bauer, O., 1999. Modelling of two-phase flows with modelica. Master's thesis, Lund University, Department of Automatic Control.

Blasius, P. R. H., 2002. VDI Wärmeatlas, 9th Edition. Springer-Verlag Berlin Heidelberg New York.

Brix, W., Kærn, M. R., Elmegaard, B., 2009. Modelling refrigerant distribution in microchannel evaporators. International Journal of Refrigeration 32 (7), 1736 – 1743.

Brix, W., Kærn, M. R., Elmegaard, B., 2010. Modelling distribution of evaporating co2 in parallel minichannels. International Journal of Refrigeration 33 (6), 1086 – 1094.

Choi, J. M., Payne, W. V., Domanski, P. A., 2003. Effects of non-uniform refrigerant and air flow distributions on finned-tube evaporator performance. In: 21th International Congress of Refrigeration. IIR/IIF, Washington, D.C.

Collier, J. G., Thome, J. R., 1996. Convective Boiling and Condensation, 3rd Edition. Oxford Science Publications.

Dittus, E. J., Boelter, L. M. K., 1930. Publications on Engineering. Vol. 2. University of California, Berkeley.

Dix, G. E., 1971. Vapor void fraction for forced convection with subcooled boiling at low flow rates. Tech. rep., General Electric Company Report NEDO-10491.

Domanski, P. A., 1999. Finned-tube evaporator model with a visual interface. In: 20th International Congress of Refrigeration. Sydney, Australia.

Domanski, P. A., Yashar, D., 2007. Application of an evolution program for refrigerant circuitry optimization. In: ACRECONF "Challenges To Sustainability". New Delhi, India.

Dymola 7.4, 2010. Dynamic Modeling Laboratory, Dymola User's Manual, version 7.4. Dynasim AB, Research Park Ideon SE-223 70, Lund, Sweden.

Eborn, J., Tummescheit, H., Prölß, K., 2005. Airconditioning - a modelica library for dynamic simulation of ac systems. In: 4th International Modelica Conference. Hamburg, Germany, pp. 185 – 192.

EN 12900, 2005. Refrigerant compressors - Rating conditions, tolerances and presentation of manufacturer's performance data. European Committee for Standardization, Brussels.

Franke, R., Casella, F., Otter, M., Sielemann, M., Elmqvist, H., Mattson, S. E., Olsson, H., May 2009 2009. Stream connectors – an extension of modelica for device-oriented modeling of convective transport phenomena. In: 7th Modelica Conference. Como, Italy.

Fritzson, P., February 2004. Principles of Object-Oriented Modeling and Simulation with Modelica 2.1. Wiley-IEEE Press.

Fösel, G., 2009. Dynamic modeling of moving boundary evaporators. Diploma thesis, nr. d 08/92, Hochschule Karlsruhe, Technik und Wirtschaft, Fakultät für Maschinenbau und Mechatronik, Karlsruhe, Germany.

Funder-Kristensen, T., Nicolaisen, H., Holst, J., Rasmussen, M. H., Nissen, J. H., 2009. Refrigeration system. US Patent, Pub. No.: US 2009/0217687 A1.

Geary, D. F., 1975. Return bend pressure drop in refrigeration systems. ASHRAE Transactions 81, 250 — 264.

Ghiaasiaan, S. M., 2008. Two-phase flow: Boiling and Condensation in Conventional and Miniature Systems, 1st Edition. Cambridge University Press.

Gnielinski, V., 1976. New equation for heat and mass transfer in turbulent pipe and channel flow. International Chemical Engineering 16, 359 – 368.

Grönnerud, R., 1979. Investigation of liquid hold-up, flow-resistance and heat transfer in circulation type of evaporators, part iv: Two-phase flow resistance in boiling refrigerants. In: Annexe 1972-1, Bull. de l'Inst. du Froid.

Gunger, K. E., Winterton, R. H. S., 1986. A general correlation for flow boiling in tubes and annuli. International Journal of Heat and Mass Transfer 29, 351 – 358.

Gunger, K. E., Winterton, R. H. S., 1987. Simplified general correlation for saturated flow boiling and comparison of correlations with data. Chem. Eng. Res. Des. 65, 148 – 156.

Incropera, F. P., DeWitt, D. P., Bergman, T. L., Lavine, A. S., 2007. Introduction To Heat Transfer, 5th Edition. John Wiley & Sons.

Ito, H., 1960. Pressure losses in smooth pipe bends. Transactions ASME, Journal of Basic Engineering 82, 131 — 143.

Jakobsen, A., Antonius, J., Høgaard Knudsen, H. J., 1999. Experimental evaluation of the use of homogeneous and slip-flow two-ophase dynamic models in evaporator modelling. In: 20th International Congress of Refrigeration. IIR/IIF, Sydney.

Jensen, J. M., 2003. Dynamic modelling of thermo-fluid systems with focus on evaporators for refrigeration. Ph.D. thesis, Technical University of Denmark, Department of Mechanical Engineering.

Jiang, H., 2003. Development of a simulation and optimization tool for heat-exchanger design. Ph.D. thesis, University of Maryland at College Park, Department of Mechanical Engineering.

Jiang, H., Aute, V., Radermacher, R., 2006. Coildesigner: A general-purpose simulation and design tool for air to refrigerant heat exchangers. International Journal of Refrigeration 29, 601 – 610.

Kim, J.-H., Braun, J. E., Groll, E. A., 2009a. Evaluation of a hybrid method for refrigerant flow balancing in multi-circuit evaporators. International Journal of Refrigeration 32, 1283 – 1292.

Kim, J.-H., Braun, J. E., Groll, E. A., 2009b. A hybrid method for refrigerant flow balancing in multi-circuit evaporators: Upstream versus downstream flow control. International Journal of Refrigeration 32, 1271 – 1282.

Kærn, M. R., Brix, W., Elmegaard, B., Larsen, L. F. S., 2011a. Compensation of flow maldistribution in fin-and-tube evaporators for residential air-conditioning. International Journal of Refrigeration 34 (5), 1230 – 1237.

Kærn, M. R., Brix, W., Elmegaard, B., Larsen, L. F. S., 2011b. Performance of residential air-conditioning systems with flow maldistribution in fin-and-tube evaporators. International Journal of Refrigeration 34 (3), 696 – 706.

Kærn, M. R., Elmegaard, B., 2009. Analysis of refrigerant mal-distribution in fin-and-tube evaporators. In: Danske Køledage 2009. Odense, Denmark, pp. 25 – 35.

Kærn, M. R., Elmegaard, B., Larsen, L. F. S., 2009. Effect of refrigerant mal-distribution in fin-and-tube evaporators on system performance. In: 50th International Conference of Scandinavian Simulation Society. Fredericia, Denmark, pp. 315 – 322.

Kærn, M. R., Elmegaard, B., Larsen, L. F. S., 2011c. Comparison of fin-and-tube interlaced and face split evaporators with flow mal-distribution and compensation. In: 23th International Congress of Refrigeration. IIR/IIF, Prague, Czech Republic.

Kærn, M. R., Elmegaard, B., Larsen, L. F. S., 2011d. Experimental comparison of the dynamic evaporator response using homogeneous and slip flow modelling. In: 8th International Modelica Conference. Dresden, Germany.

Lee, J., Kwon, Y.-C., Kim, M. H., 2003. An improved method for analyzing a fin and tube evaporator containing a zeotropic mixture refrigerant with air mal-distribution. International Journal of Refrigeration 26, 707 – 720.

Li, G., Frankel, S., Braun, J. E., Groll, E. A., 2005. Application of cfd models to two-phase flow in refrigeration distributors. HVAC&R Research 11 (1), 45 – 62.

Liang, S. Y., Wong, T. N., Nathan, G. K., 2001. Numerical and experimental studies of refrigerant circuitry of evaporator coils. International Journal of Refrigeration 24 (8), 823 – 833.

Maa, X., Dinga, G., Zhanga, P., Hana, W., Kasaharab, S., Yamaguchib, T., 2009. Experimental validation of void fraction models for r410a air conditioners. International Journal of Refrigeration 32, 780 – 790.

Mader, G., Larsen, L. F. S., Fösel, G. P. F., 2010. Low charge system behavior - interactions of heat exchanger volumes and charge. In: 2nd Workshop on Refrigerant Charge Reduction. IIR, KTH, Stockholm, Sweden.

Mader, G., Thybo, C., 2010. An electronic expansion valve with automatic refrigerant distribution control. In: Deutsche Kälte-Klima-Tagung. Magdeburg, Germany.

Mills, A. F., 1999. Heat Transfer, 2nd Edition. Prentice Hall.

Müller-Steinhagen, H., Heck, K., 1986. A simple friction pressure drop correlation for two-phase flow in pipes. Chemical engineering and processing 20, 297 – 308.

Modelica Association, March 24 2010. Modelica ® - A Unified Object-Oriented Language for Physical Systems Modeling. Language Specification Version 3.2.

Nakayama, M., Sumida, Y., Hirakuni, S., Mochizuki, A., 2000. Development of a refrigerant two-phase flow distributor for a room air conditioner. In: 8th International Refrigeration Conference at Purdue. West Lafayette, IN, USA, pp. 313 – 319.

Patankar, S. V., 1980. Numerical heat transfer and fluid flow. Taylor & Francis.

Payne, W. V., Domanski, P. A., 2003. Potential benefits of smart refrigerant distributors. Final report No. ARTI-21CR/610-20050-01, Air-Conditioning and Refrigeration Technology Institute, Arlington, VA, USA.

Premoli, A., Francesco, D. D., Prina, A., 1971. A dimensional correlation for evaluating two-phase mixture density. La Termotecnica 25, 17 – 26.

Quibén, J. M., Thome, J. R., 2007. Flow pattern based two-phase frictional pressure drop model for horizontal tubes, part ii: New phenomenological model. International Journal of Heat and Fluid Flow 28, 1060 — 1072.

Richter, C. C., 2008. Proposal of new object-oriented equation-based model libraries for thermodynamic systems. Ph.D. thesis, Technische Universität Carolo-Wilhelmina zu Braunschweig, Fakultät für Maschinenbau.

Schmidt, T. E., 1949. Heat transfer calculations for extended surfaces. Refrigerating Engineering, 351 – 357.

Shah, M. M., 1979. A general correlation for heat transfer during film condensation inside pipes. International Journal of Heat and Mass Transfer 22, 547 – 556.

Shah, M. M., 1982. Chart correlation for saturated boiling heat transfer: Equations and further study. ASHRAE Transactions 88, 185 – 196.

Sinda/Fluint, 2008. Sinda/Fluint user's manual, General Purpose Thermal/Fluid Network Analyzer, version 5.2. Cullimore & Ring Technologies Inc., Littleton, Colorado, USA.

Skovrup, M. J., 2009. Thermodynamic and thermophysical properties of refrigerants. Department of Energy Engineering, Technical University of Denmark, Nils Koppels Allé, Building 402, DK-2800 Lyngby, Denmark.

Smith, S. L., 1969. Void fractions in two-phase flow. a correlation based upon an equal velocity head model. Proc. Inst. Mech. Eng. 184, 647 — 664.

STAR-CD 3.26, 2005. STAR-CD User Guide, version 3.26. CD-adapco, Melville, NY USA.

Steiner, D., 1993. Heat transfer to boiling saturated liquids, VDI-Wärmeatlas (VDI Heat Atlas). Verein Deutscher Ingenieure (Ed.), VDI-Gessellschaft Verfahrenstechnik und Chemie-ingenieurwesen (GCV), Düsseldorf, (Translator: J.W. Fullarton).

Thome, J. R., 1996. Boiling of new refrigerants a state-of-the-art review. International Journal of Refrigeration 19, 435 — 457.

Tiller, M., May 2001. Introduction to Physical Modeling with Modelica. Springer.

Tummescheit, H., Aug. 2002. Design and implementation of object-oriented model libraries using modelica. Ph.D. thesis, Department of Automatic Control, Lund Institute of Technology, Sweden.

United States Department of Energy, March 2011. 2010 Buildings Energy Data Book. by D&R International Ltd., Silver Spring, MD USA.

VDI Wärmeatlas, 2002. VDI Wärmeatlas, Berechnungsblätter für den Wärmeübergang, Springer-Verlag, Ch. Lab. 9th Edition, Dd 20,.

Wang, C.-C., Lee, C.-J., Chang, C.-T., Lin, S.-P., 1999. Heat transfer and friction correlation for compact louvered fin-and-tube heat exchangers. International Journal of Heat and Mass Transfer 42, 1945 – 1956.

Willatzen, M., Pettit, N. B. O. L., Ploug-Sørensen, L., 1998. A general dynamic simulation model for evaporators and condensers in refrigeration. part i: moving-boundary formulation of two-phase flows with heat exchange. International Journal of Refrigeration 21, 398 – 403.

Wojtan, L., Ursenbacher, T., Thome, J. R., 2005a. Investigation of flow boiling in horizontal tubes: Part i - a new diabatic two-phase flow pattern map. International Journal of Heat and Mass Transfer 48, 2955 – 2969.

Wojtan, L., Ursenbacher, T., Thome, J. R., 2005b. Investigation of flow boiling in horizontal tubes: Part ii - development of a new heat transfer model for stratified-wavy, dryout and mist flow regimes. International Journal of Heat and Mass Transfer 48, 2970 – 2985.

Wojtan, L., Ursenbacher, T., Thome, J. R., 2005c. Measurement of dynamic void fractions in stratified types of flow. Experimental Thermal and Fluid Science 29 (3), 383 – 392.

Woldesemayat, M. A., Ghajar, A. J., 2007. Comparison of void fraction correlations for different flow patterns in horizontal and upward inclined pipes. International Journal of Multiphase Flow 33 (4), 347 – 370.

Yashar, D. A., Cho, H. H., Domanski, P. A., 2008. Measurement of air-velocity profiles for finned tube heat exchangers using particle image velocimetry. In: 12th International Refrigeration and Air-Conditioning Conference at Purdue. No. 2195. West Lafayette, IN, USA.

Yashar, D. A., Domanski, P. A., 2010. Air flow distribution through an a-shaped evaporator under dry and wet coil conditions. In: 13th International Refrigeration and Air-Conditioning Conference at Purdue. No. 2100. West Lafayette, IN, USA.

Zhang, W.-J., Zhang, C.-L., 2006. A generalized moving-boundary model for transient simulation of dry-expansion evaporators under larger disturbances. International Journal of Refrigeration 29, 1119 – 1127.

Zhang, W.-J., Zhang, C.-L., Ding, G.-L., 2009. On three forms of momentum equation in transient modeling of residential refrigeration systems. International Journal of Refrigeration 32 (5), 938 – 944.

Zivi, S. M., 1964. Estimation of steady-state steam void-fraction by means of the principle of minimum entropy production. J. Heat Transf. 86, 247 – 252.

Two-phase flow formulation

In this chapter the governing equations for each phases will be derived in their differential form. The derivation shows clearly the phase interactions and transport phenomena. For simplicity the derivation will follow from a stratified flow pattern on the figures, however, it doesn't limit the generality to other flow patterns.

The solution of the local instantaneous differential equations in three dimensions for two-phase flow (evaporating or condensing) is impractical. The focus in this work is thus on one-dimensional area-and-time-averaged models of two-phase flow in pipes, where each phase is described by area-and-time-averaged quantities. By time-averaging the information of fluctuations is lost and can be considered as somewhat similar to averaging turbulent fluctuations in single-phase turbulent flow. The time-averaging is however at much smaller time-scales than the system dynamics of interest in this thesis. The area-averaging becomes a fact of the one-dimensionality, thus it is assumed that each phase can be described by its mean quantities. A further discussion on area-and-time-averaging is given in textbooks such as Ghiaasiaan (2008) or Collier and Thome (1996).

A.1   Notation

Some basic definitions and relations that apply for two-phase flow will be introduced in the following. The definitions and relations will be used intensively throughout this appendix. In the following, subscripts L and G denote liquid

and gas, respectively, whereas subscripts f and g denote saturated liquid and saturated gas, respectively.

The mass within a given control volume is known in single-phase flow, if two independent state variables are known, e.g. temperature and pressure. For two-phase flow the mass cannot be determined within the given control volume by measuring temperature and pressure. The gas to liquid fraction within the control volume is needed to determine its corresponding mass. The answer is the *void fraction*, defined by

$$\alpha = A_G/(A_G + A_L) = A_G/A \tag{A.1}$$

where A is the cross-sectional area.

In two-phase flow this variable needs a closure relation similarly to the heat transfer coefficient and friction coefficient for single-phase flow (see appendix C). Another important variable is the *vapor quality*, which is defined by

$$
\begin{aligned}
x &= \dot{m}_G/(\dot{m}_G + \dot{m}_L) = \dot{m}_G/\dot{m} \\
&= \rho_G U_G \alpha/[\rho_G U_G \alpha + \rho_L U_L (1 - \alpha)]
\end{aligned}
\tag{A.2}
$$

where $\dot{m}$ is the mass flow rate, ρ is the mean density and U is the mass-weighted mean velocity.

The vapor quality is sometimes called the mass quality or flow quality, however, it is by definition purely hydrodynamic. The use of mass quality is ambiguous, since is may be confused with the *static quality*, which relates the mass fractions as

$$
\begin{aligned}
x_{\text{st}} &= m_G/(m_G + m_L) = m_G/m \\
&= \rho_G \alpha/[\rho_G \alpha + \rho_L (1 - \alpha)]
\end{aligned}
\tag{A.3}
$$

where m is the mass.

By comparing equation A.2 and A.3 the difference is seen in the hydrodynamic and static nature of the vapor quality and static quality, respectively. Rewriting equation A.2 in terms of void fraction shows that

$$\alpha = \left(1 + \frac{\rho_G}{\rho_L} \frac{1-x}{x} S\right)^{-1} \tag{A.4}$$

where the *slip ratio*, $S = U_G/U_L$, has been introduced.

If one assumes that the flow is homogeneous, i.e both phases travel with the same velocity, then $S = 1$ and $x = x_{st}$. This can be used as a closure relation for void fraction, i.e. the *homogeneous void fraction*, as given by

$$\alpha_H = \left(1 + \frac{\rho_G}{\rho_L} \frac{1-x}{x}\right)^{-1} \tag{A.5}$$

Using the void fraction the two-phase *mixture density* (in situ or bulk density) is defined

$$\bar{\rho} = \rho_G \alpha + \rho_L(1 - \alpha) \tag{A.6}$$

It can be shown by substituting equation A.5 into A.6 that the *homogeneous density* becomes

$$\rho_H = \left(\frac{x}{\rho_G} + \frac{1 - x}{\rho_L} \right)^{-1} \tag{A.7}$$

By using the energy conservation principle through a cross-sectional area, the vapor quality can be related to the specific *mixed cup enthalpy*

$$
\begin{aligned}
\dot{m}h &= \dot{m}_G h_G + \dot{m}_L h_L \\
\Rightarrow \quad h &= x h_G + (1 - x) h_L \\
\Rightarrow \quad x &= (h - h_L)/(h_G - h_L)
\end{aligned}
\tag{A.8}
$$

The mixed cup enthalpy is also purely hydrodynamic, i.e. carried with the flow. Furthermore, a *thermodynamic equilibrium quality* (sometimes called thermodynamic quality) can be defined as

$$x_{\text{eq}} = (h - h_f)/(h_g - h_f) \tag{A.9}$$

Only when thermodynamic equilibrium exist, i.e. the liquid and vapor phases exist at saturated pressure, then the quality of equation A.2 and A.8 becomes equal to the thermodynamic equilibrium quality, $x = x_{eq}$.

The *mass flux* or sometimes called mass velocity is defined by

$$
\begin{aligned}
G &= \dot{m}/A = \bar{\rho}U \\
&= (\dot{m}_G + \dot{m}_L)/A \\
&= \rho_G U_G \alpha + \rho_L U_L(1 - \alpha) \\
&= G_G + G_L \\
&= Gx + G(1 - x)
\end{aligned}
\tag{A.10}
$$

From the identities in equation A.10 we have the following expressions for each phasic velocity

$$U_G = \frac{Gx}{\rho_G \alpha} \quad , \quad U_L = \frac{G(1 - x)}{\rho_L(1 - \alpha)} \tag{A.11}$$
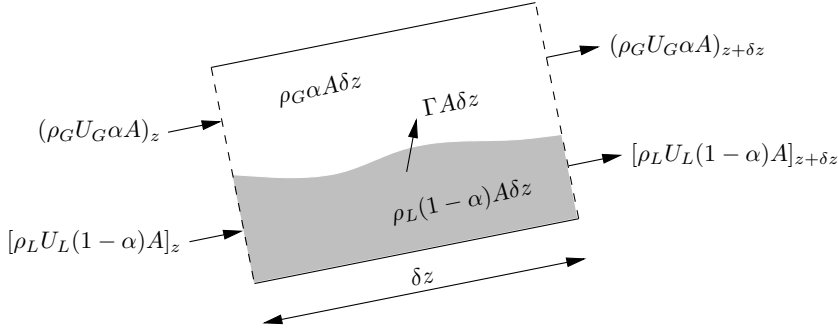
Figure A.1: Mass transfer terms on a slice of pipe

A.2   Mass conservation

To derive the mass conservation equations one applies the mass continuity principle for each phases to a slice of a pipe as depicted in figure A.1.

$$\frac{\partial}{\partial t}[\rho_L(1-\alpha)A\delta z] + \left(\rho_L U_L(1-\alpha)A + \delta z\frac{\partial}{\partial z}[\rho_L U_L(1-\alpha)A] + \cdots\right)$$
$$- \rho_L U_L(1-\alpha)A + \Gamma A\delta z = 0 \qquad\qquad\qquad (A.12)$$

$$\frac{\partial}{\partial t}(\rho_G\alpha A\delta z) + \left(\rho_G U_G\alpha A + \delta z\frac{\partial}{\partial z}(\rho_G U_G\alpha A) + \cdots\right)$$
$$- \rho_G U_G\alpha A - \Gamma A\delta z = 0 \qquad\qquad\qquad (A.13)$$

where δz is the length of the pipe element in the z-direction, t is the time and Γ is the interfacial mass transfer defined as rate of phase change per unit mixture volume and positive for evaporation.

The first term in the equations is the rate of change of mass within the phase control volume, the term in the round brackets is the outflow of mass (Taylor series expansion around z) and the third term is the inflow of mass at z. Dividing by δz and letting $\delta z \to 0$ the equations become

$$\frac{\partial}{\partial t}[\rho_L(1-\alpha)A] + \frac{\partial}{\partial z}[\rho_L U_L(1-\alpha)A] + \Gamma A = 0 \qquad\qquad (A.14)$$

$$\frac{\partial}{\partial t}(\rho_G\alpha A) + \frac{\partial}{\partial z}(\rho_G U_G\alpha A) - \Gamma A = 0 \qquad\qquad (A.15)$$

The mixture mass conservation equation is found by adding equation A.14 and A.15, where the interfacial mass transfer cancels out because of the mass

conservation across the interphase

$$\frac{\partial}{\partial t}\{[\rho_L(1-\alpha)+\rho_G\alpha]A\}+\frac{\partial}{\partial z}\{[\rho_L U_L(1-\alpha)+\rho_G U_G\alpha]A\}=0 \qquad \text{(A.16)}$$

which can be recast to the following form

$$\frac{\partial}{\partial t}(\bar{\rho}A)+\frac{\partial}{\partial z}(GA)=0 \qquad \text{(A.17)}$$

where the mixture density $\bar{\rho}$ and the mass flux G from equation A.6 and A.10 are used.

A.3 Momentum equation

The momentum equations are derived in similar manner as the mass conservation equations. Figure A.2 shows the momentum transfer terms for the two phases and figure A.3 shows the forces acting on the two phases on a slice of a pipe. U_I represents the axial interfacial velocity and F_I represents the interfacial force per unit mixture volume (positive when $U_G > U_L$). This force includes both interfacial friction and drag. The wall friction forces F_{wL} and F_{wG} are also defined per unit mixture volume and θ is the inclination angle to the horizontal plane.
To derive the momentum equation one applies Newton's 2$^{\text{nd}}$ law to each phases control volume in the flow direction.

$$\frac{\partial}{\partial t}[\rho_L U_L(1-\alpha)A\delta z]+\left(\rho_L U_L^2(1-\alpha)A+\delta z\frac{\partial}{\partial z}[\rho_L U_L^2(1-\alpha)A]+\cdots\right)$$
$$-\rho_L U_L^2(1-\alpha)A+\Gamma A\delta z U_I=$$
$$\left[p(1-\alpha)A-\left(p(1-\alpha)A+\delta z\frac{\partial}{\partial z}[p(1-\alpha)A]+\cdots\right)+p\frac{\partial}{\partial z}[(1-\alpha)A]\delta z\right]$$
$$-F_{wL}A\delta z-\rho_L(1-\alpha)gA\delta z\sin\theta+F_I A\delta z \qquad \text{(A.18)}$$

$$\frac{\partial}{\partial t}(\rho_G U_G\alpha A\delta z)+\left(\rho_G U_G^2\alpha A+\delta z\frac{\partial}{\partial z}(\rho_G U_G^2\alpha A)+\cdots\right)$$
$$-\rho_G U_G^2\alpha A-\Gamma A\delta z U_I=$$
$$\left[p\alpha A-\left(p\alpha A+\delta z\frac{\partial}{\partial z}(p\alpha A)+\cdots\right)+p\frac{\partial}{\partial z}(\alpha A)\delta z\right]$$
$$-F_{wG}A\delta z-\rho_G\alpha gA\delta z\sin\theta-F_I A\delta z \qquad \text{(A.19)}$$

The first term in the equations is the rate of change of momentum, the second term in the round brackets is the outflow of momentum, the third term is the
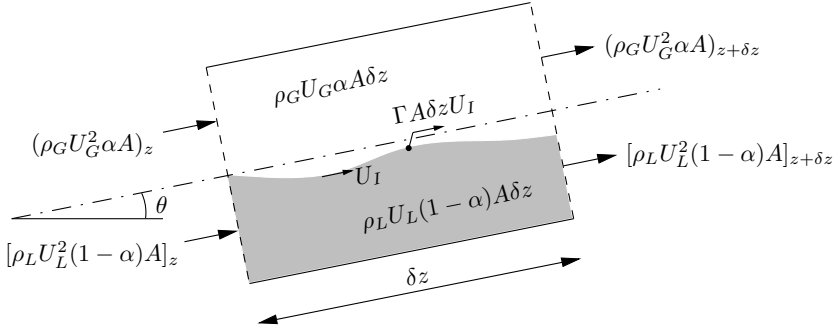
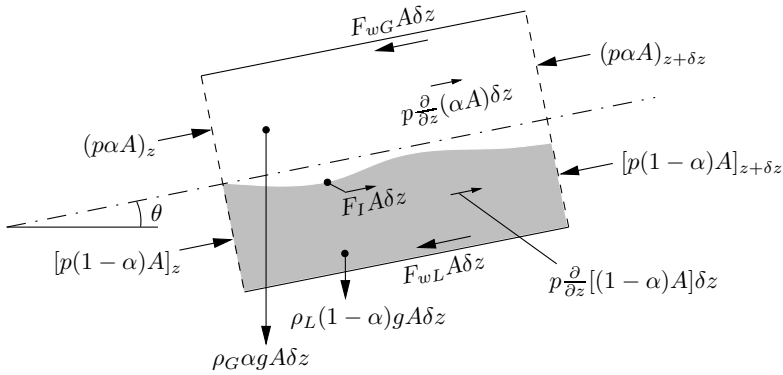Figure A.2: Momentum transfer terms on a slice of pipe

Figure A.3: Forces acting on the liquid and gas phase on a slice of pipe

inflow of momentum and the fourth term is the generation of momentum at the interphase due to mass transfer. On the right hand side the term in the square brackets is the pressure forces, the second term is the wall friction force, the third term is the gravitational force and the fourth term is the interfacial friction force. Dividing by δz and letting $\delta z \to 0$ the equations become

$$\frac{\partial}{\partial t}[\rho_L U_L(1-\alpha)A] + \frac{\partial}{\partial z}[\rho_L U_L^2(1-\alpha)A] + \Gamma A U_I =$$
$$- (1-\alpha)A\frac{\partial p}{\partial z} - F_{wL}A - \rho_L(1-\alpha)gA\sin\theta + F_I A \qquad (A.20)$$

$$\frac{\partial}{\partial t}(\rho_G U_G \alpha A) + \frac{\partial}{\partial z}(\rho_G U_G^2 \alpha A) - \Gamma A U_I =$$
$$- \alpha A \frac{\partial p}{\partial z} - F_{wG} A - \rho_G \alpha g A \sin\theta - F_I A \qquad (A.21)$$

The mixture momentum equation is obtained by adding equation A.20 and A.21, where conservation of momentum across the interphase requires that all the interfacial terms cancels out.

$$\frac{\partial}{\partial t}\{[\rho_L U_L(1-\alpha) + \rho_G U_G \alpha]A\} + \frac{\partial}{\partial z}\{[\rho_L U_L^2(1-\alpha) + \rho_G U_G^2 \alpha]A\} =$$
$$- A\frac{\partial p}{\partial z} - (F_{wL} + F_{wG})A - [\rho_L(1-\alpha) + \rho_G \alpha]\, gA \sin\theta \qquad (A.22)$$

The mixture momentum equation can be recast to the following form

$$\frac{\partial}{\partial t}(GA) + \frac{\partial}{\partial z}\left(\frac{G^2}{\rho'}A\right) = -A\frac{\partial p}{\partial z} - F_w A - \bar{\rho}g A \sin\theta \qquad (A.23)$$

where $\bar{\rho}$ and G are used from equation A.6 and A.10 and ρ' (sometimes called the momentum density) is defined

$$\rho' = \left(\frac{(1-x)^2}{\rho_L(1-\alpha)} + \frac{x^2}{\rho_G \alpha}\right)^{-1} \qquad (A.24)$$

The pressure drop for two-phase flow in steady state is then the sum of the accelerational, frictional and gravitational pressure drop, that is, the second, the fourth and fifth term of equation A.23. If the flow is assumed to be homogeneous it can be shown that $\rho' = \rho$.

A.4 Energy conservation

The energy conservation equations are derived in similar manner, although it is assumed that no heat generation occurs within the control volume and that heat diffusion/conduction is negligible in the convection dominated flow of forced evaporation or condensation. In the derivation two energy variables will be used for each phases, i.e. the total specific energy e_t and the specific convected energy e, given by

$$e_t = u + \frac{1}{2}U^2 + gz \sin\theta \qquad (A.25)$$

$$e = h + \frac{1}{2}U^2 + gz \sin\theta \qquad (A.26)$$

where u is the specific internal energy and h is the specific enthalpy, related by $u = h - p/\rho$. Figure A.4 shows the energy transfer and heat flow terms for

the two-phases and figure A.5 shows the work done on each phase on a slice of a pipe. q''_w represents the heat flux per unit surface area of the wall and P represents the perimeter. Subscripts GI and LI represents gas and liquid quantities at the interphase I, and subscripts wG and wL represents gas and liquid quantities at the wall w.

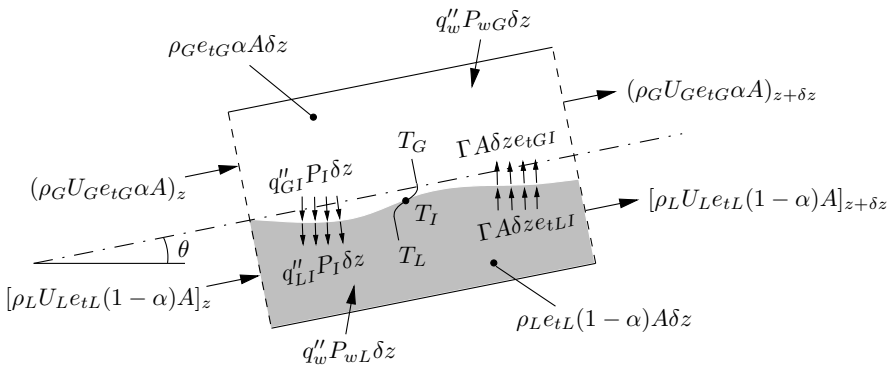To derive the energy conservation equations one applies the 1$^{\text{st}}$ law of thermodynamics to each phase control volume

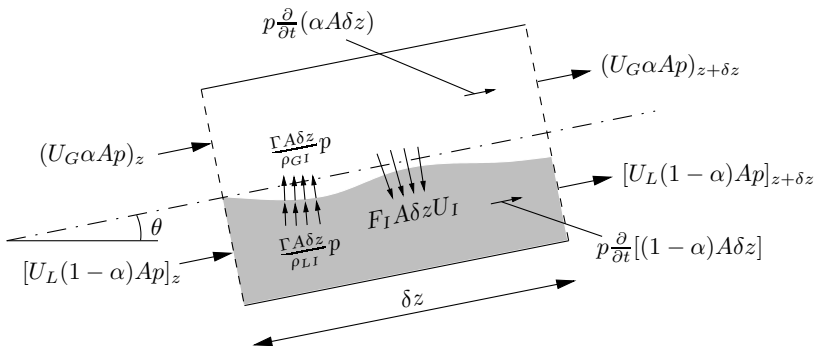Figure A.4: Energy transfer and heat flow terms on a slice of pipe

Figure A.5: Work terms on a slice of pipe

$$\frac{\partial}{\partial t}[\rho_L e_{tL}(1-\alpha)A\delta z] + \left(\rho_L U_L e_{tL}(1-\alpha)A + \delta z\frac{\partial}{\partial z}[\rho_L U_L e_{tL}(1-\alpha)A] + \cdots\right)$$
$$- \rho_L U_L e_{tL}(1-\alpha)A + \Gamma A\delta z e_{tLI} - q_w'' P_{wL}\delta z - q_{LI}'' P_I \delta z$$
$$+ \left[\left(U_L(1-\alpha)Ap + \delta z\frac{\partial}{\partial z}[U_L(1-\alpha)Ap] + \cdots\right) - U_L(1-\alpha)Ap\right]$$
$$+ p\frac{\partial}{\partial t}[(1-\alpha)A\delta z] + \frac{\Gamma A\delta z}{\rho_{LI}}p - F_I A\delta z U_I = 0 \tag{A.27}$$

$$\frac{\partial}{\partial t}(\rho_G e_{tG}\alpha A\delta z) + \left(\rho_G U_G e_{tG}\alpha A + \delta z\frac{\partial}{\partial z}(\rho_G U_G e_{tG}\alpha A) + \cdots\right)$$
$$- \rho_G U_G e_{tG}\alpha A - \Gamma A\delta z e_{tGI} - q_w'' P_{wG}\delta z + q_{GI}'' P_I \delta z$$
$$+ \left[\left(U_G\alpha Ap + \delta z\frac{\partial}{\partial z}(U_G\alpha Ap) + \cdots\right) - U_G\alpha Ap\right]$$
$$+ p\frac{\partial}{\partial t}(\alpha A\delta z) - \frac{\Gamma A\delta z}{\rho_{GI}}p + F_I A\delta z U_I = 0 \tag{A.28}$$

The first term in the equations is the rate of change of energy, the term in the round brackets is the outflow rate of energy, the third term is the inflow rate of energy and the fourth term is the rate of energy from the interphase due to mass transfer. The fifth term represents the heat flow across the wall and is defined as positive when $T_w > T_G$ or $T_w > T_L$. The sixth term is the heat flow across the interphase and is defined as positive when $T_G > T_L$. The term in the square brackets is the work done by pressure forces, whereas the remaining terms represent work done by pressure and friction at the interphase.
The equations simplify to the following form using minor mathematical manipulation, employing equation A.26, dividing by δz and letting $\delta z \to 0$.

$$\frac{\partial}{\partial t}\left[\rho_L\left(e_L - \frac{p}{\rho_L}\right)(1-\alpha)A\right] + \frac{\partial}{\partial z}[\rho_L U_L e_L(1-\alpha)A] + \Gamma A e_{LI}$$
$$- q_w'' P_{wL} - q_{LI}'' P_I - p\frac{\partial}{\partial t}(\alpha A) - F_I A U_I = 0 \tag{A.29}$$

$$\frac{\partial}{\partial t}\left[\rho_G\left(e_G - \frac{p}{\rho_G}\right)\alpha A\right] + \frac{\partial}{\partial z}(\rho_G U_G e_G\alpha A) - \Gamma A e_{GI}$$
$$- q_w'' P_{wG} + q_{GI}'' P_I + p\frac{\partial}{\partial t}(\alpha A) + F_I A U_I = 0 \tag{A.30}$$

The mixture energy equation is obtained by adding equation A.29 and A.30, where conservation of energy across the interphase requires that all the inter-

facial terms cancel out.

$$\frac{\partial}{\partial t}\{[\rho_L e_L(1-\alpha)+\rho_G e_G\alpha-(1-\alpha)p-\alpha p]A\}$$
$$+\frac{\partial}{\partial z}\{[\rho_L U_L(1-\alpha)e_L+\rho_G U_G\alpha e_G]A\}=(P_{wL}+P_{wG})q_w'' \qquad (A.31)$$

Substituting from equation A.26 shows the kinetic and potential energy contributions.

$$\frac{\partial}{\partial t}\left\{\left[\rho_L(1-\alpha)\left(h_L+\frac{U_L{}^2}{2}+gz\sin\theta\right)+\rho_G\alpha\left(h_G+\frac{U_G{}^2}{2}+gz\sin\theta\right)-p\right]A\right\}$$
$$+\frac{\partial}{\partial z}\left\{\left[\rho_L U_L(1-\alpha)\left(h_L+\frac{U_L{}^2}{2}\right)+\rho_G U_G\alpha\left(h_G+\frac{U_G{}^2}{2}\right)\right]A\right\}=$$
$$P_w q_w''-[\rho_L U_L(1-\alpha)+\rho_G U_G\alpha]Ag\sin\theta \qquad (A.32)$$

which can be recast to the following form

$$\frac{\partial}{\partial t}\left[\left(\bar{\rho}\bar{h}+\frac{G^2}{2\rho'}+\bar{\rho}gz\sin\theta-p\right)A\right]+\frac{\partial}{\partial z}\left[\left(Gh+\frac{G^3}{2\rho''^2}\right)A\right]=Pq_w''-GAg\sin\theta \qquad (A.33)$$

where $\bar{\rho}$, G and ρ' are given by equation A.6, A.10 and A.24 and ρ'' is defined

$$\rho''=\left[\left(\frac{(1-x)^3}{[\rho_L(1-\alpha)]^2}+\frac{x^3}{(\rho_G\alpha)^2}\right)^{-1}\right]^{1/2} \qquad (A.34)$$

Two different definitions of the mixture enthalpy appears, $\bar{h}$ is the specific *in situ mixture enthalpy* or bulk enthalpy (based on a frozen flow field) and defined by

$$\bar{h}=[\rho_L h_L(1-\alpha)+\rho_G h_G\alpha]/\bar{\rho} \qquad (A.35)$$

and h is the specific *mixed cup enthalpy* defined by equation A.8. It can be shown that the static quality from equation A.3 can be used to calculate the in situ mixture enthalpy as $\bar{h}=(1-x_{st})h_L+x_{st}h_G$. Again the hydrodynamic and static nature of h and $\bar{h}$ are seen from their definitions. Furthermore, if one assumes the flow to be homogeneous then $h=\bar{h}$ and $\rho''=\rho$.

A.5   Comments and assumptions

An additional force (virtual mass force) occurs when the gas phase is dispersed and even then only at high acceleration conditions like "choked flow". It occurs when one of the phases accelerates with respect to the other phase. A detailed discussion is given in Ghiaasiaan (2008). This force would have to be included in the momentum equations and energy equations for this extreme case.

The separated flow model has six equations and they can be chosen as either the individual phasic equations or one of the phases equations plus the mixture equations. If thermodynamic equilibrium conditions may be assumed then only one energy equation is needed. The fact that we assume thermodynamic equilibrium conditions, implies that the heat transfer taking place on the interphase is infinitively fast. If we had non-equilibrium conditions one had to deal with heat transfer coefficients on the interphase to each phase bulk.

By using the thermodynamic equilibrium assumption the subscripts L and G turn into subscripts f and g, thus the liquid and vapor are at saturation.

The purpose of using two momentum equations would be to model accelerational effects of evaporation or condensation. This involves determining the interfacial surface area, interfacial velocity and interfacial force, which are all flow regime dependant. The interfacial mass transfer are then given by solving two mass transfer equations. More information are given in textbooks such as Ghiaasiaan (2008).

For the purpose of this project we will use mixture equations only, that is only three equations describing mixture quantities. This way we will not have to deal with interfacial parameters. Slip between the phases may be realized through proper use of the void fraction correlation, i.e. from equation A.4 the slip can be calculated. We assume that thermodynamic equilibrium exists and that accelerational effects due to individual phase velocity difference are negligible. Furthermore, we assume that changes in kinetic and potential energies are negligible. Then the mixture equations become.

$$A\frac{\partial \bar{\rho}}{\partial t} + \frac{\partial \dot{m}}{\partial z} = 0 \tag{A.36}$$

$$\frac{\partial \dot{m}}{\partial t} + \frac{\partial}{\partial z}\left(\frac{\dot{m}^2}{\rho' A}\right) = -A\frac{\partial p}{\partial z} - F_w A - \bar{\rho}gA\sin\theta \tag{A.37}$$

$$A\frac{\partial}{\partial t}\left(\bar{\rho}\bar{h} - p\right) + \frac{\partial}{\partial z}\left(\dot{m}h\right) = Pq_w'' \tag{A.38}$$

where we have substituted the mass flux with mass flow rate divided by the cross-sectional area.

The heat flux will be described by using the heat transfer coefficient, that is

$$q_w'' = h_{\text{tc}}(T_w - T_r) \tag{A.39}$$

where subscripts w and r denote wall and refrigerant, respectively, and h_{tc} denote the heat transfer coefficient. The latter needs to be calculated by empirical correlations from the literature (see appendix C). The wall friction force defined per unit volume is in fact the frictional pressure gradient and defined by

$$F_w = -\left(\frac{dp}{dz}\right)_{fric} = \frac{\tau_w P}{A} \tag{A.40}$$

where τ_w is the wall shear stress and may be related to the *Fanning friction factor* by

$$\tau_w = f_F \frac{\bar{\rho} U^2}{2} = f_F \frac{\dot{m}^2}{2\bar{\rho} A^2} \tag{A.41}$$

For pipe flow of constant cross-sectional area, the wall friction force becomes

$$F_w = f_F \frac{P}{A} \frac{\dot{m}^2}{2\bar{\rho} A^2} \tag{A.42}$$

$$= f_F \frac{\pi d}{\frac{\pi}{4} d^2} \frac{\dot{m}^2}{2\bar{\rho} A^2} \tag{A.43}$$

$$= f_F 4 \frac{1}{d} \frac{\dot{m}^2}{2\bar{\rho} A^2} \tag{A.44}$$

$$= f_D \frac{1}{d} \frac{\dot{m}^2}{2\bar{\rho} A^2} \tag{A.45}$$

where the *Darcy-Weisbach friction factor* has been used. The Darcy-Weisbach friction factor is four times larger than the Fanning friction factor. The *Darcy-Weisbach friction factor* is also called the *Moody friction factor*, since it is referred to in *Moody diagrams*. The friction factor or frictional pressure gradient also needs to be calculated by an empirical correlation from the literature (see appendix C).

Appendix B

Moving boundary formulation

The moving boundary model will be derived in this appendix for the condenser. When one understands the methodology in the derivation, it should be easy to derive the formulation for an evaporator, which is a bit different.

The moving boundary models averages the vapor, liquid and two-phase region. Therefore, the conservation equations are only needed for these 3 regions. However, sometimes under larger disturbances the liquid in the condenser may be drained in to the evaporator, thus the liquid region will disappear and only 2 regions will exist. Therefore, it is needed to switch model equations. The switching between the model equations essentially requires a modeling environment capable of handling events.

In the following, when 3 regions exist the model is called the V-TP-L model and when 2 regions exist the model is called the V-TP model. The outlet enthalpy will be used to determine which model to use, i.e. if two-phase is flowing out of the condenser ($h_{\text{out}} \geq h_f$), then the V-TP model is used.

B.1   V-TP-L model

All regions exist in this model as shown on figure B.1. The regions are denoted by subscripts 1, 2 and 3, meaning the vapor, two-phase and liquid region, respectively. Note that the bar operator (e.g. $\bar{\rho}_2$ and $\bar{h}_2$) means averaging in

both cross-sectional area and length of the region in this appendix, whereas the use of subscripts 1 to 3 (e.g. ρ_2 and h_2) means cross-sectional area averaged only. These averaged quantities are all in situ quantities based on a frozen field. In contrast, the quantities denoted by subscripts in, out, A and B (e.g. h_B) are mixed cup quantities and hydrodynamic (carried with the flow). More information are given about the two-phase flow notation in appendix A.
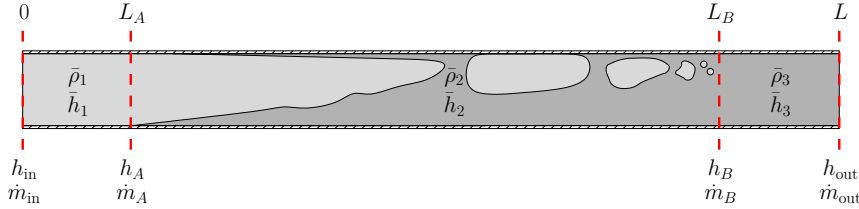

Figure B.1: Moving boundary model structure (condenser)

B.1.1 Two-phase region

Integration of the mass conservation equation (A.36) across the two-phase region yields

$$A\int_{L_A}^{L_B} \frac{\partial \rho_2}{\partial t} dz = \dot{m}_A - \dot{m}_B \qquad (B.1)$$

where ρ_2 is the mixture density defined by equation A.6. Application of the Leibnitz's rule gives

$$A\frac{d}{dt}\int_{L_A}^{L_B} \rho_2 dz + A\rho_g \frac{dL_A}{dt} - A\rho_f \frac{dL_B}{dt} = \dot{m}_A - \dot{m}_B \qquad (B.2)$$

where the first term can be integrated as

$$A\frac{d}{dt}\int_{L_A}^{L_B} \rho_2 dz = A\frac{d}{dt}\left(\bar{\rho}_2 L_B - \bar{\rho}_2 L_A\right)$$

$$= A\left[\bar{\rho}_2\left(\frac{dL_B}{dt} - \frac{dL_A}{dt}\right) + (L_B - L_A)\frac{d\bar{\rho}_2}{dt}\right] \qquad (B.3)$$

where $\bar{\rho}_2 = \frac{1}{L_B - L_A}\int_{L_A}^{L_B} \rho_2 dz$ is the mean mixture density in the two-phase region. Substituting equation B.3 in B.2 the mass conservation finally results in

$$A(L_B - L_A)\frac{d\bar{\rho}_2}{dt} + A(\rho_g - \bar{\rho}_2)\frac{dL_A}{dt} + A(\bar{\rho}_2 - \rho_f)\frac{dL_B}{dt} = \dot{m}_A - \dot{m}_B \qquad (B.4)$$

Integration of the energy conservation equation (A.38) across the two-phase region yields

$$A \int_{L_A}^{L_B} \frac{\partial \rho_2 h_2}{\partial t} dz - A(L_B - L_A)\frac{dp}{dt} = (\dot{m}h)_A - (\dot{m}h)_B + \dot{Q}_{\text{tp}} \qquad \text{(B.5)}$$

where $\dot{Q}_{\text{tp}}$ is the heat transfer in the two-phase region, h_A and h_B is the mixed cup enthalpy defined by equation A.8 and h_2 is the in situ mixture enthalpy defined by A.35. Application of the Leibnitz's rule gives

$$A\frac{d}{dt} \int_{L_A}^{L_B} \rho_2 h_2 dz + A\rho_g h_g \frac{dL_A}{dt} - A\rho_f h_f \frac{dL_B}{dt} - A(L_B - L_A)\frac{dp}{dt} =$$
$$(\dot{m}h)_A - (\dot{m}h)_B + \dot{Q}_{\text{tp}} \qquad \text{(B.6)}$$

where the first term can be integrated as

$$A\frac{d}{dt} \int_{L_A}^{L_B} \rho_2 h_2 dz = A\frac{d}{dt}\left(\bar{\rho}_2 \bar{h}_2 L_B - \bar{\rho}_2 \bar{h}_2 L_A\right)$$
$$= A\left[\bar{\rho}_2 \bar{h}_2 \left(\frac{dL_B}{dt} - \frac{dL_A}{dt}\right) + (L_B - L_A)\frac{d\bar{\rho}_2 \bar{h}_2}{dt}\right] \text{(B.7)}$$

where $\bar{h}_2 = \frac{1}{L_B - L_A} \int_{L_A}^{L_B} h_2 dz$ is the mean in situ mixture enthalpy in the two-phase region. Substituting equation B.7 in B.6 the energy conservation finally results in

$$A(L_B - L_A)\left(\frac{d\bar{\rho}_2 \bar{h}_2}{dt} - \frac{dp}{dt}\right) + A(\rho_g h_g - \bar{\rho}_2 \bar{h}_2)\frac{dL_A}{dt} +$$
$$A(\bar{\rho}_2 \bar{h}_2 - \rho_f h_f)\frac{dL_B}{dt} = (\dot{m}h)_A - (\dot{m}h)_B + \dot{Q}_{\text{tp}} \qquad \text{(B.8)}$$

The mean mixture density and the mean in situ enthalpy can be calculated from the mean void fraction in the two-phase region, similarly to the definitions from equation A.6 and A.35.

$$\bar{\rho}_2 = \rho_g \bar{\alpha} + \rho_f(1 - \bar{\alpha}) \qquad \text{(B.9)}$$

$$\bar{\rho}_2 \bar{h}_2 = \rho_g h_g \bar{\alpha} + \rho_f h_f(1 - \bar{\alpha}) \qquad \text{(B.10)}$$

where the mean void fraction in the two-phase region is computed by numerical integration of a given void fraction correlation from the literature as

$$\bar{\alpha} = \frac{1}{L_B - L_A} \int_{L_A}^{L_B} \alpha dz \approx \frac{1}{N} \sum_{n=1}^{N} \alpha_n \qquad \text{(B.11)}$$

where $N = 10$ should be reasonable accurate and is used here.

Transformation of the derivatives of $\bar{\rho}_2$ and $\bar{h}_2$ are carried out keeping in mind that the properties at saturation and the mean void fraction in the two-phase region are functions of pressure.

$$
\begin{aligned}
\frac{d\bar{\rho}_2}{dt} &= \frac{d\rho_g\bar{\alpha}}{dt} + \frac{d\rho_f(1-\bar{\alpha})}{dt} \\
&= \left(\frac{\partial \rho_g}{\partial p}\bar{\alpha} + \frac{\partial \rho_f}{\partial p}(1-\bar{\alpha}) + (\rho_g - \rho_f)\frac{\partial \bar{\alpha}}{\partial p} \right) \frac{dp}{dt}
\end{aligned}
\tag{B.12}
$$

$$
\begin{aligned}
\frac{d\bar{\rho}_2\bar{h}_2}{dt} &= \frac{d\rho_g h_g\bar{\alpha}}{dt} + \frac{d\rho_f h_f(1-\bar{\alpha})}{dt} \\
&= \left(\frac{\partial \rho_g h_g}{\partial p}\bar{\alpha} + \frac{\partial \rho_f h_f}{\partial p}(1-\bar{\alpha}) + (\rho_g h_g - \rho_f h_f)\frac{\partial \bar{\alpha}}{\partial p} \right) \frac{dp}{dt}
\end{aligned}
\tag{B.13}
$$

where the partial derivatives with respect to pressure are calculated by numerical finite difference as

$$
\frac{\partial \psi}{\partial p} = \frac{\psi(p + \Delta p) - \psi(p)}{\Delta p}
\tag{B.14}
$$

where ψ denotes ρ_g, ρ_f, $\rho_g h_g$, $\rho_f h_f$ or $\bar{\alpha}$.

Finally, we need the mean heat transfer coefficient in the two-phase region, which also is computed by numerical integration as

$$
\bar{h}_{\text{tc}} = \frac{1}{L_B - L_A} \int_{L_A}^{L_B} h_{\text{tc}} dz \approx \frac{1}{N} \sum_{n=1}^{N} h_{\text{tc,n}}
\tag{B.15}
$$

where $N = 10$ is used here.

B.1.2 Vapor region

Integration of the mass conservation equation (A.36) across the vapor region yields

$$
A \int_0^{L_A} \frac{\partial \rho_1}{\partial t} dz = \dot{m}_{\text{in}} - \dot{m}_A
\tag{B.16}
$$

Application of the Leibnitz's rule gives

$$
A \frac{d}{dt} \int_0^{L_A} \rho_1 dz - A\rho_g \frac{dL_A}{dt} = \dot{m}_{\text{in}} - \dot{m}_A
\tag{B.17}
$$

where the first term can be integrated as

$$
\begin{aligned}
A\frac{d}{dt}\int_0^{L_A}\rho_1 dz &= A\frac{d}{dt}\left(\bar{\rho}_1 L_A\right) \\
&= A\left(\bar{\rho}_1\frac{dL_A}{dt}+L_A\frac{d\bar{\rho}_1}{dt}\right)
\end{aligned} \tag{B.18}
$$

where $\bar{\rho}_1=\frac{1}{L_A}\int_0^{L_A}\rho_1 dz$ is the mean density in the vapor region. Substituting equation B.18 in B.17 the mass conservation finally results in

$$
AL_A\frac{d\bar{\rho}_1}{dt}+A(\bar{\rho}_1-\rho_g)\frac{dL_A}{dt}=\dot{m}_{\text{in}}-\dot{m}_A \tag{B.19}
$$

Integration of the energy conservation equation (A.38) across the vapor region yields

$$
A\int_0^{L_A}\frac{\partial\rho_1 h_1}{\partial t}dz-AL_A\frac{dp}{dt}=(\dot{m}h)_{\text{in}}-(\dot{m}h)_A+\dot{Q}_g \tag{B.20}
$$

where $\dot{Q}_g$ is the heat transfer in the vapor region. Application of the Leibnitz's rule gives

$$
A\frac{d}{dt}\int_0^{L_A}\rho_1 h_1 dz-A\rho_g h_g\frac{dL_A}{dt}-AL_A\frac{dp}{dt}=(\dot{m}h)_{\text{in}}-(\dot{m}h)_A+\dot{Q}_g \tag{B.21}
$$

where the first term can be integrated as

$$
\begin{aligned}
A\frac{d}{dt}\int_0^{L_A}\rho_1 h_1 dz &= A\frac{d}{dt}\left(\bar{\rho}_1\bar{h}_1 L_A\right) \\
&= A\left(\bar{\rho}_1\bar{h}_1\frac{dL_A}{dt}+\bar{\rho}_1 L_A\frac{d\bar{h}_1}{dt}+\bar{h}_1 L_A\frac{d\bar{\rho}_1}{dt}\right)
\end{aligned} \tag{B.22}
$$

where $\bar{h}_1=\frac{1}{L_A}\int_0^{L_A}h_1 dz$ is the mean enthalpy in the vapor region. Substituting equation B.22 in B.21 the energy conservation finally results in

$$
AL_A\left(\bar{\rho}_1\frac{d\bar{h}_1}{dt}+\bar{h}_1\frac{d\bar{\rho}_1}{dt}-\frac{dp}{dt}\right)+A(\bar{\rho}_1\bar{h}_1-\rho_g h_g)\frac{dL_A}{dt}=(\dot{m}h)_{\text{in}}-(\dot{m}h)_A+\dot{Q}_g \tag{B.23}
$$

The mean enthalpy is simply calculated by taking the average of h_g and h_{in}. The mean density is calculated from the mean enthalpy and pressure. The transformation of the derivatives of $\bar{\rho}_1$ and $\bar{h}_1$ are then.

$$
\begin{aligned}
\frac{d\bar{h}_1}{dt} &= \frac{d}{dt}\left(\frac{h_g+h_{\text{in}}}{2}\right) \\
&= \frac{1}{2}\frac{\partial h_g}{\partial p}\frac{dp}{dt}+\frac{1}{2}\frac{dh_{\text{in}}}{dt}
\end{aligned} \tag{B.24}
$$

$$\frac{d\bar{\rho}_1}{dt} = \frac{\partial\bar{\rho}_1}{\partial p}\bigg|_{\bar{h}_1}\frac{dp}{dt} + \frac{\partial\bar{\rho}_1}{\partial\bar{h}_1}\bigg|_p\frac{d\bar{h}_1}{dt} \tag{B.25}$$

where the partial derivatives with respect to pressure are calculated according to equation B.14, whereas the partial derivatives with respect to pressure at constant enthalpy and vice versa are calculated by

$$\frac{\partial\psi}{\partial p}\bigg|_h = \frac{\psi(p + \Delta p, h) - \psi(p, h)}{\Delta p} \tag{B.26}$$

$$\frac{\partial\psi}{\partial h}\bigg|_p = \frac{\psi(p, h + \Delta h) - \psi(p, h)}{\Delta h} \tag{B.27}$$

where ψ denotes $\bar{\rho}_1$.

Finally, we need the mean heat transfer coefficient in the vapor region, which is calculated from the thermodynamic mean state (mean enthalpy, pressure) and mean mass flow rate according to single-phase flow correlations.

B.1.3 Liquid region

It is trivial to show the derivation of the average conservation equations for the liquid region, which is exactly the same as for the vapor region. However, the final equations are summarized as

$$A(L - L_B)\frac{d\bar{\rho}_3}{dt} + A(\rho_f - \bar{\rho}_3)\frac{dL_B}{dt} = \dot{m}_B - \dot{m}_{\text{out}} \tag{B.28}$$

$$A(L - L_B)\left(\bar{\rho}_3\frac{d\bar{h}_3}{dt} + \bar{h}_3\frac{d\bar{\rho}_3}{dt} - \frac{dp}{dt}\right) + A(\rho_f h_f - \bar{\rho}_3\bar{h}_3)\frac{dL_B}{dt} = $$
$$(\dot{m}h)_B - (\dot{m}h)_{\text{out}} + \dot{Q}_f \tag{B.29}$$

where $\dot{Q}_f$ is the heat transfer in the liquid region. Similar transforms for the derivatives of $\bar{\rho}_3$ and $\bar{h}_3$ are used as for the vapor region, and similar heat transfer coefficient calculation.

B.2 V-TP model

In this model the liquid region does not exist, thus $L_B = L$ and $\dot{m}_B = \dot{m}_{\text{out}}$. The equations for the vapor region remains the same as in the V-TP-L model, however, the two-phase region must be derived from the governing equations again a little bit differently. The main difference is that the void fraction becomes a function of outlet enthalpy also, and in turn affects the mean density and mean enthalpy in the two-phase region.

Integration of the mass conservation equation (A.36) across the two-phase region yields

$$A \int_{L_A}^{L} \frac{\partial \rho_2}{\partial t} dz = \dot{m}_A - \dot{m}_{\text{out}} \qquad (B.30)$$

Application of the Leibnitz's rule gives

$$A \frac{d}{dt} \int_{L_A}^{L} \rho_2 dz + A \rho_g \frac{dL_A}{dt} = \dot{m}_A - \dot{m}_{\text{out}} \qquad (B.31)$$

where the first term can be integrated as

$$\begin{aligned} A \frac{d}{dt} \int_{L_A}^{L} \rho_2 dz &= A \frac{d}{dt} \left(\bar{\rho}_2 L - \bar{\rho}_2 L_A \right) \\ &= A \left[-\bar{\rho}_2 \frac{dL_A}{dt} + (L - L_A) \frac{d\bar{\rho}_2}{dt} \right] \end{aligned} \qquad (B.32)$$

where $\bar{\rho}_2 = \frac{1}{L-L_A} \int_{L_A}^{L} \rho_2 dz$ is the mean mixture density in the two-phase region. Substituting equation B.32 in B.31 the mass conservation finally results in

$$A(L - L_A) \frac{d\bar{\rho}_2}{dt} + A(\rho_g - \bar{\rho}_2) \frac{dL_A}{dt} = \dot{m}_A - \dot{m}_{\text{out}} \qquad (B.33)$$

Integration of the energy conservation equation (A.38) across the two-phase region yields

$$A \int_{L_A}^{L} \frac{\partial \rho_2 h_2}{\partial t} dz - A(L - L_A) \frac{dp}{dt} = (\dot{m}h)_A - (\dot{m}h)_{\text{out}} + \dot{Q}_{\text{tp}} \qquad (B.34)$$

Application of the Leibnitz's rule gives

$$A \frac{d}{dt} \int_{L_A}^{L} \rho_2 h_2 dz + A \rho_g h_g \frac{dL_A}{dt} - A(L-L_A) \frac{dp}{dt} = (\dot{m}h)_A - (\dot{m}h)_{\text{out}} + \dot{Q}_{\text{tp}} \quad (B.35)$$

where the first term can be integrated as

$$\begin{aligned} A \frac{d}{dt} \int_{L_A}^{L} \rho_2 h_2 dz &= A \frac{d}{dt} \left(\bar{\rho}_2 \bar{h}_2 L - \bar{\rho}_2 \bar{h}_2 L_A \right) \\ &= A \left[-\bar{\rho}_2 \bar{h}_2 \frac{dL_A}{dt} + (L - L_A) \frac{d\bar{\rho}_2 \bar{h}_2}{dt} \right] \end{aligned} \qquad (B.36)$$

where $\bar{h}_2 = \frac{1}{L-L_A} \int_{L_A}^{L} h_2 dz$ is the mean in situ enthalpy in the two-phase region. Substituting equation B.36 in B.35 the energy conservation finally results in

$$A(L - L_A) \left(\frac{d\bar{\rho}_2 \bar{h}_2}{dt} - \frac{dp}{dt} \right) + A(\rho_g h_g - \bar{\rho}_2 \bar{h}_2) \frac{dL_A}{dt} = (\dot{m}h)_A - (\dot{m}h)_{\text{out}} + \dot{Q}_{\text{tp}} \qquad (B.37)$$

The mean mixture density and the mean in situ enthalpy in the two-phase region can be calculated from the mean void fraction in the two-phase region, similarly to equation B.9 and B.10, however, the void fraction is computed from L_A to L as

$$\bar{\alpha} = \frac{1}{L - L_A} \int_{L_A}^{L} \alpha \, dz \approx \frac{1}{N} \sum_{n=1}^{N} \alpha_n \tag{B.38}$$

where $N = 10$ is used.

Transformation of the derivatives of $\bar{\rho}_2$ and $\bar{h}_2$ are also a bit different, since they are now dependent on the outlet enthalpy and not only on the pressure.

$$
\begin{aligned}
\frac{d\bar{\rho}_2}{dt} &= \frac{d\rho_g \bar{\alpha}}{dt} + \frac{d\rho_f (1 - \bar{\alpha})}{dt} \\
&= \frac{\partial \rho_g}{\partial t} \bar{\alpha} + \frac{\partial \rho_f}{\partial t}(1 - \bar{\alpha}) + (\rho_g - \rho_f)\frac{\partial \bar{\alpha}}{\partial t} \\
&= \left(\frac{\partial \rho_g}{\partial p} \bar{\alpha} + \frac{\partial \rho_f}{\partial p}(1 - \bar{\alpha}) \right) \frac{dp}{dt} \\
&\quad + (\rho_g - \rho_f) \left(\left.\frac{\partial \bar{\alpha}}{\partial p}\right|_{h_{\text{out}}} \frac{dp}{dt} + \left.\frac{\partial \bar{\alpha}}{\partial h_{\text{out}}}\right|_{p} \frac{dh_{\text{out}}}{dt} \right)
\end{aligned}
\tag{B.39}
$$

$$
\begin{aligned}
\frac{d\bar{\rho}_2 \bar{h}_2}{dt} &= \frac{d\rho_g h_g \bar{\alpha}}{dt} + \frac{d\rho_f h_f (1 - \bar{\alpha})}{dt} \\
&= \frac{\partial \rho_g h_g}{\partial t} \bar{\alpha} + \frac{\partial \rho_f h_f}{\partial t}(1 - \bar{\alpha}) + (\rho_g h_g - \rho_f h_f)\frac{\partial \bar{\alpha}}{\partial t} \\
&= \left(\frac{\partial \rho_g h_g}{\partial p} \bar{\alpha} + \frac{\partial \rho_f h_f}{\partial p}(1 - \bar{\alpha}) \right) \frac{dp}{dt} \\
&\quad + (\rho_g h_g - \rho_f h_f) \left(\left.\frac{\partial \bar{\alpha}}{\partial p}\right|_{h_{\text{out}}} \frac{dp}{dt} + \left.\frac{\partial \bar{\alpha}}{\partial h_{\text{out}}}\right|_{p} \frac{dh_{\text{out}}}{dt} \right)
\end{aligned}
\tag{B.40}
$$

Using the outlet vapor quality by $x_{\text{out}} = \frac{h_{\text{out}} - h_f}{h_g - h_f}$, the partial derivative of the mean void fraction can be expressed as

$$\frac{\partial \bar{\alpha}}{\partial h_{\text{out}}} = \frac{1}{h_g - h_f} \frac{\partial \bar{\alpha}}{\partial x_{\text{out}}} \tag{B.41}$$

where the partial derivatives are calculated by numerical finite difference similar to equation B.14, B.26 and B.27.

The mean heat transfer coefficient in the two-phase region is again computed by numerical integration as

$$\bar{h}_{\text{tc}} = \frac{1}{L - L_A} \int_{L_A}^{L} h_{\text{tc}} \, dz \approx \frac{1}{N} \sum_{n=1}^{N} h_{\text{tc,n}} \tag{B.42}$$

Correlations

This chapter describes the different correlations that are used from the literature. The correlated variables are:

- Refrigerant heat transfer coefficients
- Refrigerant frictional pressure gradient, or friction factor (Fanning/Darcy Weisbach)
- Refrigerant void fraction
- Air heat transfer coefficient (louvered fin-and-tube)
- Air fin efficiency (louvered fin-and-tube)

The refrigerant can be either two-phase (condensing or evaporating) or single-phase. The transition between the phases results in switching of correlations. In order to ensure a smooth transition, without any discontinuities, smooth functions are applied, see section C.3. The air heat transfer correlation involves both determining the heat transfer coefficient and fin efficiency. The correlation applies only to fin-and-tube heat-exchangers with louvered fins.

Note that we have dropped the subscripts of the heat transfer coefficient in this appendix $h_{tc} \sim h$ for simplicity and should not be confused with enthalpy.

C.1 Refrigerant correlations

The refrigerant heat transfer coefficient is defined by equation A.39. The frictional pressure gradient is defined by equation A.40, however, sometimes the

friction factor or coefficient (e.g. equation A.41 or A.45) is used. The void fraction is defined by equation A.1.

C.1.1 Flow boiling heat transfer

Shah 1982

The method of Shah (1982) involves determining the nucleate boiling heat transfer coefficient h_{NcB} and the convective boiling heat transfer coefficient h_c, and essentially take the larger value of the two as the two-phase heat transfer coefficient. The method is as follows.

For horizontal flow calculate the dimensionless parameter N by

$$N = C_o \hspace{3cm} \mathrm{Fr_{fo}} > 0.04 \hspace{2cm} \text{(C.1)}$$

$$N = 0.38 \mathrm{Fr_{fo}}^{-0.3} C_o \hspace{2cm} \mathrm{Fr_{fo}} \leq 0.04 \hspace{2cm} \text{(C.2)}$$

If the flow is vertical, use equation C.1 for all values of the liquid only Froude number $\mathrm{Fr_{fo}}$ (assuming all mass flows as liquid). The liquid only Froude number and the dimensionless parameter C_o is given by

$$\mathrm{Fr_{fo}} = \frac{G^2}{\rho_f^2 g d} \hspace{3cm} \text{(C.3)}$$

$$C_o = \left(\frac{1-x}{x} \right)^{0.8} \left(\frac{\rho_g}{\rho_f} \right)^{0.5}. \hspace{2cm} \text{(C.4)}$$

If $N > 1$, calculate h_{NcB} from

$$h_{\mathrm{NcB}} = h_f 230 \mathrm{Bo}^{0.5} \hspace{2.5cm} \mathrm{Bo} > 0.0003 \hspace{2cm} \text{(C.5)}$$

$$h_{\mathrm{NcB}} = h_f (1 + 46 \mathrm{Bo}^{0.5}) \hspace{2cm} \mathrm{Bo} \leq 0.0003 \hspace{2cm} \text{(C.6)}$$

else if $1 > N \geq 0.1$, calculate h_{NcB} from

$$h_{\mathrm{NcB}} = h_f F \mathrm{Bo}^{0.5} \exp\left(2.74 N^{-0.1} \right) \hspace{2cm} \text{(C.7)}$$

else if $N < 0.1$, calculate h_{NcB} from

$$h_{\mathrm{NcB}} = h_f F \mathrm{Bo}^{0.5} \exp\left(2.47 N^{-0.15} \right) \hspace{2cm} \text{(C.8)}$$

where h_f is the superficial liquid heat transfer coefficient calculated by the Dittus Boelter (single-phase) correlation as

$$\mathrm{Nu}_f = 0.023 \mathrm{Re}_f^{0.8} \mathrm{Pr}_f^{0.4} \hspace{2cm} \text{(C.9)}$$

$$h_f = \mathrm{Nu}_f \frac{k_f}{d} \hspace{2cm} \text{(C.10)}$$

$$\text{Re}_f = \frac{G(1-x)d}{\mu_f} \tag{C.11}$$

$$\text{Pr}_f = \frac{\mu_f c_{p,f}}{k_f} \tag{C.12}$$

where the superficial liquid Nusselts, superficial liquid Reynolds and liquid Prandtl numbers have been used. Superficial liquid numbers come from the use of the superficial liquid velocity j_f in the Reynolds number, which is defined by

$$j_f = \frac{\dot{V}_f}{A} = \frac{\dot{m}_f}{A\rho_f} = \frac{G(1-x)}{\rho_f} \tag{C.13}$$

The boiling number Bo is defined as

$$\text{Bo} = \frac{q''}{G(h_g - h_f)} \tag{C.14}$$

and the constant F is determined as follows

$$F = 14.7 \qquad\qquad \text{Bo} > 0.0011 \tag{C.15}$$
$$F = 15.43 \qquad\qquad \text{Bo} \le 0.0011 \tag{C.16}$$

Calculate h_c from

$$h_c = h_f \frac{1.8}{N^{0.8}} \tag{C.17}$$

and chose the larger value of h_{NcB} or h_c to finally find the two-phase heat transfer coefficient.

Gunger and Winterton 1986

Gunger and Winterton (1986) used a linear model between the convective boiling and nucleate boiling contributions as

$$h = Eh_f + Sh_{\text{NcB}} \tag{C.18}$$

where the superficial liquid heat transfer coefficient h_f is calculated by the Dittus Boelter (single-phase) correlation from equation C.9, employing Nu_f, Re_f and Pr_f from equation C.10, C.11 and C.12. The convective enhancement factor E is given by

$$E = 1 + 24000\text{Bo}^{1.16} + 1.37(1/X_{\text{tt}})^{0.86} \tag{C.19}$$

where Bo is defined by equation C.14 and X_{tt} is the Martinelli parameter defined by

$$X_{\text{tt}} = \left(\frac{1-x}{x}\right)^{0.9} \left(\frac{\rho_g}{\rho_f}\right)^{0.5} \left(\frac{\mu_f}{\mu_g}\right)^{0.1} \tag{C.20}$$

The boiling suppression factor S is given by

$$S = [1 + (0.000\,001\,15)E^2\text{Re}_f^{1.17}]^{-1} \qquad \text{(C.21)}$$

and the nucleate boiling coefficient is given by the Cooper correlation as

$$h_{\text{NcB}} = 55p_r^{0.12}(-0.4343\ln p_r)^{-0.55}M^{-0.5}q''^{0.67} \qquad \text{(C.22)}$$

where M is the molecular weight, q'' the heat flux and $p_r = p/p_c$ the reduced pressure, where p_c is the critical pressure.

If the flow is horizontal and the liquid only Froude number (equation C.3) is below 0.05, then E and S must be multiplied with E_2 and S_2, given by

$$E_2 = \text{Fr}_{\text{fo}}^{(0.1-2\text{Fr}_{\text{fo}})} \qquad S_2 = \text{Fr}_{\text{fo}}^{0.5} \qquad \text{(C.23)}$$

Gunger and Winterton 1987

Gunger and Winterton (1987) later proposed a simpler correlation that only takes into account the convective boiling as

$$h = Eh_f \qquad \text{(C.24)}$$

where the convective enhancement factor E is computed by

$$E = 1 + 3000\text{Bo}^{0.86} + 1.12\left(\frac{x}{1-x}\right)^{0.75}\left(\frac{\rho_f}{\rho_g}\right)^{0.41} \qquad \text{(C.25)}$$

Again E must be corrected for horizontal flow depending on the liquid only Froude number. Studies by Thome (1996) recommends the newer as the better for refrigerant R134a.

Wojtan et al. 2005

The correlation of Wojtan et al. (2005b) is a phenomenological approach (flow regime dependent) involving determination of the flow regime. The flow map used for this is specified in Wojtan et al. (2005a). The flow map and correlation are both comprehensive works, involving several equations and if-clauses. It would be superfluous to state them all here, thus it has not been chosen. However, the flow map and correlated heat transfer coefficient is shown for a number of conditions on figure C.1. The correlation and flow map are indeed good studies for students, who wish to learn more of boiling heat transfer and two-phase flow phenomena.
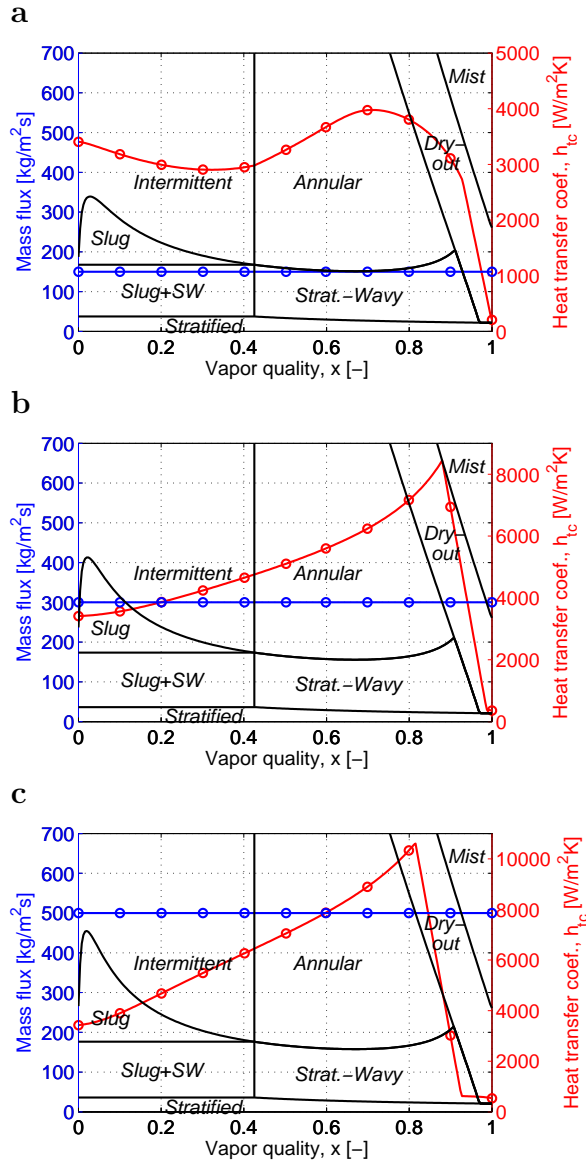
Figure C.1: Heat transfer coefficient (right) vs. vapor quality, (Wojtan et al., 2005b); Mass flux 150 (a), 300 (b) and 500 (c); R410A, $T_{\text{sat}}=10°$C, $q''=15$kWm^{-2}, $d=7.6$mm.

C.1.2 Condensation heat transfer

Shah 1979

Shah (1979) also proposed a condensation heat transfer correlation. The correlation is somewhat simple and formulated as follows

$$h = h_{\text{fo}} \left((1-x)^{0.8} + \frac{3.8 x^{0.76}(1-x)^{0.04}}{p_r^{0.38}} \right) \tag{C.26}$$

where p_r is the reduced pressure p/p_c and the liquid only heat transfer coefficient h_{fo} is calculated by the Dittus Boelter (single-phase) correlation as done by equation C.9, however, using the liquid only Reynolds number Re_{fo} (assuming all mass flows as liquid) instead of the superficial liquid Reynolds number Re_f. The liquid only Reynolds number is defined by

$$\text{Re}_{\text{fo}} = \frac{Gd}{\mu_f} \tag{C.27}$$

It means that the computed Nusselts number is the liquid only Nusselts number Nu_{fo}.

C.1.3 Two-phase frictional pressure drop

The traditional two-phase frictional pressure drop correlations is applied in the literature to both evaporation and condensation. From a fluid dynamic point of view the differences in boiling (evaporation or condensation), i.e. the nucleate boiling on the wall in the liquid film for evaporation, is not really influencing the pressure drop.

Müller-Steinhagen and Heck 1986

Müller-Steinhagen and Heck (1986) proposed a correlation that essentially is an empirical interpolation between the liquid and vapor frictional pressure gradients. The correlation is as follows.

$$\left(\frac{dp}{dz} \right)_{\text{fric}} = D(1-x)^{1/C} + Bx^C \tag{C.28}$$

where

$$D = A + 2(B - A)x \tag{C.29}$$

and the constant $C = 3$. A and B are the frictional pressure gradients of liquid only and vapor only respectively as

$$A = \left(\frac{dp}{dz}\right)_{\text{fo}} = f_D \frac{1}{d} \frac{G^2}{2\rho_f} \tag{C.30}$$

$$B = \left(\frac{dp}{dz}\right)_{\text{go}} = f_D \frac{1}{d} \frac{G^2}{2\rho_g} \tag{C.31}$$

$$\tag{C.32}$$

where $f_D = 4f_F$ and calculated from C.49 or C.50. Müller-Steinhagen and Heck (1986) used a transition between laminar and turbulent flow at Re = 1187, which is somewhat lower than expected (normally Re = 2300).

Grönnerud 1979

Grönnerud (1979) used the concept of the two-phase multiplier ϕ to the liquid only pressure drop as

$$\left(\frac{dp}{dz}\right)_{\text{fric}} = \phi \left(\frac{dp}{dz}\right)_{\text{fo}} \tag{C.33}$$

where

$$\phi = 1 + \left(\frac{dp}{dz}\right)_{\text{Fr}} \left[\frac{\left(\frac{\rho_f}{\rho_g}\right)}{\left(\frac{\mu_f}{\mu_g}\right)^{0.25}} - 1 \right] \tag{C.34}$$

where another frictional pressure gradient depending on the liquid only Froude number (from equation C.3) is introduced

$$\left(\frac{dp}{dz}\right)_{\text{Fr}} = f_{\text{Fr}} \left[x + 4 \left(x^{1.8} - x^{10} f_{\text{Fr}}^{0.5} \right) \right] \tag{C.35}$$

where the friction factor f_{Fr} is computed by

$$f_{\text{Fr}} = 1 \qquad\qquad \text{Fr}_{\text{fo}} \geq 1 \tag{C.36}$$

$$f_{\text{Fr}} = \text{Fr}_{\text{fo}}^{0.3} + 0.0055 \left(\ln \frac{1}{\text{Fr}_{\text{fo}}} \right)^2 \qquad\qquad \text{Fr}_{\text{fo}} < 1 \tag{C.37}$$

Quebén and Thome 2007

The correlation of Quibén and Thome (2007) is a phenomenological approach (flow regime dependent) involving determination of the flow regime similar to Wojtan et al. (2005b). The flow map used is also the same as Wojtan et al. (2005a). The flow map and correlation are both comprehensive works, as mentioned in section C.1.1, thus the equations are not shown here. However, a number of correlated frictional pressure gradients are depicted on figure C.2.
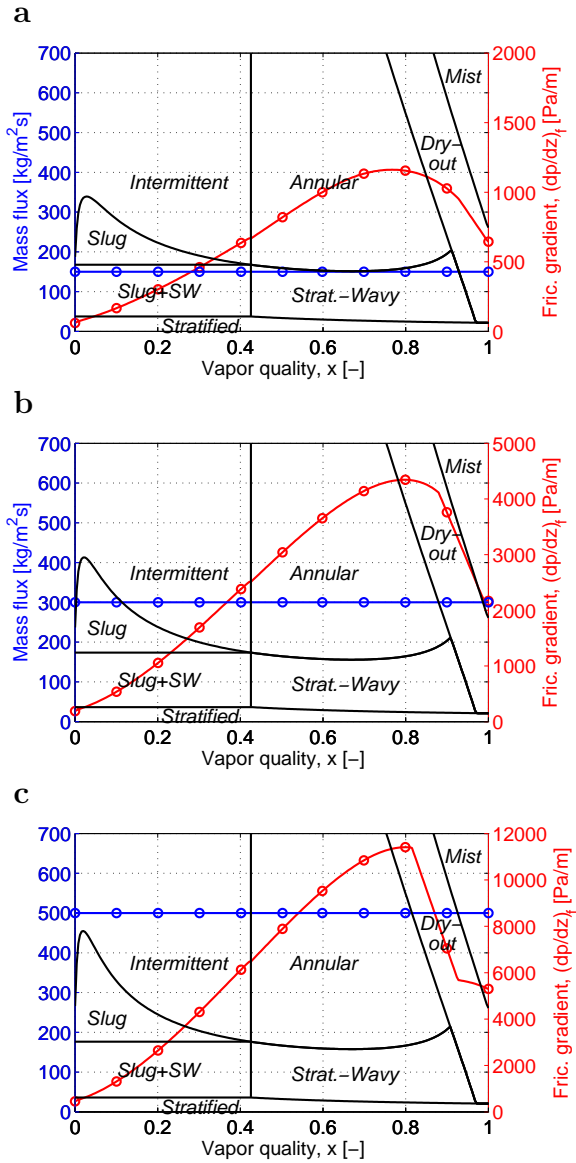
Figure C.2: Frictional pressure gradient (right) vs. vapor quality, (Quibén and Thome, 2007); Mass flux 150 (a), 300 (b) and 500 (c); R410A, T_{sat}=10°C, q''=15kWm^{-2}, d=7.6mm.

C.1.4 Void fraction

Most traditional void fraction models are in fact in the form of the slip ratio, where equation A.4 can be used to compute the void fraction as function of vapor quality. Other methods use empirical relations between the void fraction and the vapor quality. The simple void fraction models are only functions of the thermodynamic state, however, more sophisticated void fraction models take into account the mass flow, surface tension and gravity. The simplest void fraction model is the homogeneous void fraction model from equation A.5, assuming that the slip ratio equals one.

Zivi model 1964

Zivi (1964) proposed the following simple correlation for the slip ratio as

$$S = \left(\frac{\rho_g}{\rho_f}\right)^{-1/3} \tag{C.38}$$

Substituting into equation A.1 results in

$$\alpha = \left[1 + \left(\frac{1-x}{x}\right)\left(\frac{\rho_g}{\rho_f}\right)^{2/3}\right]^{-1} \tag{C.39}$$

Smith model 1969

Smith (1969) proposed another slip ratio as

$$S = K + (1 - K)\left[\frac{\frac{1}{\rho_g/\rho_f} + K\left(\frac{1-x}{x}\right)}{1 + K\left(\frac{1-x}{x}\right)}\right]^{1/2} \tag{C.40}$$

where the parameter $K = 0.4$.

Premoli model 1971

Premoli et al. (1971) proposed a more sophisticated method involving the Weber number and Reynolds number. The slip ratio is calculated by

$$S = 1 + F_1\left[\frac{y}{1 + yF_2} - yF_2\right]^{1/2} \tag{C.41}$$

where

$$F_1 = 1.578\mathrm{Re}_{\mathrm{fo}}^{-0.19}\left(\frac{\rho_f}{\rho_g}\right)^{0.22} \tag{C.42}$$

$$F_2 = 0.0273\mathrm{We}_{\mathrm{fo}}\mathrm{Re}_{\mathrm{fo}}^{-0.51}\left(\frac{\rho_f}{\rho_g}\right)^{-0.08} \tag{C.43}$$

$$y = \frac{x\rho_f}{(1-x)\rho_g} \tag{C.44}$$

Note that the liquid only Reynolds number from equation C.27 and liquid only Weber number are used. The latter defined by

$$\mathrm{We_{fo}} = \frac{G^2 d}{\sigma \rho_f} \tag{C.45}$$

where σ is the surface tension of the liquid and vapor interphase.

Steiners version of Rouhani-Axelsson drift flux model 1993

Steiner (1993) modified the Rouhani-Axelsson drift flux model as

$$\alpha = \frac{x}{\rho_g} \left[[1 + 0.12(1-x)] \left(\frac{x}{\rho_g} + \frac{1-x}{\rho_f} \right) + \frac{1.18(1-x)[g\sigma(\rho_f - \rho_g)]^{0.25}}{G\rho_f^{0.5}} \right]^{-1} \tag{C.46}$$

where g is the gravitational acceleration. The correlation is also more sophisticated taking into account mass flux, surface tension and gravity effects.

C.1.5 Single-phase correlations

Subcooled boiling can occur in the evaporator in the liquid region if the temperature of the wall is higher than the saturation temperature. Likewise if the temperature of the wall is lower than saturation, superheated condensation can occur in the condenser in the vapor region. These effects are non-equilibrium effects, in turn, the heat transfer coefficient is increased significantly by e.g. subcooled nucleate boiling near the wall as bubbles rise from the wall and collapse in the main stream. For dry-expansion systems (as considered in this thesis) subcooled boiling does not occur, however, it must be kept in mind for other applications. Superheated condensation does in fact occur, however, only very near to the two-phase area, thus these non-equilibrium effects are not addressed and simple general correlations for single-phase flow is used to both heat transfer and pressure drop.

Heat transfer

For turbulent flow and down to Re > 3000, the Gnielinski (1976) correlation is used as

$$\mathrm{Nu} = \frac{(f_D/8)(\mathrm{Re} - 1000)\mathrm{Pr}}{1 + 12.7(f_D/8)^{0.5}(\mathrm{Pr}^{2/3} - 1)} \tag{C.47}$$

where the Nusselts number is $\text{Nu} = \frac{hd}{k}$ and the *Darcy-Weisbach friction factor* is computed by

$$f_D = (0.7904 \ln(\text{Re}) - 1.64)^{-2} \tag{C.48}$$

For Laminar flow ($\text{Re} < 2300$), $\text{Nu} = 3.66$ assuming constant wall temperature. A simple linear transition has been used between the laminar and turbulent heat transfer coefficient.

Frictional pressure drop

Instead of using the friction factor computed by equation C.48, we chose to use the Blasius (2002) correlation for turbulent flow as

$$f_F = 0.0791 \text{Re}^{-1/4} \tag{C.49}$$

where the *Fanning friction factor* is used. For laminar flow $\text{Re} < 2300$ the friction is computed by

$$f_F = \frac{16}{\text{Re}} \tag{C.50}$$

C.1.6 Frictional pressure drop in U-bends

Two-phase U-bend correlations

Geary (1975) correlated the two-phase frictional pressure drop in U-bends by using the superficial vapor pressure drop as

$$\Delta p_{\text{fric}} = f \frac{L}{d} \frac{G^2 x^2}{2\rho_g} \tag{C.51}$$

where $L = \pi R$ is the length of the bend, R the radius of the bend and d the diameter of the pipe. The non-dimensional friction factor f is computed by

$$f = \frac{a \text{Re}_g^{0.5}}{\exp\left(0.215 \frac{2R}{d}\right) x^{1.25}} \tag{C.52}$$

where the superficial vapor Reynolds number is used as

$$\text{Re}_g = \frac{Gxd}{\mu_g} \tag{C.53}$$

and where the constant a in equation C.52 is $8.03 \cdot 10^{-4}$. The constant is different from the original paper, because the paper uses British units.

Single-phase U-bend correlations

Ito (1960) used the bend loss factor k to compute the single-phase frictional pressure drop as

$$\Delta p_{\text{fric}} = k\frac{G^2}{2\rho} \tag{C.54}$$

where the bend loss factor is computed by

$$k = 0.00241\alpha\theta\text{Re}^{-0.17}\left(\frac{2R}{d}\right)^{0.84} \tag{C.55}$$

and where θ is the bend angle (180 deg.) and α is computed by

$$\alpha = 1 + 116\left(\frac{2R}{d}\right)^{-4.52} \tag{C.56}$$

Equation C.55 works for small bend diameter compared to the tube diameter, i.e. $\text{Re}\left(\frac{d}{2R}\right) > 91$ and the Reynolds number must be $2 \cdot 10^4 < \text{Re} < 4 \cdot 10^5$.

C.2 Fin-and-tube air-side heat transfer

The air heat transfer coefficient and fin efficiency correlations apply to specific evaporator types and fin types of interest. In this study the evaporator type is fin-and-tube and the fin type is louvred. Wang et al. (1999) proposed the following correlation (both heat transfer coefficient and overall fin-efficiency), where the geometry and geometric symbols to be used are depicted on figure C.3, C.4 and C.5. For a staggered tube arrangement (figure C.3) the transverse tube length, $L_t = N_t P_t + \frac{P_t}{2}$. If the tubes are aligned as in-line arrangement, i.e. the tubes are as the word implies on the same line (longitudinally), then $L_t = N_t P_t$.

C.2.1 Heat transfer coefficient

For $\text{Re}_{Dc} < 1000$

$$j = 14.3117\text{Re}_{Dc}^{J1}\left(\frac{F_p}{D_c}\right)^{J2}\left(\frac{L_h}{L_p}\right)^{J3}\left(\frac{F_p}{P_l}\right)^{J4}\left(\frac{P_l}{P_t}\right)^{-1.724} \tag{C.57}$$

where j is the dimensionless *Colburn j-factor* defined by

$$j = \frac{\text{Nu}}{\text{Re}_{Dc}\text{Pr}^{1/3}} = \text{StPr}^{2/3} \tag{C.58}$$

and Re_{Dc} is the Reynolds number based on collar diameter D_c and maximum velocity $U_{\max}$, Nu is the Nusselt number, Pr the Prandtl number, St is the Stanton number defined by

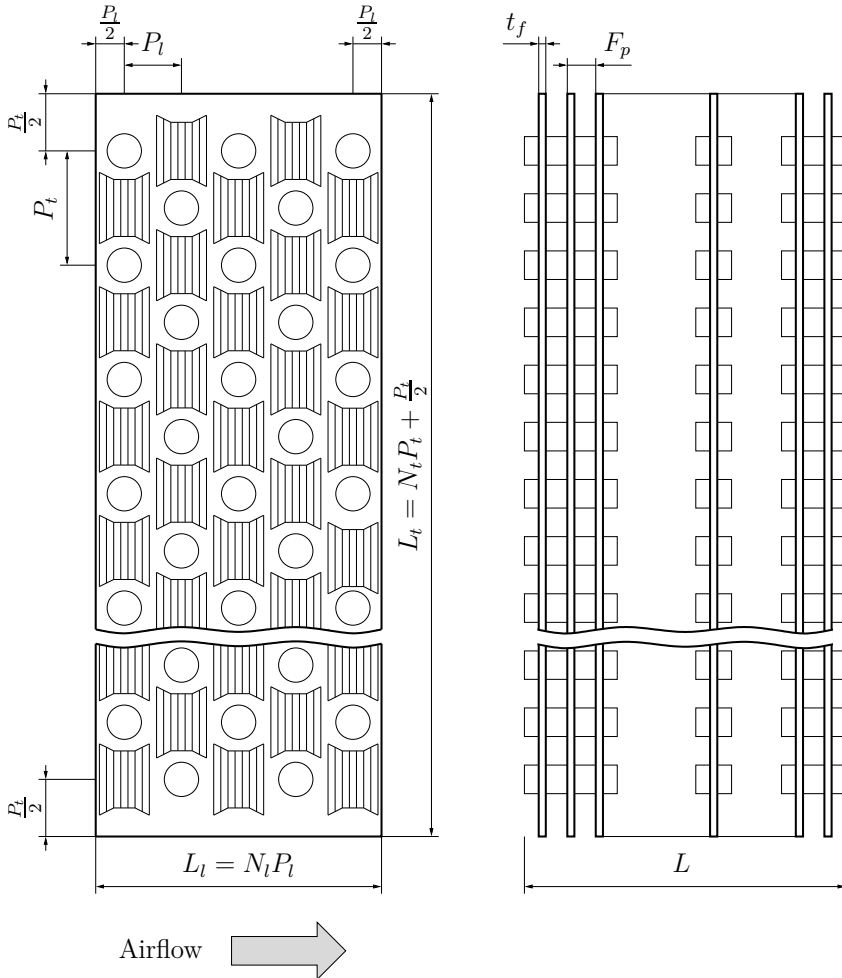$$\mathrm{St} = \frac{h}{\rho U_{\max} c_p} = \frac{\mathrm{Nu}}{\mathrm{Re}_{Dc}\mathrm{Pr}} \tag{C.59}$$

Figure C.3: Staggered fin and tube coil geometry; P_t = Transverse tube pitch, P_l = Longitudinal tube pitch, N_t = Transverse number of tube rows, N_l = Longitudinal number of tube, L_t = Transverse length of coil, L_l = Longitudinal length of coil, L = Length of tubes, F_p = Fin pitch, t_f = Fin thickness.

From which the heat transfer coefficient can be calculated, however, using the Nusselts number gives the same result. The maximum velocity is calculated by mass conservation using the frontal area A_{fr} and the minimum free flow area A_{min} through the coil as

$$U_{\text{max}}A_{\text{min}} = U_{\text{fr}}A_{\text{fr}} \tag{C.60}$$

The frontal area of a discrete heat exchanger cell is

$$A_{\text{fr}} = P_t\Delta z \tag{C.61}$$

and the minimum free flow area is then

$$A_{\text{min}} = A_{\text{fr}} - D_c\Delta z - (P_t - D_c)\frac{t_f\Delta z}{F_p} \tag{C.62}$$

which is the gray area on figure C.5. The coefficients from equation C.57 are computed as follows

$$J1 = -0.991 - 0.1055\left(\frac{P_l}{P_t}\right)^{3.1}\ln\left(\frac{L_h}{L_p}\right) \tag{C.63}$$

$$J2 = -0.7344 + 2.1059\left(\frac{N_l^{0.55}}{\ln\left(\text{Re}_{Dc}\right) - 3.2}\right) \tag{C.64}$$

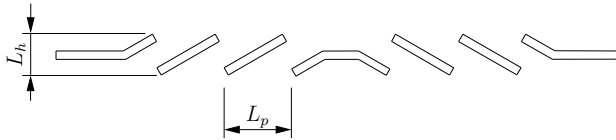$$J3 = 0.08485\left(\frac{P_l}{P_t}\right)^{-4.4}N_l^{-0.68} \tag{C.65}$$

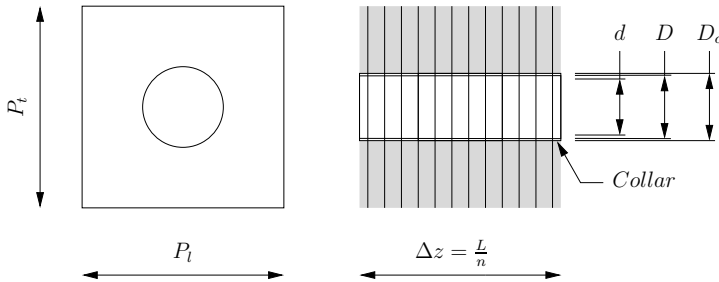Figure C.4: Louvred fin type; L_h = Louver height, L_p = Louver pitch.

Figure C.5: A discrete heat exchanger cell, A_{min} = gray area, d = Internal diameter, D = Outer diameter, D_c = Collar diameter = $D + 2t_f$, n = Number of cells.

$$J4 = -0.1741 \ln(N_l) \tag{C.66}$$

For $\mathrm{Re}_{Dc} \geq 1000$

$$j = 1.1373 \mathrm{Re}_{Dc}{}^{J5} \left(\frac{F_p}{P_l}\right)^{J6} \left(\frac{L_h}{L_p}\right)^{J7} \left(\frac{P_l}{P_t}\right)^{J8} N_l^{0.3545} \tag{C.67}$$

where

$$J5 = -0.6027 + 0.02593 \left(\frac{P_l}{D_h}\right)^{0.52} N_l^{-0.5} \ln\left(\frac{L_h}{L_p}\right) \tag{C.68}$$

$$J6 = 0.4776 + 0.40774 \left(\frac{N_l^{0.7}}{\ln(\mathrm{Re}_{Dc}) - 4.4}\right) \tag{C.69}$$

$$J7 = -0.58655 \left(\frac{F_p}{D_h}\right)^{2.3} \left(\frac{P_l}{P_t}\right)^{-1.6} N_l^{-0.65} \tag{C.70}$$

$$J8 = 0.0814 \left(\ln(\mathrm{Re}_{Dc}) - 3\right) \tag{C.71}$$

where D_h is the hydraulic diameter, defined by

$$D_h = \frac{4A}{P} = \frac{4A_{\min}}{\frac{A_T}{L}} \tag{C.72}$$

Note that the cross sectional area here is the minimum free-flow area $A_{\min}$, and that the perimeter P is the total surface area A_T including the area of fins A_f, divided by the effective flow length L, i.e. the length of the heat exchanger, thus the hydraulic diameter for a single discrete cell is the same as if the whole heat exchanger were considered. The surface area of the fins for a discrete heat exchanger cell is

$$A_f = 2 \left(P_l P_t - D_c^2 \frac{\pi}{4}\right) \frac{\Delta z}{F_p} \tag{C.73}$$

and the total surface area is then

$$A_T = A_f + D_c \pi \left(\Delta z - t_f \frac{\Delta z}{F_p}\right) \tag{C.74}$$

Smooth functions are applied to ensure a smooth transition in the heat transfer coefficient at $\mathrm{Re}_{Dc} = 1000$ (see section C.3).

C.2.2 Overall surface fin efficiency

When the heat transfer coefficient is calculated the fin efficiency η_f and overall surface fin efficiency η_o can be computed. The Schmidt approximation (Schmidt, 1949) is used as

$$\eta_f = \frac{\tanh(mr\phi)}{mr\phi} \tag{C.75}$$

where

$$m = \sqrt{\frac{2h}{k_f t_f}} \tag{C.76}$$

$$\phi = \left(\frac{R_{\text{eq}}}{r} - 1\right)\left[1 + 0.35\ln(R_{\text{eq}}/r)\right] \tag{C.77}$$

where h is the heat transfer coefficient, k_f is the thermal conductivity of the fin and r is the radius including collar thickness. For staggered tube arrangement

$$\frac{R_{\text{eq}}}{r} = 1.27\frac{X_M}{r}\left(\frac{X_L}{X_M} - 0.3\right)^{0.5} \tag{C.78}$$

and for in-line tube arrangement (or one-row coil)

$$\frac{R_{\text{eq}}}{r} = 1.28\frac{X_M}{r}\left(\frac{X_L}{X_M} - 0.2\right)^{0.5} \tag{C.79}$$

where X_M and X_L are calculated according to figure C.6.

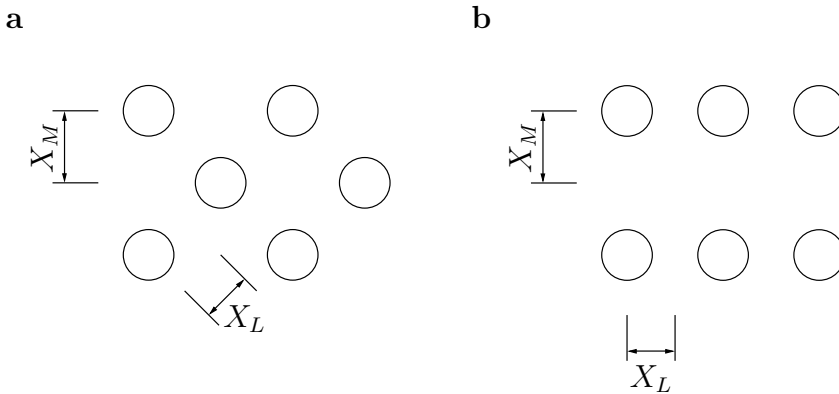**a**   **b**

Figure C.6: X_M and X_L for staggered (a) or in-line (b) tube arrangement

For both tube arrangements, X_M is computed as

$$X_M = \frac{P_t}{2} \tag{C.80}$$

For staggered tube arrangement, X_L is computed as

$$X_L = \frac{1}{2}\sqrt{\left(\frac{P_t}{2}\right)^2 + \left(\frac{P_l}{2}\right)^2} \tag{C.81}$$

and for in-line tube arrangement, X_L is computed as

$$X_L = \frac{P_l}{2} \tag{C.82}$$

The overall surface fin efficiency is finally calculated by

$$\eta_o = 1 - \frac{A_f}{A_T} \left(1 - \eta_f\right) \tag{C.83}$$

C.3   Smooth functions

Smooth transition functions are applied for all transitions between vapor, two-phase and liquid correlations or relations such as the effectiveness-NTU. Every time a modeler introduces events, one must ask if the event causes a discontinuity or even worse a jump discontinuity. If it does one must apply transition functions. It can be a simple linear transition to remove the jump or more advanced higher order continuous transitions. Figure C.7 shows a first order continuous transition from $0.95 \leq x \leq 1$, meaning that the first derivative is also continuous as depicted.

Similar smooth transitions are applied at the two-phase to liquid phase transition from $0 \leq x \leq 0.05$. If the first derivative is not continuous it may have negative effects on the solving process, since the solver has to handle discontinuous first derivatives. The transition function used here is trigonometric and implemented as follows from Richter (2008).

The switching between two functions $f(x)$ and $g(x)$ is done by

$$z(x) = f(x)T(x) + g(x)(1 - T(x)) \tag{C.84}$$

where the transition function $T(x)$ is

$$T(x) = \begin{cases} 1 & x \leq x_t - \frac{\Delta x}{2} \\ t(x) & x_t - \frac{\Delta x}{2} < x < x_t + \frac{\Delta x}{2} \\ 0 & x \geq x_t + \frac{\Delta x}{2} \end{cases} \tag{C.85}$$

where x_t is the transition point and Δx is the transition length. For $T(x)$ to have no jumps requires that

$$t\left(x_t - \frac{\Delta x}{2}\right) = 1 \qquad t\left(x_t + \frac{\Delta x}{2}\right) = 0 \tag{C.86}$$

and for $T(x)$ to be smooth requires that

$$\left.\frac{dt(x)}{dx}\right|_{x=x_t - \frac{\Delta x}{2}} = 0 \qquad \left.\frac{dt(x)}{dx}\right|_{x=x_t + \frac{\Delta x}{2}} = 0 \tag{C.87}$$
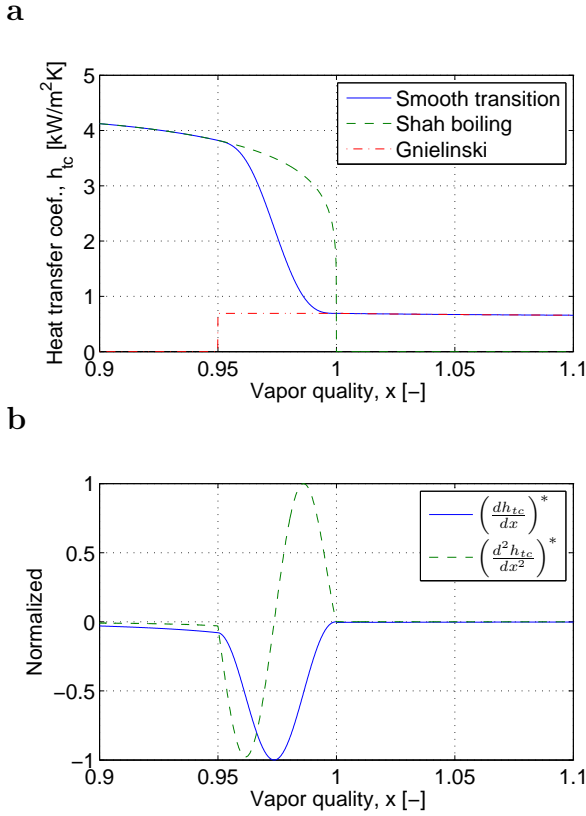
a

b

Figure C.7: A first order continuous smooth transition. (a) Smooth transition in heat transfer coefficient from two-phase to vapor phase. (b) First and second derivative of smooth transition (normalized by its maximum absolute value); R410A, $G=300\mathrm{kgm^{-2}s^{-1}}$, $T_{\mathrm{sat}}=10°\mathrm{C}$, $q''=15\mathrm{kWm^{-2}}$, $d=7.6\mathrm{mm}$.

and for $\frac{dT(x)}{dx}$ to be smooth requires that

$$\left.\frac{d^2t(x)}{dx^2}\right|_{x=x_t-\frac{\Delta x}{2}} = 0 \qquad \left.\frac{d^2t(x)}{dx^2}\right|_{x=x_t+\frac{\Delta x}{2}} = 0 \qquad (C.88)$$

The following general trigonometric function satisfies these restrictions.

$$\frac{dt(\varphi)}{d\varphi} = a\cos^n(\varphi) \qquad (C.89)$$

where a is a scaling factor, n is a positive integer and φ the phase defined by

$$\varphi = \frac{x - x_t}{\Delta x}\pi \tag{C.90}$$

Integrating yields

$$t(\varphi) = a\left(\frac{\cos^{n-1}(\varphi)\sin(\varphi)}{n} + \frac{n-1}{n}\int \cos^{n-2}(\varphi)d\varphi\right) + b \tag{C.91}$$

where a and b can be found employing equation C.86. The resulting function is $(n-1)th$ order continuous. The functions $f(x)$ and $g(x)$ must also be $(n-1)th$ order continuous for $z(x)$ to be $(n-1)th$ order continuous.

In figure C.7 n was equal to 2, thus first order continuous, $a = -\frac{2}{\pi}$, $b = \frac{1}{2}$, $x_t = 0.975$ and $\Delta x = 0.05$. Same approach is used for all function transitions from two-phase to vapor phase and from two-phase to liquid phase where $x_t = 0.025$.

Sensitivity of pressure fluctuations

The initial simulations of the discontinuous liquid injection principle showed fluctuations in important variables such as superheat and pressure. These fluctuations have a time period corresponding to the cycle time of the liquid injection model divided by the number of channels in the evaporator, when running in even flow distribution mode. The fluctuations have not been observed as high in any similar experiments carried out at Danfoss, where the sampling frequency was high enough to capture these fluctuations. The sampling frequency is often chosen to be 1 s^{-1} for refrigerant temperature and pressure at Danfoss, which is too low for capturing the injection dynamics seen in the numerical model. In the following analysis, we test the sensitivity in the numerical model with regards to these fluctuations.

D.1   Introduction

The object of the sensitivity analysis is to investigate the sensitivity of

- The amplitude of the fluctuations in p_{out}, $\dot{m}_{\text{out}}$ and T_{out}
- The time constant of a step response in p_{out}, $\dot{m}_{\text{out}}$ and T_{out}

The amplitude directly addresses the fluctuations, whereas the time constant is a measure of the evaporator response. However, they are likely to be dependant

and therefore good measures for the sensitivity analysis. The sensitivity analysis should provide better understanding of the dynamics and the fluctuations in the model.

To avoid the use of filtering of these fluctuations when evaluating the time constants, we chose to evaluate the time constants on a system with the conventional electronic expansion valve and distributor without considering the injection dynamics, i.e modeled by continuous distribution of individual channel mass flows predicted by each channel pressure drop.

Besides the evaluation of the two above mentioned variables, we also present steady state sensitivity of the two simulated systems, that is, the sensitivity in cooling capacity, UA-value and COP.

The sensitivity analysis is performed on a 8.8 kW air-conditioning system. The model is exactly the same as introduced in section 6.4. The evaporator model is including all the refrigerant channels, their refrigerant injection and circuiting. The evaporator consists of two coils each with two channels and interlaced circuitry. Each channel consists of 18 tubes and 17 U-bends. One control volume per tube was chosen for numerical discretization, i.e. 18 tubes and 17 bends and equals 35 control volumes per channel and 140 in total. We assume uniform distribution of airflow and refrigerant phases into the evaporator ($F_{\mathrm{air}} = F_x = 1$). The liquid injection model is setup to have the multi-orifice design, even distribution and a cycle time of 6 seconds.

D.2   The method

The method involves a baseline simulation with baseline input parameters. These parameters are then varied one at a time and a new simulation is performed at each variation. The input parameters are divided in *uncertainty parameters* and *other parameters*. The uncertainty parameters are actually correction factors multiplied to the correlations applied in our model. The correlations are the same as shown in table 5.1 including the use of a the constant slip ratios. The factors are varied up and down according to the typical uncertainty in these correlations, see table D.1. The other parameters are geometric constraints and input conditions to the model. These are varied within a specified realistic range as indicated in table D.2.

The simulations are performed as shown on figure D.1. We use the conventional electronic expansion valve and distributor from 0 to 500 seconds with continuous refrigerant flow to each channel. The liquid injection principle is then modeled from 500 to 900 seconds.

We simulate from 0-200 seconds with control, from 200-500 seconds without control and from 500-900 seconds with control. We do this to avoid the effects of the control devices on the time constants. By control, we mean the control of the superheat according to table D.2 and control of the subcooling to 2 K. The superheat is controlled by the opening degree of the expansion valve and

Table D.1: Uncertainty parameters

Input parameters		min		base		max
Refrigerant friction correction factor (fc)		0.6	0.8	1	1.2	1.4
Two-phase heat transfer correction factor (htc 2p)		0.6	0.8	1	1.2	1.4
Vapor heat transfer correction factor (htc vp)		0.8	0.9	1	1.1	1.2
Air heat transfer correction factor (htc air)		0.85	0.925	1	1.075	1.15
Phase velocity slip-ratio (Slip)	1*	2.04	2.72	3.4	4.08	4.76

* Homogeneous flow assumption (special case outside the uncertainty measure)

Table D.2: Other parameters

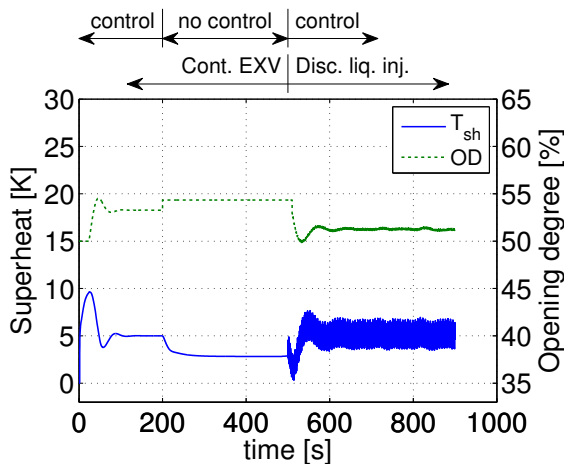| Input parameters	min		base		max
Manifold/suction pipe length [m] (Lman)	2	3.5	5	6.5	8
Superheat [K] (Tsh)			5	10	15
Outdoor temperature [°C] (Tout)	27.8	31.4	35		
Air velocity [m s^{-1}] (Vair)	0.696	0.928	1.16	1.392	1.624

Figure D.1: The method

the subcooling is controlled by the charge in the system. The time constant is defined as the time it takes for a given output variable to reach 63% of its change, based on a step change in a given input variable (here the opening degree with a 2% step change, see figure D.1). The amplitude of the liquid injection fluctuations is recorded between 700 and 900 seconds and taken as half of the maximum change.

We record the cooling capacity, UA-value and COP of the continuous EXV system at time equals 195 seconds. Between 700-900 seconds we compute the mean cooling capacity, UA-value and COP of the discontinuous liquid injection system. Both systems are controlled to similar superheat and subcooling in order to compare the sensitivity at similar conditions.

D.3   Sensitivity of steady state results

We visualize the sensitivity by spider diagrams throughout the following sections. We only include the relevant parameters from table D.1 and D.2 that actually have an effect compared to the baseline result. Figure D.2 shows the sensitivity in normalized cooling capacity, UA-value and COP for the two analyzed systems.

Even though the two systems give small differences in the cooling capacity, UA-value and COP, the normalized values become the same. The sensitivity in these performance measures of the two systems is thus the same. The most dominant parameters are the outdoor temperature, the superheat and the air-side velocity. As the outdoor temperature decrease or the air-side velocity increase the performance increases (no attention to air-side pressure drop). As the superheat increases the performance decreases. The less dominant parameters are the heat transfer coefficient and friction coefficient corrections.

The impact of the heat transfer coefficients are, however, higher in the UA-value than in the cooling capacity and COP. This is because the UA-value is decoupled from the temperature driving potential for heat transfer such that the UA-value may change, but the evaporating pressure adjusts, which means that the cooling capacity become more or less maintained, while having minor effect on COP.

A change in the air-side velocity will result in a change in air-side heat transfer coefficient, fin efficiency and heat exchanger effectiveness. Therefore, the air-side velocity change shows higher impact compared to the change in the air-side heat transfer coefficient.

The decrease in outdoor temperature does not have an impact on the UA-value, however, it gives a larger enthalpy difference across the evaporator and thus a higher cooling capacity. The COP increases even more, since the temperature difference between evaporation and condensation also decrease.

The increased superheat has a degrading effect in all performance values. The UA-value decrease because of the higher superheated region. In turn, the
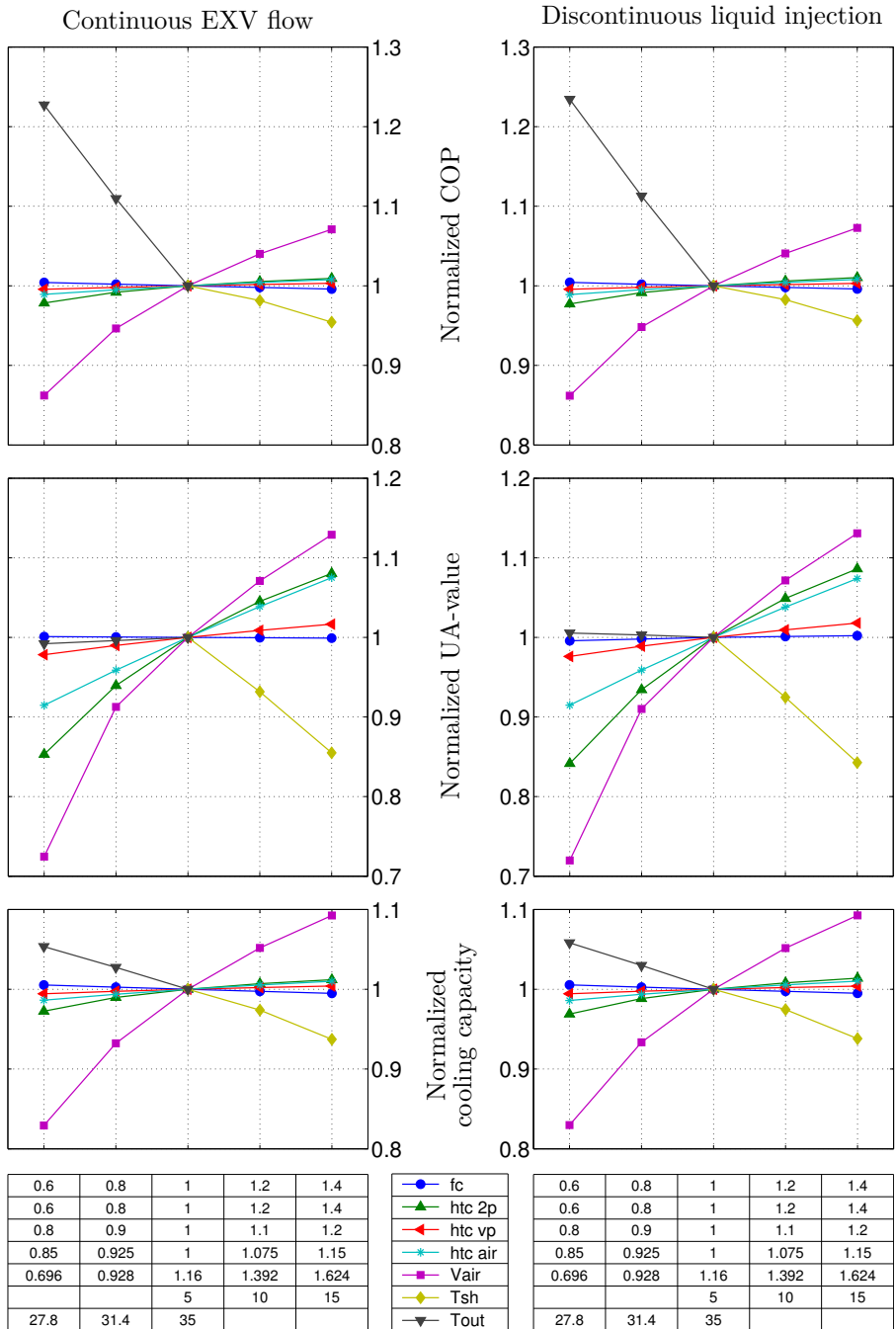
Figure D.2: Steady state sensitivity

increased superheat results in lower density to the compressor, and thus lower refrigerant mass flow and cooling capacity.

D.4   Sensitivity of the time constant

We evaluate the time constants based on both a step increase and step decrease of 2% in opening degree. We chose this because there may be differences in the two responses. The steps are performed at no control in the system and from the same initial condition, i.e. superheat according to table D.2 and subcooling set to 2 K.

Interestingly, we found that the response of the refrigerant going into the manifold and out of the manifold was quite different. The thermal capacitance of the manifold wall was the dominant mechanism for these differences. In particular, the heat transfer from the manifold wall to the refrigerant slowed the temperature response after the manifold significantly, while having no effect on the pressure response. Because of these differences we address the responses of both the mixed refrigerant entering the manifold and the refrigerant exiting the manifold in separate sections. First, we perform a small study on the response of a manifold with and without an evaporator upstream and heat transfer from the manifold wall.

D.4.1   Effect of manifold volume

We used the simpler moving boundary evaporator model in order to simplify the simulations in this section. We used the same evaporator size and refrigerant conditions entering the evaporator and entering the manifold according to the baseline sensitivity simulation. By using the moving boundary model, the circuitry was not modeled and it leads to a higher heat transfer, since all channels sees the same inlet air temperature in the moving boundary model. Therefore, we adjusted the air temperature such that the refrigerant conditions matches the baseline sensitivity simulations.

Figure D.3 shows the normalized step responses in temperature, pressure and mass flow of the refrigerant exiting the manifold based on a decrease in mass inflow by 2%. The first column in the figure is showing simulations carried out at a manifold length of 2m, whereas the second column are simulations carried out at a manifold length of 5m. The first row are simulations of the manifold only, the second row are simulations of the manifold coupled to the evaporator and the third row are simulations of the manifold coupled to the evaporator but including the thermal capacitance of the manifold wall. The moving boundary model did not include the thermal capacitance of the evaporator wall and the refrigerant heat transfer coefficient inside the insulated manifold was assumed to be 700 W $m^{-2}K^{-1}$.
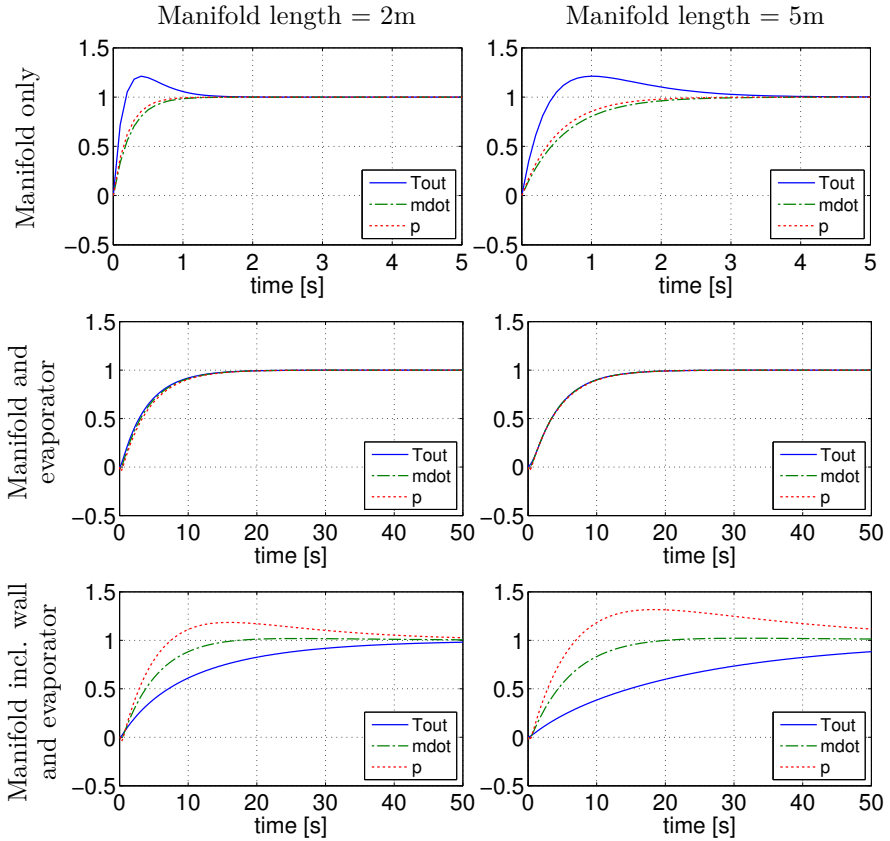
Figure D.3: Normalized step responses on a decrease in mass inflow by 2%

The results from figure D.3 shows that the time constants of the manifold considered alone are on the order of a magnitude faster than the time constants of the combined system (manifold and evaporator). We may therefore expect that the response of the manifold does not have a significant effect on the combined system. This is also indicated on figure D.3 (row 2) as the manifold length is increased, where no particular differences are seen on the response. The individual mass in the evaporator and 2m manifold was 134g and 32g, respectively. When increasing the length of the manifold to 5m the mass was 51g in the manifold. It means that the mass increases by 11.5% percent as the manifold increases from 2m to 5m for the combined system. The mass is therefore not increased significantly and therefore we see similar responses in the combined system.

Interestingly, the temperature changes faster than the pressure when considering the manifold only. It is important to note the fact that the temperature

and pressure are independent for the vapor, however, dependent for the two-phase mixture. This dependency seems to be the mechanism for the similar responses and time constants of the combined system (figure D.3, row 2) in both temperature, pressure and mass flow.

If we include the thermal capacitance of the manifold wall and describe the heat transfer from the manifold wall to the refrigerant by Newton's law of cooling (constant heat transfer coefficient), we get a significant effect on the response (figure D.3, row 3). In fact, the slower dynamics of the manifold wall causes a slower change of the refrigerant temperature. The pressure time constant is the same, however, the response produces an overshoot. The mass flow time constant increases and the response becomes a bit slower, because of the density change associated with the slow temperature change.

Because the heat transfer in the manifold alters the temperature response, we may also expect that the heat transfer in the evaporator plays an important role for the dynamic response together with the refrigerant charge. The dependency of pressure and temperature in the two-phase region causes the heat transfer to affect the pressure response also.

These results are the reason why we address the responses of both the mixed refrigerant entering the manifold and the refrigerant exiting the manifold in the sensitivity analysis to follow. It also shows that the location of temperature measurements etc. are important, when considering the refrigerant dynamics.

D.4.2 Response of the refrigerant exiting the manifold

Figure D.4 shows the normalized step responses in temperature, pressure and mass flow of the refrigerant exiting the manifold.

From these figures it is difficult to see any differences in the response based on an increase or decrease in opening degree. Furthermore, the responses are in concord with figure D.3 (row 3, 5 m manifold).
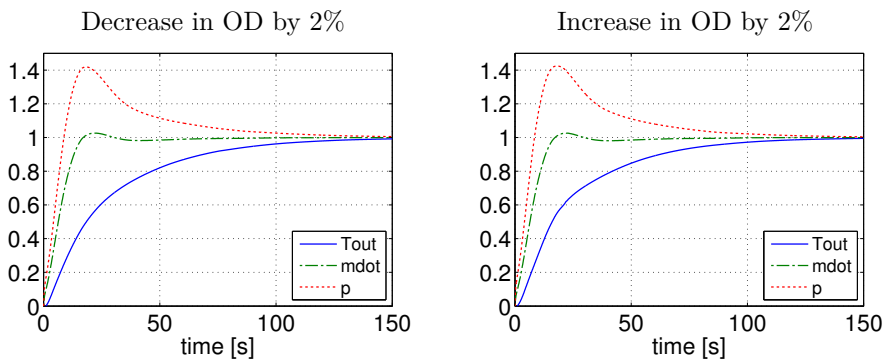

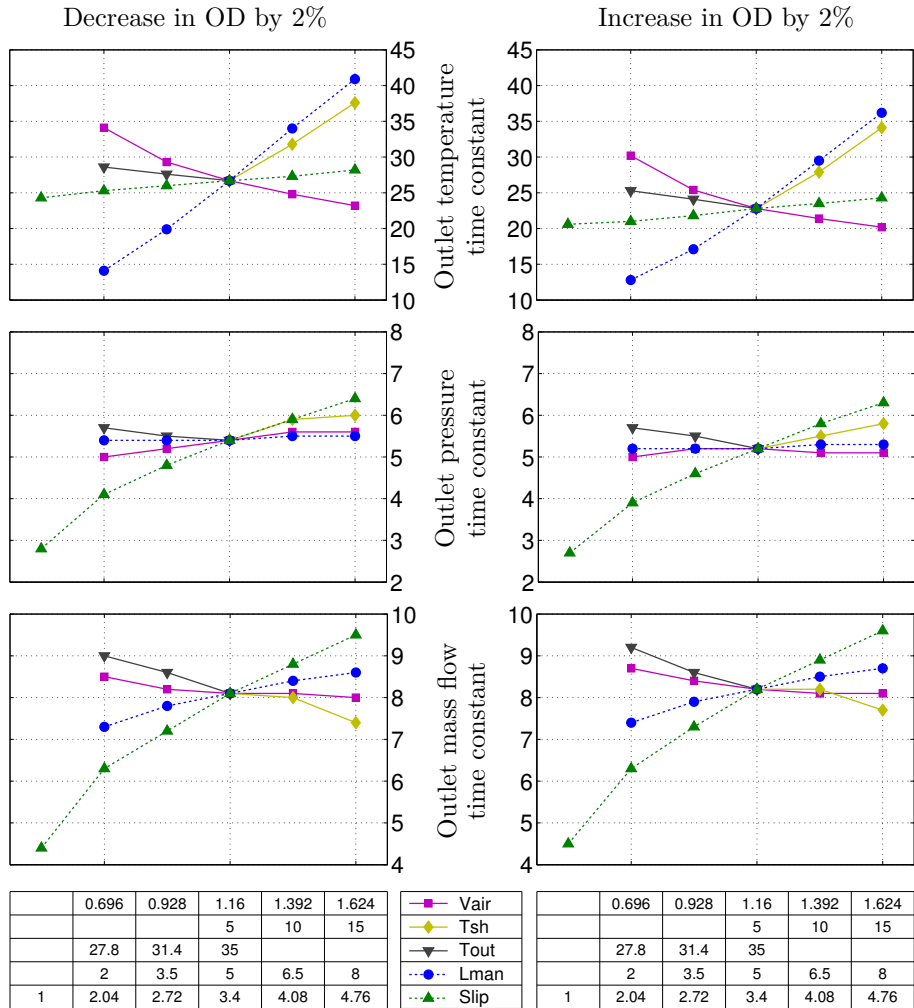Figure D.4: Normalized step responses

Figure D.5: Time constant sensitivity

The pressure response is the fastest and around 4-5 times faster than the temperature response, which is the slowest. The mass flow response is around 1.5 times higher than the pressure response. Furthermore, the pressure and mass flow rate produces an overshoot. There is a small delay in the temperature response of 1.1 seconds. The delay in pressure corresponds to the speed of sound of R410A, which for saturated vapor at $5°C$ is 168.8 ms^{-1}. It means that for the 8 meter channel length, the delay in pressure is 47 ms when considering the gas flow only.

The sensitivity of the time constants are shown in figure D.5. Again, we only include the relevant parameters from table D.1 and D.2 that actually have an effect compared to the baseline time constant.

Again, it is difficult to see the differences in the time constants based on an increase or decrease in opening degree. The trends are the same, however, the temperature response shows the highest value change and becomes around 4 seconds less on an increase in opening degree.

The pressure response is mostly influenced by the slip ratio, which essentially determines the mass of the two-phase region, i.e. main refrigerant charge in the evaporator. If the slip ratio is 1 it implies homogeneous flow, a minimum amount of refrigerant and the fastest response. The baseline slip ratio of 3.4 corresponds to the value of the Zivi (1964) slip ratio correlation. Essentially, the refrigerant mass inside the evaporator effects the pressure response such that more mass results in a slower response. This is also the case if the outdoor temperature is decreased, thereby decreasing the inlet vapor quality to the evaporator and results in more in situ mass. In contrast, the increased superheat shows a slower response. The most obvious effect would have been a faster response, since the increased superheat results in a lower in situ mass due to the increased vapor zone. However, it seems that there are other effects that causes this response.

Interestingly, the manifold length (or volume) does not effect the pressure response. This is due to the faster dynamics of the manifold volume as shown in section D.4.1. However, the heat transfer from the manifold wall to the refrigerant slows down the response of the refrigerant temperature. It also explains why the length of the manifold has an impact on the time constants of the temperature and mass flow, since the thermal capacitance of the manifold changes. Actually, the 5 meter length of the manifold equals 3.6 kg of copper. When the temperature response is slower, so is the density and therefore also the mass flow rate response.
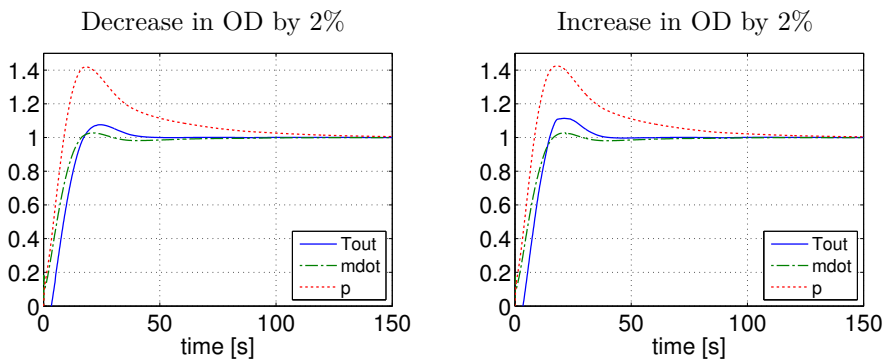

Figure D.6: Normalized step responses

D.4.3 Response of the refrigerant entering the manifold

Figure D.6 shows the normalized step responses in temperature, pressure and mass flow of the *mixed* refrigerant entering the manifold in the baseline simulation.

The response becomes something in between the results in figure D.3 (column 2, row 2-3). This is because the manifold outlet response will affect the manifold inlet response. If we did not include the thermal capacitance of the manifold wall, the response would have been close to figure D.3 (column 2, row 2). The
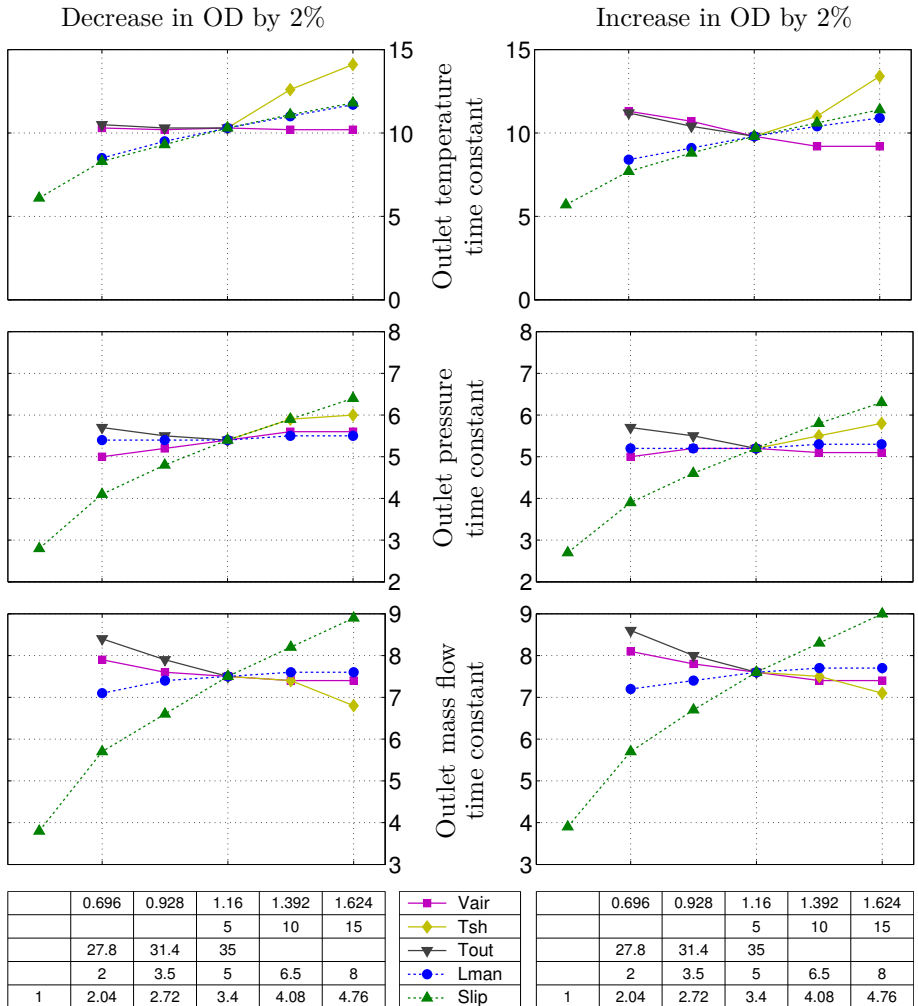

Figure D.7: Time constant sensitivity

slow temperature response as was shown for the refrigerant exiting the manifold is not observed and becomes less than 2 times slower than the pressure response. In contrast, the pressure response is exactly the same as when considering the refrigerant exiting the manifold. Again, it is difficult to see any differences in the response based on an increase or decrease in opening degree.

The sensitivity of the time constants are shown in figure D.7. Again, we only include the relevant parameters from table D.1 and D.2 that actually have an effect compared to the baseline time constant.

It seems that some parameters effects the response differently based on a decrease or increase in opening degree. These variables are the air velocity and outdoor temperature, but the difference is small.

As expected, the manifold length is not as dominant in the temperature response of the entering mixed refrigerant, in contrast to the refrigerant exiting the manifold. Besides this, the trends are fairly the same as for the exiting refrigerant, all though the temperature time constants are significantly faster.

D.5 Sensitivity of the amplitude

In this section, we only address the refrigerant exiting the manifold. We chose to use both the maximum amplitude of the simulated liquid injection principle fluctuations and the standard deviation to characterize the fluctuations, see figure D.8. We did this because the maximum amplitude may include slower fluctuations from the control of the system than what we are interested in. The standard deviation gives a better estimate of the fluctuations, however, it does not show how large the fluctuations are. Again, we only include the relevant parameters from table D.1 and D.2 that actually have an effect compared to the baseline fluctuations.

The results indicate that the considered parameters are not able to eliminate the fluctuations within their specified limits. The liquid injection principle is most likely to be responsible for these fluctuations in the model. This is because the fluctuations have a frequency corresponding to the cycle time of liquid injection model divided by the number of channels in the evaporator. Since these fluctuations have not been observed as high in experiments so far, the injection phenomenon is still to be fully understood. We believe that the fluctuations in our mixture model may be a result of or combination of different reasons:

- Use of steady state heat transfer, pressure drop and void fraction correlations at large transients in mass flow.
- The assumption of thermodynamic equilibrium.
- The absence of the liquid-vapor interfacial friction and drag dynamics.

What actually reduce the fluctuations in the model, is an increase in slip ratio, i.e. a higher refrigerant charge. However, it seems that there is a limit to
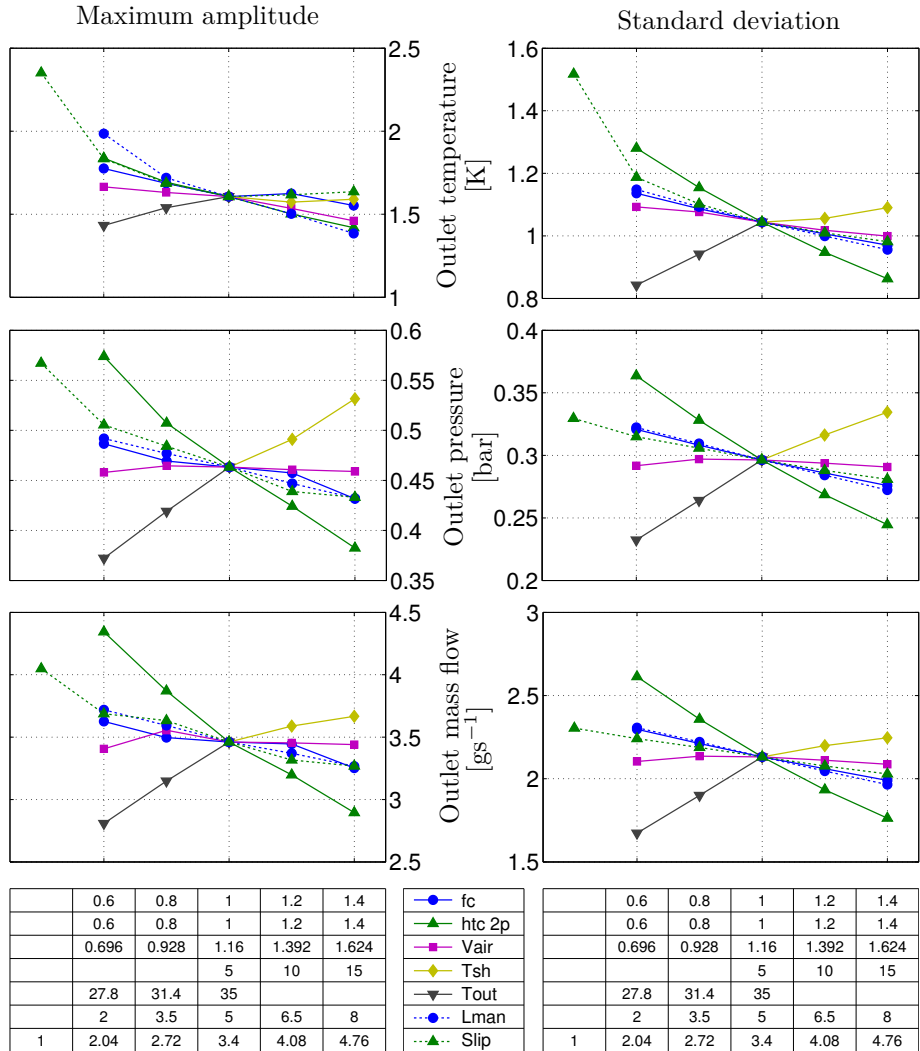
Figure D.8: Sensitivity of maximum amplitude and standard deviation

the reduction by this factor considering the maximum amplitude, since it goes towards a constant value as the slip ratio increases. In contrast, the standard deviation seems to decrease linearly as the slip ratio increases. The reduction in the fluctuations is however minor.

The two-phase heat transfer has the most significant effect together with the outdoor temperature. The two-phase heat transfer coefficient may be the first thing to study in order to eliminate the fluctuations. Indeed, the heat transfer

coefficient is believed to be altered drastically as the refrigerant are injected into the individual channels. It seems that the steady state correlations are insufficient to model the dynamic behavior with large transients in mass flow. The decrease in outdoor temperature will eventually reduce the pressure difference across the liquid injection model, and result in a higher opening degree to keep up the mass flow rate. Furthermore, the decrease in outdoor temperature results in decreased inlet vapor quality and consequently more mass in the evaporator. The manifold length also has an effect on the temperature fluctuations as expected, but show an effect on the pressure also in contrast to the conclusion of the time constant sensitivity. The effect of the manifold length is however minor.

It is difficult to generalize these results, because they were made for a specific evaporator with specified circuitry and with specific operating conditions. A variation in the operating conditions seems to have some effect on the fluctuations. For example, the increased superheat increases the pressure fluctuations, however, it does not increase the outlet temperature fluctuations. On the other hand, the air velocity seems to have an effect on the temperature fluctuations, but no effect on the pressure fluctuations.

Interestingly, the increased two-phase frictional pressure drop minimizes the fluctuations in all variables to some extend. The most obvious result would have been the opposite. However, the momentum dynamics is much faster than the energy and mass dynamics, thus we do not expect that the momentum may be the primary cause of these fluctuations.

D.6 Summary

From the investigation of the time constants, we found that the responses are different for the refrigerant entering the manifold and the refrigerant exiting the manifold. The thermal capacitance of the manifold pipe wall and the heat transfer from the wall to the refrigerant in the manifold was the mechanism for this difference. It produced a slower temperature response at the outlet of the manifold rather than in the beginning, where the refrigerant streams are mixed, while having no effect on the pressure response. The most important parameter for the dynamic response is the slip ratio, i.e. the refrigerant charge in the evaporator. The more mass the slower response.

This parameter was also important for the liquid injection fluctuations, however, the two-phase heat transfer correlation and the outdoor temperature showed larger effect on the fluctuations. The decrease in outdoor temperature increases the opening degree and decreases the inlet vapor quality (more mass), both having a dampening effect on the fluctuations. The effect of the two-phase heat transfer correlation seems more difficult to explain and should be further investigated.

We conclude the sensitivity analysis by stating that the numerical model cannot in its present form eliminate the fluctuations caused by the liquid injection principle. By choosing a void fraction (or slip flow) correlation that predicts larger refrigerant charge, the fluctuations may be minimized, but not significantly. Therefore, other phenomenons such as dynamic heat transfer, interfacial dynamics and thermodynamic non-equilibrium effects seems to prevail in this novel area of the injection dynamics. No heat transfer correlations exists for dynamic two-phase flow known to the authors, and the steady state heat transfer correlations seems to be insufficient.

Furthermore, there was not found any particular similarity between the dynamic evaporator response and the fluctuations.